An improved SPH method and its application in the turbulence multiphase flow in the bearing chamber of aeroengine

Xipeng Lyu

Thesis submitted to the university of Nottingham for the
degree of Doctor of Philosophy

March 2022

Abstract

This thesis is devoted to the propose a novel particle stabilization scheme, improve the existing Smoothed Particle Hydrodynamics (SPH) and apply it to the multi-phase turbulent flow in the bearing chamber of an aeroengine.

In SPH, the motion of particles is based on symmetric inter-particle forces, such that the conservation of momentum is guaranteed. Inter-particle forces, however, can not prevent particle clustering. Clustering may occur for several reasons. A fundamental issue is the so-called tensile instability, which is caused by the properties of the kernel gradient. Clustering may also be caused by discontinuities in the pressure (e.g. due to surface tension) and the pressure gradient (e.g. due to gravity), which may lead to instabilities around the interface between two fluids (Kruisbrink et al., 2018 [1]). Wall penetration is also a form of particle clustering.

Standard SPH is known to suffer from particle clustering, which affects the stability of simulations in particular in cases with large deformations and high fluid velocities. One of the grand challenges defined by the SPHERIC Steering Committee is the clustering of particles. Kruisbrink et al. (2018) developed a particle collision model to reduce particle clustering. This model is quite effective and performs the best for so-called inelastic collisions. However, by changing the approach velocities of colliding particles, the model is energy dissipating to some extent.

As further work, it is investigated in this thesis whether the original particle collision model may be further developed into a shift model, such that there is no dissipation of

global kinetic energy. This has resulted in the particle collision shift model, where the positions of colliding particles are changed, but not their velocities. Thus, kinetic energy is conserved. It is demonstrated that potential energy is also conserved in a constant force field, like gravitation. With these features the particle collision shift model is non-dissipative in the simulation of many real cases.

To allow for the modelling of the multi-phase flow in a bearing chamber, characterized by an incompressible (oil) phase and a compressible (air) phase, a compressible flow solver is needed. For this purpose, weakly compressible SPH is used. Moreover, at the higher rotational shaft speeds in a bearing chamber, the air flow is turbulent. Turbulence modelling is relatively underdeveloped in SPH. Some available SPH turbulence models and models from the CFD literature are explored, in particular SPH versions of the mixing length and Spalart-Almaras turbulence models, as made available in the WCSPH code Hydra of the University of Nottingham.

The particle collision shift model in WCSPH is used in combination with so-called δ-SPH, a method from the SPH literature to reduce high-frequent fluctuations in the density and pressure. In this thesis a simplified version of δ-SPH is used, to decrease the computational cost.

The above-mentioned SPH modelling approach is used to validate the two turbulence models in WCSPH against the commercial CFD code Ansys Fluent. As benchmark case the Taylor-Couette flow between two concentric rotating cylinders is chosen, as a simplified bearing chamber without sump and vent pipes. A number of two-dimensional configurations is studied, at different rotational speeds and radius ratios of the cylinders, under single phase and multi-phase, laminar and turbulent flow conditions.

The agreement of the single phase, laminar and turbulent SPH results with those of Fluent is good in terms of velocity and pressure profiles, and reasonably well in terms of turbulent viscosity. The turbulent viscosity obtained with the Spalart-Almaras turbulence model matches better with Fluent than that of the mixing length turbulence model, but the model is computationally much more expensive.

The agreement of the multi-phase, turbulent SPH results with Fluent is reasonable, in terms of velocity and pressure profiles, although the latter show more pressure fluctuations. The turbulent viscosity is underpredicted by both SPH turbulence models, compared to that of Fluent, whilst the difference between the two SPH turbulence models is small.

Finally, two and three dimensional SPH simulations are performed of a simplified bearing chamber with one suction pipe. Multi-phase turbulent flow conditions are modelled with air around a rotating inner shaft and a liquid film along the outer chamber wall. Surface tension is taken into account, as modelled by the continuum surface force model of Brackbill, in Fluent as well as SPH. The results of the 2D bearing chamber show similar trends as those of the corresponding Taylor-Couette flow. The results of the 3D bearing chamber show quite some dissipation of energy, due to a turbulent viscosity, which is much higher than that of Fluent, and affects the velocity distribution.

In summary:

An energy-conserving shift (collision shift) model to prevent the particle clustering is derived and through the comparative study with the Fickian shift model, the superiority of the collision displacement model in terms of accuracy, stability, computational efficiency and dissipation characteristics is obtained.

A hybrid method which combines the so-called δ-SPH and the collision shift model is proposed. The potential of this hybrid method in application with multiphase flow is demonstrated in five benchmark case studies.

Progress has been made in the turbulence modelling with SPH in applications that are moving towards that of a bearing chamber in aeroengines. In particular the results of the two-dimensional simulations are promising, as they show a reasonable agreement with those of Fluent, whilst further investigation is needed in the application of the SPH models to three dimensional cases, towards the real bearing chamber.

First Supervisor: Prof. Richard Jefferson-Loveday

Second Supervisor: Dr. Arno C.H. Kruisbrink

Third Supervisor: Prof. Herve Morvan

Internal Examiner: Dr Donald Giddings, Faculty of Engineering, University of Nottingham

External Examiner: Professor Antonio Gil, Faculty of Science and Engineering, Swansea University

Submitted: Nov 11th 2022

Declaration

I declare that the thesis is the result of my own work which has been mainly undertaken during the period of registration as a PhD candidate at the University of Nottingham unless otherwise referenced.

Journal articles

1. A shift model based on particle collisions - preserving kinetic energy and potential energy in a constant force field - to avoid particle clustering in SPH, Xipeng Lyu, Arno Kruisbrink*, Richard Jefferson-Loveday, Journal of Computational Physics, Date of submission: Dec 8, 2020, status: In press, pre-proof. https://doi.org/10.1016/j.jcp.2022.111530

Acknowledgements

I would like to express my gratitude to all those who helped me during the PHD.

My deepest gratitude goes first and foremost to my supervisors Dr. Arno Kruisbrink, Prof. Richard Jefferson-Loveday and Prof. Herve Morvan for their valuable advice continuous support and patience during my PHD study. Their immense knowledge and plentiful experience have encouraged me in all the time of my academic research.

I would like to thank the INNOVATIVE doctoral programme which is partially funded by the Marie Curie Initial Training Networks (ITN) action, and partially by the Institute for Aerospace Technology (IAT) at the University of Nottingham.

I would like to thank the Gas Turbine and Transmission Research Centre (G2TRC) for the HPC and the technical support.

Last my thanks would go to my beloved family for their loving considerations and great confidence in me all through these years. I also owe my gratitude to my friends, my colleges in the IAT as well as in G2TRC. They have been helpful and caring for me after my two surgeries and during the pandemic.

Contents

List of Figures

List of Tables

Chapter 1 Introduction

1.1. Background

Since the invention of the jet engine, engine manufacturers have improved engine power and efficiency by increasing air pressure and temperature. However, to prevent the temperature of turbine blades reaching their melting point, the demand for efficiency improvements in other parts of the engine, including air syphon systems, oil systems, and bearing chamber systems has increased.

An aircraft engine's bearing chamber is designed to capture the oil flowing out of the bearing and retransmit it to the oil system. The captured oil both lubricates the gearbox components and cools the engine core.

The bearing chamber is the key part of the oil system. A jet engine bearing chamber, which is a cylinder around the turbine shaft, is shown in Fig. 1. As the turbine shaft rotates on these ball bearings, oil is forced to leave the ball bearing by the turbine shaft's angular velocity. Oil is collected on the side wall of the bearing chamber.

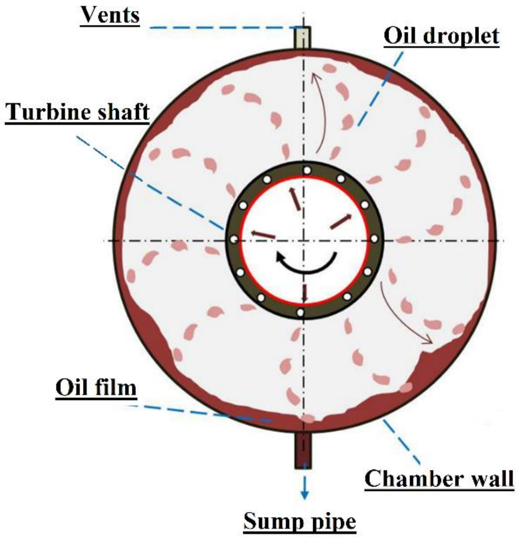

Fig. 1. A schematic representation of a bearing chamber [2].

The shaft speed can reach 15,000 rpm. The shaft’s high angular velocity accelerates the airflow which generates an airflow shear force in the chamber’s annular space strong enough to drive the oil film against the chamber wall. At the upper limit of shafts’ velocity ranges, the shear force generated by the airflow can become the oil driving force, which, together with the centrifugal force, overcomes gravity.

Oil should be removed from the system to prevent oil build-up, overheating and degradation. When oil is discharged from the system, some air is also discharged automatically.

1.2. The Challenge

1.2.1. Challenge in bearing chamber

Engine designers need a powerful numerical method that can completely model aero-engine bearing chambers. However, simulating aero-engine bearing chambers is challenging due to high-density ratios and high-speed multiphase flows inside such bearing chambers. Modelling mass, momentum and heat exchanges in multiphase flows and selecting a way to model fluid interactions are significant challenges. In bearing chambers, the oil film is driven by the airflow, and it is, therefore, illogical to treat the multiphase flow as a single-phase flow. When liquid in the bearing chamber is a flowing film, it exists as a continuum and sometimes forms droplets. Dispersed air bubbles can also be trapped on the surface of the liquid continuum or film. Since the interface is moving, its location cannot be determined in advance. Furthermore, the film can be deformed into any shape under the influence of velocity, viscosity, surface tension and density. For example, different rotational speeds at the inner shaft produce different flow patterns (laminar or turbulent). Different flow patterns, in turn, lead to different interface deformations, and the interface may even roll or break up. When the interface rolls, air gets trapped in the liquid film; when the interface breaks up, oil droplets form.

Modelling these phenomena simultaneously is complicated. It is critical to use computational fluid dynamics (CFD) method to analyse challenges and make engineering design choices. Comprehending the multiphase flow processes and turbulent flow patterns in aero-engine bearing chambers is difficult. Most bearing chamber research is conducted via experimentation, mathematical analysis and grid-based CFD modelling, often under single-phase, two-dimensional and isothermal conditions.

However, the grid-based CFD method has no advantages for simulating multiphase flow problems. Volume of fluid and level-set methods, in combination with Lagrangian methods to simulate droplets, are used to capture interfaces with large deformations. Nonetheless, smoothed particle hydrodynamics (SPH), as a pure Lagrangian method, may become an alternative for simulating the multiphase flow in aero-engine bearing chambers.

1.2.2. Challenge in SPH

Although researchers have been developing the SPH method for nearly fifty years, there is still no easy way to simulate multiphase turbulent flow in bearing chambers Developing the SPH method into a practical solution will require reducing particle clustering, which is prevalent in single-phase and multiphase flows (including static), in SPH [1,3–6]. Clustering may occur for several reasons. A fundamental issue is the so-called tensile instability, which is caused by properties of the kernel gradient. Clustering may also be caused by pressure discontinuities (caused by surface tension and other factors) and the pressure gradient (influenced by such factors as gravity). Pressure-induced clustering can lead to instabilities around the interface between two fluids [1]. Wall penetration is another form of particle clustering. Most particle stabilisation methods apply to single-phase flows and are energy dissipating. No method for dealing with particle clustering in multiphase flows while preserving energy has yet been identified.

A related challenge is reducing non-physical/numerical fluctuations in the pressure around the interface. Huge pressure fluctuations influence how interfaces move. Most well-known turbulence models are designed for grid-based methods. The literature on SPH and turbulence models is limited, and all SPH turbulence models are applied in hydrodynamics (single-phase flow). Developing a simple and effective turbulence model for the multiphase flow in bearing chambers is another challenge. Finally, modelling a bearing chamber requires identifying proper boundaries, such as inlets, outlets and pressure boundaries, and a proper treatment for the rotating shaft. Each boundary condition may influence the turbulence property near the chamber wall.

1.3. The Thesis

1.3.1. Specific objectives

The aim of this work is to develop an improved SPH method to model the complex multiphase flow of air and oil in aeroengine bearing chambers. The major objectives of the work presented in this thesis are:

1. survey the literature on particle stabilisation methods and turbulence models in SPH;
2. develop a shift model based on particle collisions to help prevent particle clustering in SPH and validate the model;
3. contribute to the stability and accuracy of the SPH method for high-density ratio multiphase flow and validate improved methods against theoretical and experimental data from existing literature;
4. apply the improved SPH method to modelling the multiphase turbulence flow in a 2D/3D bearing chamber.

Two SPH methods are used in this study:

Incompressible SPH (ISPH) is mainly used to develop and validate the above-mentioned shift model. The simulations of a variety of benchmark cases are performed with the ISPH code, developed at the Harbin Engineering University, China by amongst others Prof. Xing Zheng

Weakly compressible SPH (WCSPH) is used to validate the turbulence models in SPH. The simulations of the Taylor-Couette flow and bearing chamber are performed with the WCSPH code Hydra, developed at the University of Nottingham by amongst others my supervisor Dr. Arno C.H. Kruisbrink.

1.3.2. Thesis Overview

This chapter introduces the background of the thesis. It also discusses the challenges associated with multiphase flow and the SPH method. This chapter also describes the thesis’s specific objectives.

In Chapter 2, the chapter briefly reviews the application of conventional CFD to multiphase flow in bearing chambers the survey of all of the relevant literature is presented. Chapter 2 also provides an overview of the SPH method as well as of the improved SPH models used in this study.

Chapter 3 explains the SPH methodology. This chapter describes the SPH models and model coefficients used in this study’s simulations.

The basic principles of ISPH and WCSPH are described in sections 3.3 and 3.5. Section 3.4 describes an improved δ-SPH model for multiphase flow in WCSPH, which deals with pressure fluctuations, and the simplified version used in this study. The well-known mixing length (ML) turbulence model and the Spalart-Allmaras (SA) turbulence model are described in sections 3.9.1 and 3.9.2. The Fickian shift model, a popular shift model in the literature, used for comparison, is described in section 3.10. The new shift model for reducing particle clustering based on particle collisions is described in section 3.11.2. These models are indispensable for the simulation of the multiphase turbulent flow in a bearing chamber.

In Chapter 4, the results of four benchmark cases and two engineering cases are presented. This chapter discusses single-phase simulations performed with ISPH. The particle collision shift model's results are compared with those of the Fickian shift model. Both shift models' conservative properties, accuracy and computational efficiency are then assessed.

Whereas Chapter 4 presents the simulation of the particle collision shift model with ISPH for a single-phase flow, Chapter 5 presents numerical studies of the particle collision shift model with δ-SPH for multiphase cases, including low-/high-density ratio, static and dynamic, and short- and long-duration flows. The work presented in these two chapters perfectly verifies the particle collision shift with both ISPH and δ-SPH and for both single-phase and multiphase cases. This result lays a solid foundation for simulating multiphase flows in bearing chambers.

Chapter 6 presents a series of single-phase Taylor-Couette flows with three different radius ratios obtained by using improved δ-SPH (δ-SPH_CS) with ML and SA turbulence models. The simulation results are comparable with the Fluent results, also with SA, and thus lead into the work presented in Chapters 7 and 8.

Chapters 7 presents the multiphase Taylor-Couette flow at different rotational speeds obtained with δ-SPH_CS (SA and ML). The simulation results are also validated with Fluent (k-ω). Chapter 7 also compares ML and SA. Based comparison results, δ-SPH_CS (SA) is chosen for the work discussed in Chapter 8.

Based on results in Chapters 6 and 7, Chapter 8 presents the simulation of multiphase turbulent flow in simplified 2D and 3D bearing chambers. The simulations presented in this chapter provide qualitative insight into modelling turbulent flow in bearing chambers by comparing the results with those of Fluent.

Chapter 9 provides a summary and conclusion of the thesis. This chapter also includes recommendations for future work and summarises this thesis's unique contribution to SPH method and jet engine research.

Chapter 2 Literature review

2.1. Conventional CFD model

Farral et al. [7] modelled the oil film formed on the walls of the bearing chamber by a depth averaged method and implemented it with a commercial computational fluid dynamics (CFD) code CFX 4.3 which accounts for the effect of shear force and gravity. Although the model ignores the variation of axial direction, the error in the prediction of results for this model was still under 15% when compared to the experimental data. Farrall et al. [8] used a Euler-Lagrange solver to model the interaction between the oil film and the oil droplets, as well as the motion of the oil film along the bearing chamber walls. However, this method is computationally expensive and only valid for thin oil films. Robinson et al. [9] also used a commercial CFD code, Fluent 6, to model the draining flow perpendicular to the moving oil film, with surface tension and sharpening algorithms used to increase the accuracy of the simulation. This numerical study validated their experimental work. Glahn [10] illustrated the air/oil flow heat transfer using a temperature gradient method based on a two-dimensional finite element method. To satisfy the safety and reliability criteria for the bearing chamber, especially at high rotational speeds, Stefan [11] introduced a function for the bearing chamber heat transfer and used the flow rate, shaft speed and chamber geometry to build the Nusselt number.

Among the available simulation techniques, the volume of fluid (VOF) method has been widely applied to the flow in the bearing cavity, especially for capturing the oil-gas interface. Young and Chew [12] introduced many complex multiphase flow applications, such as air/oil system applications in the aeroengine, in which the VOF method plays an important role. Hasmhi et al. [13] investigated several multiphase models and concluded that the VOF method is the most useful oil-gas model for shear driven wall film flow and introduced the $k-\varepsilon$ turbulence model to investigate the complex multiphase flow in the bearing chamber. Peduto et al [14] also used the $k-\varepsilon$ turbulence model and VOF method as a correction of their own CFD simulation. In this method, the interface needs to be reconstructed during the simulation, and the interface shear force from the air flow needs to be handled correctly. When shaft and pressure velocity are low, the simulation results are very reliable. Alexandre et al. [15] describe a new multiphase flow simulation model based on the Adaptive Mesh Approach (AMA). Not only was the computational requirement reduced, but also the breakup of interface could be captured. The level set (LS) method is another method for capturing the interface, however, in this method, the mass is not conserved. Recently, several studies have developed the LS method further to improve on this disadvantage. Menard [16] improved the LS method by combining it with the ghost fluid and VOF methods to capture the discontinuities for pressure, density and viscosity, and the conservation of mass. Yaguo et al. [17] use coupled level set and volume of fluid (CLSVOF) in ANSYS-Fluent 14.5 to simulate the oil-gas multiphase flow and the performance of the oil return system.

Adeniyi et al. [18] presented a CFD method which combines the Eulerian-Lagrangian method with the CLSVOF method to simulate the oil droplets and complex multiphase flow, with encouraging results. Based on this work, Adeniyi et al. [19] applied the

CLSVOF method as well as $k-\omega$ turbulence model to simulate the transition of oil droplets emerging into the bearing chamber.

2.2. Smoothed particle hydrodynamics

Smoothed Particle Hydrodynamics (SPH) was introduced by Gingold and Monaghan [20] and Lucy [21] in 1977 to simulate astrophysical problems. It is now frequently used to simulate the dynamics of continuous media like fluid flows. The Lagrangian SPH technique approximates the continuous flow field using particles, with variables such as pressure, density, and velocity interpolated by a kernel function. It offers several significant benefits over conventional Eulerian CFD techniques. SPH is capable of simulating fluid motion with large deformations, and the free surface and interface between two fluids are captured in a straightforward manner. SPH has found a position in aero-engine design as a truly mesh-free Lagrangian approach [22,23].

In the SPH method, the fluid incompressibility can be exerted in two distinct ways. Initially, incompressible fluid flows were simulated using a weakly compressible SPH method (WCSPH), in which the fluid was assumed to be somewhat compressible, with its pressure solved by an equation of state based on the density and the artificial sound speed introduce by Monaghan [24]. The standard WCSPH method is simple and easy to programme, however, the time step of this method must be short, and the oscillation of the density causes significant pressure fluctuations in the spatial and temporal domains [6].

To decrease this kind of fluctuation in the pressure, Antuono et al. [25] introduced the δ-SPH method to obtain a smoothed pressure by applying a zeroth-order density smoothing term to the continuity equation. For the simulations of complex free surface flow, this has been proven to be accurate and robust [26] although it will case extra dissipation. As mentioned by Sun [27] the δ-SPH method is simple to implement and is effective for avoiding high frequency pressure fluctuations and the occurrence of non-physical energy by numerical error in standard SPH. In recent years this method has become popular and widely used for hydrodynamics problems in different scientific areas [13–21].

To overcome the timestep limitation of WCSPH, a strictly incompressible SPH (ISPH) approach has been proposed. In ISPH, the pressure is solved by the Poisson equation, making it more stable and precise than WCSPH [28]. Shao and Lo [29] developed a density-invariant ISPH method, while Lee et al. [30] developed a velocity divergence-free ISPH. Additionally, Hu and Adams [31] improved the stability of ISPH by combining a divergence-free velocity field with a density-invariant field.

2.2.1. Multiphase model

Fluid phenomena in nature, engineering, and scientific research often involve multiple fluids. The particles that comprise each fluid are different and exhibit unique characteristics. One notable difference is the fluid’s density. The ratio of the heavy fluid to the lighter fluid is known as the density ratio and typically ranges 1 and 1.3 under ambient temperature and pressure. For instance, the typical water–silicone oil density ratio is around 1.25. The density ratio between two gases can be larger than between two liquids. For example, the oxygen–hydrogen density ratio is 16. Furthermore, the density ratio in a liquid-gas system can be even higher [32]. For example, the typical oil–air density ratio is around 1000.

J.J. Monaghan and A. Kocharyan [33] used the conventional SPH technique to study the dusty gas that results from volcanic activity. They demonstrated the ability of SPH to handle broken free surfaces, highlighting its capability of analysing multiphase flow at small densities ratios. However, this method is not suitable for multiphase flows with high density ratios due to interfacial instabilities. Valizadeh et al. [34] determined the conventional SPH technique is only valid for multiphase flows with density ratios ($\frac{\rho_{dense}}{\rho_{light}}$) below 10. However, in most gas–liquid flows, the density ratio is more than 10, often reaching the hundreds or thousands.

Colagrossi and Landrini [35] also determined that for density ratios larger than 10 numerically and suggested a modified approximation for spatial derivatives based on this concept. In their scheme, pressure is calculated separately for dense and light fluids. For dense fluids, the equation of state is the Tait equation; for light fluids, the equation of state is the modified Tait equation, which includes a linked cohesive pressure term to describe the surface tension. A moving least squares method is used to reinitialize the density periodically at intermediate time steps. Artificial viscosity and XSPH can stabilise the flow field. In addition to these non-physical improvements, small time steps are required. Hu and Adams [31,36] proposed a multiphase SPH method that uses a particle smoothing function in which neighbouring particles contribute to the volume but not the density. Their method resolves a density discontinuity at a phase interface and fulfils mass conservation since it uses a density summation equation. Their technique was successfully applied to macroscopic and mesoscopic multiphase flows. Monaghan and Rafiee [32] found that despite a high density ratio, air must be considered because its thermodynamic pressure has a substantial impact on the dynamics. Thus, they developed an SPH method that incorporates a repulsion term between the phases. Their algorithm effectively analyses multiphase flows with high density ratios. Kruisbrink et al. [37] proposed a quasi-buoyancy correction term to simulate multiphase flow at high density ratios. Their approach produced acceptable results for modelling stratified flow and internal gravity waves for multiphase fluid with a density ratio of 100. Kruisbrink et al. [1] used particle collisions to avoid particle clustering and stabilise the fluid–fluid interface. Their approach targeted water–air applications with density ratios up to 1000 and physically realistic wave speed ratios.

To reduce the pressure fluctuation in the multiphase flow, Zheng and Chen [38] proposed a first-order density correction term, instead of the zeroth-order density smoothing term in δ-SPH [25], which could effectively suppress density oscillation in multiphase flow.

2.2.2. Surface tension model

Oil will be introduced into the bearing chamber simulation and will strike the wall as a kind of droplet. Surface tension is an important physical property that results in numerous phenomena in gas–liquid and liquid–liquid multiphase flow simulations. Surface tension is the dominant force acting on the interface at small length scales, such as the micron scale. Thus, properly represented surface tension is critical for accurate numerical analysis of two-phase flow in SPH. Surface tension results from a force imbalance at the interface when the molecules at the interface experience uneven attraction to their neighbouring molecules.

The Continuum surface force (CSF) model developed by Brackbill et al. [39], treats surface tension as a body force. In this model, the interface is defined as a transition zone with a specified thickness.

Morris [40] first introduced the CSF model with the colour function and used it to compute the surface tension. Different phases are represented by a colour function in this approach, and the interface is defined as a transitional band. Within this band, the surface tension force is approximated as a continuous force. The curvature and normal vector of the interface is determined using the colour function. Significant errors occur in the surface tension calculation when using the SPH method to discretise the normal vector and the interface curvature. Hu and Adams [36] used a sharp colour function with an interface discontinuity to evaluate the surface tension. The surface curvature was achieved by introducing a colour gradient-dependent surface stress tensor. A density-weighted colour gradient formulation represents an asymmetric surface tension distribution. The interface's curvature can also be determined by recording the location of particles at the interface.

2.2.3. Turbulence model

Turbulence is more common than laminar flow in nature and industrial applications. Exact and numerical solutions of laminar flow have been determined. However, no precise solution exits for transition to turbulence flow and fully developed turbulence flow, outside of a few classic academic examples. Several generations of scientists from around the globe have studied this topic because of its practical importance and complexity. The academic and industry interest in this topic has motivated many researchers to develop concepts and models that describe turbulent flow. All well-known turbulence models were initially designed and verified for the mesh-based method at early stage. In recent years, efforts have been made to use various turbulence models in particle methods.

2.2.3.1. The $k - \varepsilon$ turbulence model

The $\mathrm{k} - \varepsilon$ model was proposed by Launder and Spalding [41] in 1974 and is one of the most used models for industrial applications.

Shao [42] coupled the turbulence model with the incompressible SPH method to investigate spilling and plunging waves breaking over a slope and obtained results that compared favourably with experiments. Following this, Shao[43] used his model to investigate wave breaking and overtopping a sea wall and obtained results in good agreement with experimental results from the literature. Monaghan [44] introduces the $\mathrm{SPH} - \varepsilon$ model for decaying turbulence in a square box with no-slip boundary conditions, where a smoothed velocity models the effect of turbulent viscosity. This model conserves linear and angular momentum and satisfies a discrete form of Kelvins circulation theorem. Ferrand et al. [45] proposed a unified semi-analytical wall boundary condition and used it for the diffusion term in the $\mathrm{k} - \varepsilon$ turbulence model, producing simulation results that match those from the FVM method. Leroy [46] proposed an ISPH model that included the semi-analytical boundary conditions and a $\mathrm{k} - \varepsilon$ turbulence model, which is effective for cases with inflow and outflow.

However, as described by Shao[43], the $k - \varepsilon$ model has some disadvantages, such as inaccurately addressing the initiation of turbulence in a rapidly distorted shear flow region, such as in the wave breaking

A turbulence model based on sub-particle scale (SPS) in the moving particle semi-implicit (MPS) method is applied to SPH to avoid this issue.

2.2.3.2. Large Eddy Simulation

Arena et al. [47] determined artificial viscosity has similar effects as a sub-grid scale turbulence model. They simulated protoplanetary discs and concluded that turbulent properties could be partially mimicked, but only for less intense fluctuation fields, and turbulent eddies cannot be resolved. Shao et al. [48] combined the Large Eddy Simulation (LES) model with the SPH method. The computed turbulent eddy viscosity and velocity distributions demonstrate the robustness of the incorporated LES sub-particle scale turbulence model. Subsequently, Shao and Ji [49] presented a 2D-LES model based on the SPH method and calculated the turbulent viscosity using the Smagorinsky model. They obtained satisfactory results of turbulence under breaking waves. Dalrymple and Rogers [50] used XPSH to smooth the velocity and Shephard filtering to smooth the density, making the free surface physically acceptable. They also determine the eddy viscosity using the Smagorinsky model. Mayrhofer et al. [51] performed LES simulations with SPH using unified semi-analytical wall boundary conditions. The model was validated with the Taylor–Green vortex, a well-known benchmark case. They concluded that agreement with reference data was poor and the result of insignificant resolution. Di Mascio et al. [52] illustrated that the SPH smoothing procedure has the same property as Lagrangian filtering used for LES. Meringolo et al. [53] proposed a δ–LES–SPH model by using the turbulence closure models to determine the magnitude of the viscous and density diffusion terms considering the local flow conditions at every instant. They used this model to analyse the interaction between waves and structures.

2.2.3.3. Mixing length turbulence model

The mixing length hypothesis, developed by Prandtl, attempts to characterise momentum transfer via turbulent Reynolds stresses using eddy viscosity within a Newtonian fluid boundary layer. Violeau et al. [54] successfully described the eddy viscosity concept using the mixing length model, and it was verified by the turbulent Poiseuille flow solved using the Lagrangian form of the N-S equations. De Padova et al. [55] applied a mixing length model to the case without strong turbulent rollers, yielding a reasonable prediction of water levels and wave patterns in 2D and 3D undular hydraulic jumps, similar to that of the $k-\varepsilon$ model. Kazemi et al. [56] constructed the SPS model based on the mixing length model rather than the Smagorinsky model to improve the model's performance in open channel flow. Subsequentially, Kazemi [57] proposed a generalised three-layer mixing length model that represents the different eddy flow structure sizes in different flow regions. He used this model to simulate turbulent flow over two porous beds and achieved good results in all eight test cases.

Mayrhofer et al. [58] incorporated an additional volume diffusion term into the continuity equation to mitigate errors caused by the SPH discretisation. The extra diffusion term estimated by an eddy–viscosity model with a mixing-length approach can correct the free surface [45]. This scheme produces results comparable to the VOF method for dam-break flow over a wedge. The mixed length model is simple for calculating the eddy viscosity but lacks generality and is unsuitable for complicated flows with uncertain turbulent length scale distributions.

2.2.3.4. Other turbulence model

Lopez et al. [59] used a variable artificial viscosity to achieve good accuracy without a turbulence model for the hydraulic jump case. Bertevas et al.[60] detailed the implementation of the $k-\omega$ SST RANS model, the wall treatment, the discretization of the various governing equations, and their boundary conditions. This turbulence model produced simulation results that show good agreement with experiments when applied to two-phase flow.

Based on the in-house code of Gas Turbine and Transmission Research Centre (G2TRC) in the University of Nottingham, the mixing length model is chosen for the turbulent flow in the bearing chamber. A single-equation turbulence model called the Spalart–Allmaras (SA) turbulence model developed by Spalart and Allmaras[61] is also applied. The SPH formulation of these two turbulence models will be introduced in Chapter 3.

2.2.4. Stabilization method

Particle clustering is an unavoidable phenomenon, due to the properties of the kernel gradient, which approaches zero at small particle distances [1]. This in particular is seen in the simulation of strong vortices (e.g. the Taylor-Green vortex [1,62]) or violent waves (e.g. the solitary wave [6,63]). A regular particle distribution is the crux of veracity and robustness of simulations, and if this is not the case, it will seriously influence the accuracy and stability of the results. For this reason, it is very important to reduce particle clustering as much as possible. Besides in fluid dynamics, tensile instability is also common in solid dynamics simulation using SPH method. Different with the fluid dynamics, many researchers, such as J. Bonet and S. Kulasegaram [64–66] C.H. Lee et al. [67] and F.R. Ming et al. [68] have been demonstrated the tensile instability can be solved by the totally Lagrangian SPH method in the solid dynamics. However, for the research in this thesis, more stabilization methods are needed.

In the past 30 years, several remedies have been published to deal with particle clustering. In literature, a distinction is made between six types of stabilization methods, which are described below.

The first type is based on a virtual viscosity introduced by artificial viscosity or by smoothing the velocity which is the main idea in the XSPH method [35,69]. As early-stage methods, they can prevent particle penetration effectively, but they are energy dissipating.

The second type is kernel-based stabilization methods. Several researchers have introduced kernel functions. Schüssler and Schmitt [70] introduced a kernel with a gradient that tends to infinity for small inter-particle distances, but it does not have a continuous first derivative. The piecewise polynomial kernels introduced by Wendland [71] are commonly used, due to their favourable properties. Others have modified the kernel features. Read et al [72] take the inner part of the kernel gradient as a constant, by extending its (negative) minimum value to smaller distances. Convex kernels are constructed such that the kernel gradient is no longer zero and may even reach its minimum value at zero distance [73], although density estimates of convex kernels become more sensitive to changes in neighbour particle positions [74]. Corrective kernel estimates, such as e.g. introduced by Dilts [75], are more accurate and may reduce the so-called tensile instability, but involve substantially more work [76]. Sigalotti and López [76] introduce an adaptive density kernel estimation with variable (pairwise averaged) smoothing length, which is computationally rather expensive. Although these kernel-based remedies have a stabilizing effect and are momentum conserving, the suppression of particle clustering is not guaranteed with smoothing kernels used in the evaluation of pair-wise forces [1].

The third type of preventing particle clustering is controlling the pressure gradient. Sriram and Ma [77] introduced the minimum pressure method. In this method, the minimum pressure within the support domain of a particle is used to replace the pressure of that particle, in the evaluation of the pressure gradient. However, due to the replacement of pressures, the inter-particle pressure gradient is no longer symmetrical, so that the conservation of momentum is violated to some extent. Zhang et al. [6] combine the minimum pressure method with a Fickian shift method in a hybrid method, which improves the accuracy and stability. Adami et al. [78] introduced the concept of a constant background pressure as a remedy for the so-called tensile instability. The gradient of the background pressure is taken into account in a so-called transport velocity, which is used for the advection of particles. The concept makes an irregular particle distribution more homogeneous. It is momentum conserving but can only be used if the kernel is fully supported (i.e., not at free surfaces). Zhang et al. [79] extend the concept by introducing a variable background pressure, which is proportional to the particle pressure and/or the bulk modulus. The concept is applied to fluids as well as solids with large deformations. The concept with variable background pressure is no longer momentum conserving.

The fourth type is a periodic reinitialization method in which the position of the particles is reinitialized at certain time steps during the simulation when needed. This method, described by Chaniotis et al. [80], may prevent particle clustering, although it is computationally very expensive.

The fifth type is based on particle shifting, which has become more popular in recent years and is now commonly used to maintain a regular particle distribution. In this method, the shift is relatively small compared to the displacement of the particles within a time step. The direction of the shift is based on the anisotropy of the particles. Xu et al. [4] introduced a method based on particle concentration. Lind et al. [62] introduced a method based on Fick's law, called the Fickian shift model, in which particles are shifted from regions of high concentration to low concentration. It should be noted that the Fickian shift model needs a special treatment at the free surface and, according to the authors, conservation of momentum is not satisfied. The method is based on several coefficients and some of these are case dependent. Khayyer et al. [5] proposed an optimized particle shift scheme which improves the performance of the Fickian shift model.

The sixth type is based on particle collisions. The method is obtained from kinetic collision theory, which ensures the conservation of momentum (for inelastic and elastic collisions), and non-dissipative for elastic collisions. This has resulted in the particle collision model as introduced by Kruisbrink et al. [1], which is based on velocities rather than forces. This inter-particle model is only applied when particles are too close together. If detected, the approach velocity between the particles is changed. This approach has been used in WCSPH.

2.3. Summary

Although previous studies have shown that the SPH method is superior to those traditional CFD methods when dealing with the violent waves and large deformation of interfaces in terms of the Largrangian property, the study of the turbulence model in the SPH method and the particle clustering in multiphase flow is still in an early stage, and many challenges are yet to be overcome.

First of all, in the SPH method, particle clustering is an unavoidable phenomenon without the numerical stabilised method such as the background pressure and Fickian shift model. However, the coefficient of the background pressure and the Fickian shift model are case-dependent, and the latter is very complex when dealing with multiphase flow and the free surface of single-phase flow. Furthermore, in WCSPH, the pressure fluctuates without the diffusion term due to the slight variation of density. The multiphase flow simulation is limited by the fluctuation of pressure and the particle clustering by using the WCSPH method. After that, the turbulence model in SPH is not fully developed yet. Using the SPH method to simulate the high-density ratio multiphase turbulent flow in the bearing chamber is another challenge.

From the literature review, the existing challenges and research gaps were concluded as below:

1. The movement of particles suffers from clustering when particles move along the streamline. The existing stabilised methods are all case-dependent and complex, especially for multiphase flows. A simple and efficient stabilised particle shift method needs to be investigated.
2. The application of existing turbulence models has rapidly developed in recent years based on the Eulerian CFD method. However, in the SPH method, the development of turbulence models is not as many as in the mesh-based CFD method.
3. The mainstream numerical method for the multiphase flow in the bearing chamber is based on Eulerian CFD techniques. It is complex to deal with the interface when it has large deformations such as rolling or breaking, even with the combination of the Lagrangian method. The volume of fluid method and level set method are always needed to capture and stabilise the interface. However, SPH as a pure Lagrangian method should have superiority in the simulation of high-density ratio multiphase turbulence flow, but it has not been conducted. Furthermore, the application of the pure Lagrangian method, such as the SPH method, in an aero-engine bearing chamber has not been demonstrated.

Chapter 3 SPH methodology

In this section, the methodology of SPH is described. In a Lagrangian framework, the mass and momentum conservation equations can be written as

$$\rho\, \nabla \cdot \vec{u} + \frac{d\rho}{dt} = 0\,, \tag{1}$$

$$\rho \frac{d\vec{u}}{dt} = -\nabla p + \overrightarrow{F^V} + \overrightarrow{F^S} + \overrightarrow{F^B}, \tag{2}$$

where ρ is the fluid density, $\vec{u}$ is the velocity, t is the time, p is the pressure, $\overrightarrow{F^V}$ is viscous force, the $\overrightarrow{F^S}$ is the surface tension force and $\overrightarrow{F^B}$ is the external body force. The body force always means the gravity, and $\overrightarrow{F^V}, \overrightarrow{F^S}, \overrightarrow{F^B}$ have different discrete equation which will be described in this chapter.

3.1. Kernel approximation

SPH is a Lagrangian method where the flow field can be considered as a group of discrete particles. Each particle carries physical quantities such as density, pressure and velocity, etc.

In SPH method, the SPH formulation is basically made up of kernel approximation and particle approximation. The particle properties are estimated from a convolution integral, known as the kernel approximation. In the kernel approximation, a field function $f(\vec{r})$ at position $\vec{r}$ can be transformed to an integral form, which is as follows

$$f(\vec{r}) = \int_{\Omega} f(\vec{r}\,')\, \delta(\vec{r} - \vec{r}\,')dr', \tag{3}$$

where $f(\vec{r})$ represents a continuous function defined on a domain Ω, dr' represents a volume element and Ω denotes the integral domain. The Dirac delta function $\delta(\vec{r} - \vec{r}\,')$ is as follows

$$\delta(\vec{r}-\vec{r}') = \begin{cases} +\infty, & \vec{r}=\vec{r}', \\ 0, & \vec{r}\neq\vec{r}'. \end{cases} \tag{4}$$

Dirac delta function $\delta(\vec{r}-\vec{r}')$ only has value at one point ($\vec{r}=\vec{r}'$), so that it is not suitable for field function discretisation. To solve this problem, the smoothing function is constructed to replace Dirac delta function. Thus, the kernel approximation of $f(\vec{r})$ can be converted to the following equation,

$$< f(\vec{r}) >= \int_{\Omega} f(\vec{r}')\, W(\vec{r}-\vec{r}',h)dr'. \tag{5}$$

The angle brackets < > indicate an approximation, and h is the smoothing length. $W(\vec{r}-\vec{r}',h)$ is a smoothing kernel function defined on a support domain which is a circle with radius of κh, and κ is a constant based on different kernel function. Despite the fact that $W(\vec{r}-\vec{r}',h)$ is not the Dirac delta function, these conditions make kernel function $W(\vec{r}-\vec{r}',h)$ have the same attributes as Dirac delta function [81].

The first condition is called the unity condition, which is

$$\int_{\Omega} f(\vec{r}')\, W(\vec{r}-\vec{r}',h)dr' = 1. \tag{6}$$

The second condition guarantee the $W(\vec{r}-\vec{r}',h)$ has the same attributes as the Dirac delta function, which is

$$\lim_{h\to 0} W(\vec{r}-\vec{r}',h)dr' = \delta(\vec{r}-\vec{r}'). \tag{7}$$

The third condition is called the compact condition, which is

$$W(\vec{r}-\vec{r}',h) = 0 \; when \; |\vec{r}-\vec{r}'| > \kappa h. \tag{8}$$

With these conditions, the kernel approximation has first order accuracy [82].

Following the kernel approximation of the $f(\vec{r})$, the kernel approximation of the spatial derivatives of the $f(\vec{r})$ can be derived by substituting $\nabla\cdot f(\vec{r})$ for $f(\vec{r})$ in Eq. (2), which is as follows

$$< \nabla\cdot f(\vec{r}) >= \int_{\Omega}[\nabla\cdot f(\vec{r}')]\, W(\vec{r}-\vec{r}',h)dr' = -\int_{\Omega} f(\vec{r}')\nabla W(\vec{r}-\vec{r}')dr', \tag{9}$$

where ∇W is the kernel gradient. In this thesis, the Wendland kernel is applied, and it is defined as

$$W(\vec{r}-\vec{r}',h) = \alpha_d(1.0-0.5q)^4(1.0+2.0q)\ (q \le 2.0) \tag{10}$$

$$\nabla W(\vec{r}-\vec{r}',h) = \alpha_d[2.0(1.0-0.5q)^4 - 2.0(1.0-0.5q)^3(1.0+2.0q)] \tag{11}$$

in which $q = |\vec{r} - \vec{r}'|/h$, in 2D case $\alpha_d = \frac{7.0}{4.0\pi h^3}$, while in 3D case $\alpha_d = \frac{7.0}{8.0\pi h^4}$.

3.2. Particle approximation

Following [83], the function and its gradient of particle i can be further approximated in discretized form by a summation of neighbour particles (particles in the support domain of particle i), which is known as particle approximation, as follows

$$f(\vec{r}_i) = \sum_j f(\vec{r}_j)\,\frac{m_j}{\rho_j}\,W(\vec{r}_i-\vec{r}_j,h), \tag{12}$$

$$\nabla f(\vec{r}_i) = -\sum_j f(\vec{r}_j)\,\frac{m_j}{\rho_j}\,\nabla W(\vec{r}_i-\vec{r}_j,h), \tag{13}$$

With these two equations, the function value and the gradient value of particles can be obtained from Eqs. (6) and (9). According to Monaghan’s approach [84], Eq. (9) can be rewritten by introducing the density to the differential operator with the following two formulas,

$$\nabla \cdot f(\vec{r}_i) = \frac{1}{\rho_i}\left[\sum_{j=1}^{N} m_j\left(f(\vec{r}_j) - f(\vec{r}_i)\right)\cdot \nabla_i W(\vec{r}_i-\vec{r}_j,h)\right], \tag{14}$$

$$\nabla \cdot f(\vec{r}_i) = \frac{1}{\rho_i}\left[\sum_{j=1}^{N} m_j\left(\frac{f(\vec{r}_j)}{\rho_j^2} + \frac{f(\vec{r}_i)}{\rho_i^2}\right)\cdot \nabla_i W(\vec{r}_i-\vec{r}_j,h)\right]. \tag{15}$$

Eqs. (14) and (15) have several advantages over Eq.(13). To start, derivatives of the field function are defined in the particle pair-wise form. This increases the stability and robustness of SPH simulations [85].

Due to a second order derivative term is a part of the right side of the momentum equation, it is important to find an accurate way to discretize it. One option is using Eq. (13) twice [86], and the other option is using the second order derivative of the smoothing kernel function. However, both of these two methods may produce higher errors at low resolution. To overcome this shortage, Brookshaw [87] proposed a novel discretizing way to improve the accuracy of the second-order derivative. Following this way, the approximation of the Laplacian of a function can be evaluated as

$$\nabla^2 f(\vec{r}_i) = \sum_{j=1}^{N} \frac{\nabla_i W(\vec{r}_i - \vec{r}_j, h) \cdot (\vec{r}_i - \vec{r}_j)}{|\vec{r}_i - \vec{r}_j|^2} \left(f(\vec{r}_i) - f\left(\vec{r}_j\right)\right) V_j. \tag{16}$$

This method is a finite difference approximation of a first-order derivative. Some researchers discretize the second order derivative in this way [88–91]. For the SPH method, various discretization schemes based on finite difference like formulae have been proposed (e.g. [92,93]). Morris [88] applied this Brookshaw type SPH formula to the approximating Laplace operator for discretization of the viscosity term in the Navier–Stokes equations, and this scheme is one of the most widely used in the SPH method for discretization of the Laplacian.

Following the kernel approximation and particle approximation mentioned before, the continuity and momentum equations can then be discretized. In SPH method, the continuity equation can be discretized as follows in these two forms. One way is to calculate the density by the summation of neighbouring particles by using Eq. (12) when the field function is the density, which is as follows:

$$\rho_i = \sum_{j=1}^{N} m_j W_{ij}. \tag{17}$$

The other way is to calculate the $\frac{\mathrm{D}\rho}{\mathrm{Dt}}$ through Eq. (1), which is as follows,

$$\frac{d\rho_i}{dt} = -\rho_i \sum_{j=1}^{N} \frac{m_j}{\rho_j} (\vec{u}_j - \vec{u}_i) \nabla_i W_{ij}. \tag{18}$$

The density is updated from Eq. (18). In this work, Eq. (18) is used in WCSPH.

The divergence of the velocity in Eq. (1) and the pressure gradient and viscosity term in Eq. (2) are evaluated as

$$\nabla \cdot \vec{u} \quad = -\frac{1}{\rho_i} \sum_j m_j (\vec{u}_i - \vec{u}_j) \nabla_i W_{ij} \tag{19}$$

As for the momentum equation, due to the different forms of different terms of Eq. (2), the momentum equation is more complex than the continuity equation. For the pressure gradient, these three forms are usually used [93,94].

$$-\frac{1}{\rho}\nabla p = -\sum_{j=1}^{N} m_j (\frac{p_i + p_j}{\rho_i \rho_j}) \nabla_i W_{ij} \tag{20}$$

$$-\frac{1}{\rho}\nabla p = -\sum_{j=1}^{N} m_j (\frac{p_i}{\rho_i^2} + \frac{p_j}{\rho_j^2}) \nabla_i W_{ij} \tag{21}$$

$$-\frac{1}{\rho}\nabla p = \sum_{j=1}^{N} m_j (\frac{p_i - p_j}{\rho_i \rho_j}) \nabla_i W_{ij} \tag{22}$$

Eq. (20) is used in WCSPH. It is suited to multi-phase flows with very different densities. This can be seen by considering the pressure gradient force by multiplying Eq. (20) with m_i . The force is based on volumes (Vi = mi/ρi and Vj = mj /ρj) and as such the formulation is suited to multi-phase flows with different densities. This does not hold for Eq. (21), which is based on densities.

When the boundary is truncated by solid boundaries, the accuracy of the above equations is heavily affected by the particle distributions and the shape of the solid boundary. To decrease the error caused by the boundary, Zheng et al. [95] use the Simplified Finite Difference Interpolation (SFDI) method, originally developed by Sriram and Ma (2012) [77], to calculate the first-order derivative of the pressure on the solid boundary. SFDI is a second-order accurate numerical scheme based on the Taylor series expansions. In 2D case, the key formulas of the pressure derivative are

$$(\frac{\partial p_i}{\partial x}) = \sum_{j=1.j\neq i}^{N} \frac{n_{i,x_m} B_{ij,x_k} - n_{i,xy} B_{ij,y}}{n_{i,x_1} n_{i,x_2} - n_{i,xy}^2} (p_i - p_j) \tag{23}$$

$$(\frac{\partial p_i}{\partial Y}) = \sum_{j=1.j\neq i}^{N} \frac{n_{i,x_1} B_{ij,y} - n_{i,xy} B_{ij,x}}{n_{i,x_1} n_{i,x_2} - n_{i,xy}^2} (p_i - p_j) \tag{24}$$

$$n_{i,xy} = \sum_{j=1.j\neq i}^{N} \frac{(r_{j,x_m} - r_{i,x_m})(r_{j,x_k} - r_{i,x_k})}{|\vec{r}_i - \vec{r}_j|^2} W \tag{25}$$

$$B_{ij,x_m} = \frac{(r_{j,x_m} - r_{i,x_m})}{|\vec{r}_i - \vec{r}_j|^2} W \tag{26}$$

where m = 1 and k = 2 or m = 2 and k = 1, N is the number of neighbour particles of particle i; $x_1 = x$ and $x_2 = y$ are defined; and r_{j,x_m} is the component of position vector in x (or y) direction.

For the viscous term $\overrightarrow{F^V}$, several viscosity models are available in SPH [96,97], which can be presented as follows,

$$\nu\nabla^2\vec{u}_i = 4\sum_j m_j \frac{\nu_i+\nu_j}{\rho_i+\rho_j}\frac{(\vec{r}_i-\vec{r}_j)(\vec{u}_i-\vec{u}_j)}{(|\vec{r}_i-\vec{r}_j|^2+(0.01h)^2)}\nabla_i W_{ij} \tag{27}$$

$$\nu\nabla^2\vec{u}_i = -16\sum_j m_j \frac{\nu_i+\nu_j}{\nu_j\rho_j+\nu_i\rho_i}\frac{(\vec{r}_i-\vec{r}_j)(\vec{u}_i-\vec{u}_j)}{|\vec{r}_i-\vec{r}_j|h}\nabla_i W_{ij} \tag{28}$$

The equation of discretization of the continuity equation and the momentum equation should be chosen based on the simulation requirement. The continuity and momentum equation will be closed once the pressure has been solved.

At present, for incompressible flows, the pressure is usually solved in two ways: (1) in weakly compressible SPH (WCSPH), the fluid is considered to be slightly compressible, and the pressure is explicitly solved by the equation of state (Monaghan [98]), and (2) in incompressible SPH (ISPH), the fluid is considered to be fully incompressible, and the pressure is solved through the projection method by the Poisson equation. The details of these two ways to solve the pressure will be discussed in the next section.

3.3. Weakly compressible SPH method

As previously stated, there are two ways to calculate pressure. The ISPH and WCSPH will be introduced in detail.

WCSPH use the state equation to build a relationship between the pressure and density. The Tait equation [24] is the most frequently used, which is as follows,

$$p = c_0^2 \rho_0 / [\left(\frac{\rho}{\rho_0}\right)^{\gamma} - 1]. \tag{29}$$

where c_0 is the speed of sound at the reference density ρ_0. Based on Courant–Friedrich– Levy (CFL) condition the realistic speed of sound will make the time step of the simulation very small, and it will increase the computation cost. Monaghan and Kos [99] prove that artificial sound speed can also get satisfying results. So that the artificial sound speed is used here, it should be noted that the sound speed should be at least 10 times higher than the maximum fluid velocity. γ is a constant and 1.4 for air, 7 for water is commonly used. From Eq. (29), the pressure suffers from significant fluctuations, even if the density is slightly changed in WCSPH.

3.4. δ-SPH

As mentioned before, one of the disadvantages of the WCSPH is the instability in the pressure. To prevent the pressure fluctuation from the density, Antuono et al [100] first defined δ-SPH and then further developed by many researchers and have a very wide range of applications e.g. [26,101–103]. In this method, a specific diffusive term is added to the right side of the continuity equation, which can reduce the high-frequency stray noise of density/pressure fields. In δ-SPH, the continuity equation (18) is changed to,

$$\frac{d\rho_i}{dt} = -\rho_i \sum_{j=1}^{N} \frac{m_j}{\rho_j} (\vec{v}_j - \vec{v}_i) \cdot \nabla_i W(\vec{r}_i - \vec{r}_j, h) + \delta h c_0 \mathcal{D}_i \tag{30}$$

$$\mathcal{D}_i = 2 \sum_{j=1}^{N} \psi_{ji} \frac{(\vec{r}_j - \vec{r}_i) \cdot \nabla_i W(\vec{r}_i - \vec{r}_j, h)}{|r_{ji}|^2} V_j \tag{31}$$

$$\psi_{ji} = \left\{ \left(\rho_j - \rho_i\right) - \frac{1}{2} (\langle \nabla\rho \rangle_j^L + \langle \nabla\rho \rangle_i^L) \cdot \vec{r}_{ji} \right\} \tag{32}$$

$$\langle \nabla\rho \rangle_i^L = \sum_{j=1}^{N} \left(\rho_j - \rho_i\right) L_i \nabla_i W(\vec{r}_i - \vec{r}_j, h) V_j \tag{33}$$

$$L_i = [\sum_{j=1}^{N} (\vec{r}_j - \vec{r}_i) \otimes \nabla_i W(\vec{r}_i - \vec{r}_j, h) V_j] \tag{34}$$

The above equation can only apply to single phase flow. In the multiphase flow, the large density difference may lead to huge errors in the above equations. For multiphase flow, B. Zheng and Z. Chen [38] assume that the oscillation of the density increment $\delta\rho$ is the essential reason for the oscillation of the pressure, and more general form of δ-SPH is proposed. The continuity equation is changed to

$$\frac{d\rho_i}{dt} = -\rho_i \sum_{j=1}^{N} \frac{m_j}{\rho_j} (\vec{v}_j - \vec{v}_i) \cdot \nabla_i W_{ij} + \vartheta \langle \nabla^2 \delta\rho_i \rangle \tag{35}$$

$$\vartheta \langle \nabla^2 \delta\rho_i \rangle = -2\lambda c_s \sum_{j=1}^{N} [(\delta\rho_j - \delta\rho_i) - \frac{1}{2} (\langle \delta\rho \rangle_j^L - \langle \delta\rho \rangle_i^L) \cdot \vec{r}_{ij}] \frac{\partial W_{ij}}{\partial |\vec{r}_{ij}|} \frac{1}{|\vec{r}_{ij}|} V_j \tag{36}$$

$$\langle \delta\rho \rangle_i^L = \sum_{j=1}^{N} (\delta\rho_j - \delta\rho_i) \, L_i \nabla_i W(\vec{r}_i - \vec{r}_j, h) V_j \tag{37}$$

To avoid an extra loop to calculate the Eq. (34), in this paper, a simple version of the δ-SPH is used. Eq. (32) and Eq. (36) are simplified as follows,

$$\psi_{ji} = (\rho_j - \rho_i) \tag{38}$$

$$\vartheta \langle \nabla^2 \delta\rho_i \rangle = -2\lambda c_s \sum_{j=1}^{N} (\delta\rho_j - \delta\rho_i) \frac{\partial W_{ij}}{\partial R} \frac{1}{|\vec{r}_{ij}|} V_j \tag{39}$$

It is very interesting to see that δ-SPH scheme is very similar to the Jameson-Schmidt-Turkel (JST) stabilization scheme which is always applied to the SPH method in solid dynamics.[67,104]. C.H. Lee et al. [105] proposed a new JST-SPH method, which also obtain great improvement for large strain solid dynamics.

3.5. Incompressible SPH method

In ISPH the pressure needs to be solved by a complex pressure Poisson equation through a prediction-correction solution scheme, which is more stable and accurate than in WCSPH. In ISPH, the incompressibility of the fluid is enforced by setting $D\rho/Dt = 0$ at each particle. This is done using the method proposed by Chorin [106] based on a divergence-free ISPH during the correction step in the time integration. The prediction–correction solution scheme of the ISPH method includes two steps.

(a) Prediction step

In the prediction step of the projection method, the intermediate particle velocity $\vec{u}_*$ and position $\vec{r}_*$ are

$$\Delta\vec{u}_* = (\vec{g} + \nu\nabla^2\vec{u}(t))\Delta t, \tag{40}$$

$$\vec{u}_* = \vec{u}(t) + \Delta\vec{u}_*, \tag{41}$$

$$\vec{r}_* = \vec{r}(t) + \vec{u}_*\Delta t, \tag{42}$$

where $\vec{u}(t)$, $\vec{r}(t)$ are the velocity and position at time t, Δt is the time step and $\Delta\vec{u}_*$ is the change of particle velocity during the prediction step.

(b) Correction step

In the correction step, the pressure is solved by

$$\nabla^2 p(t + \Delta t) = \frac{\rho\, \nabla\cdot\vec{u}_*}{\Delta t}. \tag{43}$$

The velocity change $\Delta\vec{u}_{**}$ during the correction step is

$$\Delta\vec{u}_{**} = -\frac{1}{\rho}\nabla p(t + \Delta t)\,\Delta t. \tag{44}$$

The velocity and position of a particle at the new time step are

$$\vec{u}(t + \Delta t) = \vec{u}_* + \Delta\vec{u}_{**}, \tag{45}$$

$$\vec{r}(t + \Delta t) = \vec{r}(t) + \frac{\vec{u}(t+\Delta t) + \vec{u}(t)}{2}\Delta t. \tag{46}$$

The above equation uses the divergence of the intermediate velocity field as the source term of pressure of Poisson equation (PPE), which is similar to the study of Lee [30], and it is solved by Biconjugate gradient stabilized method.

In ISPH method, The Laplacian term of left-hand-side of Equation (34) is commonly discretized by the combination of gradient formulation with a first-order finite difference scheme (e.g. [88,107,108]), which is as follows

$$\nabla^2 p_i = \sum_{j=1}^{N} 2\frac{m_j}{\rho_j}\frac{(p_i - p_j)(\vec{r}_i - \vec{r}_j)}{r_{ij}^2 + \eta^2} \cdot \nabla_i W_{ij} \tag{47}$$

3.6. Boundary condition

In order to get the accurate results of the governing equation, a proper way to deal with the truncation of the boundaries is important. In this part, two different types of boundaries are introduced for WCSPH and ISPH, respectively.

3.6.1. Fixed ghost particle.

The fixed ghost particle model is also called the image particle model. Before the simulation, the fixed ghost particles are placed outside of the fluid domain and just behind the boundary. Marrone et al. [26] describe a fixed ghost particle, which can describe the wall boundary accurately, but it is difficult to get the properties of the fixed ghost particle, when the boundaries have a complex shape. To place the fixed ghost particle Kruisbrink et al. [22] introduced a so-called parameterized wall, which is based on the body's fitted coordinates, allowing curved walls to match the shape of the real walls. The parameterized wall allows for the modelling of more complex geometries. Moreover, in this wall concept a hexahedral particle distribution is used, which is better than the uniform distribution seen in many SPH applications.

The Neumann boundary condition is a well-known, very useful and simple concept to impose zero gradients. A zero-pressure gradient on a fluid particle i is obtained by imposing $p_j = p_i$ to neighbouring ghost particles j. This simple concept fits very well in the SPH concept. For the case with large pressure gradient near the boundary, a dynamic boundary particle (DBPs) [109]) is used to obtain the pressure of the fixed ghost particle, which is as follows,

$$p_j = p_i + \frac{1}{N}\sum_{j=1}^{N}\frac{dp_j}{d\vec{r}_{ji}}(\vec{r}_j - \vec{r}_i) \tag{48}$$

where N is the number of fluid particle j near the fixed ghost particle i. As for the velocity of the ghost particle, a no-slip condition is applied.

3.6.2. SFDI boundary treatment

In this part, the SFDI boundary treatment following Zheng et al. [95] is used. There is only one layer of particles arranged on the boundaries. The particles on the solid boundary should satisfy the continuity of the pressure gradient, which is represented by the following momentum equation as

$$\vec{n} \cdot \nabla P = \rho(\vec{n} \cdot \vec{g} - \vec{n} \cdot \dot{\vec{U}}) \qquad (49)$$

where $\vec{n}$ is the normal unit vector on the solid boundary, $\dot{\vec{U}}$ is the velocity of the solid boundary and $\vec{g}$ is the gravity (if it is needed).. The above equation can be used to replace the standard PPE. The advantage of this approach is that the second-order pressure derivative is avoided and replaced by an exact first-order derivative, which can be more precisely calculated by the SPH particles even with disordered distributions. This should be able to preserve the pressure stability at complex solid boundaries. By using Eqs. (23) to (26), Eq. (49) can be rewritten as

$$\vec{n} \cdot \{\sum_{j=1.j\neq i}^{N} \frac{n_{i,x_1} B_{ij,y} - n_{i,xy} B_{ij,x}}{n_{i,x_1} n_{i,x_2} - n_{i,xy}^2} (p_i - p_j) + \sum_{j=1.j\neq i}^{N} \frac{n_{i,x_m} B_{ij,x} - n_{i,xy} B_{ij,y}}{n_{i,x_1} n_{i,x_2} - n_{i,xy}^2} (p_i - p_j)\} = \rho(\vec{n} \cdot \vec{g} - \vec{n} \cdot \dot{\vec{U}}) \qquad (50)$$

By adopting this practice, there is no need to generate the mirror particles outside of the solid boundary. This makes the ISPH computations more efficient and accurate.

3.7. Surface tension model

In the bearing chamber in the aeroengine, the oil droplet will be formed and move from the oil film from one side to the other side. The surface tension model of Adami et al.

[36] based on Brackbill et al. [39] is implemented in our in-house SPH code and used in the thesis. Adami’s model is a continuum surface force model in which the force can be expressed as

$$\overrightarrow{F^S} = -\sigma\kappa\vec{n}\delta_\Sigma \tag{51}$$

The surface tension force in this model is computed by the curvature and the normal vector of the interface, and the surface-delta function δ_Σ. A colour function c is introduced to approximate the surface tension, which is as follows:

$$c_l^k = \begin{cases} 1, & if\ the\ k_{th}\ particle\ does\ not\ belong\ to\ thephase\ of\ particle\ l, \\ 0, & if\ the\ k_{th}\ particlebelongs\ to\ the\ phase\ of\ particle\ l. \end{cases} \tag{52}$$

The gradient of the colour function is

$$\nabla c_i = \frac{1}{V_i}\sum_j [V_i^2 + V_j^2]\tilde{c}_{ij}\frac{\partial W}{\partial r_{ij}}\vec{e}_{ij}. \tag{53}$$

$\tilde{c}_{ij}$ is the inter-particle average value of the colour function, which is as follows:

$$\tilde{c}_{ij} = \frac{\rho_j}{\rho_i+\rho_j}c_i^i + \frac{\rho_i}{\rho_i+\rho_j}c_j^i. \tag{54}$$

This gradient of colour function has the same attribute as the surface-delta function δ_Σ in Eq. (51) which usually used to replace the δ_Σ. Furthermore, the normal direction at the interface can be obtained from the colour gradient by

$$n = \frac{\nabla c}{|\nabla c|} \tag{55}$$

The curvature is the divergence of the normal vector which is as follows:

$$\kappa_i = \nabla \cdot \left(\frac{\nabla c}{|\nabla c|}\right)_i = d\frac{\sum_j \left(\frac{\nabla c}{|\nabla c|}\right) \cdot \frac{\vec{r}_{ij}}{|r_{ij}|}\frac{\partial W}{\partial r_{ij}} V_j}{\sum_j \vec{r}_{ij}\frac{\partial W}{\partial r_{ij}} V_j}. \tag{56}$$

Substitution of Eqs. (53), (55) and (56) into (51), the SPH form of the surface tension is obtained.

3.8. Artificial viscosity

The above sections describes all the term is on the right side of Eq. (2), however for the practical engineering case with high impact force or violation interface movement multiphase problem, a small artificial viscous term need be added [38,102,110,111]. Usually the viscosity term is calculated together with the pressure gradient in the momentum equation. For $\vec{v}_{ij} \cdot \vec{r}_{ij} < 0$,

$$\frac{d\vec{u}_i}{dt} = -\sum_{j=1}^{N} m_j \left(\frac{p_i + p_j}{\rho_i \rho_j} - \alpha c_s \frac{h \vec{v}_{ij} \cdot \vec{r}_{ij}}{\left| \vec{r}_{ij} \right|^2 + h^2} \right) \nabla_i W_{ij} + \frac{\overrightarrow{F^V} + \overrightarrow{F^S} + \overrightarrow{F^B}}{\rho_i}, \tag{57}$$

where α is the coefficient of the artificial viscosity. $\vec{v}_{ij} = \vec{v}_i - \vec{v}_j$. Among various existing multiphase models, artificial viscosity is used throughout the whole flow field. The artificial viscosity is only used in the multiphase sloshing tank and multiphase dam break.

3.9. Turbulence model

For the turbulence flow in the bearing chamber, the implementation of turbulence models in SPH method is needed. A good and useful turbulence model should have wide applicability, be accurate, simple, and economical to run. In this part, two RANS based eddy viscosity models will be coupled in SPH method. In this thesis, the turbulence property is characterised by turbulent viscosity ν_t. In this part, two turbulence models are introduced to calculate the ν_t. In 1877, Boussinesq established the concept of eddy viscosity, known as the Boussinesq eddy viscosity hypothesis, in an effort to build a mathematical explanation of turbulent stresses. This hypothesis established a relationship between Reynolds stresses and eddy viscosity. In contrast to molecular viscosity, eddy-viscosity is a flow characteristic rather than a property of the fluid. The Boussinesq eddy-viscosity hypothesis is the core of the eddy-viscosity turbulence model. Boussinesq assumed that the vortex viscosity ν_t, can describe the momentum transfer caused by turbulent eddies. The one equation model of the Reynolds stress tensor under the Boussinesq hypothesis can be written in the following way:

$$-\rho\overline{u_i'u_j'} = 2\mu_T S_{ij} \tag{58}$$

3.9.1. Prandtl's Mixing length model

In mixing length model, the eddy-viscosity is related to the mean strain rate from Prandtl's theory by using a turbulence characteristic length l_m as follows:

$$\nu_t = l_m^2 \left|\frac{\partial U}{\partial y}\right| \tag{59}$$

where l_m is the mixing length and $\frac{\partial U}{\partial y}$ is the velocity gradient normal to the flow direction. The mixing length is different for each flow and must be known in advance to obtain a solution. The flow in the bearing chamber is similar to the pipe flow. Following Nikuradse [10], the mixing length is evaluated following,

$$\frac{l_m}{r_0} = 0.14 - 0.08\left(1 - \frac{y}{r_0}\right)^2 - 0.06\left(1 - \frac{y}{r_0}\right)^4 \tag{60}$$

where r_0 is the half radius of the pipe.

In turbulent flows the velocity gradients near walls are very high. The fluid velocity may be very different from the velocity of boundaries, such as e.g. the rotating shaft in a bearing chamber. It is explored and concluded that the standard evaluation of the velocity gradient from the particle approximation (see Eq.(13)), where boundary particles are included in the kernel gradient evaluations, leads to poor estimates. For this reason, the Simplified Finite Difference Interpolation (SFDI) is used as an alternative method. This method is described in Section 2.2, where it is applied to the pressure. Here the method is applied to the velocity (components), which may be formulated as

$$(\frac{\partial u_i}{\partial Y}) = \sum_{j=1.j\neq i}^{N} \frac{n_{i,x_1}B_{ij,y} - n_{i,xy}B_{ij,x}}{n_{i,x_1}n_{i,x_2} - n_{i,xy}^2}(u_i - u_j) \tag{61}$$

combine the Eqs. (25) and (26) the $\frac{\partial u}{\partial y}$ can be calculated.

where the coefficients $n_i$and B_{ij} are given in the Eqs. (25) and (26). The velocity u is the velocity in flow direction, which is further defined below. The mixing length model is explored in the 2D Taylor-Couette flow cases (Chapter 6 and Chapter 7). In these cases, the flow direction is assumed to coincide with the tangential direction of the rotational flow between two concentric cylinders. Around each particle i a local Cartesian coordinate system is defined, with the origin on particle i, the x-direction parallel to the walls and the y-direction perpendicular to the walls. The velocity components u_i ad u_j of particle i and its neighbouring particles j are all taken as the velocity components in the x-direction. Mixing length model as a zero-equation model is very simple to code and inexpensive, but it only works well for relatively simple problems and it is directly influenced by the distance to the boundary.

3.9.2. Spalart-Allmaras model

This one-equation turbulence model, developed by Spalart and Allmaras [61], is basically intended for aerodynamic flow. The Spalart-Allmaras model is selected out of a wide variety of turbulence models, since it is originally based on vorticity and it is based on one equation, contrary to several others, like e.g. the $k - \varepsilon$ and $k - \omega$ turbulence models. The transport equation in the tensor notation can be written as,

$$\frac{D\tilde{\upsilon}}{Dt} = G_V + \frac{1}{\sigma}\left[\nabla \cdot \left((\nu + \tilde{\upsilon})\nabla\tilde{\nu} + C_{b2}(\nabla\tilde{\nu})^2\right)\right] - Y_V \tag{62}$$

where G_V is the production of turbulent viscosity, Y_V the destruction of turbulent viscosity that occurs in the near-wall region due to wall blocking and viscous damping. The term between square brackets represents the diffusion of turbulent viscosity. These three terms are defined below. The transport equation solves ν "tilde", which is the turbulent kinematic viscosity, except in the near-wall region. This variable is defined such that it equals $\kappa y u_\tau$ all the way to the wall, so that the turbulent dynamic viscosity μ_t satisfies the log-wall function. This allows for an enhanced wall treatment, which is less sensitive to the dimensionless wall distance y^+. The turbulent dynamic viscosity is obtained from

$$\mu_t = \rho \tilde{\nu} f_{v1} \tag{63}$$

$$f_{v1} = \frac{\chi^3}{\chi^3 + C_{v1}^3} \; ; \; \chi = \frac{\tilde{\nu}}{\nu} \; ; \; c_{v1} = 7.1 \tag{64}$$

where $f_{v1}$is a viscous damping function and χ is the ratio of turbulent and laminar viscosity.

The production term is

$$G_v = C_{b1} \tilde{S} \tilde{\nu} \tag{65}$$

with

$$\tilde{S} = S + \frac{\tilde{\nu}}{\kappa^2 d^2} f_{v2} \; ; \; f_{v2} = 1 - \frac{\chi}{1 + \chi f_{v1}} \; ; \; S = \sqrt{2 S_{ij} S_{ij}} \; ; \; S_{ij} = \frac{1}{2} \left(\frac{\partial u_i}{\partial x_j} - \frac{\partial u_j}{\partial x_i} \right) \tag{66}$$

where *S* is the vorticity as a scalar measure of the deformation tensor, S_{ij} the mean rate-of-rotation tensor, and *d* the distance from the wall. The vorticity is normalized so that it reduces to a velocity gradient in a simple shear flow. The justification for the expression of S is that for shear flows, vorticity and strain rate are identical.

The destruction term is

$$Y_V = c_{w1} f_w \left(\frac{\tilde{\nu}}{d} \right)^2 \tag{67}$$

With

$$f_w = g\left[\frac{1+C_{w3}^6}{g^6+C_{w3}^6}\right] \; ; \; g = r + C_{w2}(r^6 - r) \; ; \; r \equiv \frac{\tilde{\nu}}{\tilde{S}\kappa^2 d^2} \tag{68}$$

$$c_{w1} = \frac{C_{b1}}{\kappa^2} + \frac{(1 + C_{b2})}{\sigma} \; ; \; C_{b1} = 0.1355 \; ;$$

$$C_{b2} = 0.622; \sigma = \frac{2}{3} \; ; \; C_{w2} = 0.3 \; ; \tag{69}$$

$$C_{w3} = 2 \; ; \; \kappa = 0.4187$$

The diffusion term is rewritten as

$$D_v = \frac{1}{\sigma}\{\nabla \cdot [(\upsilon + \tilde{\upsilon})\nabla\tilde{\upsilon}] + C_{b2}|\nabla\tilde{\upsilon}|^2\} = \frac{1}{\sigma}\{\tilde{\upsilon} + (1 + C_{b2})|\nabla\tilde{\upsilon}|^2\} \tag{70}$$

At the right-hand side of this equation, the Laplacian operator (∇^2) appears. This form is more suited to SPH. Note that the laminar viscosity is neglected. The Laplacian is evaluated following Eq. (16)

$$\nabla^2\tilde{\upsilon} = \sum_{j=1}^{N} \frac{\nabla W_{ij} \cdot (\vec{r}_i - \vec{r}_j)}{|\vec{r}_i - \vec{r}_j|^2} (\tilde{\upsilon}_j - \tilde{\upsilon}_j) V_j \tag{71}$$

Following Eq. (14), the gradient term in Eq. (70) is evaluated as

$$\nabla\tilde{\upsilon} = -\frac{1}{\rho}\sum_{j=1}^{N} m_j (\tilde{\upsilon}_i - \tilde{\upsilon}_j) \nabla_i W_{ij} V_j \tag{72}$$

In this way, all the terms in Eq. (62) is approximate in SPH form. This turbulence model is explored in the chapter 5.

3.10. Fickian shift model

In this section the commonly used Fickian shift model is described, which is used for comparison with our particle collision shift model (Section 4). In particle shift models, the trajectory of particles is changed by adding a relatively small artificial displacement $\delta\vec{r}_s$. In the shift model described by Lind et al. [62], Fick's law is used to shift particles from regions of high concentration to low concentration.

Fick's law is

$$J = -D'\nabla C, \tag{73}$$

where J is the flux, C is the concentration and $\mathcal{D}'$ is the diffusion coefficient. The shift vector is

$$\delta\vec{r}_i = -D\nabla C_i, \tag{74}$$

where $\mathcal{D}$ is a shift coefficient, which should be chosen as $\mathcal{D} \leq 0.5\, h^2$. The concentration of particle i is obtained from the kernel function (W)

$$C_i = \sum_j V_j\, W_{ij}, \tag{75}$$

where V_j is the volume of neighbour particles j. The gradient of the concentration is obtained from the kernel gradient as

$$\nabla C_i = \sum_j V_j\, \nabla W_{ij}. \tag{76}$$

Monaghan [112] introduced an artificial function to stabilize the pressure

$$f_{ij} = R(\frac{W_{ij}}{W(dx)})^n, \tag{77}$$

where R and n are coefficients with values $R = 0.2$ and $n = 4$. This function is also used in the gradient of the concentration, which now becomes

$$\nabla C_i = \sum_j V_j\, (1 + f_{ij})\, \nabla W_{ij}. \tag{78}$$

The shift of an inner particle is described by

$$\delta\vec{r}_i = -D\, \sum_j V_j\, (1 + f_{ij})\nabla W_{ij}. \tag{79}$$

The above result cannot be applied at the free surface, for which a special treatment is needed. Here, the shift vector is described by

$$\delta\vec{r}_i = -D\, \left(\frac{\partial C}{\partial s}\vec{s} + \alpha\, \left(\frac{\partial C}{\partial n} - \beta\right)\vec{n}\right), \tag{80}$$

where $\vec{s}$ and $\vec{n}$ denote the tangent and normal vectors to the free surface, β is a reference concentration gradient at the free surface. α is a coefficient between 0 and 1 to control the shift in the normal direction. The upper limit of the particle shift is 0.2 h [62], where h is the smoothing length.

The linear correction of the velocity in the Fickian shift model, as proposed by [62] is

$$\overrightarrow{v'}_i = \vec{v}_i + (\nabla\vec{v}_i) \cdot \delta\vec{r}_i, \tag{81}$$

in which $\nabla\vec{v}_i$ is the velocity gradient. The Fickian shift model does not conserve momentum [62]. A relatively small numerical error is introduced in the interpolation of the velocity and the velocity gradient may introduce an error when the support domain is truncated, at the free surface.

The above algorithms show that the Fickian shift model is rather complex and relies on several coefficients. The model (with velocity correction) is applied in the case studies (Section 5).

3.11. Models based on particle collisions

In this section, the novel particle collision shift model is derived from the original particle collision model. For this purpose, the particle collision model [1] is described first.

3.11.1. Particle collision model

In the particle collision model, kinetic collision theory is applied to SPH particles, to deal with particle clustering. This is only performed when particles are (too) close together. The collisions are applied to the relative approach velocity so that the velocity components in other directions remain unchanged. To deal with collisions between more than two particles, the model is extended to simultaneous collisions, although this rarely occurs if the time step is chosen sufficiently small. Both elastic and inelastic collisions are considered, and the extent of elasticity is controlled by a coefficient of restitution $(0 \leq C_R \leq 1)$. The principle of the original particle collision model is described below, where collisions between particles are considered.

Collisions between particles are applied when the following two criteria are satisfied:

$$d_{ij}(t) < d_{col} \text{ and } \vec{r}_{ij}(t) \cdot \vec{v}_{ij}(t) < 0, \tag{82}$$

where $d_{ij}(t)$ is the distance between particle i and j at time t, d_{col} is the collision distance, $\vec{r}_{ij}(t) = \vec{r}_i(t) - \vec{r}_j(t)$ and $\vec{v}_{ij}(t) = \vec{v}_i(t) - \vec{v}_j(t)$ are the relative position and velocity vectors, respectively. If the second term in Eq. (82) is negative, the particles approach each other. In the particle collision model, the change of the velocity of a particle *i* due to simultaneous collisions with neighbour particles *j* is

$$\Delta\vec{v}_{i\to j} = -\frac{1}{m_i+\sum m_j}\sum m_j\,(1+C_R)\frac{(\vec{r}_{ij}(t)\cdot\vec{v}_{ij}(t))}{d_{ij}(t)}\frac{\vec{r}_{ij}(t)}{d_{ij}(t)}. \tag{83}$$

For a collision between two particles, the above equation reduces to

$$\Delta\vec{v}_{i\to j} = -\frac{1}{m_i+m_j}m_j(1+C_R)\frac{(\vec{r}_{ij}(t)\cdot\vec{v}_{ij}(t))}{d_{ij}(t)}\frac{\vec{r}_{ij}(t)}{d_{ij}(t)}, \tag{84}$$

where m is a particle mass, and C_R is the coefficient of restitution, representing the elasticity of the collision. The change of the velocity is proportional but opposite to the approach velocity $(\vec{r}_{ij}(t) \cdot \vec{v}_{ij}(t))/d_{ij}(t)$. With the above equation, it follows for the relative velocity between two particles due to a collision (superscript ’)

$$\vec{v}'_{ij}(t) = \left[\vec{v}_{ij}(t) - \frac{(\vec{r}_{ij}(t)\cdot\vec{v}_{ij}(t))}{d_{ij}(t)}\frac{\vec{r}_{ij}(t)}{d_{ij}(t)}\right] + \left\{\frac{(\vec{r}_{ij}(t)\cdot\vec{v}_{ij}(t))}{d_{ij}(t)}\frac{\vec{r}_{ij}(t)}{d_{ij}(t)}\right\} - (1+C_R)\frac{(\vec{r}_{ij}(t)\cdot\vec{v}_{ij}(t))}{d_{ij}(t)}\frac{\vec{r}_{ij}(t)}{d_{ij}(t)}. \tag{85}$$

Note that the relative velocity $\vec{v}'_{ij}$ is here split into the velocity in inter-particle direction {between braces} and the component perpendicular to that [between square brackets]. The last term is the change of the relative velocity due to a collision. This change of velocity is only in inter-particle direction, so that the perpendicular component always remains unchanged. This equation shows that for $C_R = 0$ the approach velocity is reduced to zero, so that the particle velocities become (almost) parallel. For $C_R = 1$ the approach velocity is reversed, so that the particle velocities diverge. Inelastic collisions ($C_R = 0$) appear to give more stable results, however, energy is dissipated [1], and with parallel particle velocities the separation of particles is not guaranteed.

The above concept is used in the derivation of the particle collision shift, which guarantees particle separation whilst the shift model itself is non-dissipative.

3.11.2. Particle collision shift model

In this section the new particle collision shift model is introduced and derived from the original particle collision model. For this purpose, the velocity term in Eq. (84) is considered. In Appendix A it is shown that the approach velocity can be approximated as

$$\frac{\vec{r}_{ij}(t)\cdot\vec{v}_{ij}(t)}{d_{ij}(t)} \approx \frac{d_{ij}(t)-d_{ij}(t-\Delta t)}{\Delta t}. \tag{86}$$

Substitution of Eq. (86) into Eq. (84) gives

$$\Delta\vec{v}_{i\to j} \approx -\frac{m_j}{m_i+m_j}(1+C_R)\left(\frac{d_{ij}(t)-d_{ij}(t-\Delta t)}{\Delta t}\right)\frac{\vec{r}_{ij}(t)}{d_{ij}(t)}. \tag{87}$$

The shift induced by the collision velocity in timestep Δt is

$$\Delta\vec{r}_{i\to j} = -\frac{m_j}{m_i+m_j}(1+C_R)(d_{ij}(t)-d_{ij}(t-\Delta t))\frac{\vec{r}_{ij}(t)}{d_{ij}(t)}. \tag{88}$$

In this result the previous distance $d_{ij}(t-\Delta t)$ appears. In case of an inelastic collision ($C_R = 0$), the particles are bounced back to their previous distance. This can be easily seen if the particle masses are equal ($m_i = m_j$). The bouncing back of particles is not the intention, it may even lead to instabilities and is undesirable. The intention is to avoid particle distances smaller than the collision distance. Therefore, the particle distance $d_{ij}(t-\Delta t)$ is replaced by d_{col}, leading to

$$\Delta\vec{r}_{i\to j} = -\frac{m_j}{m_i+m_j}(1+C_R)(d_{ij}(t)-d_{col})\frac{\vec{r}_{ij}(t)}{d_{ij}(t)}. \tag{89}$$

The above result describes the particle collision shift between two particles, if their distance is too small.

Following Eq. (89), the shift of particle *j* due to a collision with particle *i* is

$$\Delta\vec{r}_{j\to i} = -\frac{m_i}{m_i+m_j}(1+C_R)(d_{ji}(t)-d_{col})\frac{\vec{r}_{ji}(t)}{d_{ji}(t)}. \tag{90}$$

The relative position after the collision shift between the particles *i* and *j* now becomes

$$\vec{r}_{ij}'(t) = \vec{r}_{ij}(t) + \Delta\vec{r}_{i\to j} - \Delta\vec{r}_{j\to i} = \left[(1+C_R)\frac{d_{col}}{d_{ij}(t)} - C_R\right]\vec{r}_{ij}(t). \tag{91}$$

So that the distance between particles *i* and *j* is

$$d_{ij}'(t) = (1+C_R)\,d_{col} - C_R\,d_{ij}(t). \tag{92}$$

For $C_R = 0$, the distance becomes

$$d_{ij}'(t) = d_{col}, \tag{93}$$

and for $C_R = 1$

$$d_{ij}'(t) = 2\,d_{col} - d_{ij}(t). \tag{94}$$

The above two equations show that the particle distance after an inelastic collision shift is constant and equal to the collision distance, whilst after an elastic collision shift, the distance is variable and larger than the collision distance. This shows that the inelastic collision shift is more stable than the elastic collision shift. This is consistent with the conclusion that inelastic collisions are more stable than elastic collisions [1].

For collisions between more than two particles, the concept of simultaneous collisions from [1] is applied. Substitution of Eq. (86) in Eq. (83) and following the steps from Eq. (88) to Eq. (89) leads to ($d_{ij} < d_{col}$).

$$\Delta\vec{r}_{i\to all j} = -\frac{\sum m_j(1+C_R)(d_{ij}-d_{col})\frac{\vec{r}_{ij}}{d_{ij}}}{m_i+\sum m_j}. \tag{95}$$

The above result is the full particle collision shift model. The process of collision shifting is shown in Fig. 2 for two and three particles, which are separated if they are too close together.

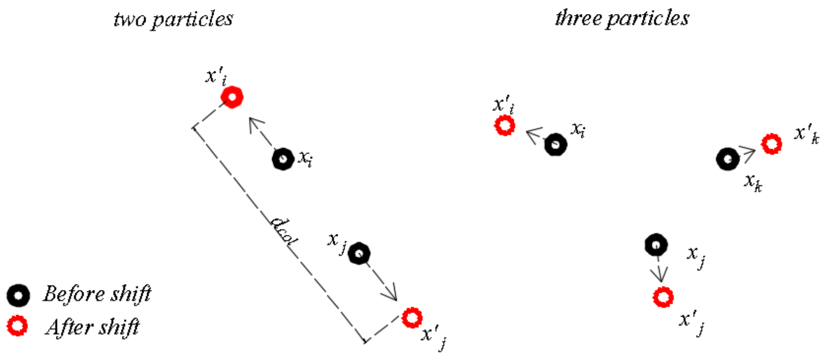

Fig. 2. The shift process after collisions of two and three particles with equal mass.

When Eq. (95) is applied to more than two particles, the particle distances are no longer exactly equal to the collision distance for $C_R = 0$. However, the distance between each particle becomes much closer to d_{col} than it was before the collision. The (first) distance criterion ($d_{ij} < d_{col}$) in Eq. (82) is also used in the particle collision shift model. Note that the (second) criterion in Eq. (82) is no longer necessary since the term $(\vec{r}_{ij} \cdot \vec{v}_{ij})$ no longer appears in the above equation. It is important to note that in the particle collision model, velocities are updated (and not positions), whilst in the particle collision shift model particle positions are updated (and not velocities). Thus, kinetic energy and linear momentum are conserved in the shift model. In Appendix B, it is proven that the conservation of potential energy is satisfied, so that the particle collision model in itself is energy conserving and non-dissipative. In this appendix it is also shown that angular momentum cannot be conserved in a shift process that conserves kinetic energy.

3.12. Summary

In this chapter, the basic methodology of SPH and the physical model in SPH as well as those coefficients are introduced. In addition, the derivation and demonstration of the novel collision shift model is conducted. This novel shift model will be validated in benchmark cases by the comparison with the Fickian shift model in next chapter.

Chapter 4 Validation of particle collision shift model in incompressible SPH (single-phase flow)

4.1. Introduction

In last chapter, a new particle collision shift model is proposed. The shift is based on the change of velocity due to collisions, however the velocity itself remains unchanged. Owing to the latter, this not only satisfies the conservation of momentum, but also kinetic energy. It is proven that potential energy is conserved in a constant force field. Thus, the shift model is non-dissipative in real cases with gravitation. To avoid particle clustering (when particles are too close together) collision shifts are applied, noting that clustering is a local phenomenon at a scale smaller than the kernel support domain. Our model is validated in six benchmark cases, which are the decay of Taylor-Green vortices, the lid driven cavity, the rotation of a square fluid patch, the oscillation of a droplet, the propagation of a solitary wave and the dam break. The Fickian shift model (Section 3.10) and the new particle collision shift model (Section 3.11.2) are explored and compared in six case studies. For convenience, the following abbreviations are made: Fickian Shift (FS) and Collision Shift (CS).

Following [62], the coefficients in FS are taken as follows, unless otherwise stated. The shift coefficient $\mathcal{D} = 0.5\,h^2$ in most cases. In the cases without free surface (Taylor-

Green vortex in Section 4.2 and lid-driven cavity in Section 4.3), the free surface treatment in Eq. (80) is not applied. For slow flows of long durations (oscillation of droplet in Section 4.4 and rotation of square fluid patch in Section 4.5) $\alpha = 0.1$ and β is the concentration gradient at the unperturbed plane free surface. For high-speed violent flows (solitary wave in Section 4.6 and dam break in Section 4.7) $\alpha = 0$, so that there is no shift in normal direction at the free surface.

In the particle collision shift model, the collision distance d_{col} is chosen equal to the initial particle distance in all cases. When the original particle collision model is applied in WCSPH, the collision distance is obtained from a minimum particle distance, occurring in a compressed state at maximum pressure [1]. The minimum particle distance also depends on the compressibility, as represented by the (artificial) wave speed [1]. The coefficient of restitution is chosen $C_R = 0$ in all cases, representing an inelastic CS. In all cases a cube spline kernel [113] is used and the smoothing length is 1.2 Δx, where Δx, is the initial particle distance. To allow for a direct comparison of FS and CS, fixed time stepping is used (Δt = 0.001s).

4.2. Taylor-Green vortex

The Taylor-Green vortex is a benchmark case which represents the unsteady flow of decaying vortices. This case is studied by e.g. [1,4,5,62]. In this case, an exact solution of the incompressible Navier-Stokes equations exists. In the two-dimensional case, the velocity and pressure fields are

$$\begin{pmatrix} u(r,t) \\ v(r,t) \end{pmatrix} = \begin{pmatrix} -U_0 cos\,(\frac{2\pi x}{L}) sin\,(\frac{2\pi x}{L}) e^{-bt} \\ U_0 sin\,(\frac{2\pi x}{L}) cos\,(\frac{2\pi x}{L}) e^{-bt} \end{pmatrix}, \tag{96}$$

$$p(r,t) = -\frac{\rho U_0}{4} (cos\left(\frac{4\pi x}{L}\right) + cos\,(\frac{4\pi y}{L})) e^{-2bt}\,, \tag{97}$$

where U_0 is the velocity amplitude ($U_0 = 1\ m/s$), L is the size of the squared fluid domain (L = 1 m), the exponent b represents the decay ($b = 8\pi^2/Re$), x and y are the horizontal and vertical axis, u and v are the horizontal and vertical velocity components, respectively and p is the pressure. The Reynolds number is here defined as $Re = U_0 L/\nu$, where ν is the kinematic viscosity of the fluid. The fluid density ρ = 1 kg/m^3 and the kinematic viscosity is varied to obtain the desired Reynolds numbers which are $\nu = 10^{-2}, 10^{-3}$ and 10^{-6}.

As an initial condition a hexahedral particle distribution is chosen with 4200 particles. Simulations are performed at three different Reynolds numbers Re = 10^2, 10^3 and 10^6. The results of the simulations with FS and CS are shown in Fig. 3, in which the pressure contour and particle distribution are compared at $Re = 10^3$ at the dimensionless time $tU_0/L = 0.15$. Standard ISPH suffers from particle layering as shown in Fig. 3 (a). The results obtained with FS in Fig. 3 (b) and the new particle collision shift model in Fig. 3 (c) are much better and show an almost regular particle distribution. Next, the decay of kinetic energy and maximum velocity is analysed to reveal the differences between FS and CS.

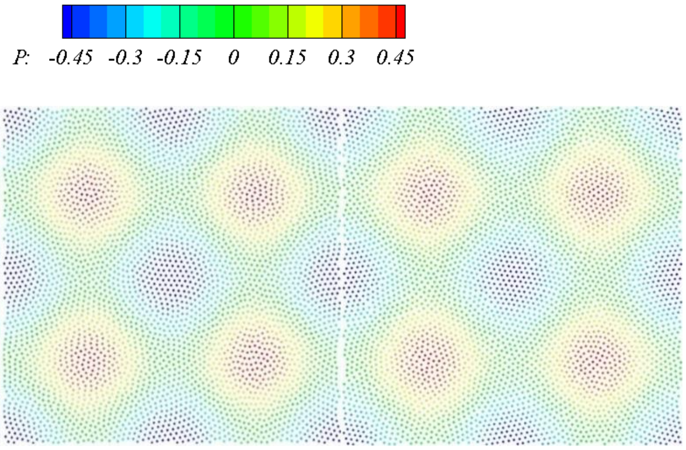

(a) Standard ISPH (b) FS (c) CS

Fig. 3. Taylor-Green vortex (Re=10^3). Particle distribution at time $tU_0/L = 0.15$,

simulations with (a) standard ISPH, (b) FS, (c) CS.

In Fig. 4 to Fig. 6 the decay of kinetic energy and maximum velocity is presented on the log scale, together with the relative errors of the FS and CS models at three Reynolds numbers Re = 10^2, 10^3 and 10^6, respectively. The kinetic energy of the system and the maximum velocity are used as a measure for the accuracy and stability of these models. The relative error is defined as

$$E_{rel} = \frac{f_{sph} - f_{theo}}{f_{theo}} \times 100\%, \tag{98}$$

where f_{sph} is the simulation result whilst f_{theo} is the theoretical data.

Fig. 4 shows the results at Re = 10^2. It can be seen in the Fig. 4(a) and (b) that the decay obtained with the schemes is very similar, although there are small differences found in the relative errors. The results of FS are slightly better than CS, for both kinetic energy and maximum velocity. Fig. 5 shows the results at Re = 10^3. The results of CS here are the best for both kinetic energy and maximum velocity. The differences between the schemes are larger here. At Re = 10^3 the errors in CS are 4% lower in kinetic energy and 3% lower in maximum velocity than in FS at t = 10 s. Fig. 6 shows the results at Re = 10^6. This case is no longer laminar but turbulent. It should be noted that no turbulence model is used in this case, like other researchers have done [1,5]. Now the decay is very slow, resulting in an almost constant kinetic energy and maximum velocity. The fluctuation in the maximum velocity is the highest here, which may be expected in this more violent case. FS is performing reasonably well for both kinetic energy and maximum velocity. However, the error in the kinetic energy of CS is about 10% lower whilst the error in the maximum velocity is 10% higher than that of FS at t = 10 s. High Reynolds numbers will cause turbulent viscosity, however, physical dissipation and numerical dissipation are hard to be separated, and there is no turbulence model implementation for this case. The dissipation here can be considered as numerical dissipation.

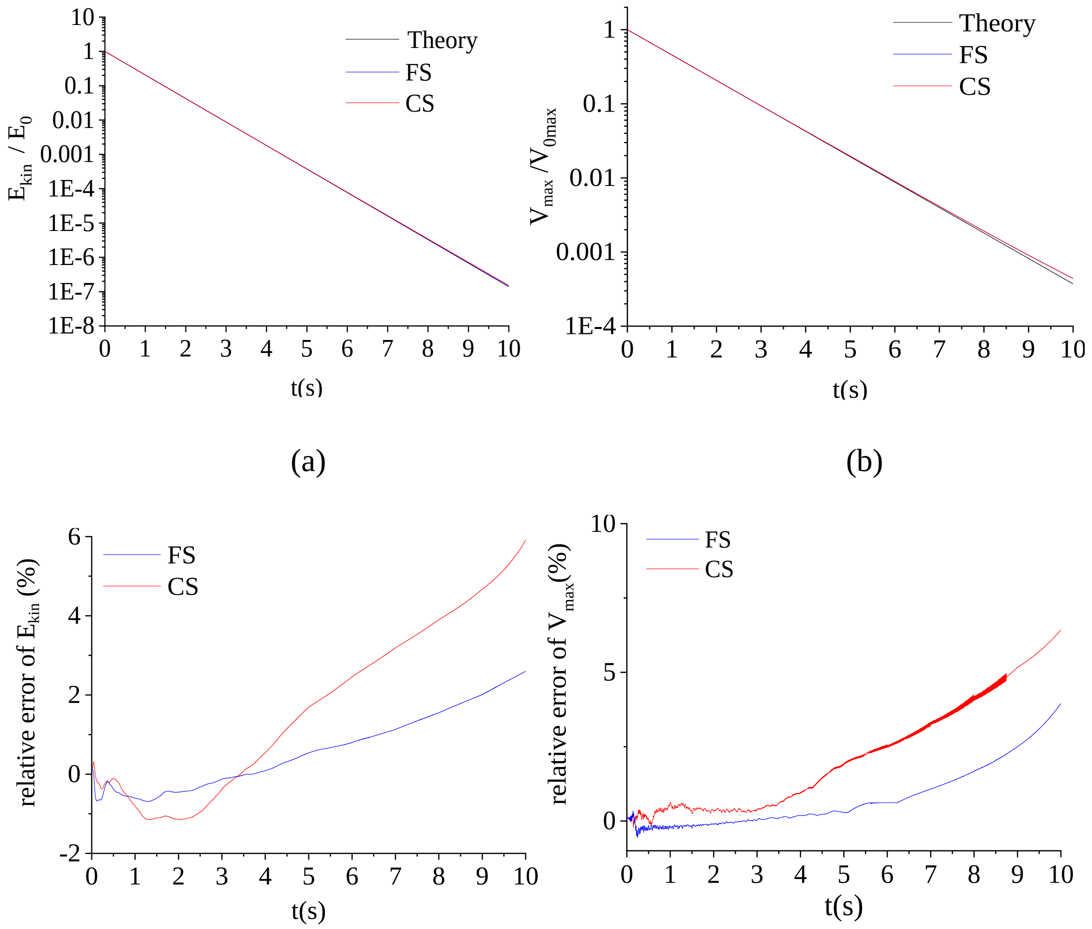

(a)

(b)

(c)

(d)

Fig. 4. Taylor Green vortex. Comparison of FS and CS models at *Re* = 10^2. The panels show (a) kinetic energy, (b) maximum velocity, (c) relative error of kinetic energy, (d) relative error of maximum velocity.

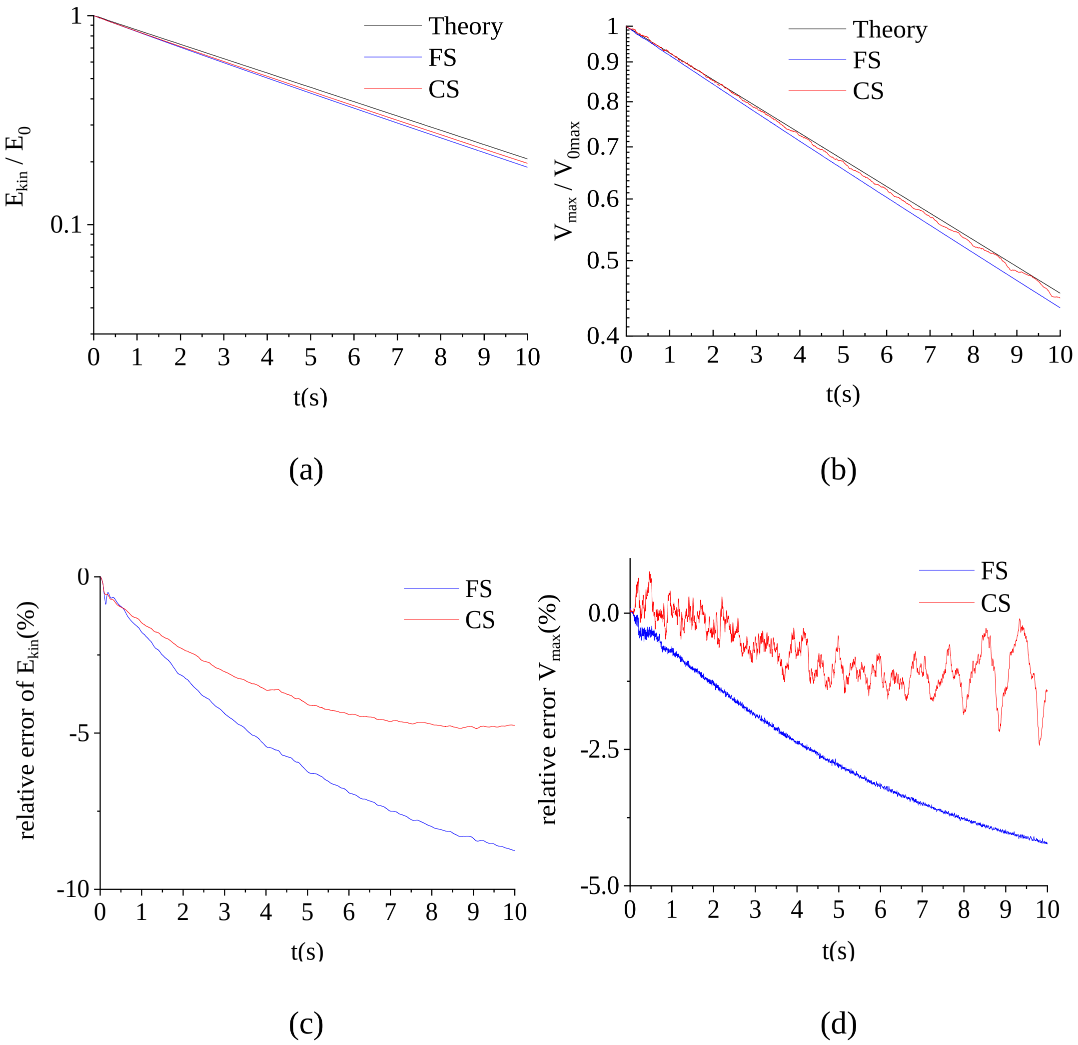

(a) (b)

(c) (d)

Fig. 5. Taylor Green vortex. Comparison of FS and CS models at *Re* = 10^3. The panels show (a) kinetic energy, (b) maximum velocity, (c) relative error of kinetic energy, (d) relative error of maximum velocity.

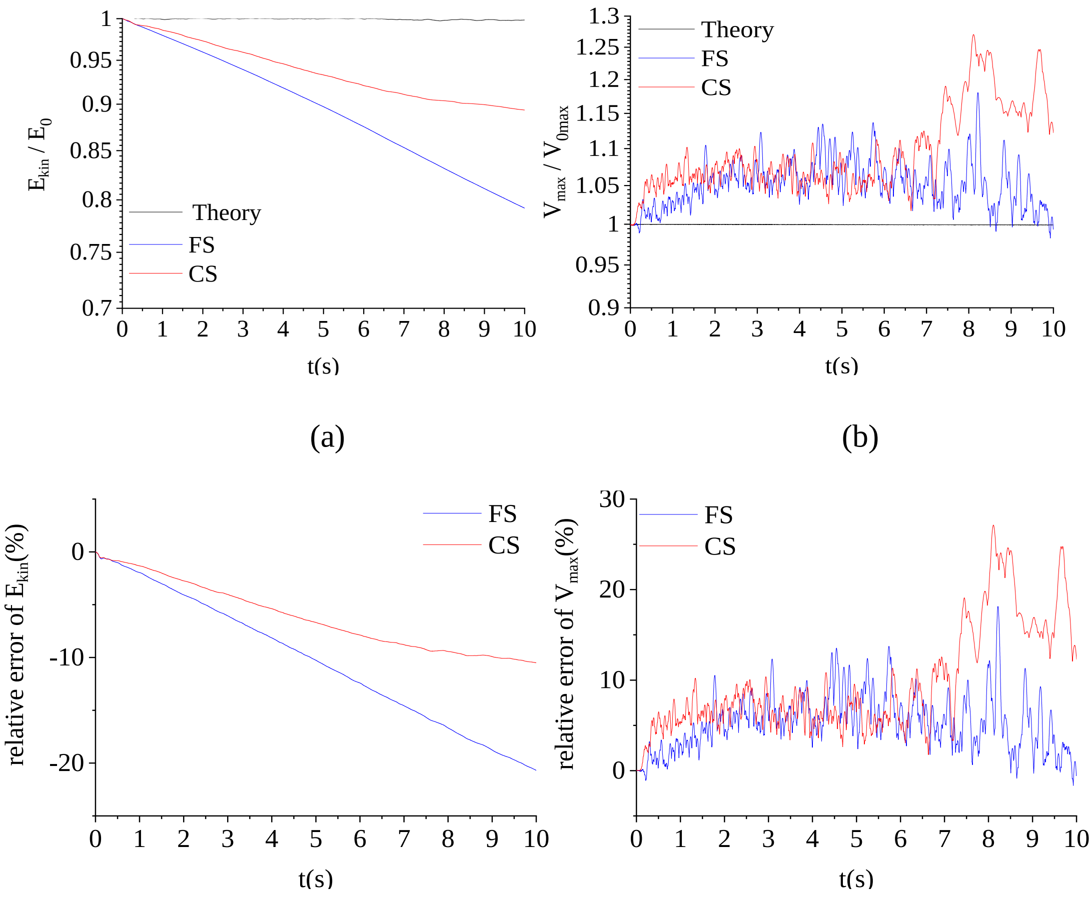

(a)

(b)

(c)

(d)

Fig. 6. Taylor Green vortex. Comparison of FS and CS models at *Re* = 10^6. The panels show (a) kinetic energy, (b) maximum velocity, (c) relative error of kinetic energy, (d) relative error of maximum velocity.

Table 1. Average absolute error of pressure, horizontal and vertical velocity at the instant $t = 1$ s.

Reynolds number	$Re=10^2$		$Re=10^3$		$Re=10^6$	
Shift scheme	CS	FS	CS	FS	CS	FS
P	0.008	0.011	0.014	0.019	0.022	0.026
U	0.025	0.026	0.020	0.021	0.025	0.023
V	0.028	0.028	0.022	0.022	0.0276	0.016

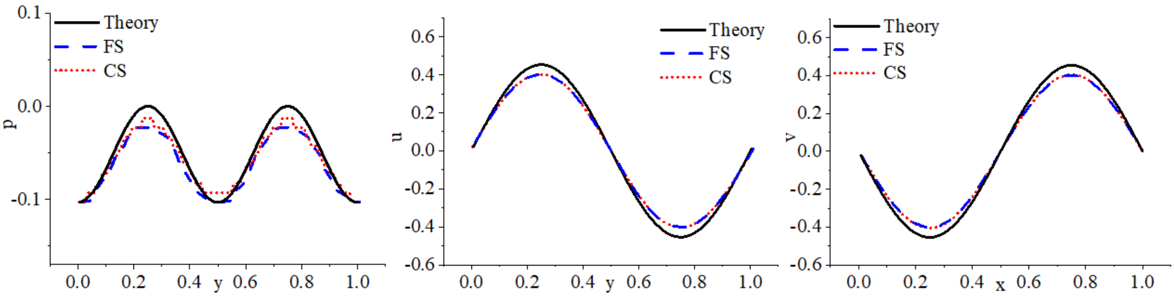

(a) (b) (c)

Fig. 7. Taylor Green vortex. Comparison of FS and CS at $Re = 10^2$ and $t = 1$ s. The panels show (a) pressure profiles along $x = 0.5$ m, (b) horizontal velocity profiles along $x = 0.5$ m, (c) vertical velocity profiles along $y = 0.5$ m.

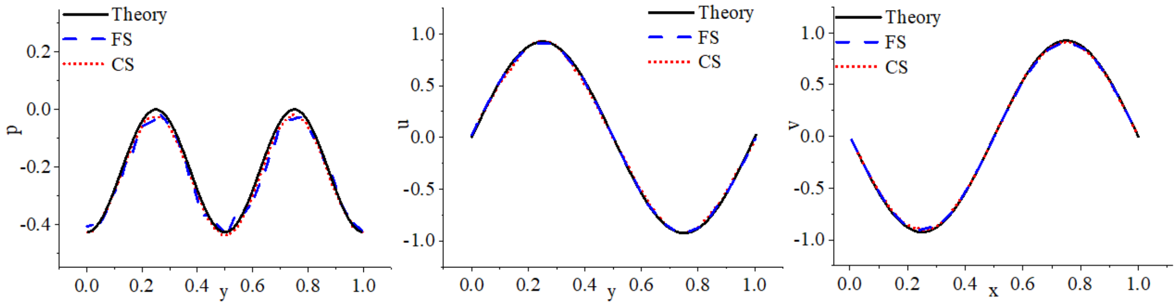

(a) (b) (c)

Fig. 8. Taylor Green vortex. Comparison of FS and CS at *Re* = 10^3 and *t* = 1 s. The panels show (a) pressure profiles along *x* = 0.5 m, (b) horizontal velocity profiles along *x* = 0.5 m, (c) vertical velocity profiles along *y* = 0.5 m.

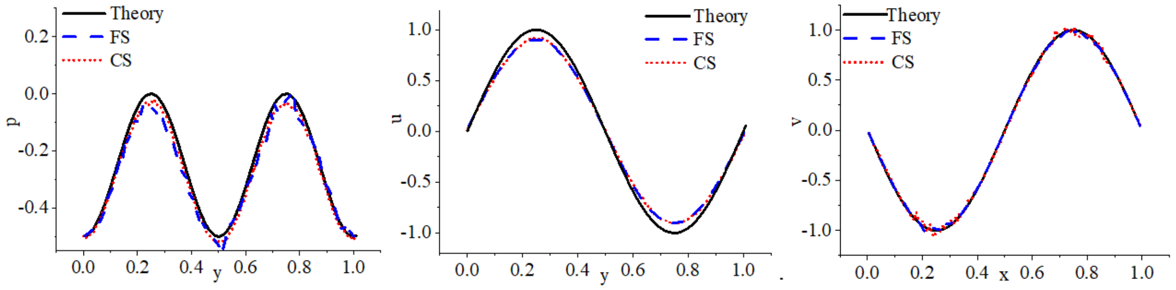

(a) (b) (c)

Fig. 9. Taylor Green vortex. Comparison of FS and CS at *Re* = 10^6 and *t* = 1 s. The panels show (a) pressure profiles along *x* = 0.5 m, (b) horizontal velocity profiles along *x* = 0.5 m, (c) vertical velocity profiles along *y* = 0.5 m.

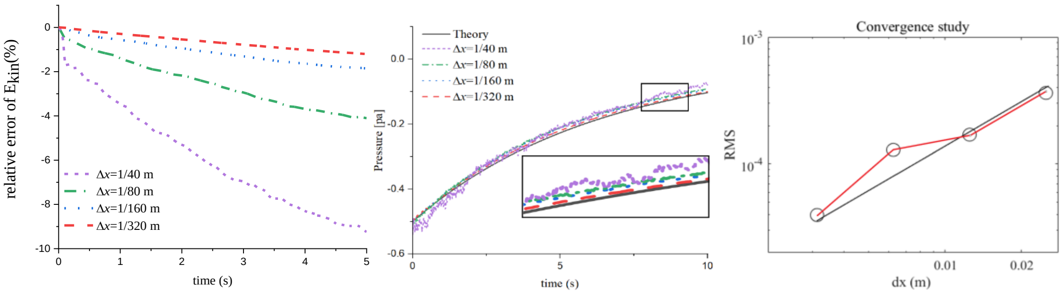

(a) (b) (c)

Fig. 10. Taylor Green vortex, results of CS. (a) Relative error of kinetic energy in time at four particle resolutions. (b) Pressure at centre point (0.5, 0.5) in time at four particle resolutions. (c) Convergence of the RMS error of pressure with increasing particle resolution ($\Delta x \rightarrow 0$).

In Fig. 7 to 8 pressure and velocity profiles at the three above-mentioned Reynolds numbers are shown at the instant t = 1 s like [4,5,62]. The pressure and horizontal velocity of particles along the vertical line x = 0.5 m, and the vertical velocity of particles along the horizontal line y = 0.5 m are shown in the panels (a), (b) and (c), respectively. Both FS and CS show a reasonable agreement with theory. The average absolute error is defined as

$$\bar{E}_{abs} = \frac{\sum_{i=1}^{N}\left|f_i^{sph}-f_i^{real}\right|}{N}, \qquad (99)$$

where N is the total number of the particles within a bandwidth Δx of the two lines. The results in

Table 1 show that the errors in pressure obtained with CS are all lower than with FS, whilst the errors in velocity are lower with CS, except at the highest Reynolds number.

Fig. 10(a) and (b) show the relative error of the kinetic energy and pressure at centre point (0.5, 0.5) at four resolutions, obtained with CS. Both errors are decreasing with increasing resolution and showing convergence. Fig. 10(c) shows the order of convergence of the root of the mean square (RMS) of the relative error in the pressure at the centre point, which is approximately 1.07.

Table 2 provides information about the required CPU (Intel(R) Xeon(R) CPU E5-1620 v4@ 3.50GHz) time for each of the shift schemes. FS needs a kernel summation to evaluate the shift of all particles, which is computationally more expensive. CS is an inter-particle concept, which does not need a kernel summation. The inter-particle concept is here computationally 16% cheaper as shown in Table 2.

Table 2. Taylor green vortex. Required CPU time for 5 seconds of simulation time at a resolution $\Delta x = \frac{1}{200} m$.

Method	CS	FS
CPU time [s]	3805.83	4432.75

4.3. Lid driven cavity

The lid driven cavity is a typical shear driven flow, where no-slip boundaries play a significant role. Several researchers have used this case to validate their SPH methods [4,96,108,114]. The parameters are commonly chosen as follows. The size of the square fluid domain is $D = 1.0\ m$, the velocity of the lid at the top of the cavity is $U = 1.0\ m/s$ and the Reynolds number is $Re = UD/\nu$, where the kinematic viscosity is varied to obtain the desired Reynolds numbers (Re = 100, 400, 1000). The density of the fluid is 1 kg/m^3.

In Fig. 11, the steady state solution is shown as obtained with standard ISPH, FS and CS. Standard ISPH suffers from particle clustering from the start of the simulation. This can be seen in Fig. 11(a) at the left and right top corners before any vortex is formed. In contrast, the particle clustering does not appear in the results obtained with FS and CS. Here the vortex is very stable and shows excellent agreement between the two methods.

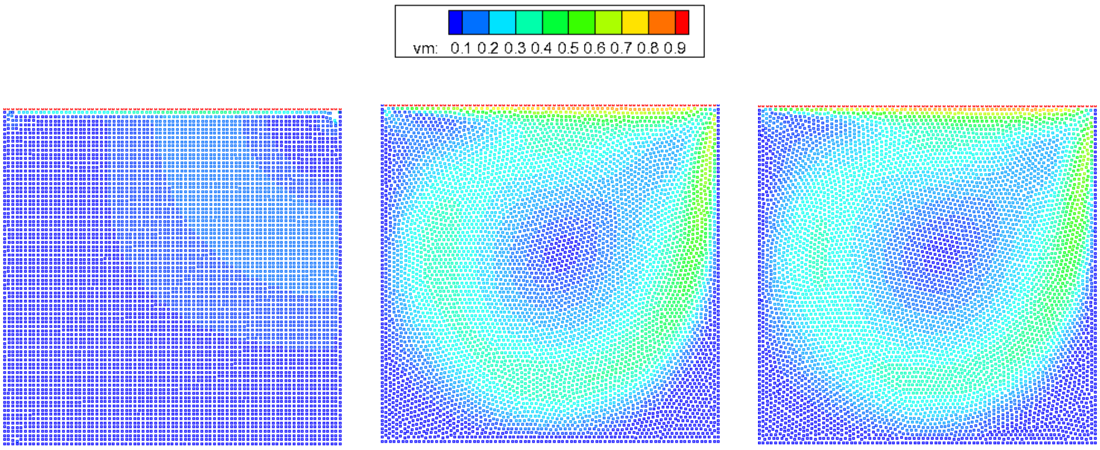

(a) Standard ISPH (t = 0.06 s) (b) FS (t = 5 s) (c) CS (t = 5 s)

Fig. 11. Lid-driven cavity (Re = 1000). Particle distribution with velocity magnitude (colour bar), simulations with (a) standard ISPH; (b) FS; (c) CS.

To assess the accuracy of the results, profiles of the horizontal velocity component (u) along the vertical at x = 0.5 m and vertical velocity component (v) along the horizontal at y = 0.5 m are considered in the Fig. 12 to 16.

In the Fig. 12 to 14 the velocity profiles at Re = 100, 400, 1000 are presented, as obtained with CS for three resolutions (Δx = 1/80 m, Δx = 1/160 m and Δx = 1/240 m), with a validation against simulations obtained with a multigrid finite volume method from Ghia et al. [37]. The figures show that with increasing resolution, the results are closer to those of Ghia et al [115]. This tendency can also be seen in Table 3 where the average absolute error of the horizontal velocity is given for *Re* = 1000.

Table 3. Lid driven cavity. Average absolute error of CS in the horizontal velocity at *Re* = 1000 for different resolutions.

Δx (m)	1/80	1/160	1/240
Average absolute error	0.997 %	0.257%	0.132 %

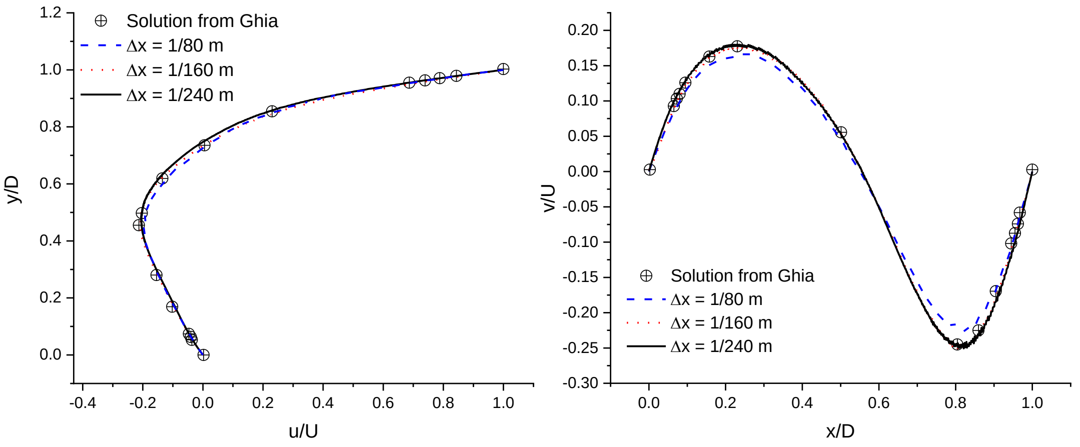

(a) (b)

Fig. 12. Lid driven cavity. Velocity profiles of CS for three resolutions at *Re* = 100. (a) Horizontal velocity at *x* = 0.5 m, (b) vertical velocity at *y* = 0.5 m.

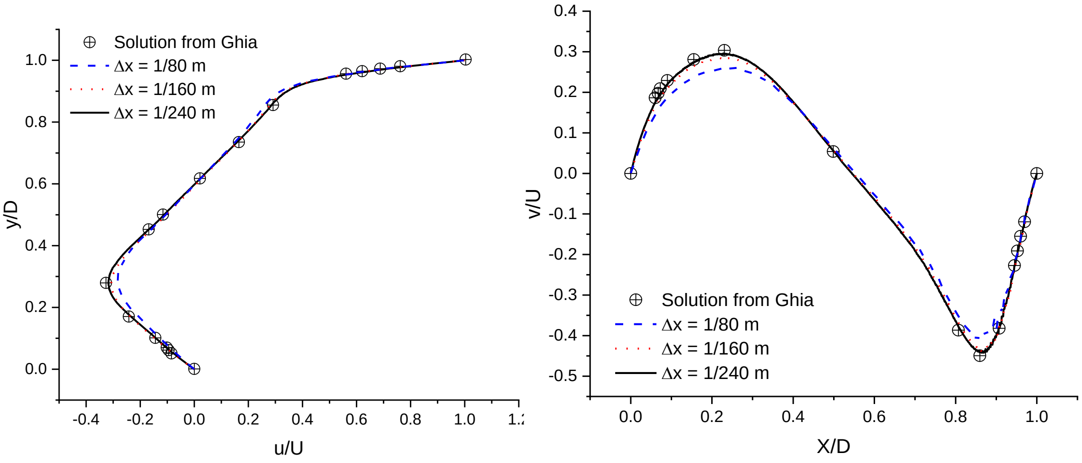

(a) (b)

Fig. 13. Lid driven cavity. Velocity profiles of CS for three resolutions at *Re* = 400. (a) Horizontal velocity at *x* = 0.5 m, (b) vertical velocity at *y* = 0.5 m.

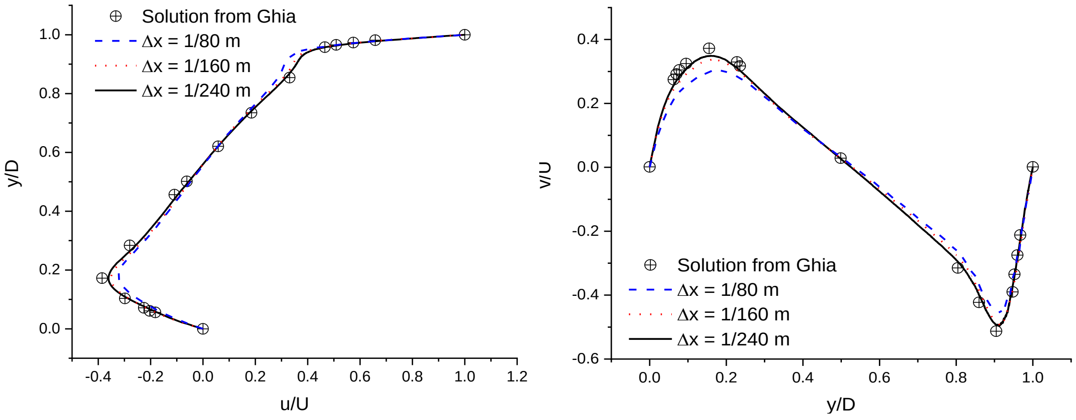

(a) (b)

Fig. 14. Lid driven cavity. Velocity profiles of CS for three resolutions at *Re* = 1000. (a) Horizontal velocity at *x* = 0.5 m, (b) vertical velocity at *y* = 0.5 m.

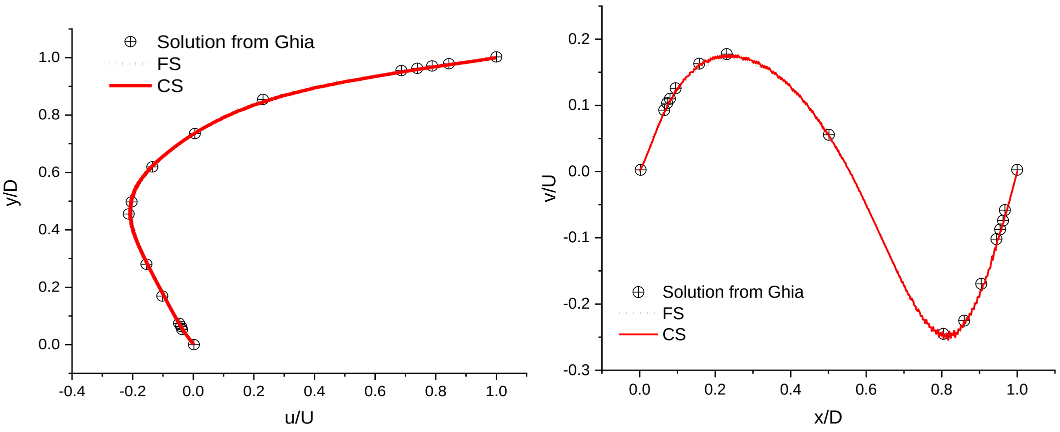

(a) (b)

Fig. 15. Lid driven cavity. Velocity profiles of FS and CS at *Re* = 100 and medium resolution. (a) Horizontal velocity at *x* = 0.5 m, (b) vertical velocity at *y* = 0.5 m.

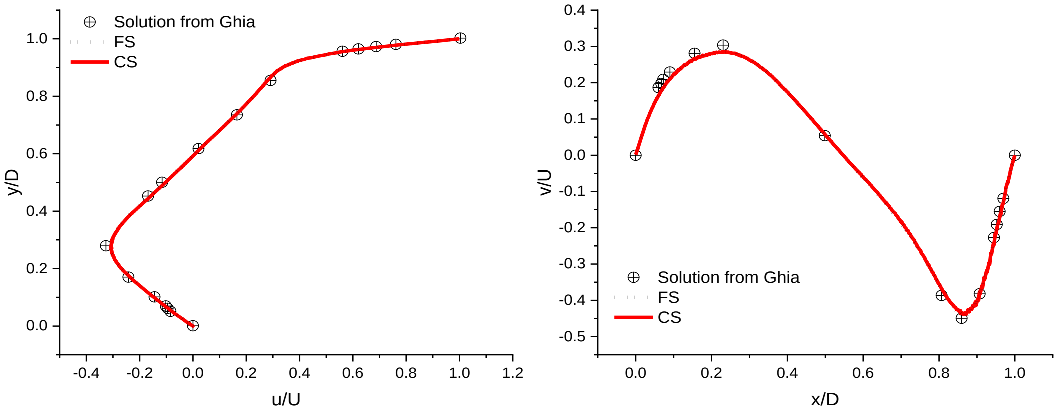

(a) (b)

Fig. 16. Lid driven cavity. Velocity profiles of FS and CS at *Re* = 400 and medium resolution. (a) Horizontal velocity at *x* = 0.5 m, (b) vertical velocity at *y* = 0.5 m.

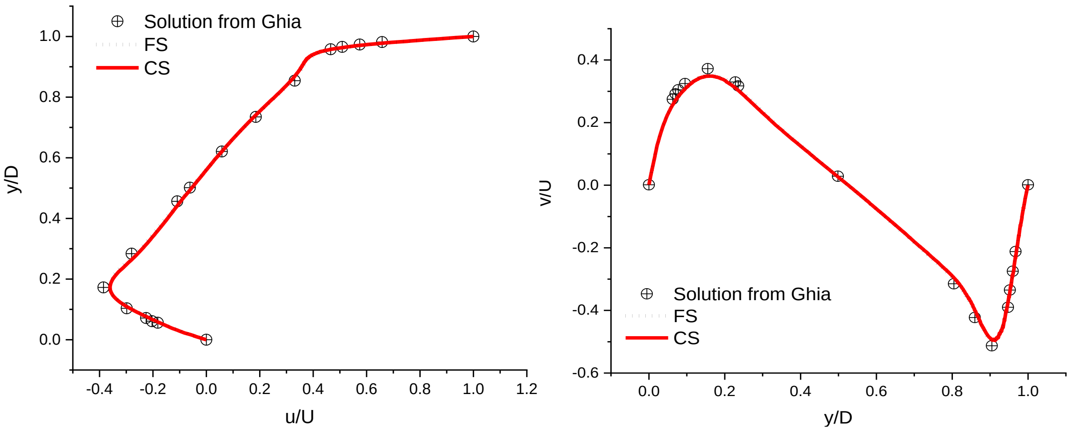

(a) (b)

Fig. 17. Lid driven cavity. Velocity profiles of FS and CS at *Re* = 1000 and medium resolution. (a) Horizontal velocity at *x* = 0.5 m, (b) vertical velocity at *y* = 0.5 m.

Table 4. Average absolute error of horizontal and vertical velocity at medium resolution (Δx = 1/160m).

	Re = 100	*Re* = 400	*Re* = 1000
CS horizontal velocity	2.016%	0.217%	0.257%
FS horizontal velocity	2.697%	0.429%	0.130%
CS vertical velocity	0.123%	0.808%	2.761%
FS vertical velocity	0.201%	0.214%	1.858%

In the Figs. 15 to17 velocity profiles at *Re* = 100, 400, 1000 and medium resolution (Δx = 1/160 m) are presented, obtained with FS and CS, and again compared with the results from Ghia et al. [115]. The results of FS and CS are nearly the same and are in a reasonable agreement with those of Ghia.

Table 4 shows the average absolute error of the horizontal and vertical velocity components, obtained with FS and CS at medium resolution. The errors of FS and CS are of the same order.

In Fig. 18(a) the pressure profiles at *Re* = 1000, as obtained with CS for four resolutions (Δx = 1/40 m, Δx = 1/80 m, Δx = 1/160 m and Δx = 1/320 m), are validated against simulations performed with STAR_CD commercial CFD software, taken from [4]. The figure shows that with increasing resolution, the results are closer to those of STAR_CD. In Fig. 18(b) the order of convergence, evaluated as the root of the mean square (RMS) of the error in the pressure along the diagonal line (from (0.0, 0.0) to (1.0, 1.0)), is plotted for *Re* = 1000. The results show that the order of convergence is approximately 1.36.

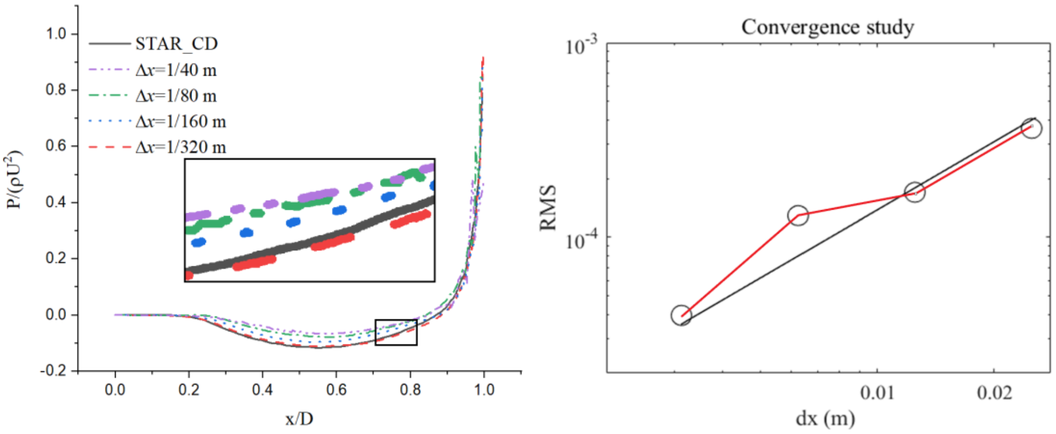

(a) (b)

Fig. 18. Lid driven cavity. (a) Pressure profile along the diagonal line, from (0.0, 0.0) to (1.0, 1.0) for CS at four particle resolutions. (b) Convergence of the RMS error of pressure for *Re* = 1000 with increasing particle resolution ($\Delta x \rightarrow 0$).

4.4. Oscillation of a droplet

The third case is an inviscid free surface flow in which a two-dimensional droplet is oscillating under a fictive force. This case is proposed and analysed by Monaghan and Rafiee [32], followed by Antuono et al. [116], Sun et al. [117] and Khayyer et al. [5]. The periodic motion of the droplet is driven by a conservative field $-\Omega^2 r$, where Ω is a dimensional parameter which is chosen to be equal to 1.2 s^{-1}. The initial shape of the droplet is a circle with radius of 0.5 m. And the initial velocity distribution at $t = t_0$ is

$$\begin{cases} u(t_0) = \quad A(t_0)x \\ v(t_0) = -A(t_0)y\,, \end{cases} \tag{100}$$

where $A(t_0)$ is 0.4 s^{-1}. The period of the oscillation is $T = \sqrt{2}\pi/\Omega \approx 3.70\ \mathrm{s}$. The resolution is varied from low to high by choosing five different initial particle distances of $\Delta x = 1/50$, 1/100, 1/150, 1/200, and 1/300 m. The density of the fluid is 1000 kg/m^3.

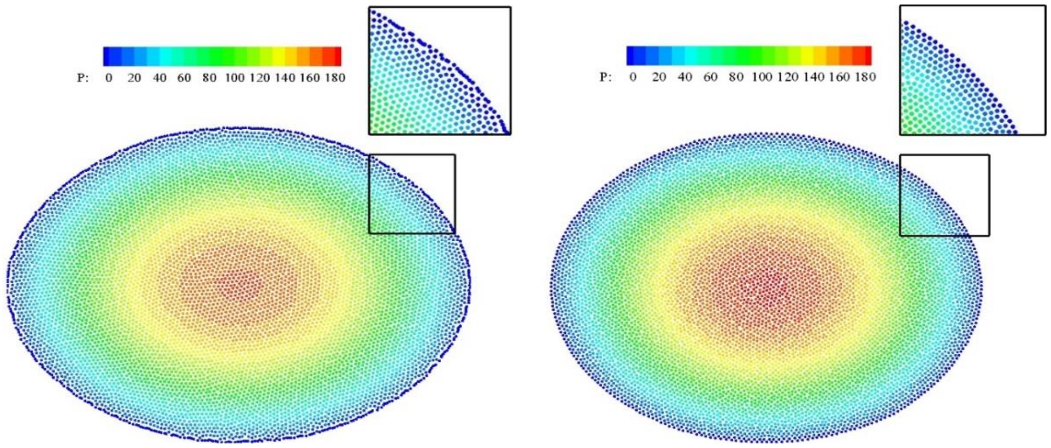

(a) (b)

Fig. 19. Oscillation of droplet. Particle distribution and pressure (color bar) after 5.4 oscillations (t = 20 s), at resolution Δx = 1/100 m, (a) FS, and (b) CS.

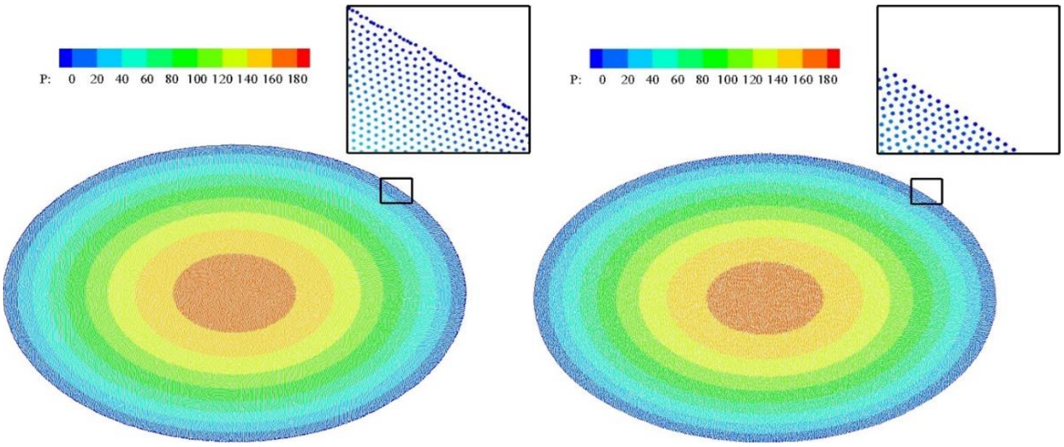

(a) (b)

Fig. 20. Oscillation of droplet. Particle distribution and pressure (color bar) after 5.4 oscillations (t = 20 s), at resolution $\Delta x = 1/300$ m, (a) FS, and (b) CS.

The results of FS and CS are shown in Fig. 19(a) and (b) after a simulation time of 20 s for the low resolution $\Delta x = 1/100$ m case. The details of the free surface are shown in the square boxes. In FS the free surface treatment in Eq. (80) is applied to free surface particles. However, the details in Fig. 19(a) still show a small unphysical gap between the outer particle layer and inner particles, which is also observed and shown in [5]. In CS no free surface treatment is needed. Here, the gap between free-surface particles and inner particles does not exist. In Fig. 20(a) and (b) the results of the two schemes are shown at a higher resolution Δx = 1/300 m. At this resolution, the droplets in both figures have nearly the same elliptical shape. In the details of Fig. 20 (a) the gap between the free-surface particles and inner particles still exists. Again, with CS, no gap appears, as shown in the details of Fig. 20 (b).

The oscillation of the droplet is quantified by considering the expansion and contraction of the semi-major axis, the decay of kinetic energy and decay of potential energy ($\sum_{i=1}^{N} 0.5\, m_i \Omega^2 (x_i^2 + y_i^2)$) in time, following [5,32]. In Fig. 21 the expansion of the vertical semi-major axis, obtained with FS and CS is compared with theory. The results at low and high resolution are presented in Fig. 21(a) and (b). The half-length of the semi-major axis obtained with FS is no longer oscillating around b = 0.5 m but drifts away from the theoretical solution for both resolutions. The results simulated with CS show no drifting and almost no decay, as it should be according to theory.

Fig. 22(a) and (b) show the decay of kinetic energy at low and high resolution. The kinetic energy obtained with FS decays faster at low resolution than at high resolution. The results of CS are nearly 15% closer to the theoretical solution at a lower resolution at *t* = 20 s. For an inviscid flow, the total energy remains conserved, so that there is no decay in the kinetic energy. Fig. 23 (a) and (b) show the potential energy in time at low and high resolution. The potential energy obtained with FS is increasing in time, whilst the decay of kinetic energy decreases. This is attributed to the unphysical gap near the free surface. The shift of the particles at the free surface affects the potential energy, which is larger than the theoretical value in both resolutions. In contrast, the results obtained with CS show a good agreement with theory at high resolution, whilst a slight decay can be seen at low resolution. At high resolution, there is no visible decay of potential energy. It is thus demonstrated that, although potential energy is strictly not conserved with CS in this case with the radial fictive force field, it is practically conserved.

Fig. 24 (a) shows the relative error of CS in the total energy, defined as the sum of potential and kinetic energy, for five resolutions. The error is 6% for the lowest resolution and 0.03% for the highest resolution at *t* = 20 s and shows convergence with increasing resolution. Fig. 24 (b) illustrates the order of convergence of the root of the mean square (RMS) of the relative error in the total energy. The results show that the order of convergence is approximately 2.6.

Table 5 provides information about the required CPU (Intel(R) Xeon(R) CPU E5-1620 v4@ 3.50GHz) time for both shift schemes at all five resolutions. This table shows again that an inter-particle concept (CS) is computationally cheaper than a concept based on a kernel summation (FS). From table 5 it is concluded that the total CPU time is on average reduced by 20% with CS compared to FS.

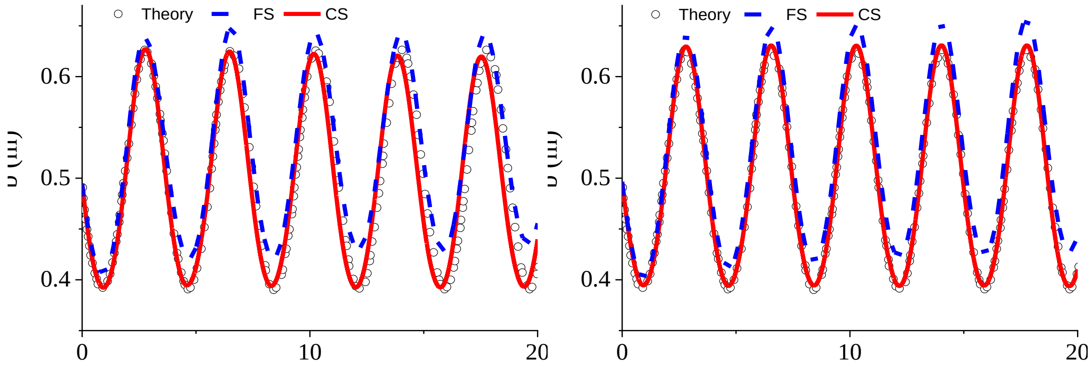

(a) (b)

Fig. 21. Expansion of vertical semi-axis of oscillating droplet. FS and CS at resolutions: (a) $\Delta x = 1/100$ m, (b) $\Delta x = 1/300$ m.

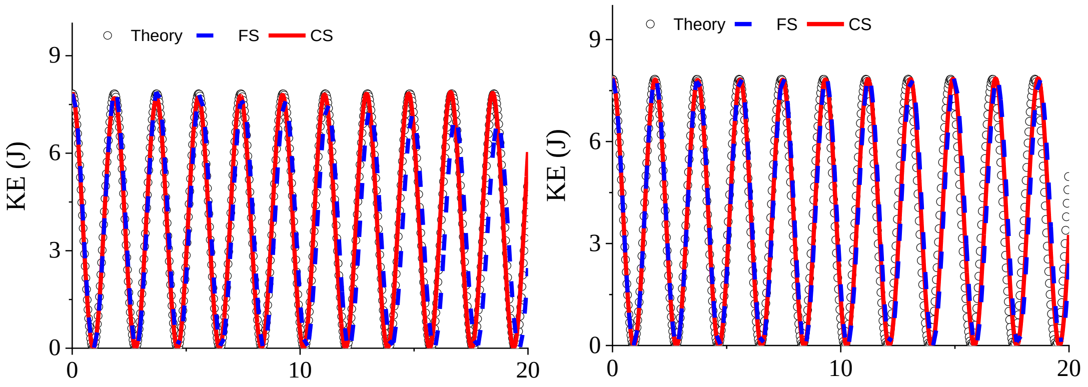

(a) (b)

Fig. 22. Kinetic energy of oscillating droplet. FS and CS at resolutions: (a) $\Delta x = 1/100$ m, (b) $\Delta x = 1/300$ m.

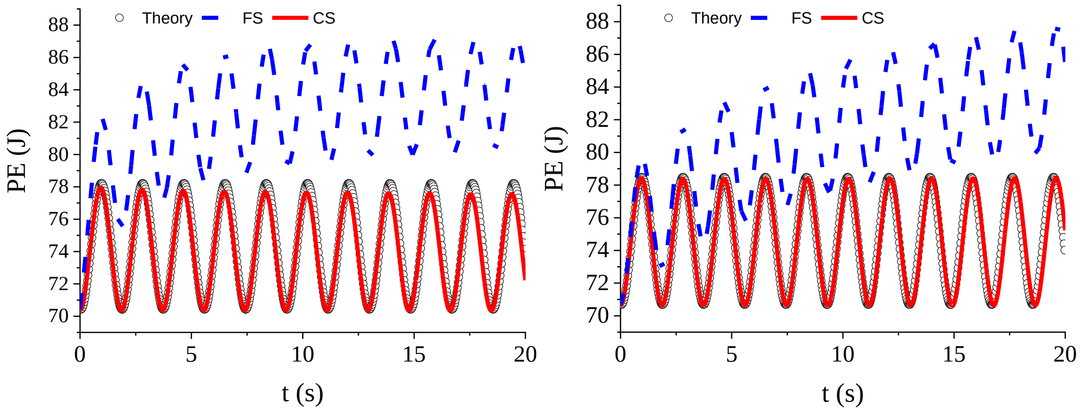

(a) (b)

Fig. 23. Potential energy of oscillating droplet. FS and CS at resolutions: (a) $\Delta x = 1/100$ m, (b) $\Delta x = 1/300$ m.

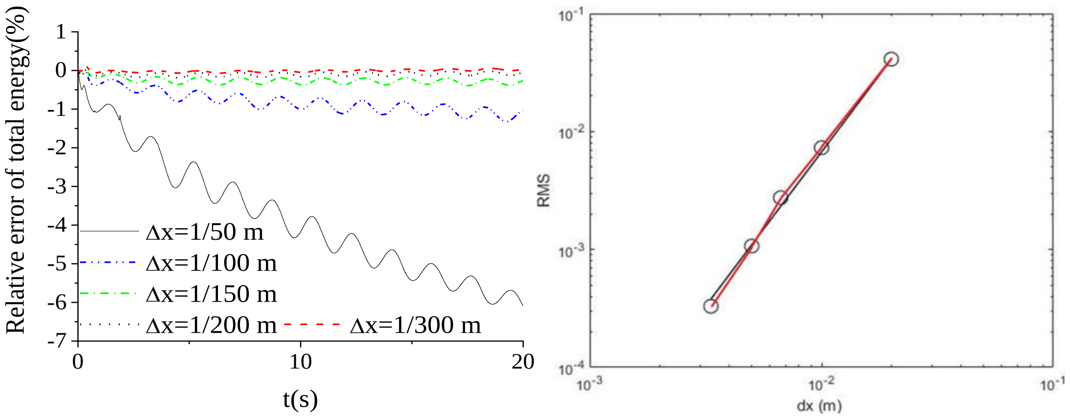

(a) (b)

Fig. 24. (a) Relative error of the total energy in time, for CS at five particle resolutions. (b) Convergence of the RMS error of total energy with increasing particle resolution ($\Delta x \rightarrow 0$).

Table 5. Oscillation of a droplet. Required CPU time for 20 seconds of simulation time at five resolutions

	$\Delta x = 1/50\text{m}$	$\Delta x = 1/100\text{ m}$	$\Delta x = 1/150\ m$	$\Delta x = 1/200\text{ m}$	$\Delta x = 1/300\text{ m}$
FS	1207.73s	3818.81s	8476.52s	15863.65s	53275.98s
CS	976.22s	2737.26s	6573.86s	13341.94s	45340.26s

4.5. Evolution of a square patch of fluid

In this case the evolution of a square patch of an inviscid fluid is studied, which deforms under a prescribed constant vorticity. The case is used previously to evaluate stabilization methods, including shift schemes based on Fick's law, both in ISPH and WCSPH (e.g. [5,117]). Here the case is used to compare CS and FS. The initial state of the fluid is a square patch with size L = 1 m, and the vorticity of the flow field is a constant 2ω, where the angular velocity is chosen as ω =10 rad/s. The density of the fluid is 1000 kg/m^3. The initial velocity distribution at $t = t_0$ is

$$\begin{cases} u(t_0) = \quad \omega y \\ v(t_0) = -\omega x \end{cases} \tag{101}$$

Simulations with FS and CS are performed at resolution $\Delta x = 1/100$ m, until the stage $t\omega = 8$ rad is reached. The shift coefficient $\mathcal{D}$ in FS is varied from 0.0 to 0.5 h^2. The best results are obtained with $\mathcal{D} = 0.1\, h^2$ and presented here. The results of FS and CS are shown in Fig. 25 to Fig. 31.

In Fig. 25 to 26 snapshots are shown obtained with standard ISPH, FS and CS at $t\omega =$ 1.2, 2.0 and 4.0 rad, together with the Lagrangian finite-difference method (LFDM) [118] in Fig. 25 and 26 and boundary element method (BEM) [118] in Fig. 27 solution for the free surface. The result obtained with standard ISPH in Fig. 25(a) shows some particle layering and clustering near the free surface. This is not seen with FS and CS in Fig. 25 (b) and (c). The free surface contours obtained with FS and CS are nearly the same and match well with the LFDM solution. The particle distribution at a later stage is shown in Fig. 26. Here, the results obtained with standard ISPH show a severe particle clustering such that the free surface and pressure distribution are affected, whilst the particle distributions of FS and CS still fit well within the BEM solution. Fig. 27 shows that the result of standard ISPH is now rather chaotic. The free surfaces with FS and CS still have a good agreement with the BEM solution. The details of Fig. 27 for FS ($\mathcal{D} = 0.1\, h^2$) and CS at $t\omega$ = 4.0 rad are shown in Fig. 28, where the result of FS ($\mathcal{D} = 0.2\, h^2$) is added for comparison. The result with FS ($\mathcal{D} = 0.2\, h^2$) shows some peaks at the free surface, violating the BEM solution, which are not seen with FS ($\mathcal{D} = 0.1\, h^2$) and CS, demonstrating that the shift coefficients in FS are case dependent.

Further results at $t\omega = 8.0$ rad are shown in Fig. 29 (BEM solution is not available here). The result with standard ISPH is seriously clustering. In contrast, with CS and FS ($\mathcal{D} = 0.1\ h^2$) particle clustering is effectively prevented, even at this late stage.

The error in the kinetic energy obtained with FS and CS is shown in Fig. 30. For this case with an inviscid fluid, the kinetic energy theoretically remains at its initial value. With both shift schemes, the error is less than 5% when $t\omega < 4.0$ rad. The result obtained with CS is again slightly better than FS.

Next the pressure time history of the centre of the fluid patch is considered, following [5,117]. The results in Fig. 31 show that the dimensionless pressures obtained with FS and CS have the same trend as the BEM solution. However, a small deviation is shown between the SPH results and the BEM solution from the beginning to the end. The result of CS is slightly better than FS as revealed in Fig. 31(b).

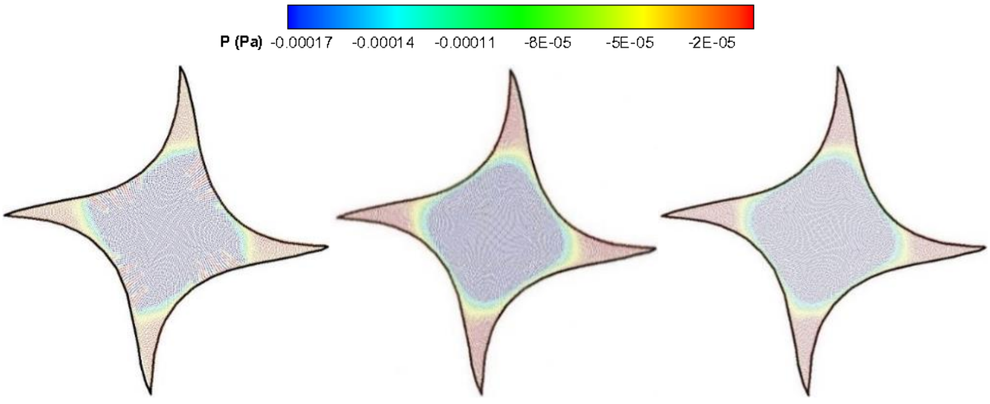

(a) (b) (c)

Fig. 25. Square fluid patch. Particle distribution with pressure at $t\omega = 1.2$ (a) standard ISPH, (b) FS, (c) CS.

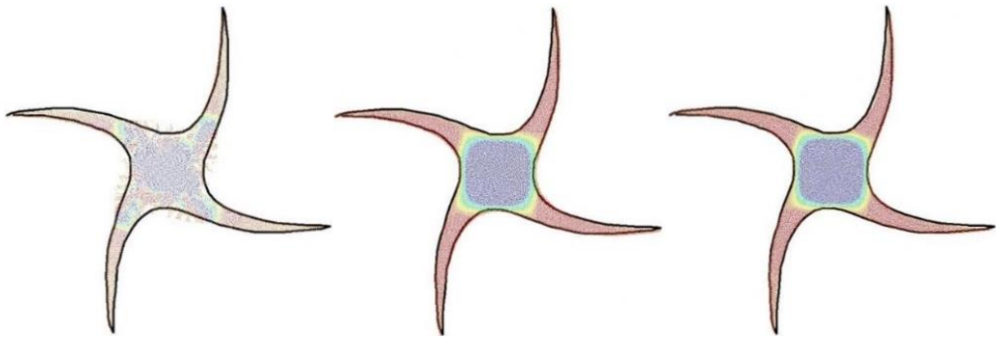

(a) (b) (c)

Fig. 26. Square fluid patch. Particle distribution with pressure at $t\omega = 2.0$ (a) standard ISPH, (b) FS, (c) CS.

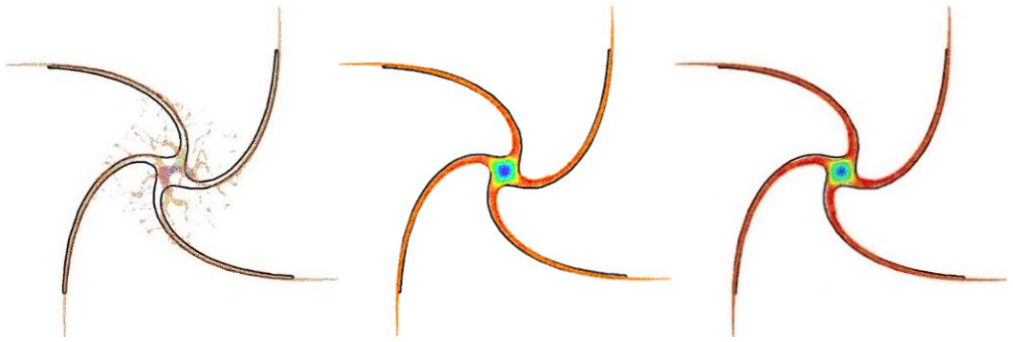

(a) (b) (c)

Fig. 27. Square fluid patch. Particle distribution with pressure at $t\omega = 4.0$ (a) standard ISPH, (b) FS, (c) CS.

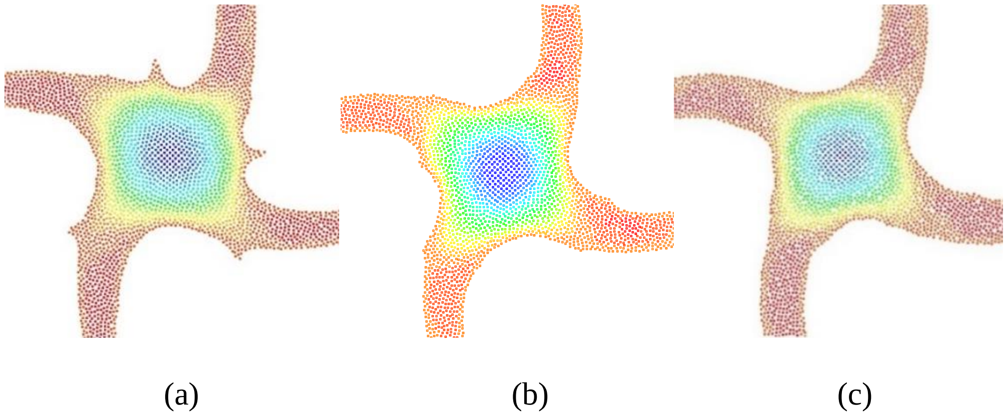

(a) (b) (c)

Fig. 28. Square fluid patch. The details of particle distribution with pressure at $t\omega = 4.0$, (a) FS ($\mathcal{D} = 0.2\ h^2$), (b) FS ($\mathcal{D} = 0.1\ h^2$), (c) CS.

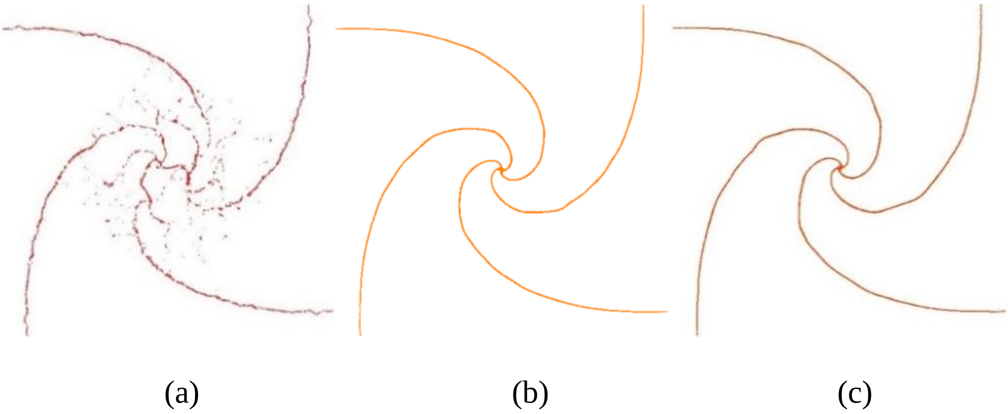

(a) (b) (c)

Fig. 29. Square fluid patch. Particle distribution with pressure at $t\omega = 8.0$ (a) standard ISPH, (b) FS, (c) CS.

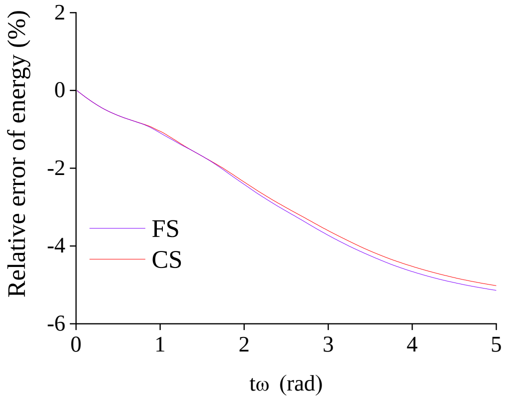

Fig. 30. Square fluid patch. The relative error of kinetic energy.

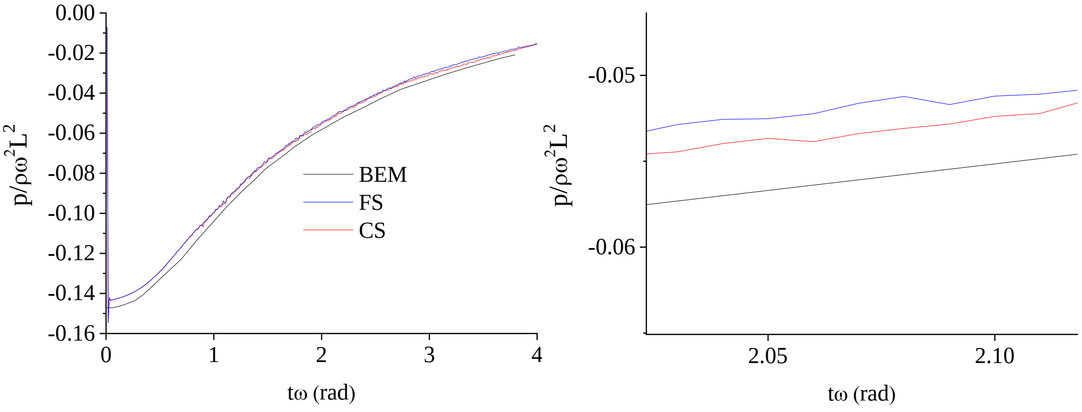

(a) (b)

Fig. 31. Square fluid patch. (a) Pressure time history of mid-point and (b) its detail.

4.6. Solitary wave

The four cases in the previous sections are theoretical cases. The fifth case is an engineering problem. Also, here CS is explored and compared with FS. Solitary waves are violent sea waves in complex ocean environments. During an earthquake for example waves are generated by the intense movement of the earth's crust. Following Zheng et al. [63] and Ma and Zhou [119], the impact of a solitary wave on a vertical wall is studied. The case set up is shown in Fig. 32. The length of the reservoir is 10 m and its depth is 0.25 m. The pressure is recorded at point P_1 on the wall, 0.05 m above the base. The fluid is water with a density of 1000 kg/m^3 and viscosity of 0.001 Pa·s. The wave is generated by a vertical pushing plate, following [119].

This case is simulated with standard ISPH, FS and CS at a resolution of $\Delta x = 1/100$ m and compared with experimental data from [63].

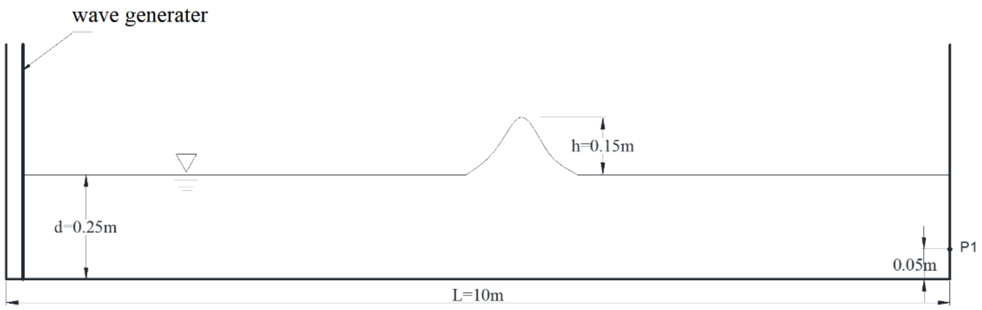

Fig. 32. Impact of a solitary wave on a vertical wall.

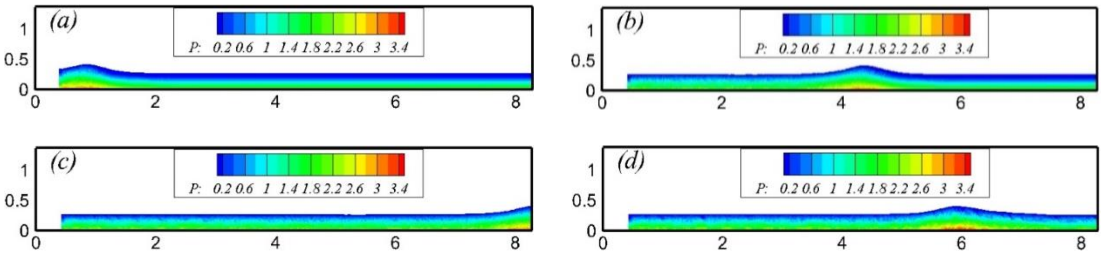

Fig. 33. Solitary wave simulated with CS at (a) t = 1.2 s, (b) t = 3 s, (c) t = 5 s and (d) t = 8 s. Pressure on color bar.

The results of a simulation obtained with CS at four different instants are shown in Fig. 33. The pressure distribution of the stratified flow shows layers that remain stable whilst no particle clustering is seen.

Fig. 34 (a) to (c) shows the particle distribution obtained with standard ISPH, FS and CS at *t* = 1.2 s. With standard ISPH the layering of the pressure is broken due to particle clustering, as seen in Fig. 34 (a). With FS and CS, the particle distribution and layering remain stable.

In Fig. 35(a) and (b) the free surface obtained with FS and CS is compared with an analytical solution from [6] at the instants *t* = 2.0 s and *t* = 3.1 s. The results of FS and CS are very similar. At the peak of the wave, CS shows a slightly better agreement with the analytical solution at *t* = 3.1 s.

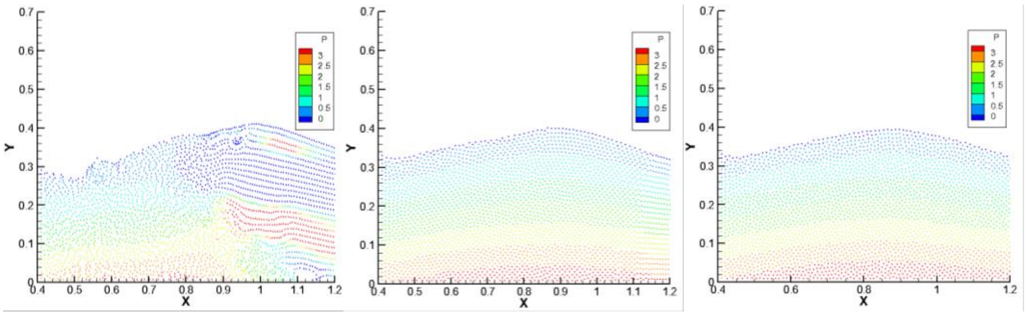

(a) (b) (c)

Fig. 34. Solitary wave. Particle distribution at t = 1.2 s obtained with (a) Standard ISPH, (b) FS and (c) CS.

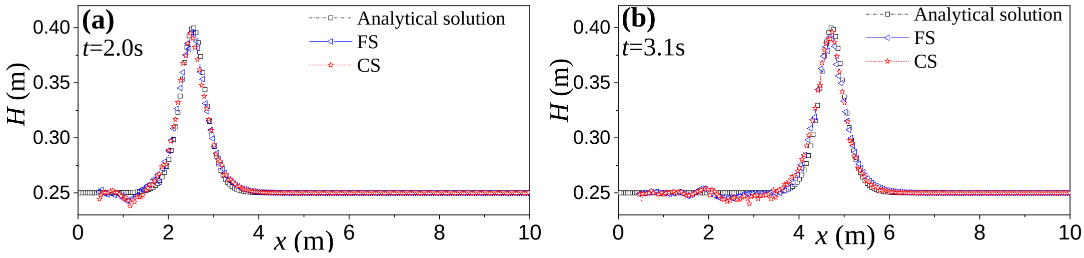

(a) (b)

Fig. 35. Free surface of solitary wave. Comparison of FS and CS with analytical solution, (a) t = 2 s, (b) t = 3.1 s.

In Fig. 36 the pressure at point P_1 obtained with FS and CS is compared with experimental data from [63]. With FS the impact pressure of the solitary wave exceeds the experiment, the first peak appears slightly earlier and both peak values are larger. With CS the impact pressure is still larger but closer to the experiment. Here the first peak appears at the same instant as in the experiment, but the instant of the second peak is later than in the experiment. And the value of those two peaks of CS are closer to experiment than FS. Overall, CS performs slightly better.

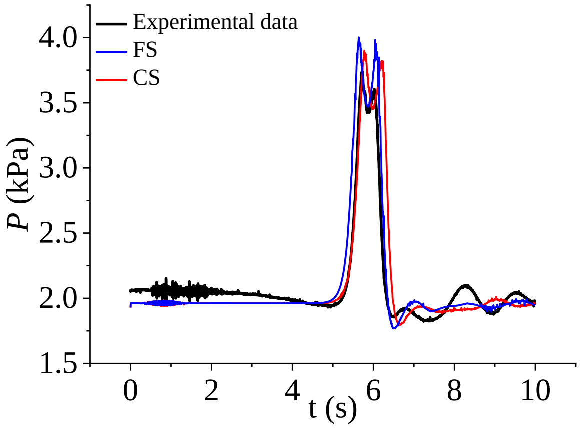

Fig. 36. Pressure at point P_1 in solitary wave. Comparison of CS and FS with experimental data.

4.7. Dam break

The two-dimensional dam-break is also an engineering problem, which is a classic SPH benchmark case with free-surface (e.g.[6,26,63,120]). In this case CS and FS are compared and evaluated against experimental data. The set-up is given in Fig. 37 with water column length L, height H and basin length D, with a pressure measuring point P_1 on the right wall at height h_1. The fluid is water with a density of 1000 kg/m^3 and viscosity of 0.001 Pa·s. Two scenarios are simulated. In both cases the diffusion coefficient $\mathcal{D}$ in FS is varied from 0.0 to 0.5 h^2.

In the *first scenario* L = 2 m, H =1 m, D = 5.366 m and h_1 = 0.14 m, following [35,62]. The initial particle distance is 0.01 m. The best results with FS are obtained for $\mathcal{D} = 0.1\ h^2$ and presented here.

In Fig. 38 to 39 results obtained with standard ISPH, FS and CS are shown at the dimensionless instant of time $t\sqrt{g/H} = 0.85$. From the detailed view of Fig. 38(b) it is observed that standard ISPH suffers from particle clustering and layering, which affects the pressure distribution. The results of FS and CS are nearly the same and much better than those of standard ISPH.

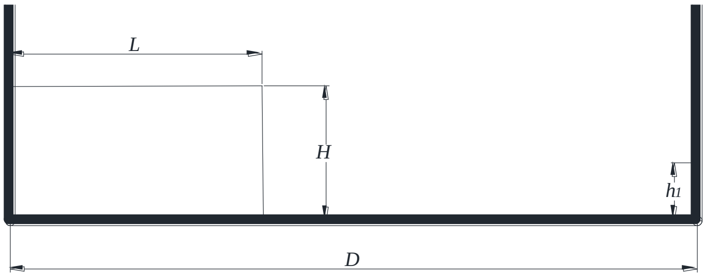

Fig. 37. Set-up of the dam break case.

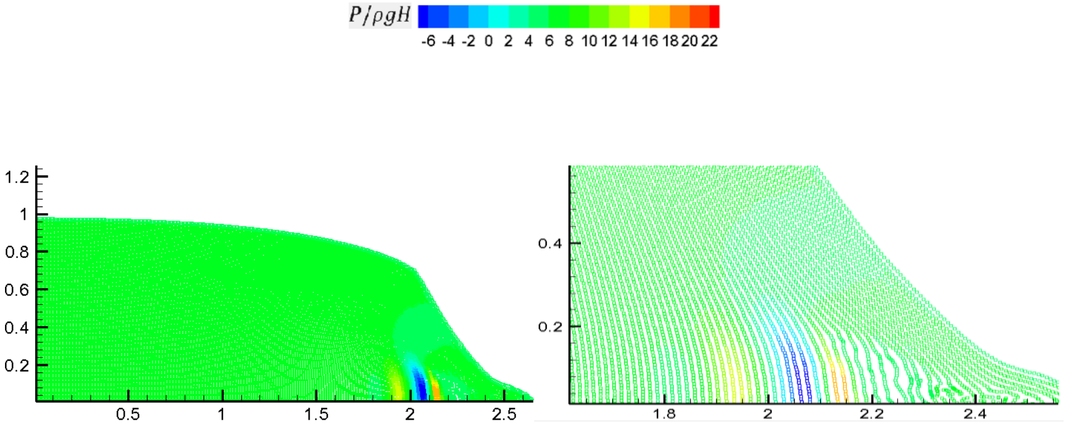

(a) (b)

Fig. 38. Dam break. Standard ISPH at time $t\sqrt{g/H} = 0.85$, (a) global view, (b) detailed view at water front.

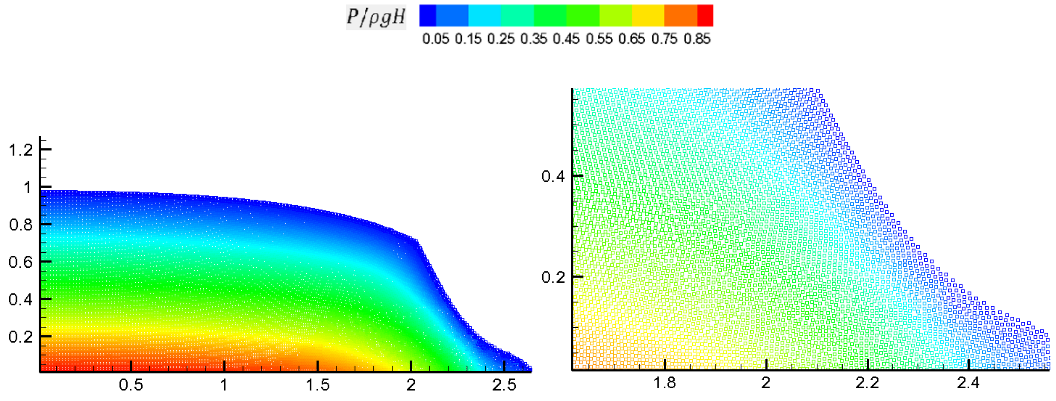

(a) (b)

Fig. 39. Dam break. FS at time $t\sqrt{g/H} = 0.85$. (a) global view, (b) detailed view at water front.

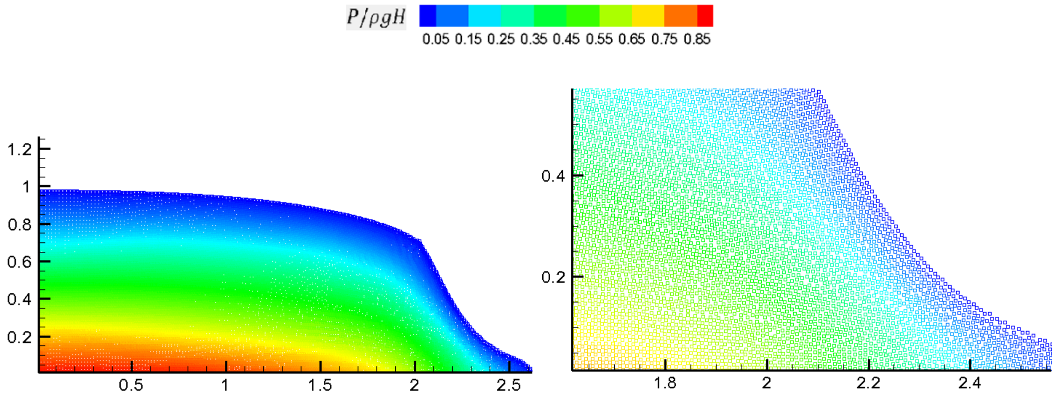

(a) (b)

Fig. 40. Dam break. CS at time $t\sqrt{g/H} = 0.85$. (a) global view, (b) detailed view at water front.

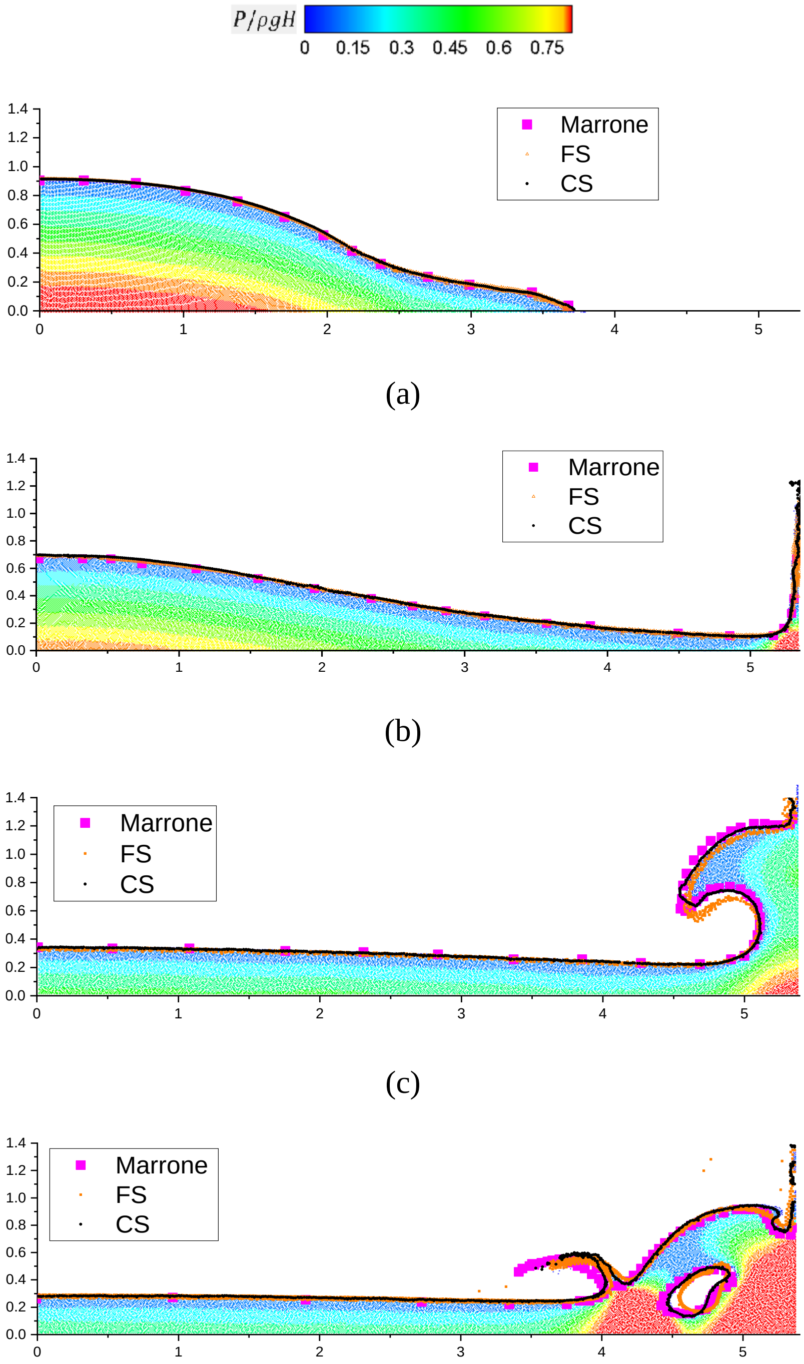

(a)

(b)

(c)

(d)

Fig. 41. Evolution of dam break. Comparison of the free surface contours of FS and CS with Marrone et al. [26] at instants (a) $t\sqrt{g/H} = 1.5$, (b) $t\sqrt{g/H} = 3.0$, (c) $t\sqrt{g/H} = 5.7$, (d) $t\sqrt{g/H} = 6.45$, together with the particle distribution of CS (dimensionless pressure on color bar).

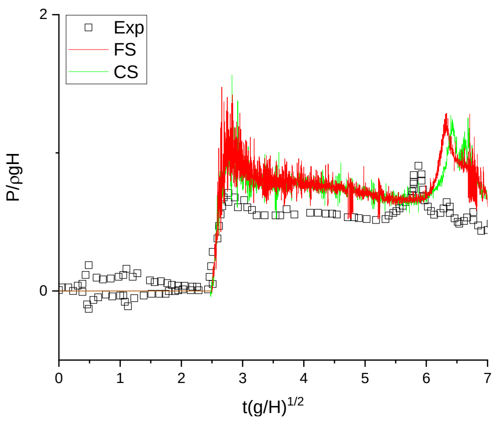

Fig. 42. Time histories of pressure at point P_1 in dam break case Validation of FS and CS against experimental data from Zhou et al. [121].

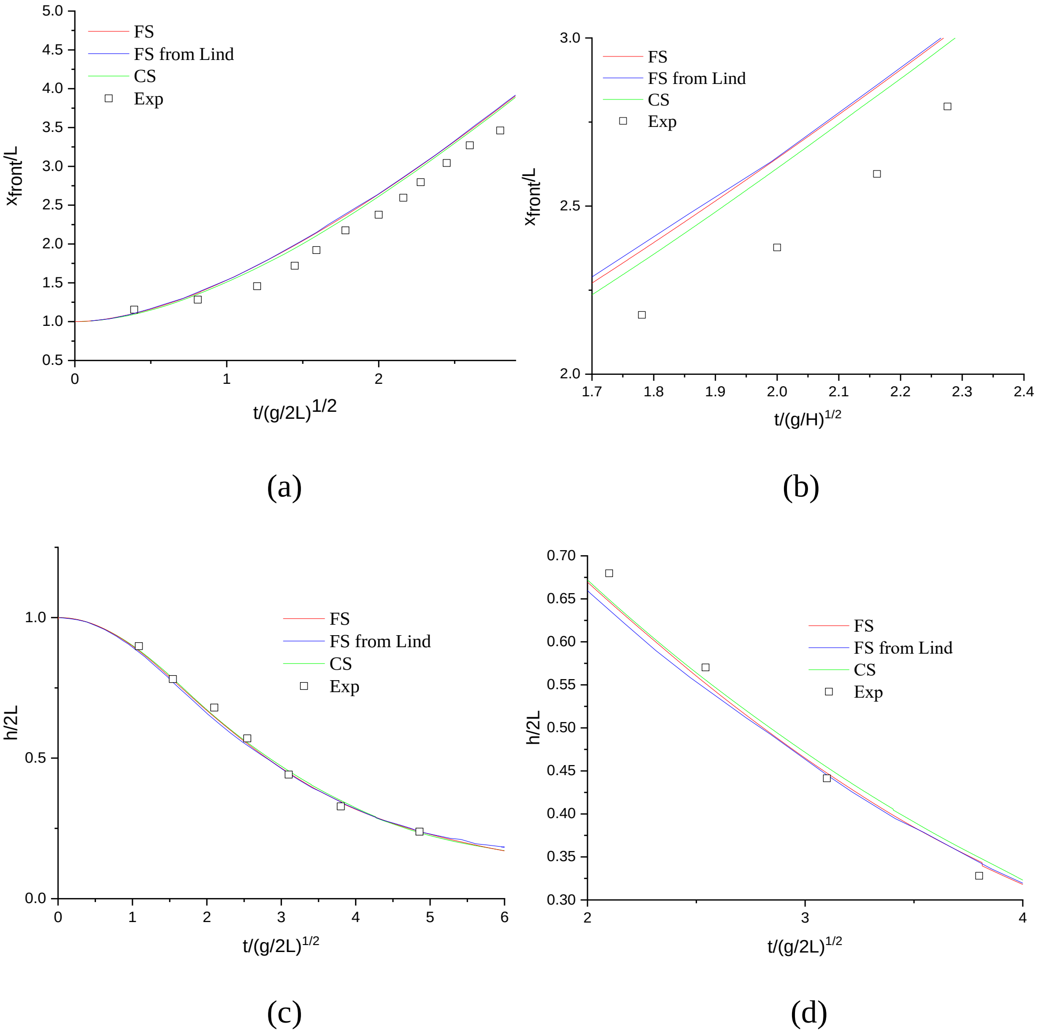

Fig. 43. Dam break. A comparison of numerical results (lines) with experimental data (squares) (a) waterfront evolution in time, (b) detail of (a), (c) water column height (highest point of water column) evolution in time, (d) detail of (c). Note in either case the lengths are scaled with respect to their initial values L, while times are scaled by $\sqrt{g/H}$.

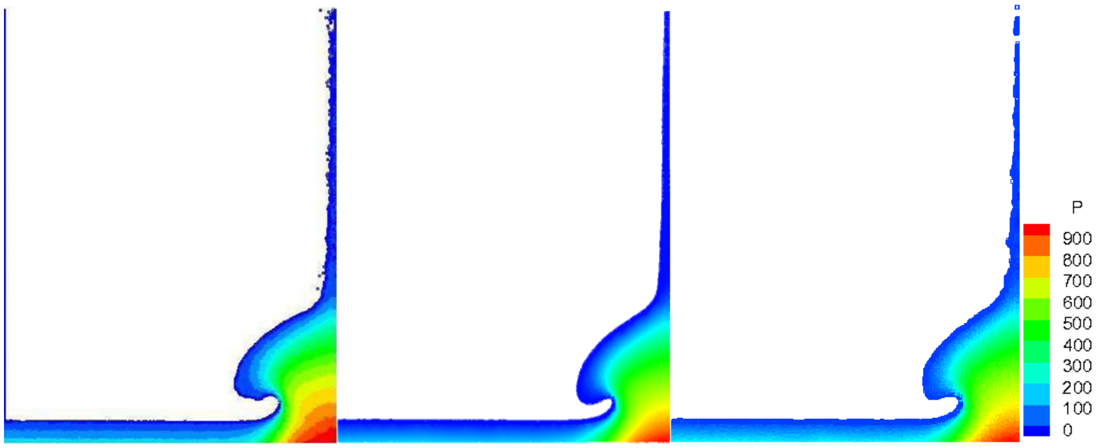

(a) (b) (c)

Fig. 44. Pressure distrbution at instant $t\sqrt{g/H} = 4.2$ obtained with (a) FS of Lind et al. [62], (b) FS and (c) CS.

In Fig. 41 the evolution of the dam break is shown at four instants $t\sqrt{g/H} = 1.5$, 3.0, 5.7 and 6.45. Here the particle distribution of CS is shown together with the free surface profiles of CS, FS and δ-SPH from Marrone et al. [26] which is stable and accurate. Before the wave front impacts at the right wall, the free surface contours of CS and FS are in good agreement with δ-SPH as shown in Fig. 41 (a) and (b). After this impact, the free surface contours of CS match better with δ-SPH than FS, before the cavity appears in Fig. 41 (c) and around the cavity in Fig. 41 (d). It is interesting to see those results of ISPH with CS are very similar to those of δ-SPH here.

In Fig. 42 the pressure time histories at point P_1 are shown. The results obtained with FS and CS are validated against experiments from Zhou et al.[121]. The results of FS and CS are similar, and both show higher transient pressures than in the experiment, whilst the second pressure peak appears later than in the experiment.

In the *second scenario* the dimensions are L = 0.1 m, H = 2.0 L and D = 4.0 L. The best results with FS are obtained for $\mathcal{D} = 0.05\ h^2$ and presented here. In Fig. 43 the time evolution of the waterfront and height of the water column obtained with FS and CS are validated against experiments from Martin et al. [122]. The waterfront moves faster than in the experiment, whilst the water column heights of the SPH methods show a reasonable match with the experiment. The results of our FS are almost the same as the results of Lind et al. [62], which may be expected since the same Fickian shift model is applied. The details of the waterfront in Fig. 43 (b) show that the results of CS are slightly closer to the experiment. The details of the water column height in Fig. 43 (d) show that the results of our FS, FS of Lind and CS are practically the same. In Fig. 44 the pressure distribution of the breaking wave is shown at the instant $t\sqrt{g/H} = 4.2$. The results obtained with CS, FS and FS of Lind et al. [62] are also here very similar, whilst the results of both FS and CS show a steep vertical wave that is smoother and without particle scatter.

4.8. Summary

A new particle shift model based on collisions to avoid particle clustering is introduced. It is based on the particle collision model from Kruisbrink et al. [1]. The latter is obtained from kinetic collision theory, which ensures the conservation of momentum, whilst no energy is dissipated for fully elastic collisions. In the particle collision shift model, the shift is also evaluated from kinetic collision theory. However, the change of velocity due to collisions is no longer applied, so that the kinetic energy is not affected. Just like in the original particle collision model, the shift is applied in the inter-particle direction only, whilst the magnitude of the shift depends on the particle masses. The concept is introduced as the “particle collision shift” (CS) model.

A comparative study into the accuracy, stability, computational efficiency, and dissipative properties is conducted between the particle collision shift model and the Fickian shift model. These are explored in six case studies. In the Taylor-Green vortex case, the collision shift model is more stable and accurate than the Fickian shift model, both at low and high Reynolds numbers. The collision shift model as an inter-particle model is computationally faster than the Fickian shift model. In the lid driven cavity case, the results obtained with the collision shift and Fickian shift models are nearly the same as those of a multigrid finite volume solution. In the oscillating droplet, the Fickian shift model suffers from dissipation, whilst the collision shift model does not. In the evolution of a square fluid patch, the free surface obtained with the collision shift model is slightly smoother and in closer agreement with the BEM solution from literature than the Fickian shift model. In the solitary wave case, the impact pressure obtained with the collision shift model slightly matches better with experimental data. In the two scenarios of the dam break case, the results obtained with the collision shift model also show a slightly better match with the experiment. The solitary wave and dam break cases demonstrate that the collision shift model can be applied to engineering problems.

The particle collision shift model is an inter-particle model that is only active when the distance between two particles is too small. On the other hand, the Fickian shift model is a kernel-based model that is always active, i.e. all particles are shifted at every time step. The collision shift model in itself preserves kinetic energy as well as potential energy in a constant force field, like gravitation. As such, the model is non-dissipative in many real cases. Linear momentum is conserved, whilst angular momentum cannot be conserved in a shift process that conserves (kinetic) energy. The collision shift model does not need a special treatment at the free surface, whilst this is needed in the Fickian shift model because the support domain is truncated here.

In conclusion, the results obtained with the collision shift model show a slight improvement compared with the Fickian shift model, whilst the model is much simpler and computationally cheaper. The collision shift model is a stable, efficient and robust model, which has great potential for application in engineering problems.

Chapter 5 Validation of particle collision shift model in weakly compressible SPH (multi-phase flow)

5.1. Introduction

In Chapter 4, the accuracy, stability, computational efficiency, and dissipative features of the particle collision shift model were validated against the Fickian shift model in single-phase flow by ISPH. In this chapter, the particle collision shift model in multiphase flow is verified. As discussed in Chapter 3, weakly compressible SPH (WCSPH) is more suitable for multiphase flow but exhibits greater pressure fluctuation, whereas δ-SPH can improve the pressure stability in standard WCSPH. A hybrid method, which combines the δ-SPH and collision shift models, was investigated in five benchmark case studies, including one single-phase case and four multiphase cases. For convenience, the following abbreviations are used: standard WCSPH and collision shift model (SPH_CS) and δ-SPH and collision shift model (δ-SPH_CS).

In the single-phase case (Taylor–Green vortex in Section 5.1), a comprehensive analysis of δ-SPH_CS was conducted by comparing it with standard SPH, δ-SPH and SPH_CS. For the remaining four multiphase cases, only δ-SPH_CS was applied. The parameters of the artificial coefficient (λ) and artificial viscosity (α) of δ-SPH were case-dependent [38]. For the low-density ratio ($\frac{\rho_{dense}}{\rho_{light}} < 10$) flow (Rayleigh–Taylor instability in Section 5.2) and static flow (stagnate multiphase flow in Section 5.3), λ = 1 and $\alpha = 0$. For the high-density ($\frac{\rho_{dense}}{\rho_{light}} > 10$) ratio dynamic flow (multiphase dam break in Section 5.4 and multiphase sloshing tank in Section 5.5), λ = 1 and $\alpha = 0.03$. The collision distance d_{col} was selected to be equal to the initial particle distance, and the coefficient of restitution C_R was selected to be 0 in all cases.

5.2. Taylor–Green vortex in WCSPH

The first benchmark case was the Taylor–Green vortex as described in Chapter 3, in which it was tested using the ISPH method. To investigate the collision shift model in WCSPH, this case used in Chapter 4 was simulated again using WCSPH. Here, the initial condition, properties of the fluid and exact solution followed Eqs. (96) and (97) in Chapter 4.

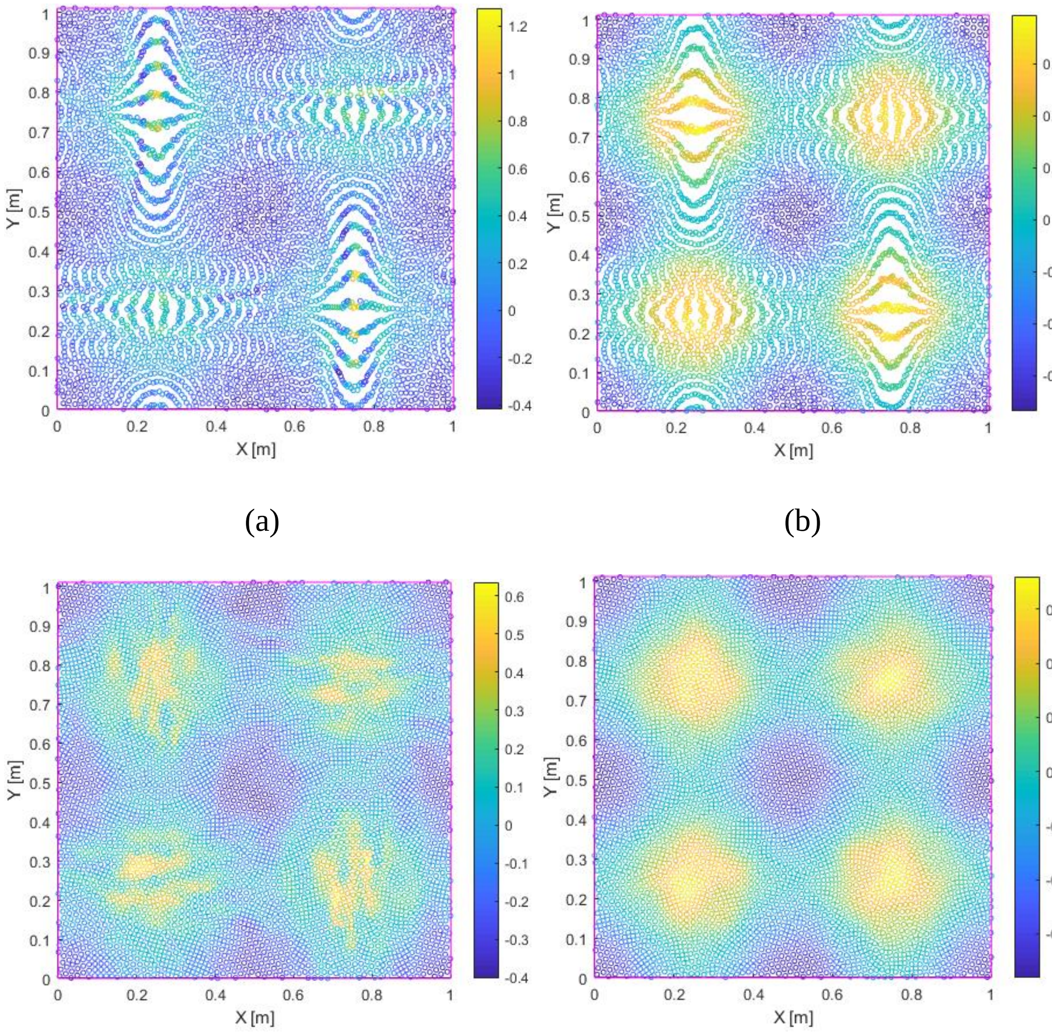

(a) (b)

(c) (d)

Fig. 45. Taylor-Green vortex (Re=10^2). Particle distribution at time $tU_0/L = 0.3$, simulations with (a) standard WCSPH; (b) δ-SPH; (c) SPH_CS, (d) δ-SPH_CS.

Simulations were performed at a Reynolds number Re of 10^2. The results of the simulations obtained with standard WCSPH, δ-SPH, SPH_CS and δ-SPH_CS are shown in Fig. 45, in which the pressure contour and particle distribution are compared at $Re = 10^2$ at the dimensionless time $tU_0/L = 0.3$. Standard WCSPH exhibited particle layering, as shown in Fig. 45(a). The particle distribution obtained with δ-SPH in Fig. 45(b) shows the same degree of particle clustering as that of standard WCSPH;

however, the pressure improved with δ-SPH. Compared with δ-SPH, the particle distribution of SPH_CS in Fig. 45(c) is better and shows an almost regular particle distribution, but the pressure distribution is not favourable. The best results were obtained with δ-SPH_CS. The particle distribution of δ-SPH_CS shown in Fig. 45 (d) is nearly the same as that of SPH_CS shown in Fig. 45(c), and the pressure distribution of δ-SPH_CS was identical to that of δ-SPH. Next, the decay of kinetic energy, maximum velocity and pressure is analysed to reveal the differences between standard SPH, δ-SPH, SPH_CS and δ-SPH_CS.

In Fig. 46 to 49, the pressure of the centre point of the fluid domain, the decay of kinetic energy and maximum velocity are presented together with their relative errors obtained with standard WCSPH, δ-SPH, SPH_CS and δ-SPH_CS at *Re* = 10^2. The kinetic energy of the system, maximum velocity and pressure of the centre point of the fluid domain were used as measures of accuracy and stability for these models. The relative error was defined by Eq. (98).

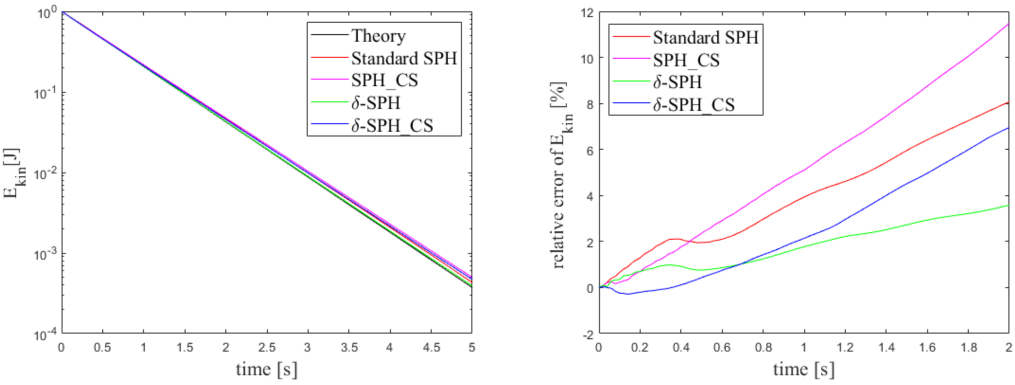

(a) (b)

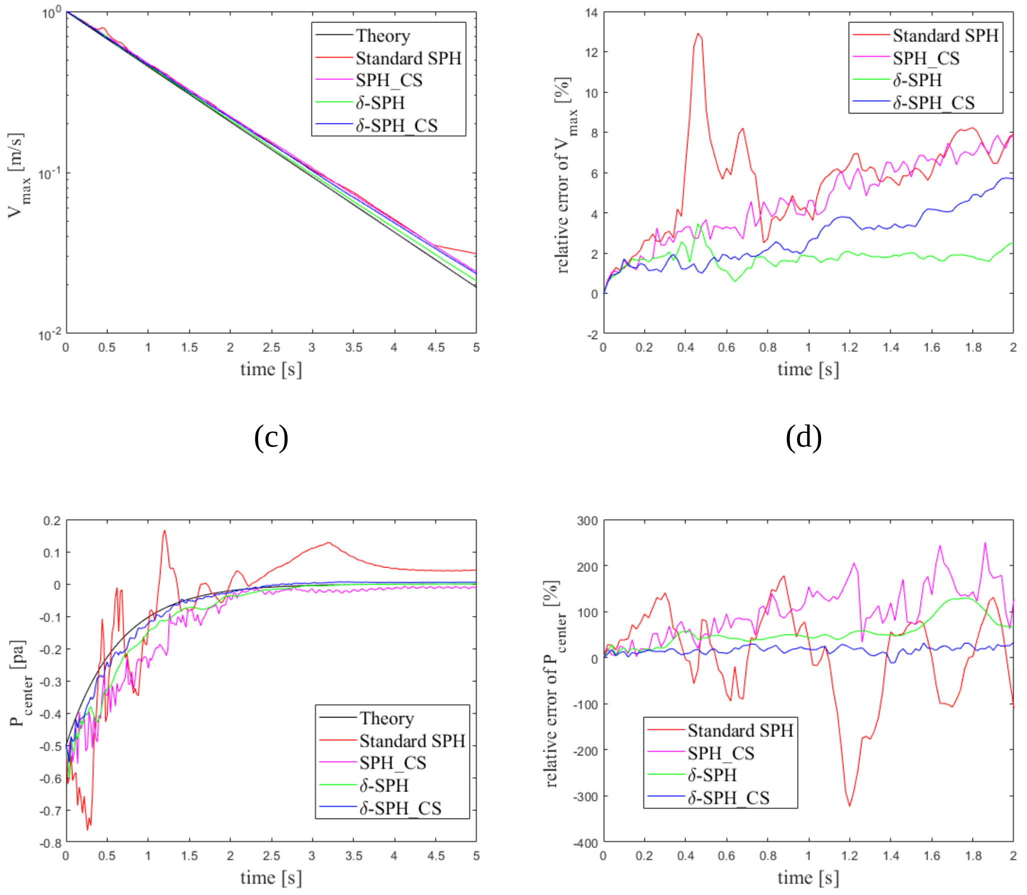

(c)

(d)

(e)

(f)

Fig. 46. Comparison of standard WCSPH, SPH_CS, δ-SPH, and δ-SPH_CS at Re = 100. The panels show (a) kinetic energy, (b) maximum velocity, (c) relative error of kinetic energy, (d) relative error of maximum velocity, (e) pressure at centre point, and (f) relative error of pressure at centre point.

Fig. 46 shows the decay of kinetic energy, maximum velocity and pressure of the standard WCSPH, δ-SPH, SPH_CS and δ-SPH_CS models at *Re* = 100. Compared with standard WCSPH, the stability and accuracy of the simulation results of the three improved models (δ-SPH, SPH_CS and δ-SPH_CS) were improved, as demonstrated by the relative errors shown in Fig. 46(b), (d) and (f). Although the particle distribution of SPH_CS was considerably better than that of δ-SPH, the relative error of the results for SPH_CS was nearly double that of both δ-SPH and δ-SPH_CS. The relative errors of the kinetic energy and maximum velocity of δ-SPH_CS and δ-SPH were both less than 10% before 2 s. The δ-SPH model exhibited 4% and 2% higher kinetic energy and maximum velocity, respectively, than δ-SPH_CS at *t* = 2 s. However, the relative error of the pressure of δ-SPH_CS was 50% less than that of δ-SPH at *t* = 2 s.

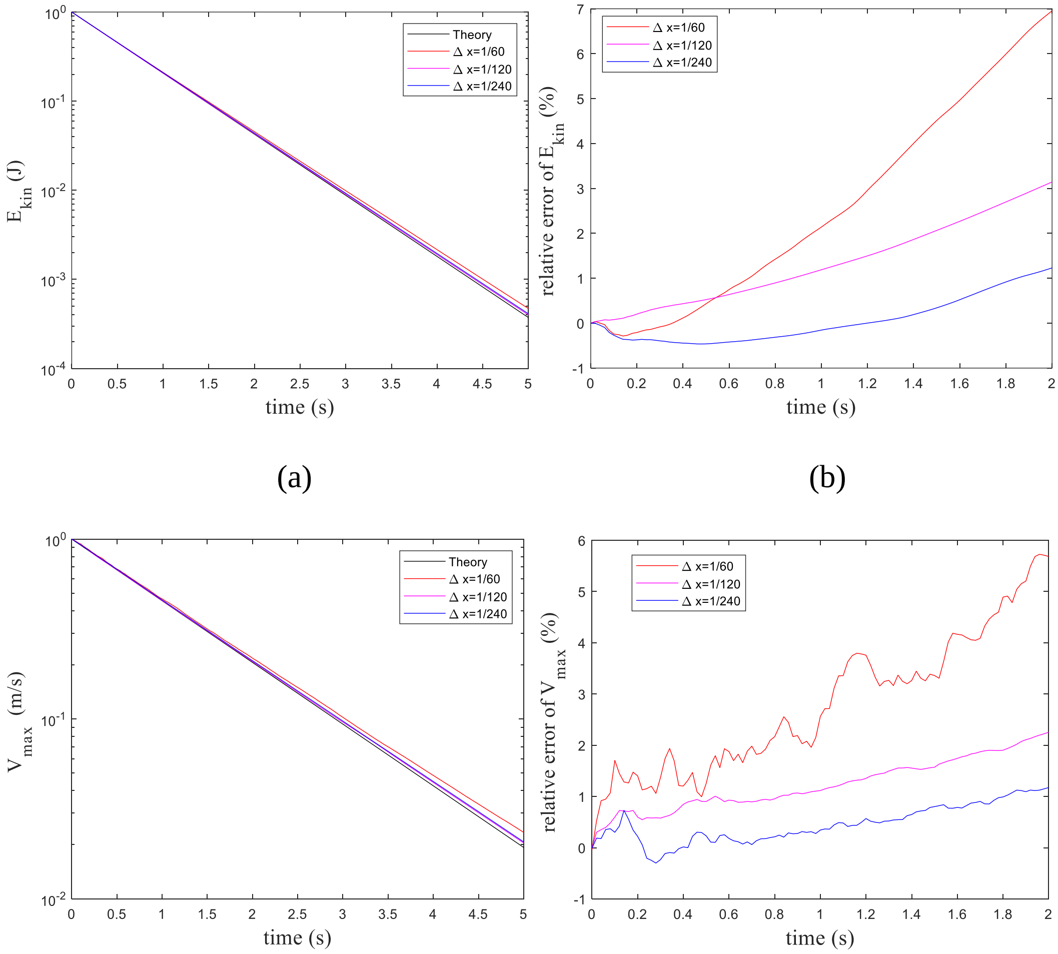

(a) (b)

(c) (d)

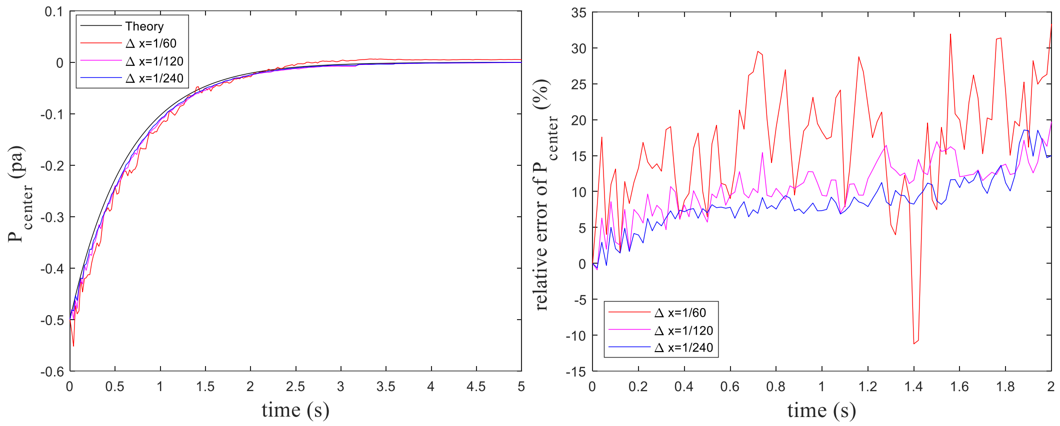

(e) (f)

Fig. 47. Comparison of three particle resolutions at Re = 10^2 obtained with δ-SPH_CS. The panels show (a) kinetic energy, (b) maximum velocity, (c) relative error of kinetic energy, (d) relative error of maximum velocity, (e) pressure at centre point, (f) relative error of pressure at centre point

In Fig. 47, the pressure of the centre point, the decay of kinetic energy and maximum velocity are presented along with the relative errors at $Re = 10^2$. These were obtained with δ-SPH_CS for three resolutions (Δx = 1/60 m, Δx = 1/120 m and Δx = 1/240 m) and validated against the theoretical values. These figures illustrate that, with increasing resolution, the results approached the theoretical values.

5.3. Rayleigh–Taylor instability

The low-density ratio ($\frac{\rho_{dense}}{\rho_{light}}$) Rayleigh–Taylor instability is a classical two-phase flow that has been studied by many researchers through a variety of numerical approaches based on the SPH method [38,91,123]. In this section, Rayleigh–Taylor instability is used to validate the δ-SPH_CS model, specifically at the interface between the low-density ratio phases. In this case, two immiscible fluids were placed in a rectangular container with dimensions of $1m \times 2m$.The geometrical details of the Rayleigh–Taylor instability at the initial state are presented in Fig. 48. As illustrated in Fig. 48, yellow particles represent the heavier fluid with a density of ρ_1 = 1.8 kg/m^3 while blue particles represent the lighter fluid with a density of ρ_2 = 1 kg/m^3. Initially, the interface of these two fluids was located at $y = 1.0 - 0.15\sin(2\pi x)$ to generate instability. The gravity acceleration was set to g = 1 m/s^2 [38]. The Reynolds number was $Re = \sqrt{H^3 g}/\nu = 420$ and the kinematic viscosity ν for both fluids was assumed to be the same. The no-slip condition was enforced on all solid boundaries.

In Fig. 49, the results obtained with standard SPH and δ-SPH_CS at a resolution Δx of 1/100 m are shown at a dimensionless instant of time, $t(g/H)^{1/2} = 1.23$. As shown in the detail view of Fig. 49(a), standard SPH suffered from particle clustering. Around the interface, the particles showed a laying distribution and gathered around the bottom corner. Fig. 49(b) shows that δ-SPH_CS did not exhibit particle clustering, even at the interface.

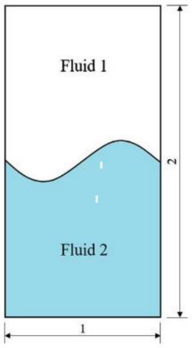

Fig. 48. Geometrical details of Rayleigh-Taylor instability at the initial state.

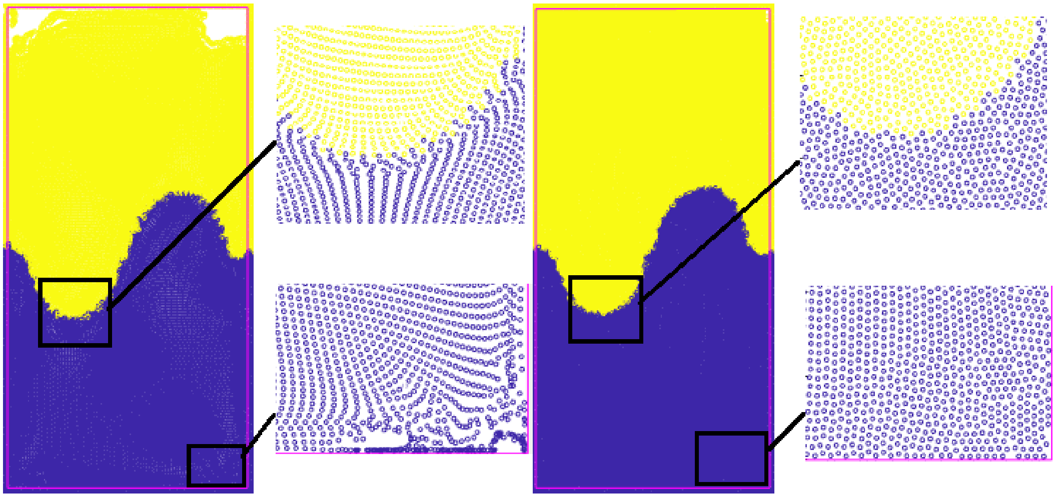

(a) (b)

Fig. 49. Rayleigh-Taylor instability with $\Delta x = 0.01$. Density distribution at time $t(g/H)^{1/2} = 1.23$, simulations with (a) standard WCSPH, (b) δ-SPH_CS.

Fig. 50 shows the interface shapes and pressure fields of heavier and lighter fluids at instants $t = 3$ s and $t = 5$ s with a particle resolution of $\Delta x = 1/200$ m. At each time step, the left column represents the distribution of different phases, and the right column shows the pressure field and interface of the whole domain. From these results, it can be observed that δ-SPH_CS clearly captured the complex interface between heavier and lighter fluids, and the pressure field was continuous and smooth at the multiphase interface. Fig. 51 shows a comparison of the interface obtained with δ-SPH_CS with the level-set solver [38]. Compared with the interface of the level-set method, the interface of δ-SPH_CS became a mushroom-like shape at $t = 3$ s, which showed good agreement with the level-set method. Although there were a few differences at $t = 5$ s, the overall trend of δ-SPH_CS was similar to the level-set method.

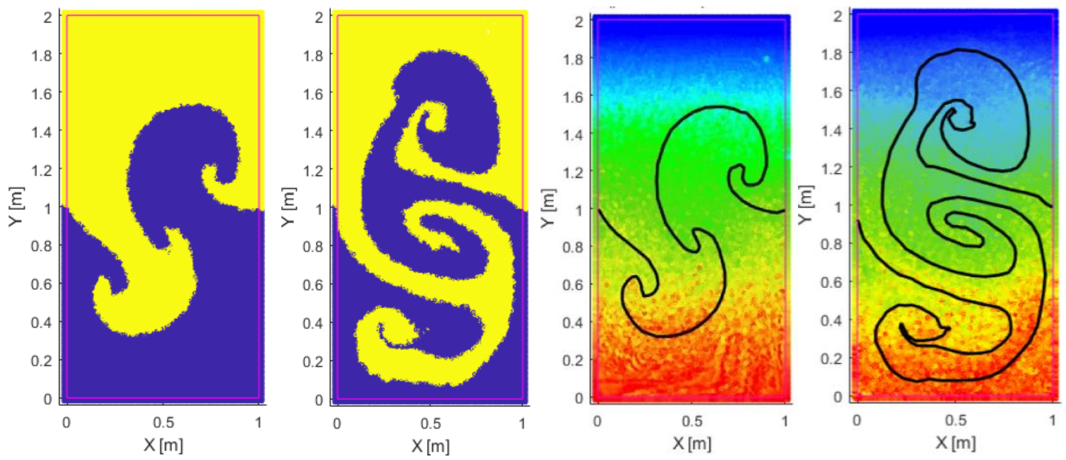

(a) (b)

Fig. 50. Rayleigh-Taylor instability. (a) density distribution, (b) pressure field obtained by δ-SPH_CS at $t(g/H)^{1/2} = 3$ and 5.

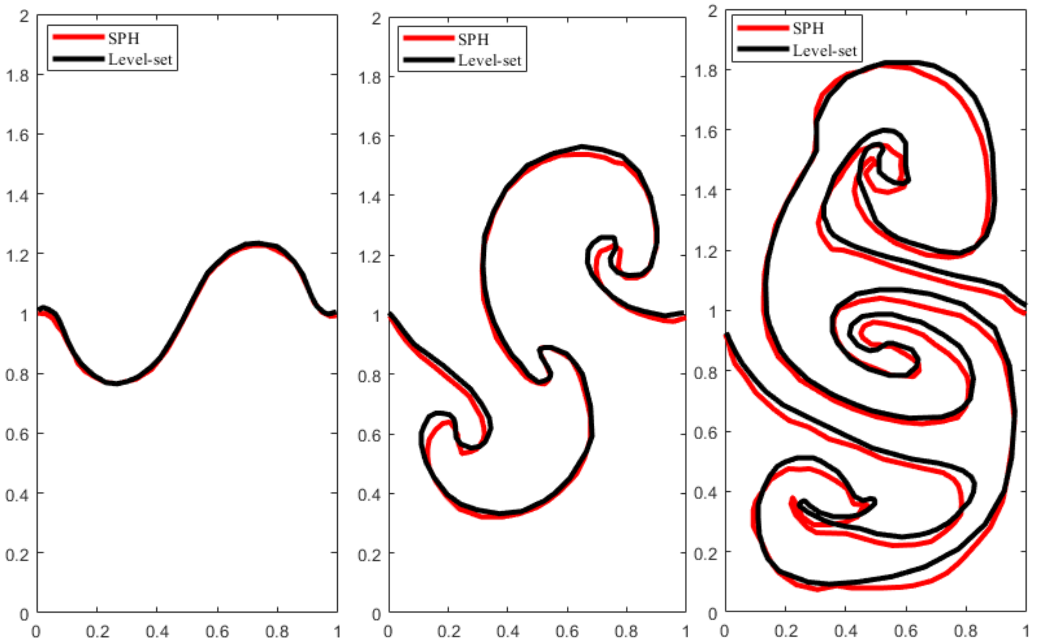

(a) (b) (c)

Fig. 51.Comparison of the interface of δ-SPH_CS and Level-Set [38] at $t(g/H)^{1/2} = 1, 3$ and 5(from left to right).

As illustrated in Fig. 52 and Fig. 53, the vorticity contours and interface simulated by the presented methodology at resolution Δx = 1/200 m are compared to the level-set method [38] at three instants. The distributions of vorticity were similar, thus validating the accuracy of the δ-SPH_CS.

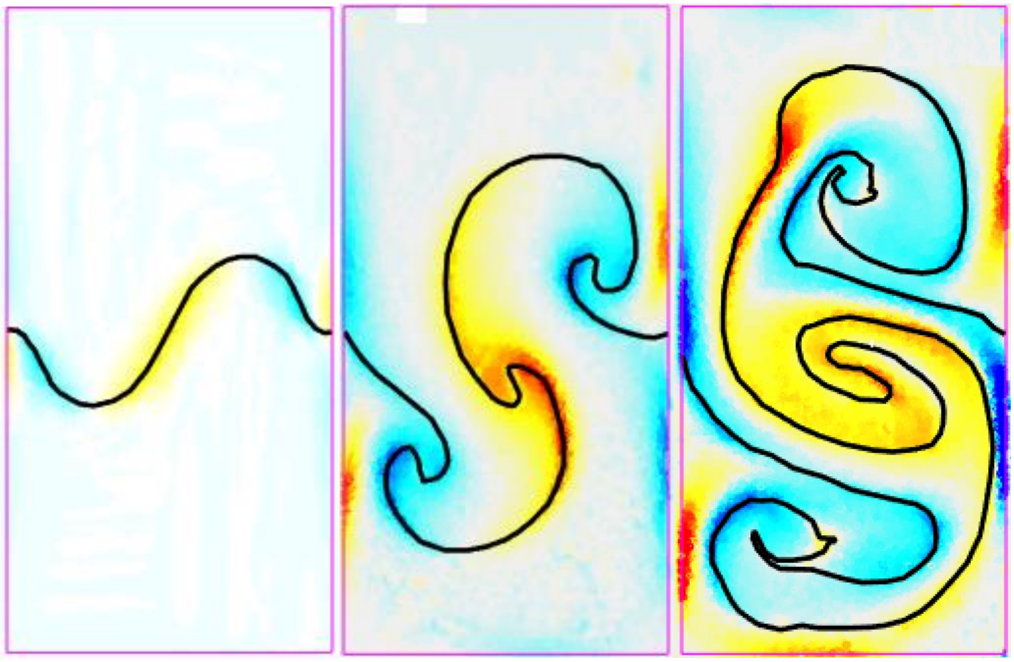

(a) (b) (c)

Fig. 52. Vorticity contour obtained with δ-SPH_CS at instants (a) $t(g/H)^{1/2} = 1$, (b) $t(g/H)^{1/2} = 3$, (c) $t(g/H)^{1/2} = 5$.

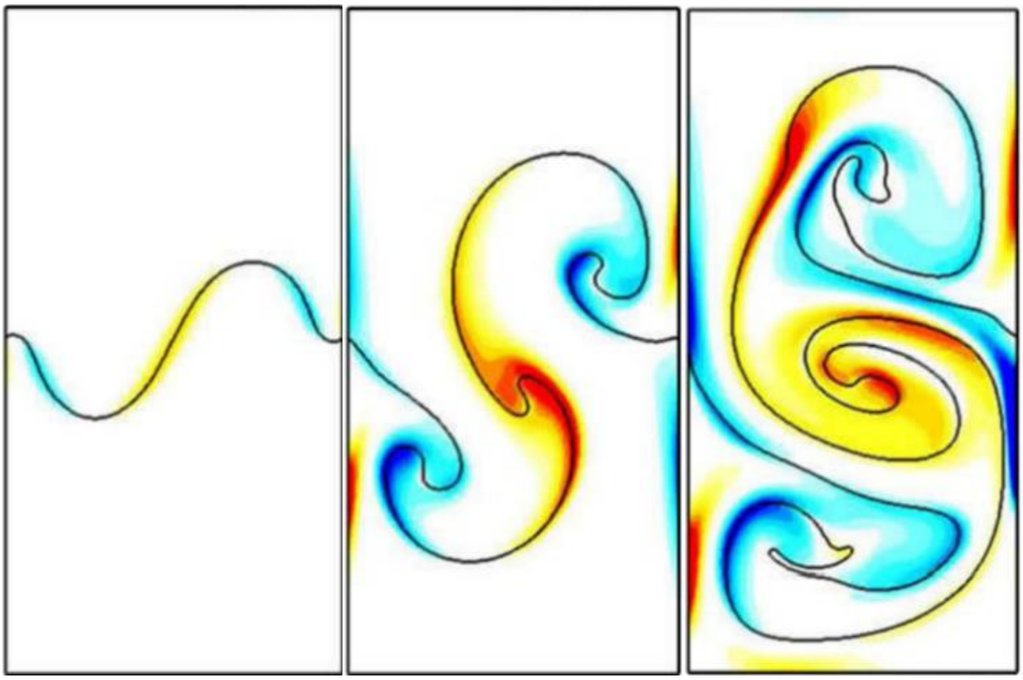

(a) (b) (c)

Fig. 53. Vorticity contour obtained with Level-Set method in Grenier et al.[124] at $t(g/H)^{1/2} = 1, 3$ and 5 (from left to right).

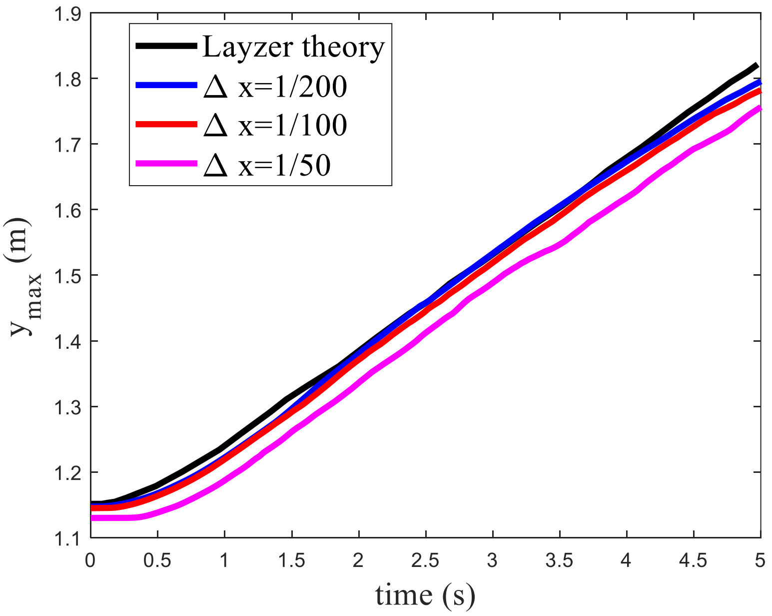

Fig. 54. The time variation of the highest point of the low-density fluid.

The results are compared with those from the theory of Layzer [32], which are shown in black in Fig. 54. The position of the maximum y-coordinate of the low-density fluid is shown on a graph for three different resolutions (Δx = 1/200 m, Δx = 1/100 m and Δx = 1/50 m) in order to investigate convergence. In particular, for t > 2.4 s, the data demonstrated convergence and was in excellent agreement with the Layzer theory at the greatest resolution.

5.4. Stagnate multiphase flow

The third case was a multiphase hydrostatic test in a rectangular reservoir. The heavier fluid was water with a density of 1000 kg/m^3 and a viscosity of 0.001 Pa·s, while the lighter fluid was air with a density of 1 kg/m^3 and a viscosity of 0.00001 Pa·s. The length of the reservoir was L = 1.0 m and the height was H = 1.0 m. The lower part of the reservoir was composed of water and the depth of the water was D = 0.5 m, while the upper part was composed of air. The bottom and top walls of the reservoir were represented by three fixed layers of ghost particles. Periodic boundaries were used to represent the two vertical walls of the reservoir. The initial particle spacing was Δx = 1/60 m, giving a total of 4,080 particles.

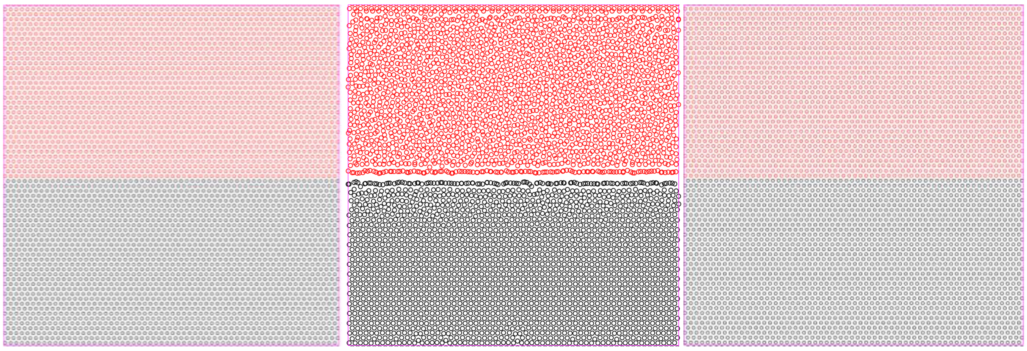

(a) (b) (c)

Fig. 55. Stagnate multiphase flow. Density distribution, (a) Initial state; (b) Standard WCSPH (t = 2.0 s); (c) δ-SPH_CS (t = 2.0 s).

Fig. 55 illustrates the particle distributions obtained with standard WCSPH and δ-SPH_CS. The black circles represent water particles, while the red circles represent air particles. As Fig. 55(b) shows, the particles around the interface as well as the air particles exhibited particle clustering. Particle clustering was effectively prevented by the δ-SPH_CS model, as demonstrated in Fig. 55(c).

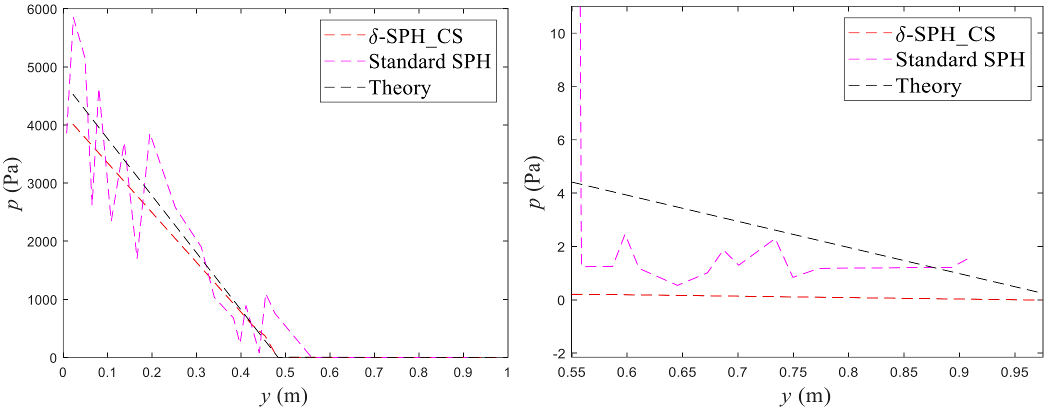

(a) (b)

Fig. 56. Pressure profiles along x = 0.5 m. Comparison of standard WCSPH, δ-SPH_CS and theory at t = 2.0 s (a) Full reservoir; (b) Top part of reservoir.

The pressure distribution along x = 0.5 m at t = 2.0 s can be seen in Fig. 56. Because of particle clustering around the interface, the pressure significantly fluctuated around the theoretical value with standard WCSPH. The pressures were substantially closer to the theoretical value and thus more stable when using the δ-SPH_CS model.

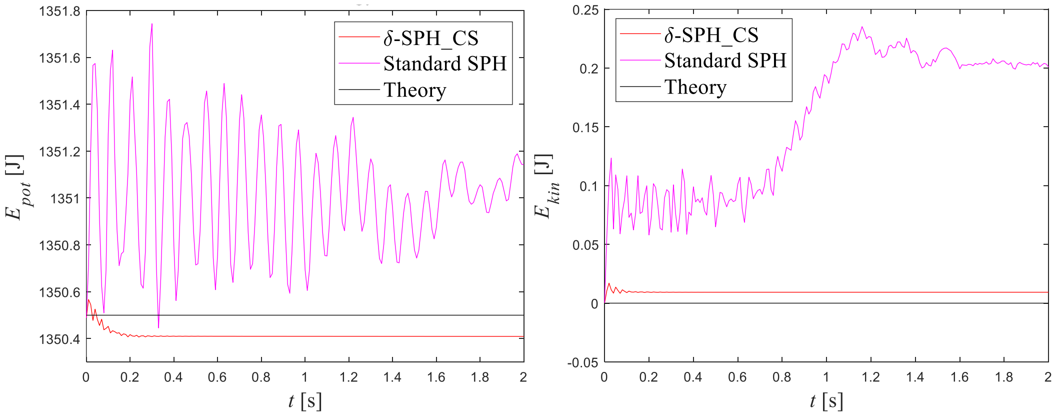

(a) (b)

Fig. 57. The evolution of potential and kinetic energy of the static multiphase flow in time. Comparison of standard WCSPH, δ-SPH_CS and theory. (a) Potential energy; (b) Kinetic energy.

The time history of the potential and kinetic energy of the static multiphase flow is displayed in time in Fig. 57, which illustrates the stability of δ-SPH_CS. When using standard WCSPH, the potential energy and kinetic energy both increased shortly after the simulation began and then fluctuated around a relatively high value, indicating that the particles were in an unstable state. In contrast, with δ-SPH_CS, the potential energy decreased shortly after the simulation began. Compared with the increase in potential energy with standard WCSPH, the decrease in potential energy with δ-SPH_CS was less severe and accompanied by a tiny increase in kinetic energy.

5.5. Multiphase dam break

The results of the multiphase dam break to test the δ-SPH_CS model are presented in this section. The two-dimensional dam break is a representative SPH benchmark case that is simulated not only in the single-phase with a free surface [125] but also in the multiphase with an interface [38]. Multiphase dam break is a classic problem of fluid–structure interactions (FSI), which is characterised by a high-density ratio of 1000:1, a complicated interface and a significant impact. It has been simulated by many researchers to test multiphase SPH models. Zheng and Chen [38] used multiphase dam break to analyse artificial viscosity in detail. In the current work, the coefficient of artificial viscosity was set at a fixed value (0.03), the collision shift model was tested and the results were compared with those of Zheng and Chen [38]. The initial condition was the same as in [24,25], in which the length and height of the computation domain were 3.22 m and 1.8 m, respectively. The water column, which had a reference density of 1000 kg/m^3, was located at the left bottom of the containers with a length of 1.2 m and a height of 0.6 m. The rest of the container was filled with air particles, which had a reference density of 1 kg/m^3. The domain boundary consisted of ghost particles. The initial particle spacing was selected to be $\Delta x/h$ = 0.01667 m, which is the same as in [38]. The wave speeds for water and air were 60 and 15 m/s, respectively.

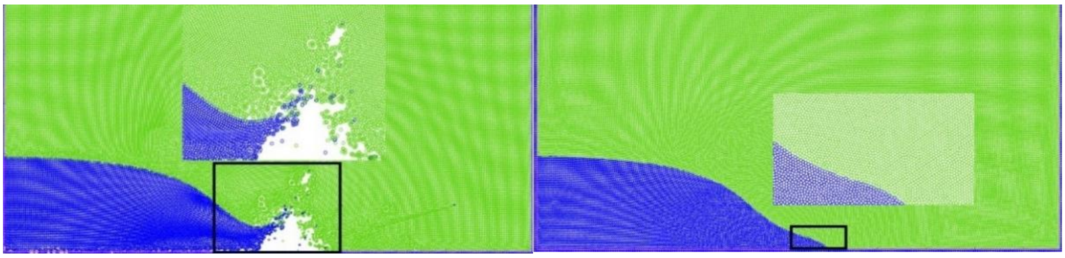

(a) (b)

Fig. 58. Phase distribution and their details of multiphase dam break flow at $t\sqrt{g/H}$ = 1.09. (a) standard WCSPH, (b) δ-SPH_CS.

The particle distributions obtained with standard WCSPH and δ-SPH_CS are presented in Fig. 58 at the dimensionless instant $t\sqrt{g/H} = 1.09$. With standard WCSPH, particle clustering was evident, as shown in Fig. 58 (a), and poor particle distribution caused the simulation to crash. In contrast, with δ-SPH_CS, the particle distribution was good even around the interface at the same instant. The later instant of particle distribution and free surface will be presented next.

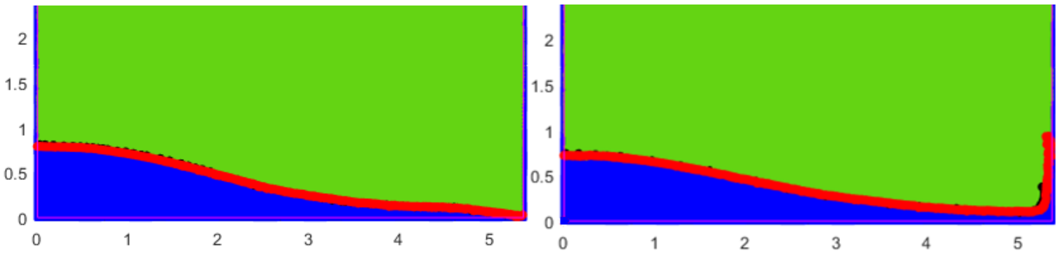

(a) (b)

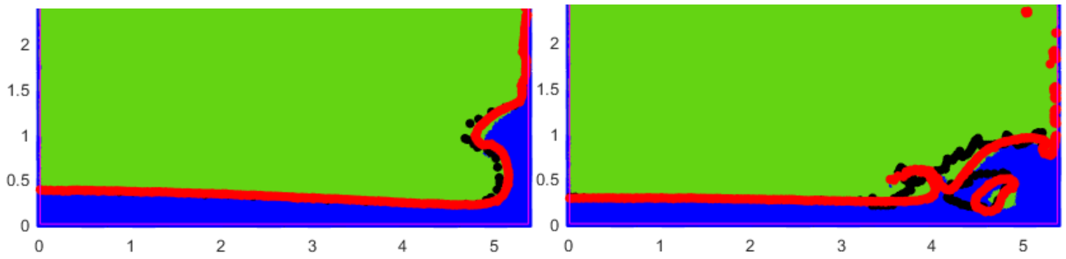

(c) (d)

Fig. 59. Evolution of the dam break. Comparison of the interface contours of δ-SPH_CS and Zheng and Chen [38] with ISPH results at instants (a) $t\sqrt{g/H} = 2.4$, (b) $t\sqrt{g/H} = 2.8$, (c) $t\sqrt{g/H} = 5.2$, (d) $t\sqrt{g/H} = 6.4$, together with the particle distribution of δ-SPH_CS. Red line represent the free surface particle of ISPH, while the black dots represents the interface particles of Zheng and Chen's model [38].

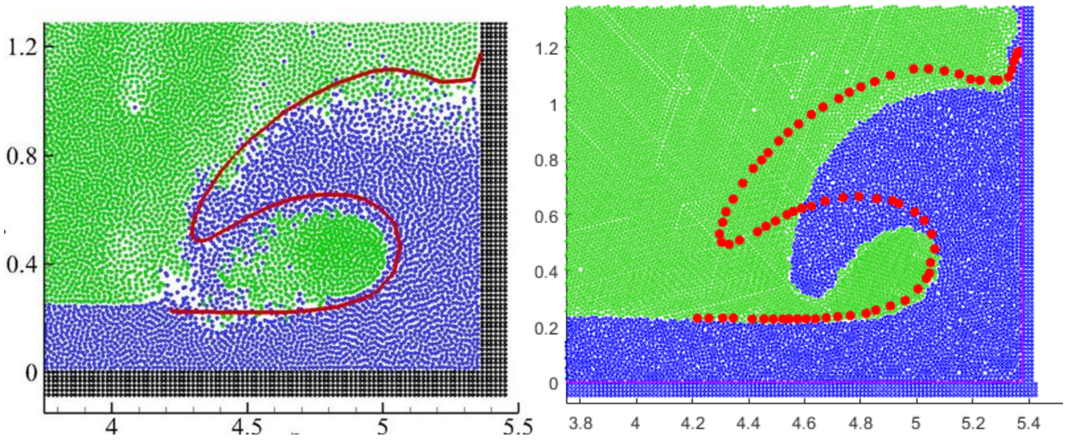

Fig. 60. Details of dam break flow at $t\sqrt{g/H} = 6.0$.

The progression of the multiphase dam break is shown at four instants: $t\sqrt{g/H} = 2.4$, 2.8, 5.2 and 6.4. The particle distribution of δ-SPH_CS is illustrated above, together with the free surface profiles from Zheng and Chen [38] as well as ISPH_CS. The free surface contours of δ-SPH_CS and that of Zheng and Chen were in excellent agreement with ISPH_CS before the wavefront reached the right wall, as shown in Fig.

59 (a) and (b). After this impact, the free surface contours of δ-SPH_CS aligned better with ISPH_CS than with δ-SPH, as shown in Fig. 59 (c) before the cavity appeared and in Fig. 59 (d) around the cavity. The results of δ-SPH_CS were similar to those of ISPH_CS.

Fig.60 illustrates the phase distribution of δ-SPH_CS and δ-SPH reported by Zheng and Chen [38] as well as a comparison of the free surface with the BEM solution at $t\sqrt{g/H} = 6.0$. The result of Zheng and Chen [38] was closer to the BEM solution, but the particle distribution of δ-SPH_CS improved compared to the BEM solution.

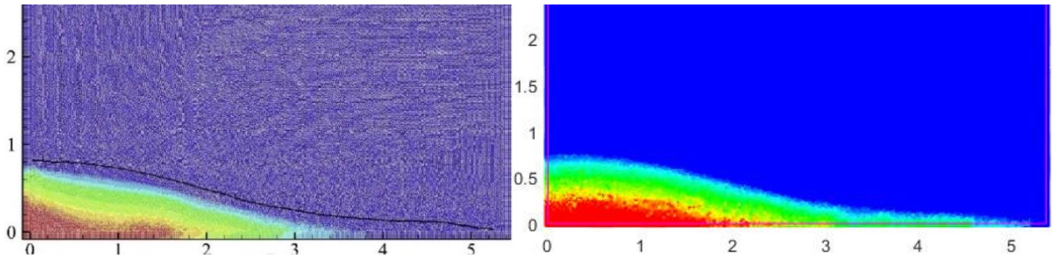

(a) (b)

Fig. 61. Pressure distribution of multiphase dam break flow at $t(g/H)^{1/2} = 2.4$. (a) Zheng and Chen’s model, (b) δ-SPH_CS.

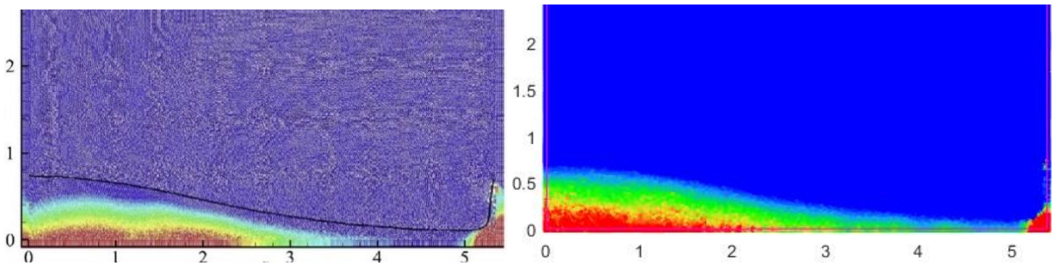

(a) (b)

Fig. 62. Pressure distribution of multiphase dam break flow at $t(g/H)^{1/2} = 2.8$. (a) Zheng and Chen’s model, (b) δ-SPH_CS.

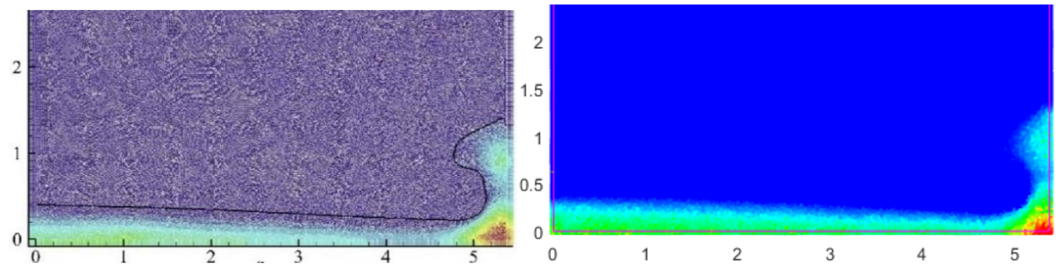

(a) (b)

Fig. 63. Pressure distribution of multiphase dam break flow at $t(g/H)^{1/2} = 5.2$. (a) Zheng and Chen's model, (b) δ-SPH_CS.

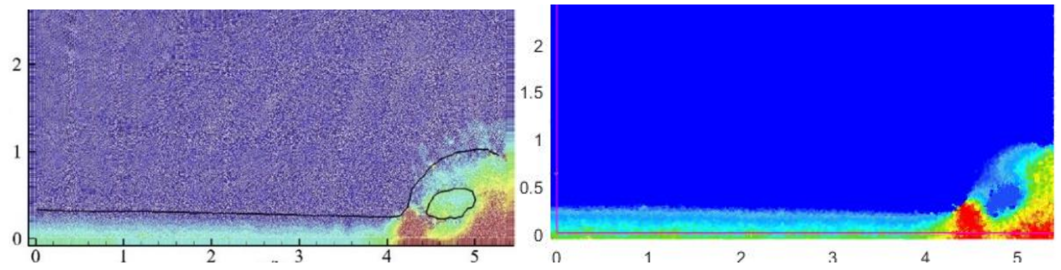

(a) (b)

Fig. 64. Pressure distribution of multiphase dam break flow at $t(g/H)^{1/2} = 6.1$. (a) Zheng and Chen's model, (b) δ-SPH_CS.

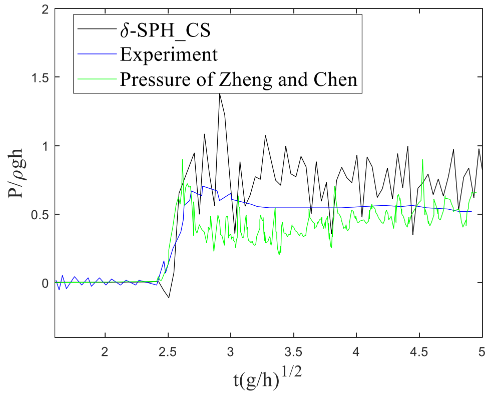

Fig. 65. Time histories of dimensionless pressure at point P_1 in dam break case.

Figs. 61 to 64 show the pressure distribution obtained with δ-SPH_CS as well as the results from Zheng and Chen [38] at four instants: $t\sqrt{g/H} = 2.4$, 2.8, 5.2 and 6.1, and they are very similar. To further illustrate the effect of the collision shift model on the computational results, the time histories of the dimensionless pressure at P_1 are presented in Fig. 65. The pressure of δ-SPH_CS is comparable with the experimental measurements and the results from [38].

5.6. Multiphase sloshing tank

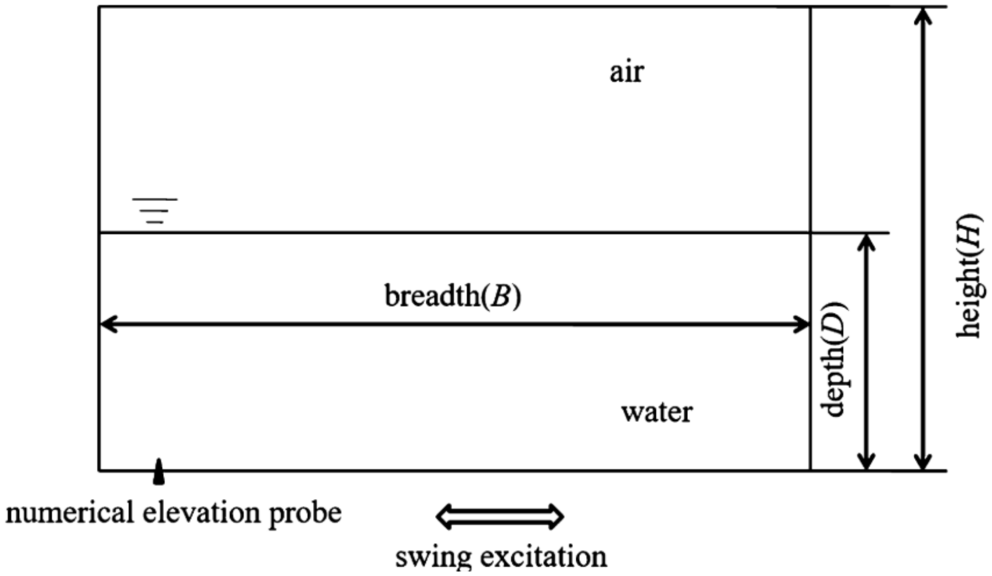

Fig. 66. Set up of liquid sloshing.

The case of a liquid sloshing in a rectangular tank was considered to evaluate the performance of δ-SPH_CS. In contrast to the dam break case, this case had a high density ratio as well as a long physical duration, resulting in an unstable particle distribution around the interface [126]. The set-up of the liquid sloshing case is given in Fig. 66 with water depth D and width B. The sloshing of the liquid was caused by the swinging motion of the tank and followed $x = A\sin\omega t$, where A is the amplitude and ω is the frequency, which was chosen to be 6.0578 s^{-1}. In the first scenario, B = 0.57 m, D = 0.15 m, A = 0.005 m and ω = 6.0578 s^{-1}. The density of water is 1000 $\mathrm{kg/m^3}$ while the density of air is 1.27 $\mathrm{kg/m^3}$. The dynamic viscosity of water is 1.01×10^{-3} while the viscosity of air is 1.96×10^{-5}. The parameter setting of the swinging motion followed [126] and the initial particle distance was Δx = 0.002 m.

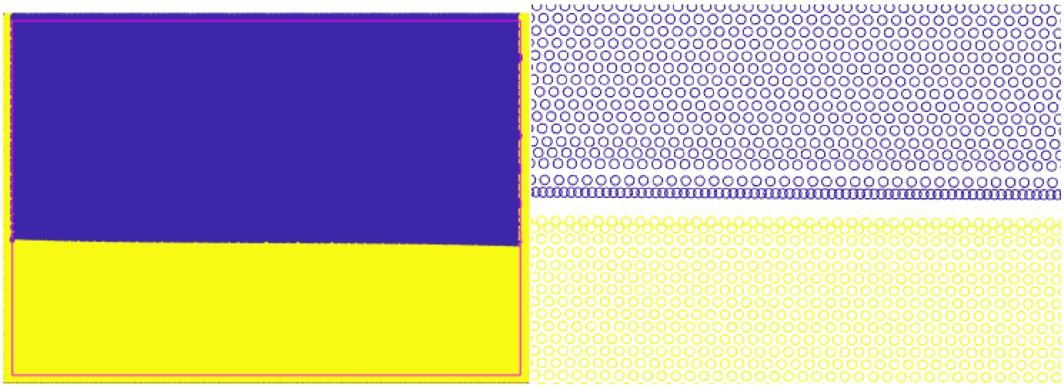

(a) (b)

Fig. 67. Sloshing tank. Standard WCSPH at time $t = 0.15\,s$, (a) global view, (b) detailed view .

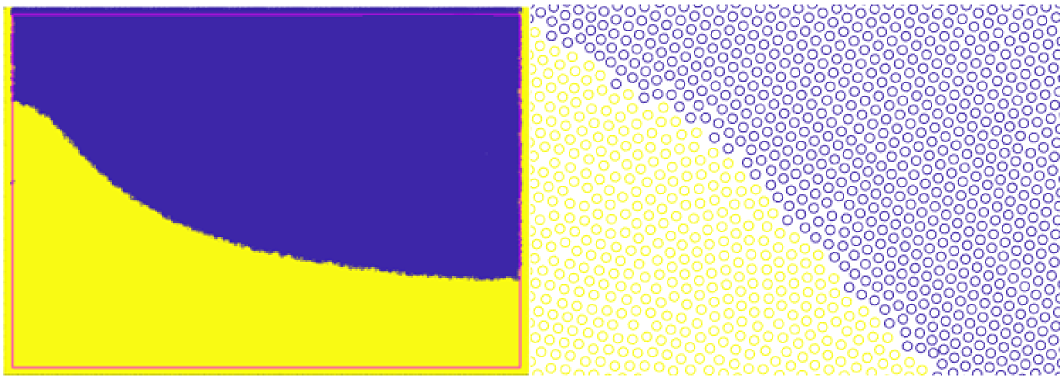

(a) (b)

Fig. 68. Sloshing tank. δ-SPH_CS at time $t = 6.72$ s, (a) global view, (b) detailed view.

In Figs. 67 and 68, the results obtained with standard WCSPH and δ-SPH_CS are shown at the instants *t* = 0.15 s and *t* = 6.72 s. Standard WCSPH simulation will be crashed at *t* = 0.15 s due to the particle clustering, while δ-SPH_CS can stabilize the simulation and have a very good result. From the detailed view Fig. 67(b), it can be observed that standard WCSPH suffered from particle clustering and layering while the particle distribution of δ-SPH_CS was favourable compared to standard WCSPH.

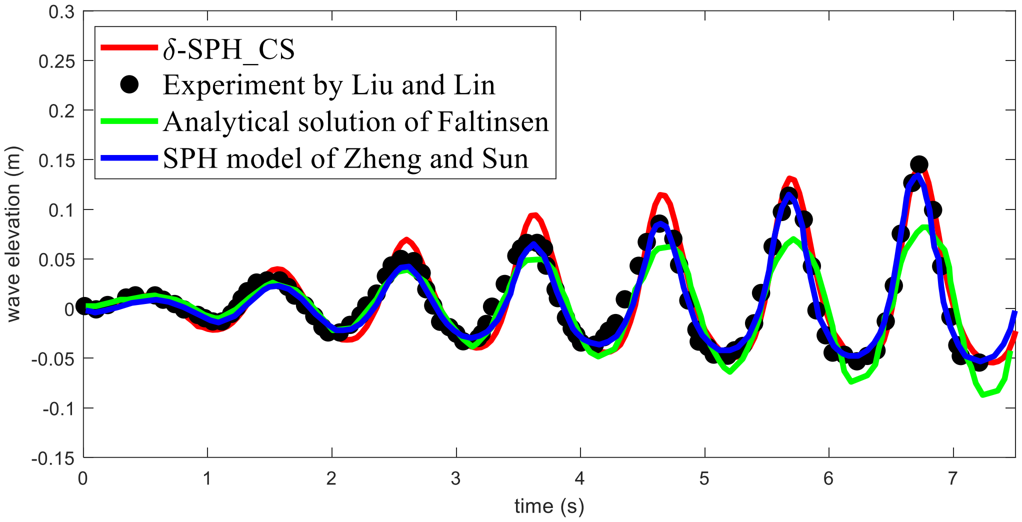

Fig. 69 The wave elevation at 0.02 m from the left wall.

To record the change in the wave height during the sloshing of the tank, a numerical probe was placed at x = 0.02 m. The height of the highest water particle between $x = x - \Delta x$ and $x = x + \Delta x$ was used to represent the height of the wave. Fig. 69 illustrates the wave height over time compared to the SPH results of Zheng and Sun [126], the analytical solution offered by Faltinsen [127] and the experimental measurements published by Liu and Lin [128]. The simulation result corresponded well with the experimental data and SPH results in [126], indicating that the δ-SPH_CS method is accurate and reliable.

To further validate the pressure in δ-SPH_CS, a second scenario was studied. In this scenario, B = 1 m, D = 0.125 m, A = 0.003 and ω = 3.927 s^{-1}. A pressure sensor was located on the right wall, and the distance to the bottom was 0.115 m. The parameter setting of the swinging motion followed [129] and the initial particle distance was Δx = 0.005 m.

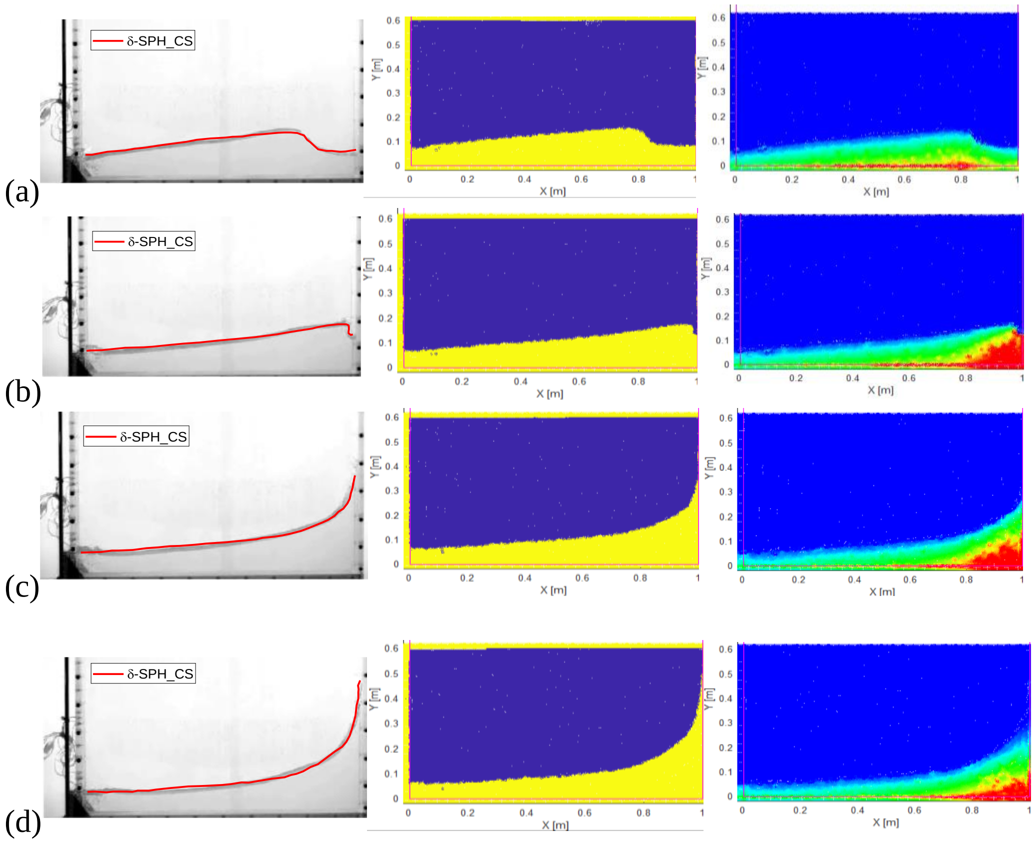

Fig. 70. From top to bottom: a sequence of images illustrating the evolution of the free surface (left), particle distribution (middle), and pressure distribution (right) during a flip through ($\Delta t = \frac{2}{23}$ s).

In Fig. 70, the evolution of the sloshing tank during a flip through is shown from *t* = 4.28 s to *t* = 4.58 s. The free surface contours of δ-SPH_CS together with the experimental photo from [130] are shown on the left side of Fig. 70. These contours are very close to the experimental photo. The centre of Fig. 70 indicates that the particle distribution of δ-SPH_CS was stable throughout the entire simulation process. The pressure distributions of δ-SPH_CS are shown on the right side of Fig. 70. The pressure distribution was nearly hydrostatic before the wave impacted the right wall, as shown in Fig. 70 (a), (c) and (d), and the maximum pressure was at the bottom of the tank. The maximum pressure was at the impact region on the right wall during the impact process, as shown in Fig. 70 (b). During the flip process, the maximum pressure was obtained by the hydrostatic distribution.

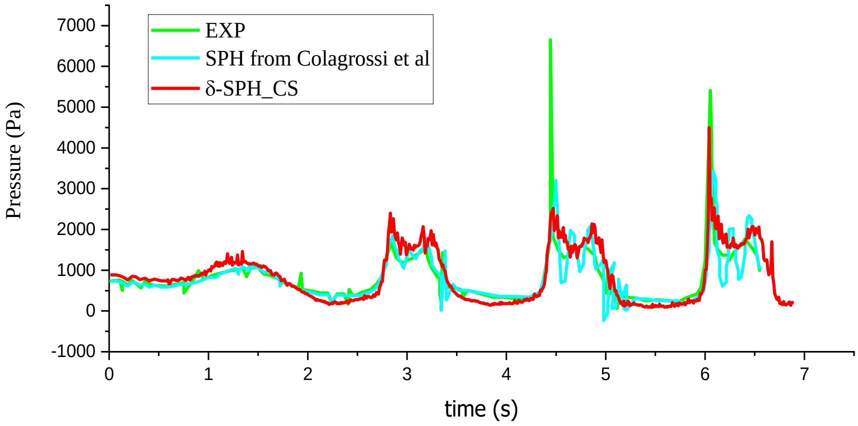

Fig. 71. Time histories of the pressure along the right wall.

In Fig. 71, the pressure–time histories at point P_1 (on the right wall at height 0.05 m)are shown. The result obtained with δ-SPH_CS was validated against experiments and the SPH pressures of Colagrossi et al. [129]. The result of δ-SPH_CS was smoother and closer to the experimental data than the results in [120], especially after 6 s.

5.7. Summary

A hybrid SPH method based on δ-SPH and the collision shift model was presented. The δ-SPH model was introduced in Chapter 3 and its stability has been verified by many researchers in single-phase [25,27,101,131,132] and multiphase [38,126]. However, although δ-SPH can reduce pressure fluctuation, it cannot avoid particle clustering during simulation. The collision shift model can only guarantee a uniform particle distribution but not a stable pressure in the fluid domain. The disadvantages of each model can be enhanced by the advantages of the other. A hybrid method based on the properties of δ-SPH and the collision shift model, was introduced (δ-SPH_CS).

In the Taylor–Green vortex case, standard SPH, δ-SPH, SPH_CS and δ-SPH_CS were compared in terms of stability, particle distribution and dissipative properties. Not only did δ-SPH_CS maintain pressure stability, but it also prevented particle clustering. In the Rayleigh–Taylor instability case, δ-SPH_CS effectively prevented particle clustering, and the interface and vorticity distribution were comparable to those of the level-set method. In the static multiphase flow case, the pressure distribution, kinetic energy, and potential energy obtained showed significant improvement compared with those of the standard WCSPH model. Additionally, particle clustering around the interface of δ-SPH_CS disappeared. In the multiphase dam break case, δ-SPH_CS exhibited a better particle distribution and interface compared with the results of δ-SPH by other researchers. Additionally, the pressure had good agreement with experimental data. In the multiphase sloshing tank case, the wave evaluation obtained with δ-SPH_CS aligned well with the experimental data in the first scenario. In the second scenario, both the interface and the pressure were identical to the experimental data.

In conclusion, δ-SPH_CS demonstrated its potential in applications with long duration multiphase flow. This serves as the basis for its use in the bearing chamber of an aero-engine in the chapters that follow.

Chapter 6 Single-phase Taylor–Couette flow (2D)

The previous chapter examined the applicability of δ-SPH in combination with the particle collision shift model to multiphase flows at high-density ratios (liquid, gas). This combination not only suppresses particle clustering but also smooths the pressure distribution, which could not be achieved with the standard SPH approach. The combination is held for benchmark cases with relatively low fluid velocities compared to the high rotational speeds in an aeroengine.

In this chapter, the Taylor–Couette (TC) flow between two concentric cylinders is studied as the next step towards the modelling of a bearing chamber. The proper modelling of the single-phase 2D flow between a rotating inner cylinder and a non-rotating outer cylinder is a crucial step towards the modelling of the complex 3D flow in high-speed rotating elements of engines, turbines and pumps. The model is not only a foundation for the multiphase flow in a bearing chamber but also forms an excellent benchmark case for the validation of turbulence models, though turbulence is typically a 3D phenomenon. Simulation results are presented of the laminar and turbulent single-phase TC flow. The laminar flow results are validated against analytical solutions, while the turbulent flow results are validated against simulations performed with Fluent and against Direct Numerical Simulation (DNS) results available in the literature.

6.1. Case description and initial conditions

6.1.1. Case setup

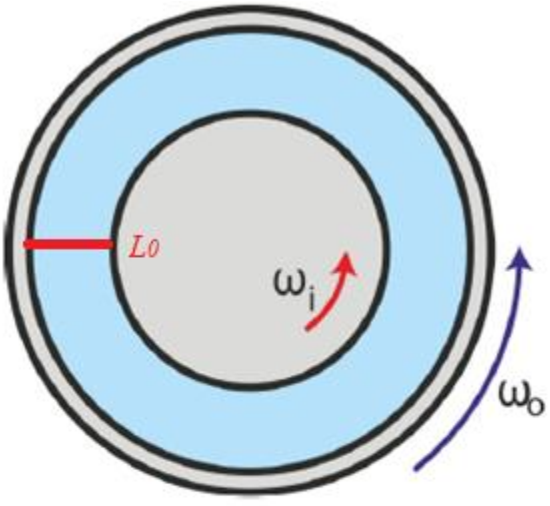

Fig. 72. Setup of the 2D TC flow.

The setup of the 2D TC flow is shown in Fig. 72. The definitions are as follows: R and ω are the radius and rotational speed of the inner or outer circles, respectively. The ratio of the inner and outer radius is

$$\eta = \frac{R_{inner}}{R_{outer}} \tag{102}$$

Instead of the Reynolds number, one can alternatively characterise the flow between concentric cylinders by the Taylor number [133].

$$T_a = \frac{(1+\eta)^4 (R_{outer}-R_{inner})^2 (R_{outer}+R_{inner})^2 (\omega_{outer}-\omega_{inner})^2}{64\eta^2 \upsilon^2} \tag{103}$$

When T_a is larger than 10^8, the flow can be treated as turbulent flow; otherwise, the flow is laminar.

For systematic research, a series of single-phase 2D TC flow with three different radius ratios is studied in this chapter, including laminar and turbulent flows. For the turbulence models in the 2D TC flow, the mixing length turbulence model (ML) and

Spalart–Allmaras model (SA) are applied. The dimensions and fluid properties of the following simulation are shown in Table 6.

Table 6. Dimensions and fluid properties of single-phase Taylor–Couette flow.

	η	μ *(m^2/s)*	T_a	Turbulent model
Case1	0.7	0.01	10^8	No
Case2	0.5	0.001	10^{10}	ML, SA
Case3	0.7	0.001	10^{10}	ML, SA
Case4	0.9	0.001	10^{10}	ML, SA

6.1.2. Initial and boundary conditions

In this section, the initial velocity and pressure distribution at $t = t_0$ are obtained with the laminar flow distribution. The laminar flow between two rotating cylinders forms an exact solution of the Navier–Stokes equations. The solution for the velocity and pressure distribution, given in cylindrical coordinates (R, θ, z), is

$$v_R = 0\,; v_\theta = \frac{C_7}{R} + C_8 R; v_z = 0 \tag{104}$$

$$p(R) = \rho[-\frac{C_7^2}{2}\left(\frac{1}{R^2} - \frac{1}{R_{inner}^2}\right) + 2C_7C_8\, ln\left(\frac{R}{R_{inner}}\right) + \frac{1}{2}C_8^2(R^2 - R_{inner}^2)] \tag{105}$$

With the coefficients in the angular velocity

$$C_7 = -\frac{R_{inner}^2 R_{outer}^2(\omega_{outer} - \omega_{inner})}{R_{outer}^2 - R_{inner}^2} \tag{106}$$

$$C_8 = -\frac{\omega_{outer} R_{outer}^2 - \omega_{inner} R_{inner}^2}{R_{outer}^2 - R_{inner}^2} \tag{107}$$

Following the above equation, the velocity and pressure distribution of laminar TC flow are determined. In the following sections, the initial conditions for the case study follow Eqs. (104) and (105). The boundary condition is referred to in Section 2. The profiles of pressure, velocity and viscosity are presented on the horizontal axis (y = 0) between ($-R_{outer}$ < = x < = $-R_{inner}$), as indicated by the solid line L_0 (red) in Fig. 72.

6.1.3. SPH and CFD model coefficients

The authors also simulate the single-phase laminar and turbulent TC flow by using Fluent (2019 R2), which is an industry-leading fluid simulation software. Fluent is known for its advanced physics modelling capabilities and industry-leading accuracy. In this way, the accuracy of δ-SPH_CS can be validated against the results of Fluent in the next sections. In the fluent, the initial condition is the same as SPH simulation and the resolutions in fluent and SPH are roughly the same while only SA model is applied for the turbulent flow.

The rest of the sections are organised as follows: Numerical results for the 2D laminar TC flow are first presented in Section 6.2. Based on the knowledge acquired from the 2D TC flow, we conduct an elaborate study in Section 6.3 on the different radius ratios relevant to the single-phase 2D turbulent flow. The influence of the radius ratio and convergence study are presented in Section 6.4. Finally, the major research findings are summarised in Section 6.5.

6.2. Single phase laminar Taylor–Couette flow (2D)

In this case, $\eta = 0.7$, and $T_a = 10^8$. The viscosity term is calculated through laminar viscosity.

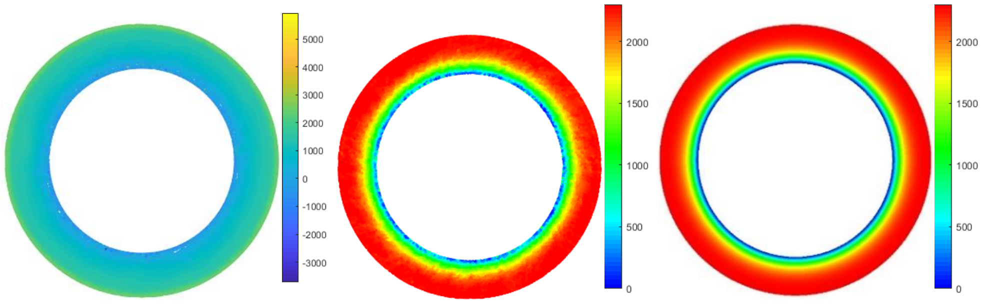

(a) (b) (c)

Fig. 73. Pressure distribution at time t = 0.12 s, (a) standard SPH, (b) δ-SPH_CS, (c) Fluent.

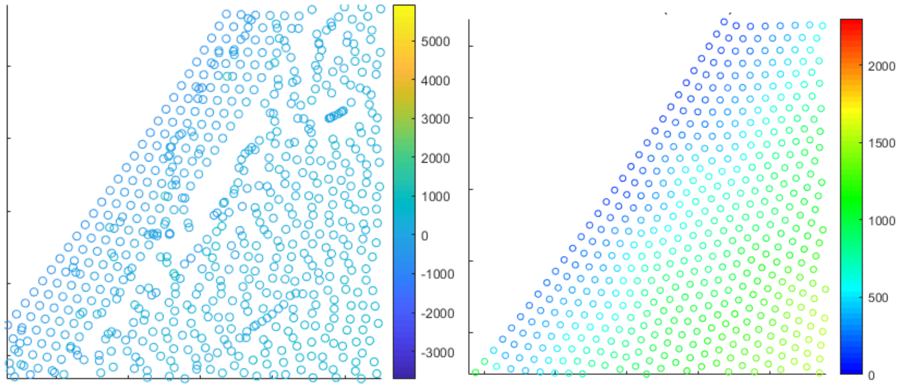

(a) (b)

Fig. 74. Detailed view of the pressure distribution at time t = 1.2 s, (a) standard SPH, (b) δ-SPH_CS.

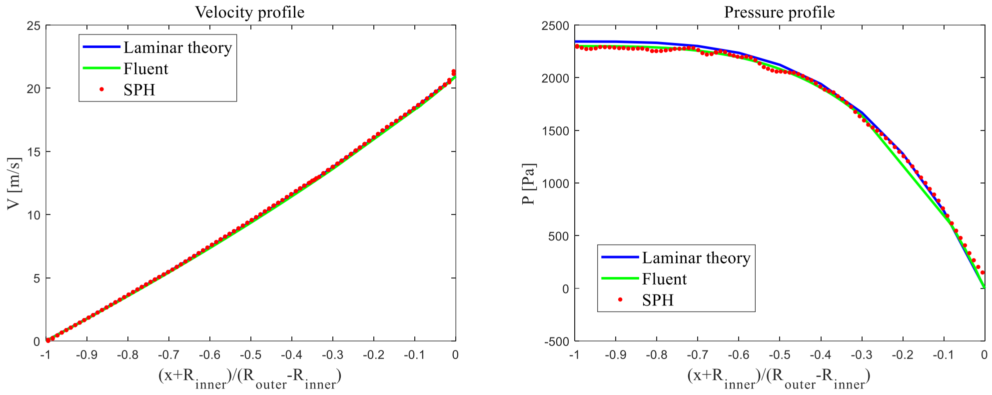

(a) (b)

Fig. 75. Results comparison between δ-SPH_CS and Fluent at t = 1.2 s. (a)velocity profile from ($-R_{outer}$, 0.0) to ($-R_{inner}$, 0.0), (b) pressure profile from ($-R_{outer}$, 0.0) to ($-R_{inner}$, 0.0).

Fig. 73 illustrates the particle distribution with pressure presented in colour obtained with standard WCSPH, δ-SPH_CS and Fluent at instant t = 0.12 s. As shown in the pressure legend in Fig. 73(a), standard SPH suffers from unrealistic and fluctuated pressure distribution. The results obtained with δ-SPH_CS in Fig. 73(b) and Fluent in Fig. 73(c) are much better. The pressure distribution is quite smooth only a slight fluctuation can be seen in the distribution of δ-SPH_CS. To make the particle distribution clearer, a detailed view of the particle distribution obtained with Standard SPH and δ-SPH_CS is shown in Fig. 74. According to the detailed view of Fig. 74(a), the standard WCSPH suffers from particle clustering near the inner shaft as well as particles penetrating, which also affects the pressure distribution. In contrast, results at instant t = 1.2 s obtained with the δ-SPH_CS are shown in Fig. 74(b), which is much improved over standard SPH and shows an almost regular particle distribution.

To further verify the correctness of δ-SPH_CS, the pressure and velocity distribution along $y = 0$ of the δ-SPH_CS method are compared with laminar theory and the results of Fluent in Fig. 75. The velocity and pressure profile of δ-SPH_CS and Fluent are almost the same in laminar theory.

From the above figures, the collision shift model results in a significant improvement in the particle distribution. The combination with δ-SPH also leads to a highly stable pressure distribution in the laminar flow. The turbulence in the single-phase flow is discussed in the following section. δ-SPH_CS is further denoted as SPH in this chapter.

6.3. Single phase turbulent Taylor–Couette flow (2D)

To systematically verify the ML model and SA model presented in Chapter 3 and determine the influence of the radius ratio on the turbulent properties, a series of 2D TC flows with three different η (0.5, 0.7, 0.9) are simulated by SPH when $T_a = 10^{10}$ in the following subsections. To verify the SPH, the same series of cases are also simulated by Fluent with the SA model. The turbulent viscosity calculated by the SA and ML models will be added to the laminar viscosity to calculate the viscous term in the momentum equation.

6.3.1. $\eta = 0.5$

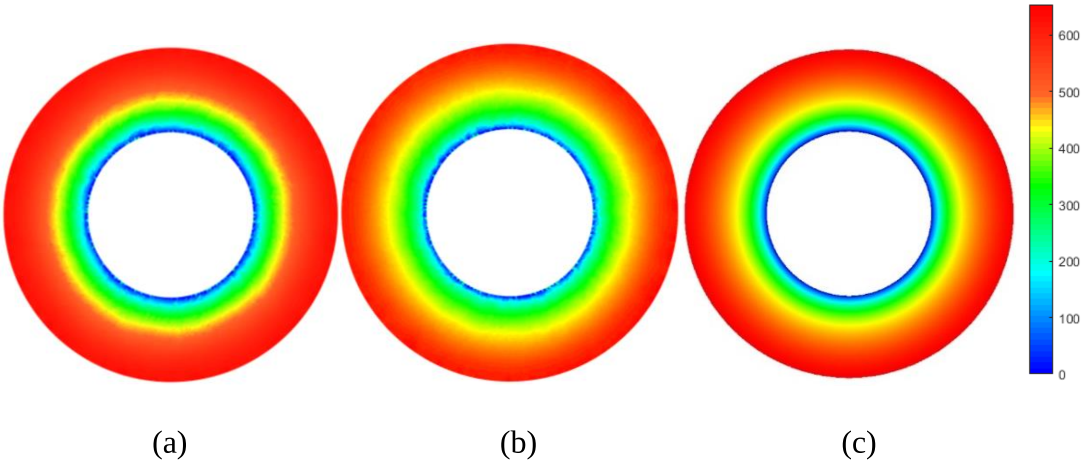

Fig. 76. Pressure distribution at time t = 1.2 s. (a) SA (SPH), (b) ML (SPH), (c) SA (Fluent).

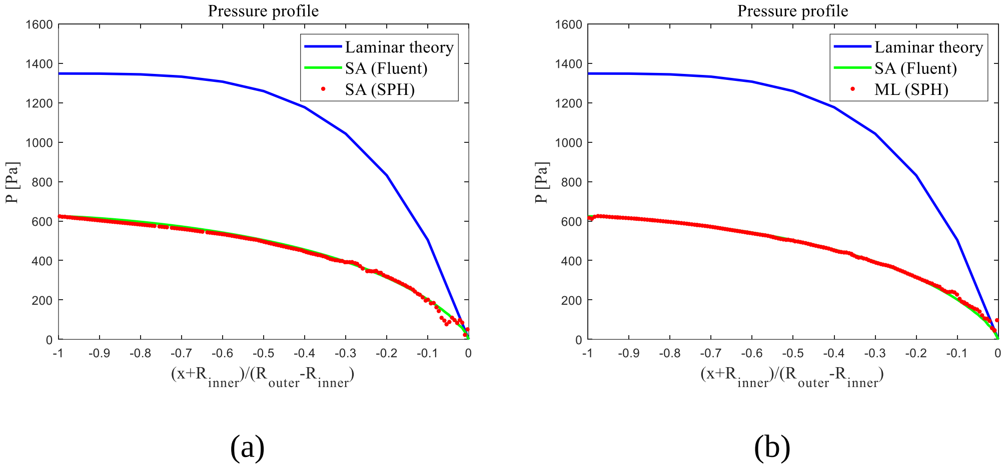

Fig. 77. Pressure profile at time t = 1.2 s. (a) SA (SPH), (b) ML (SPH).

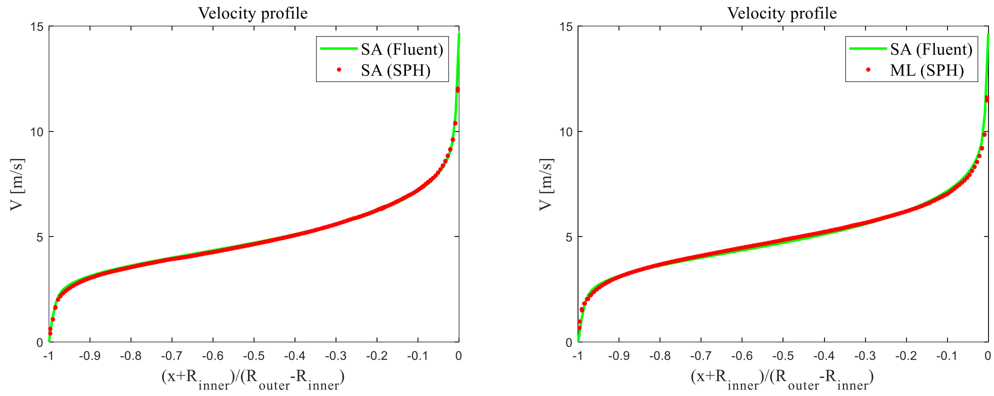

(a) (b)

Fig. 78. Velocity profile at time t = 1.2 s. (a) SA (SPH), (b) ML (SPH).

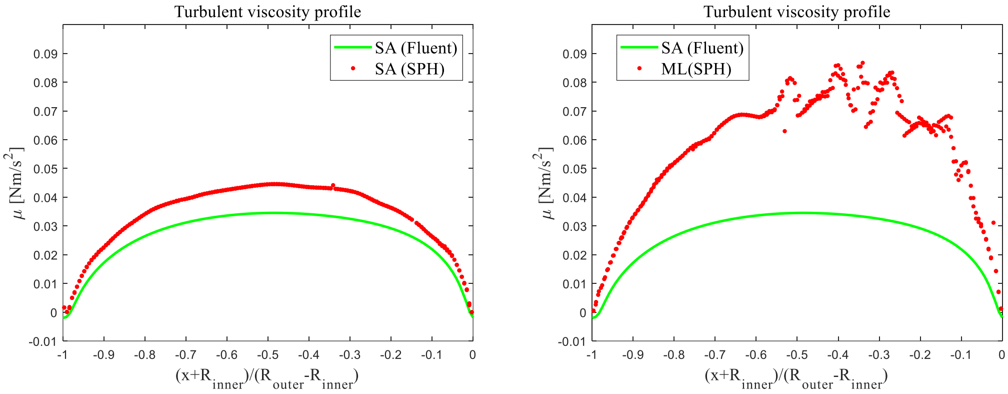

(a) (b)

Fig. 79. Turbulent viscosity profile at time t = 1.2 s. (a) SA (SPH), (b) ML (SPH).

Fig. 76 displays the pressure distribution of SA (SPH), ML (SPH) and SA (Fluent), and the results of each model are nearly the same. Fig. 77 to 79 illustrate profiles along the line L_0 from $(-R_{outer}, 0.0)$ to $(-R_{inner}, 0.0)$ for pressure, velocity and viscosity. As indicated in Fig. 77, the pressure profiles of SA (SPH) and ML (SPH) are smooth and identical to SA (Fluent). As revealed in Fig. 78, the velocity profiles of SA (SPH) and ML (SPH) are almost consistent with the results of SA (Fluent), including near the boundary. The velocity profile SA (SPH) is slightly closer to the Fluent results than ML (SPH). As seen in Fig. 79, the turbulent viscosity of SA (SPH) is similar to that of

SA (Fluent), while the turbulent viscosity of ML (SPH) is almost double that of SA (Fluent). This viscosity disparity might be the reason for the slightly different velocity profile.

6.3.2. $\eta = 0.7$

This radius ratio is always applied in the bearing chamber in the aeroengine. Similar to the results of $\eta = 0.5$, the comparison of pressure distribution and pressure, velocity and viscosity profiles along the line L_0 from $(-R_{outer}, 0.0)$ to $(-R_{inner}, 0.0)$ is also present in this section.

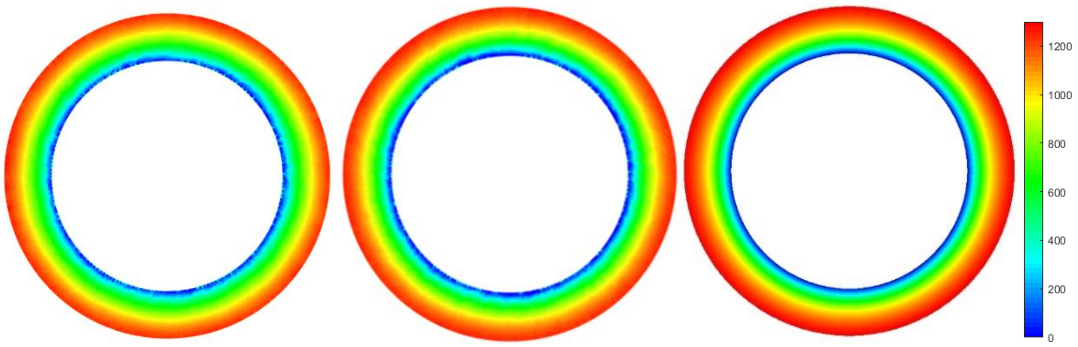

(a) (b) (c)

Fig. 80. Pressure distribution at time t = 1.2 s. (a) SA (SPH), (b) ML (SPH), (c) SA (Fluent).

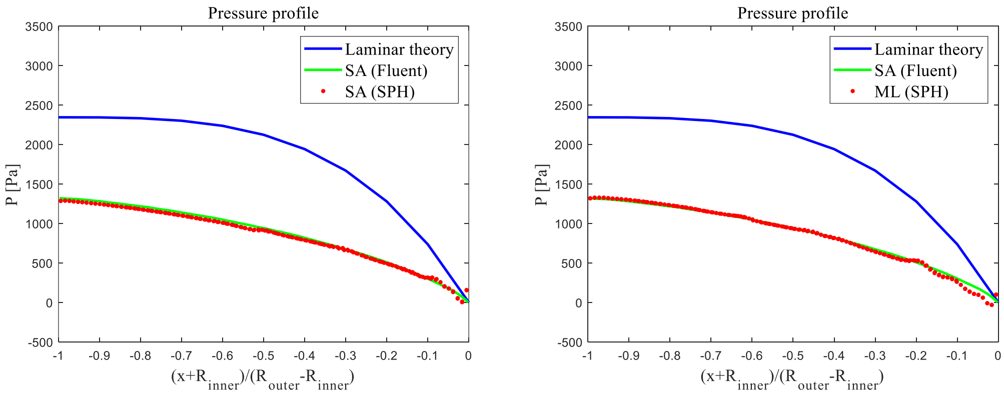

(a) (b)

Fig. 81. Pressure profile at time t = 1.2 s. (a) SA (SPH), (b) ML (SPH).

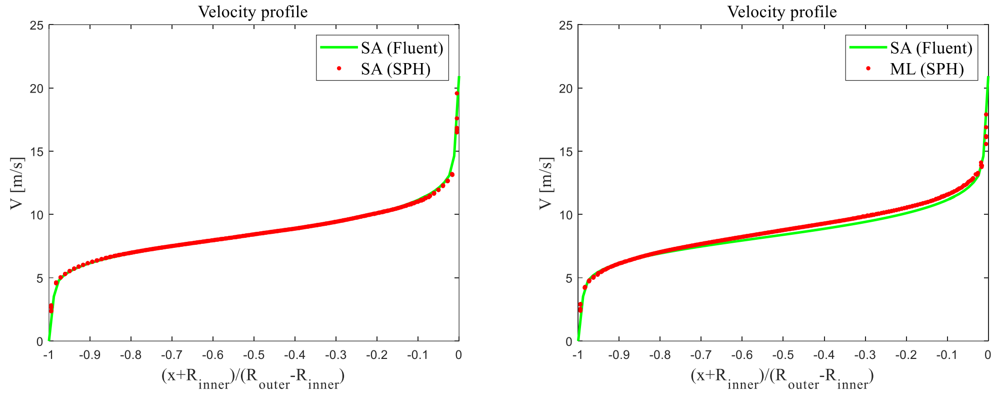

(a) (b)

Fig. 82. Velocity profile at time t = 1.2 s. (a) SA (SPH), (b) ML (SPH).

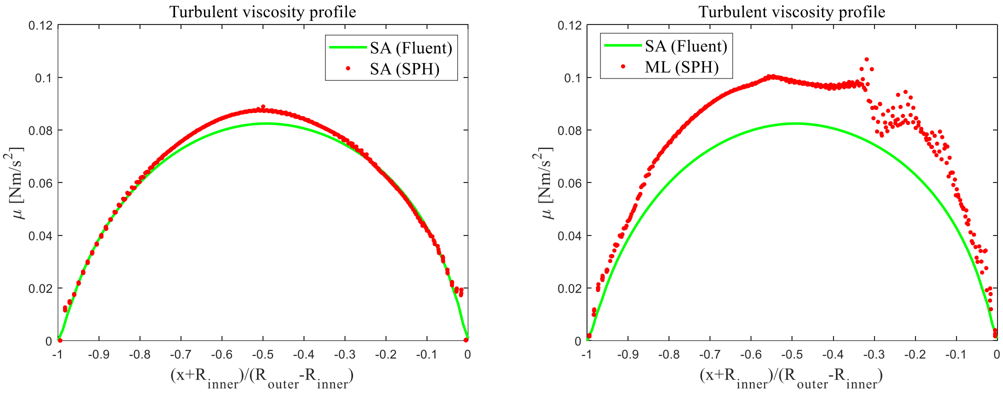

(a) (b)

Fig. 83. Turbulent viscosity profile at time t = 1.2 s. (a) SA (SPH), (b) ML (SPH).

The pressure distribution of SA (SPH), ML (SPH) and SA (Fluent) is shown in Fig. 80, and the results of each model are nearly identical to one another. The pressure profiles of SA (SPH) and ML (SPH) can be seen in Fig. 81. The results of both turbulence models are quite smooth and consistent with SA (Fluent). Fig. 82 depicts the velocity profile of ML (SPH) and SA (SPH), where the result of SA (SPH) is better than that of ML (SPH). Although the results of ML (SPH) and SA (Fluent) are almost the same, the results of SA (SPH) and SA (Fluent) are completely consistent. The turbulent viscosity profiles of ML (SPH) and SA (SPH) are illustrated in Fig. 83. The turbulent viscosity of SA (SPH) is nearly the same as SA (Fluent), while the turbulent viscosity of ML (SPH) is a bit larger than that of SA (Fluent). This discrepancy might be the reason for the slightly different velocity profile.

6.3.3. $\eta = 0.9$

Note that the radius ratio of the journal bearing is always between 0.9 and 1 in engineering applications. Analogous to the above sections, the turbulence models are validated in this section regarding pressure, velocity and viscosity along the line L_0 from $(-R_{outer}, 0.0)$ to $(-R_{inner}, 0.0)$.

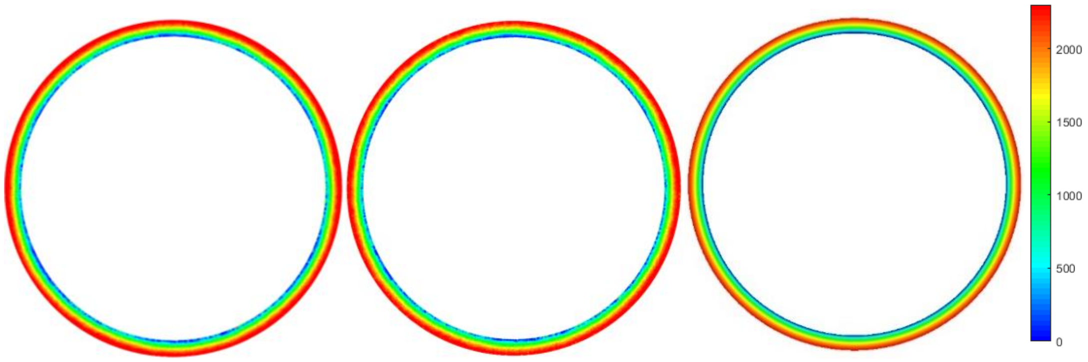

(a) (b) (c)

Fig. 84. Pressure distribution at time t = 1.2 s. (a) SA (SPH), (b) ML (SPH), (c) SA (Fluent).

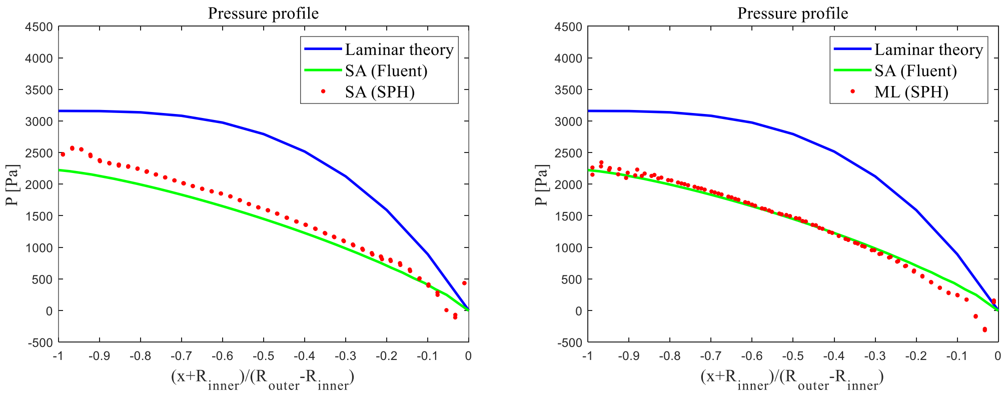

(a) (b)

Fig. 85. Pressure profile at time t = 1.2 s. (a) SA (SPH), (b) ML (SPH).

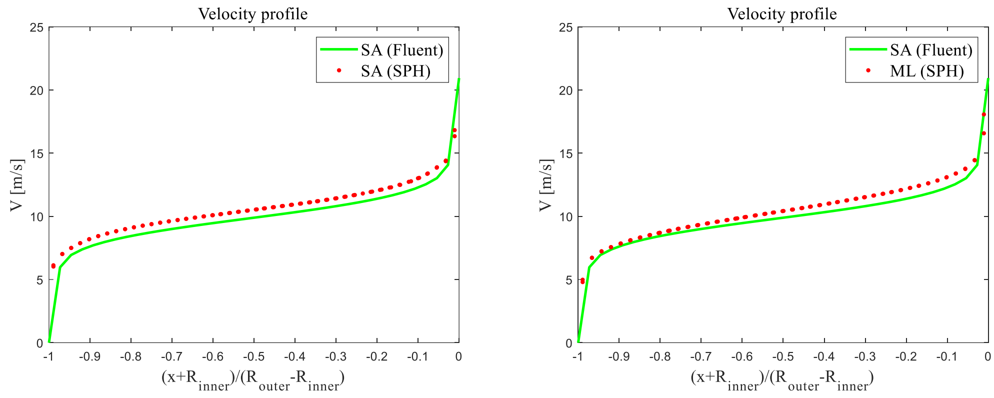

(a) (b)

Fig. 86. Velocity profile at time t = 1.2 s. (a) SA (SPH), (b) ML (SPH).

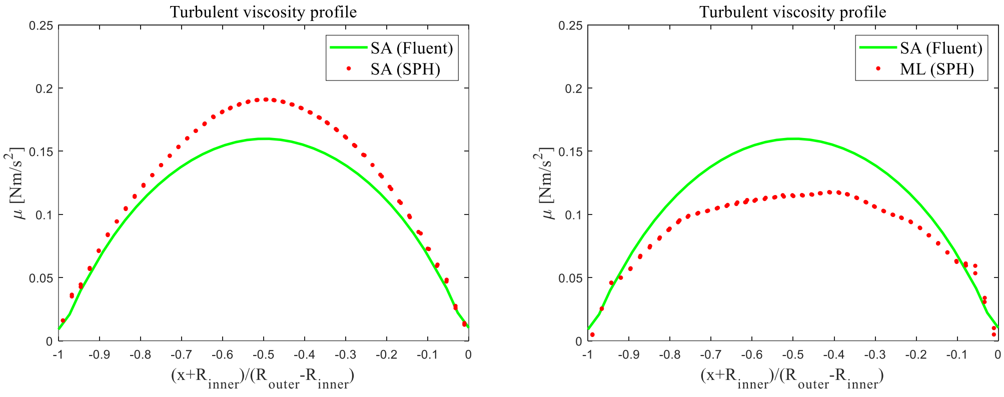

(a) (b)

Fig. 87. Turbulent viscosity profile at time t = 1.2 s. (a) SA (SPH), (b) ML (SPH).

The pressure distribution of the simulations with SA (SPH), ML (SPH), and SA (Fluent) is displayed in Fig. 84. The pressure distributions obtained with these three models have no visible difference. However, as shown in Fig. 85, the pressure profile of SA (SPH) and ML (SPH) is slightly larger than SA (Fluent), particularly near the outer wall. Fig. 86 depicts the velocity profile of ML (SPH) and SA (SPH). The velocity of ML (SPH) and SA (SPH) is slightly larger than SA (Fluent), although the trend is almost the same. As illustrated in Fig. 87, the turbulent viscosity of SA (SPH) is greater than SA (Fluent), while the turbulent viscosity of ML (SPH) is less than that of SA (Fluent).

6.4. Analysis of results

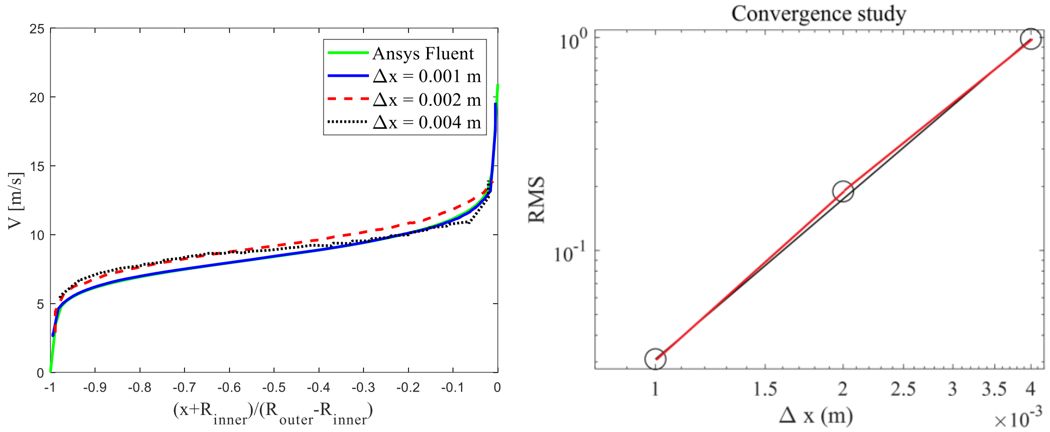

(a) (b)

Fig. 88. 2D TC flow ($\eta = 0.7$). (a) Velocity profile along the horizontal line from ($-R_{outer}$, 0.0) to ($-R_{inner}$, 0.0) for SA (SPH) at three particle resolutions. (b) Convergence of the RMS error of velocity with increasing particle resolution ($\Delta x \rightarrow 0$).

In Fig. 88(a), the velocity profiles at $T_a = 10^{10}$, as obtained with SA (SPH) for three resolutions (Δx = 0.001 m, Δx = 0.002 m, Δx = 0.004 m), are validated against simulations performed with SA (Fluent). The figure shows that with increasing resolution, the results are closer to those of Fluent. In Fig. 88(b), the order of convergence, evaluated as the root of the mean square (RMS) of the error in the velocity profile along the line from ($-R_{outer}$, 0.0) to ($-R_{inner}$, 0.0), is plotted for $\eta = 0.7$ and $Ta = 10^{10}$. The results show that the order of convergence is approximately 2.4.

To further consider the influence of different radius ratios on the fluid properties, velocity and pressure profiles are shown below. As Section 6.3 illustrates, the results of SA and ML in SPH are almost the same in various radius ratios, and the turbulence model in Fluent is SA. Here, the results of SA (SPH) represent the results of SPH compared with Fluent.

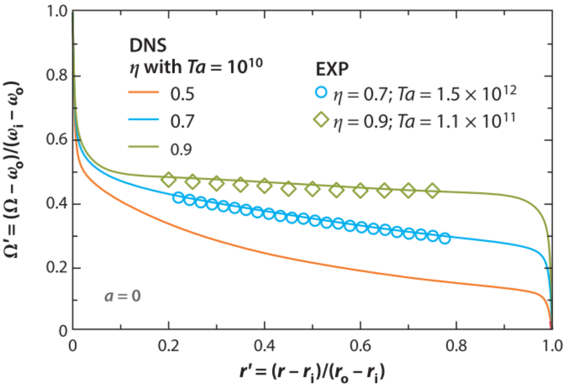

Fig. 89. Angular velocity for varying radius ratios across the Taylor–Couette gap for only inner cylinder rotation from [133].

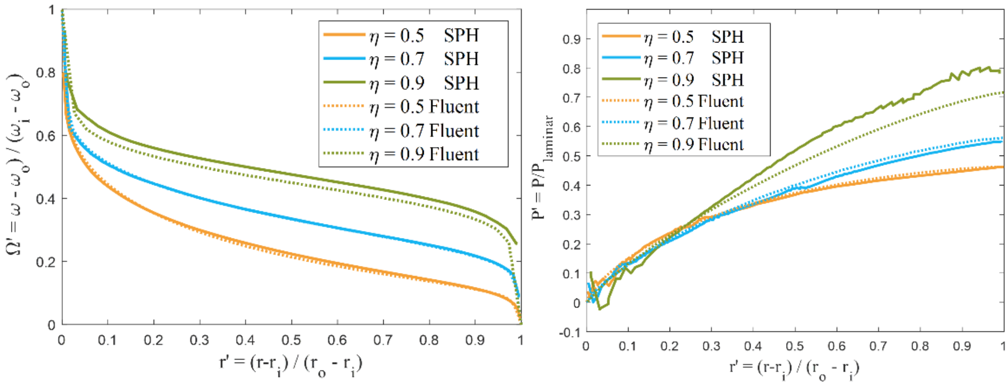

(a) (b)

Fig. 90. Angular velocity and pressure profiles for several radius ratios across the Taylor–Couette gap for only inner cylinder rotation obtained with SA (SPH) and SA (Fluent) at $Ta = 10^{10}$. (a) Angular velocity, (b) viscosity ratio.

The angular velocity and pressure profile strongly depend on the radius ratio, η, as seen from the results of SPH and Fluent in Fig. 90. The angular velocity from ($-R_{outer}$, 0.0) to ($-R_{inner}$, 0.0) of SPH and Fluent are nearly the same, particularly when η = 0.5 and 0.7, the profiles almost overlap in Fig. 90(a). The same trend can also be seen in the profiles obtained with DNS (3D), as shown in Fig. 89. The angular velocity gradient decreases with increasing η, and the profile of η = 0.9 is the flattest (most turbulent characteristics) among these three η. In contrast, for small η = 0.5, a large decrease of Ω' to less than 0.5 is observed in both Fig. 89 and Fig. 90 (a). The varying extent of the pressure decrease can correspondingly be seen in Fig. 90 (b). The pressure for η = 0.5 also represents the largest decrease (almost 60%). However, it also means that the largest radius ratio leads to the closest pressure to laminar flow (most laminar characteristics). This result seems to be contradictory to the velocity profile. To further analyse these two profiles, the viscosity ratio $(\mu/\mu_{laminar})$ and the so-called viscosity loss $(\frac{\mu(r_o-r_i)}{\mu_{laminar}r_i})$ profiles are shown in Fig. 91.

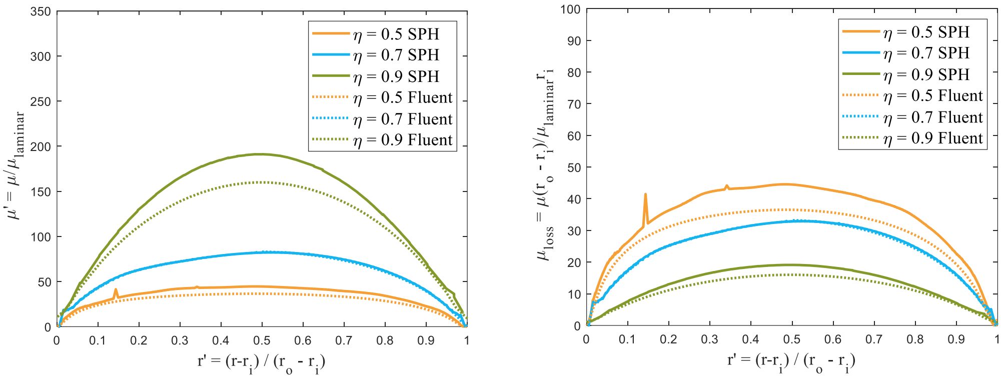

(a) (b)

Fig. 91. Dimensionless profiles for varying radius ratios across the Taylor–Couette gap for only inner cylinder rotation obtained with SA (SPH) and SA (Fluent) at $Ta = 10^{10}$, (a) viscosity ratio, (b) viscosity loss.

Fig. 91(a) shows the viscosity ratio. The smaller radius ratio leads to a larger viscosity ratio (more turbulent characteristics), which matches Fig. 90 (a) quite well. The decrease in velocity and pressure can be treated as a kind of dimensionless loss in the bearing chamber. The loss is not only related to the viscosity but also to the gap between the inner and outer radius. The value of the loss can therefore be validated through a dimensionless variable called ‘viscosity loss’ in Fig. 91(b). The figure demonstrates that the smaller radius ratio will create a large dimensionless loss at the same Ta, which verifies the large decrease in velocity and pressure in Fig. 90.

6.5. Summary

The single-phase two-dimensional Taylor–Couette flow is modelled using δ-SPH in combination with the particle collision shift model in this chapter. Simulations are performed for several configurations represented by the radius ratio and rotational speeds represented by the Taylor number (T_a). All simulations are performed at $T_a = 10^{10}$.

The SPH simulations under turbulent flow conditions are performed with the mixing length turbulence model (ML) as well as the Spalart–Allmaras turbulence model (SA). The results are validated against Fluent, also using the Spalart–Allmaras model.

The SPH results for the configuration with a low radius ratio (η = 0.5, large clearance) show a reasonable match with Fluent. The pressure and velocity profiles obtained with ML and SA are both in excellent agreement with Fluent. The turbulent viscosity profile of ML shows values that are about twice as high as those of Fluent, with quite some fluctuation in an asymmetrical profile. The turbulent viscosity profile of SA is much closer to that of Fluent, without fluctuation. Here, note that none of the results is time averaged.

The SPH results for the configuration with a medium radius ratio ($\eta = 0.7$, medium clearance) show a similar match with Fluent. The pressure and velocity profiles are all in good agreement. The turbulent viscosity profile of ML shows values that are now closer to those of Fluent, although the level of turbulent viscosity has more than doubled. The turbulent viscosity profile of SA coincides well with that of Fluent, again without fluctuation.

The SPH results for the configuration with a high radius ratio ($\eta = 0.9$, small clearance) show more deviation than those of Fluent. The pressure and velocity profiles of both ML and SA are no longer in agreement with Fluent, though there is still a reasonable match. This is revealed in the slightly higher velocity gradients, which have a small clearance. The turbulent viscosity profile of ML shows values somewhat lower than Fluent, while those of SA are higher.

Comparing the results of all four cases, it can be seen that the pressure increases from the inner cylinder towards the outer cylinder. The lower radius ratio leads to lower pressure and velocity. In contrast, the higher radius ratio makes the velocity profile flatter. With the increasing of the radius ratio, the difference of the turbulent pressure and laminar pressure is getting smaller

Chapter 7 Multiphase Taylor–Couette flow (2D)

In Chapter 6, the 2D single-phase Taylor–Couette (TC) flow is examined under laminar as well as turbulent flow conditions. This chapter studies the 2D multiphase TC flow between two concentric circles. The multiphase case is more analogous to that in the bearing chamber of an aeroengine. At the high rotational speeds in a bearing chamber, the airflow is typically turbulent, whilst the oil flow along the wall remains laminar. Simulation results are presented of relative lower and higher rotational speeds. For validation in this chapter, these flow regimes are also modelled in the multiphase TC case.

7.1. Case description

7.1.1. Case setup

The dimensions of the multiphase TC flow are different with a single-phase, due to the dimensions is confidential, here using R_{inner} and R_{outer} to represent the dimensions. The fluid properties are $\mu_{air} = 1 \times 10^{-5} Pa \cdot s$, $\mu_{oil} = 2.7 \times 10^{-2} Pa \cdot s$, $\rho_{air} = 1\ kg/m^3$ and $\rho_{oil} = 1000\ kg/m^3$. To analyse the effects of the different rotational speeds on the flow states, two cases are simulated at different rotational speeds of the inner shaft. The relatively lower rotational speed of the inner shaft is ω_{inner}^{low} , and the relatively higher rotational speed is ω_{inner}^{high}, yield $T_a = 1.1 \times 10^{10}$ and $T_a = 7.2 \times 10^{10}$ respectively.

7.1.2. Initial and boundary conditions

The initial condition of the 2D multiphase TC flow is shown in Fig. 92. A thin layer of oil film (red) is put onto the circumference of the outer wall and will be driven by the rotating airflow (blue). The profiles of velocity, pressure, vorticity and viscosity are presented on the horizontal axis (y = 0) between ($-R_{outer} <= x <= -R_{inner}$), as indicated by the solid line L_1 (pink) in Fig. 92. The thickness of the oil film is h_{oil}. The initial condition of the multiphase TC flow is given by Eqs.(104) and (105) in Chapter 6. To make the pressure at the interface continuous, the initial pressure of the oil film is calculated by using ρ_{air} instead of ρ_{oil} in Eq. (105). The boundary condition is referred to in Section 3.6.1. It should be noted that in this case the gravity is not considered.

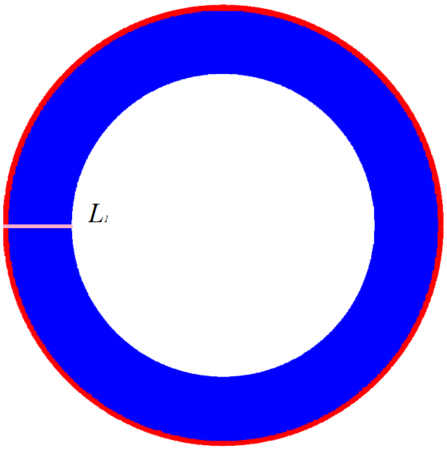

Fig. 92. Setup of 2D multiphase TC flow.

7.1.3. SPH and CFD model coefficients

Chapters 5 and 6 conclude that a combination of the particle collision shift model (CS) and density smoothing (δ-SPH) gives the best SPH results. The diffusive term in continuity equation has a direct effect on the pressure distribution, which becomes smoother. This combination of models is used in all SPH simulations with the mixing length (ML) and Spalart–Allmaras (SA) turbulence model presented in this chapter. This SPH approach is further denoted as SPH in this chapter. SPH is validated against Fluent, differing from the single-phase TC flow, the parameter setting of multiphase TC flow is more complex in Fluent. Following Adeniyi et al. [19] the $k - \omega$ SST model is used as the turbulence model. VOF and level-set models are applied to deal with interfaces. In this chapter, the continuum surface force proposed by Brackbill [39] is used in both SPH and Fluent. The surface tension coefficient is 0.032 *N/m* for the oil. The number of the orthogonal mesh in Fluent is 332298, while the number of particles of SPH is 242,142 in which the initial particle distance $\Delta x = 4 \times 10^{-4}\ m$.

The rest of the sections are organised as follows. Numerical results for the 2D turbulent multiphase TC flow at relatively low rotational speed are first presented in Section 7.2, while the result at relatively high rotational speed is in Section 7.3. Section 7.4 analyses the effects of the different rotational speeds of the inner shaft as well as the influence of the different turbulence models in SPH through the comparison with the results of Fluent. Finally, the main research findings are summarised in Section 7.5.

7.2. Multiphase Taylor–Couette flow at relatively lower rotational speed

In this section, the 2D turbulence multiphase flow at a relatively lower rotational speed is simulated with ML (SPH) and SA (SPH).

7.2.1. Simulation with mixing-length turbulence model

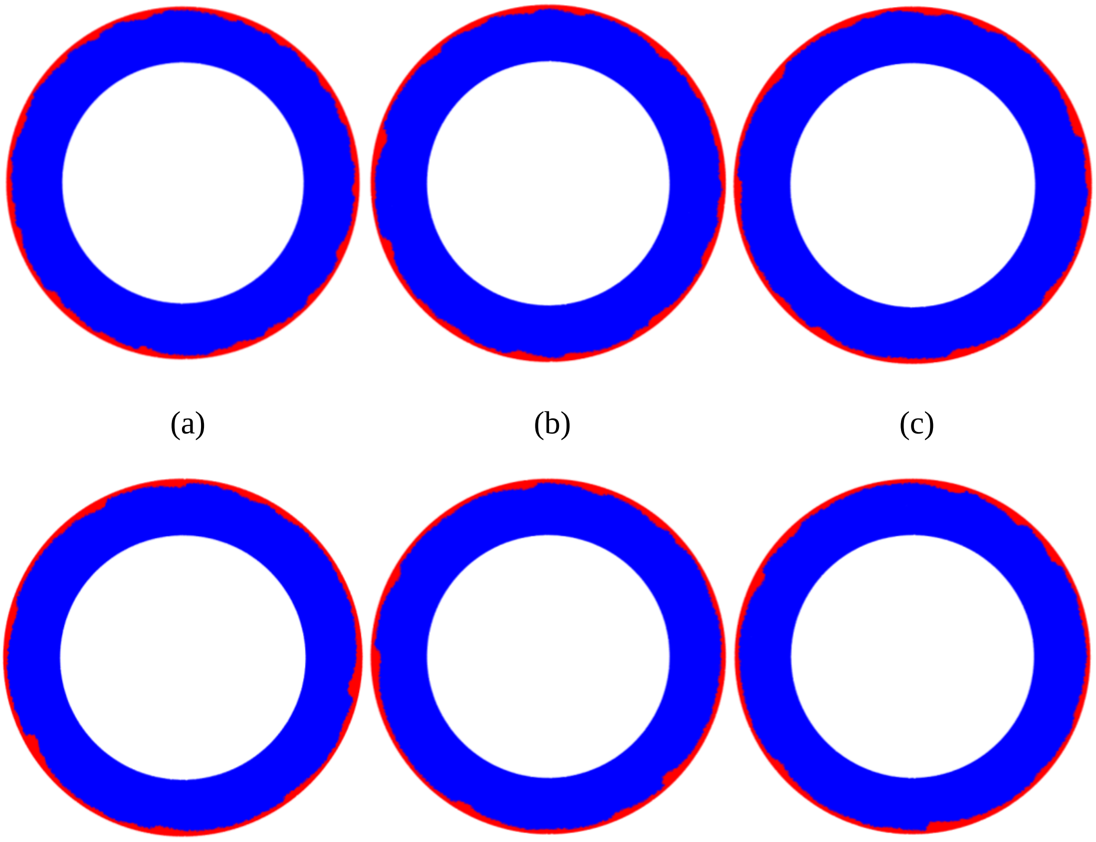

(a) (b) (c)

(d) (e) (f)

Fig. 93. Density distribution of ML (SPH). (a) 0.6 s, (b) 1.2 s, (c) 1.8 s, (d) 2.4 s, (e) 3.0 s, (f) 3.6 s.

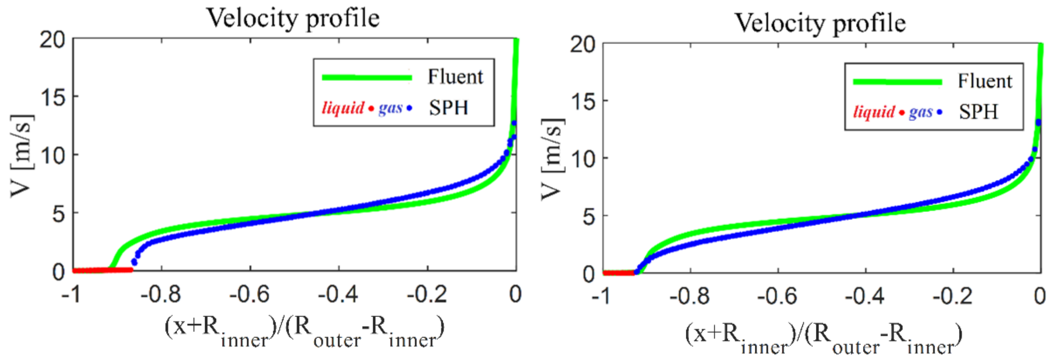

(a) (b)

Fig. 94. Velocity distribution of ML (SPH). (a) 1.8 s, (b) 3.6 s.

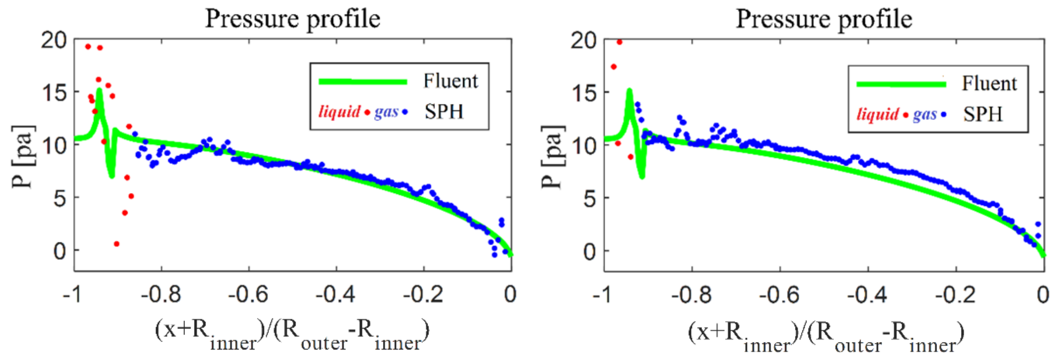

(a) (b)

Fig. 95. Pressure distribution of ML (SPH). (a) 1.8 s, (b) 3.6 s.

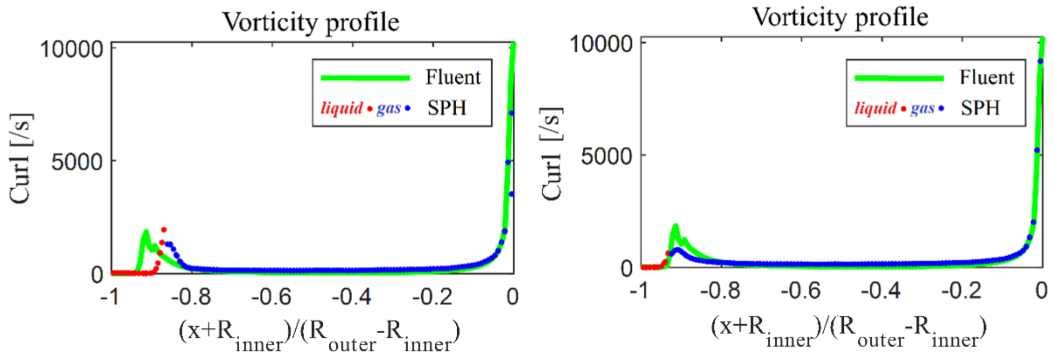

(a) (b)

Fig. 96. Vorticity distribution of ML (SPH). (a) 1.8 s, (b) 3.6 s.

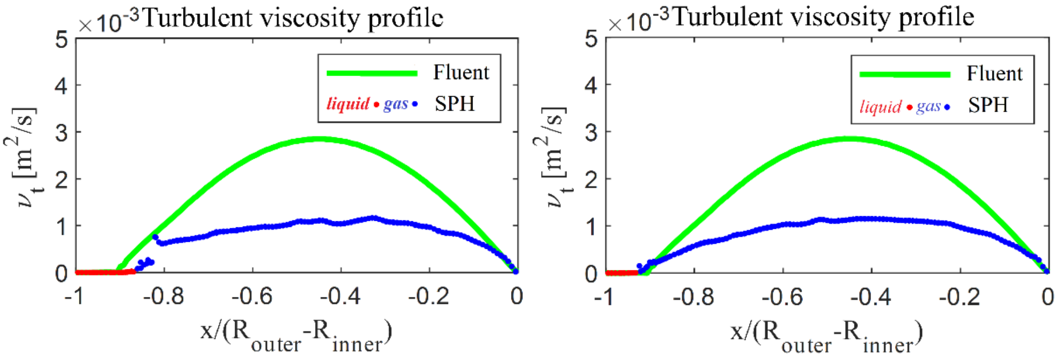

(a)

(b)

Fig. 97. Turbulent viscosity distribution of ML (SPH). (a) 1.8 s, (b) 3.6 s.

Fig. 93 shows the density distributions obtained with ML (SPH) at various instants from 0.6 s to 3.6 s. The development of the waveform can be seen in Fig. 93. Fig. 94 to 97 illustrate the comparison of the velocity, pressure, vorticity and viscosity profiles along the line L_1 of ML (SPH) and $k-\omega$ (Fluent) at different instants. Although the velocity profile of ML (SPH) is not as flat as that of $k-\omega$ (Fluent) in Fig. 94, it is still in good agreement with the results of $k-\omega$ (Fluent). As a consequence, the vorticity profile in Fig. 96 is comparable with the results of $k-\omega$ (Fluent). Considering the serious pressure fluctuations in the standard SPH method, the pressure profile in Fig. 95 is very smooth and similar to the results of $k-\omega$ (Fluent). However, as indicated in Fig. 97, the viscosity profile of ML (SPH) has a larger difference than that of $k-\omega$ (Fluent). The viscosity of ML (SPH) is almost half that of $k-\omega$ (Fluent). However, the effects of the two turbulence models on velocity and pressure are approximately the same, although the turbulence models applied to SPH and Fluent are different. Due to the differences in the turbulence models of SPH and Fluent, the difference in viscosity is acceptable. As the thickness of the oil film at the point (y = 0, x =$-R_{outer}$) will change with the movement and deformation of the oil film, the mixing length cannot be accurately obtained, especially with thicker oil films. This difference explains the discontinuity in the viscosity profile, as shown in Fig. 97 (a).

7.2.2. Simulation with the Spalart-Allmaras turbulence model

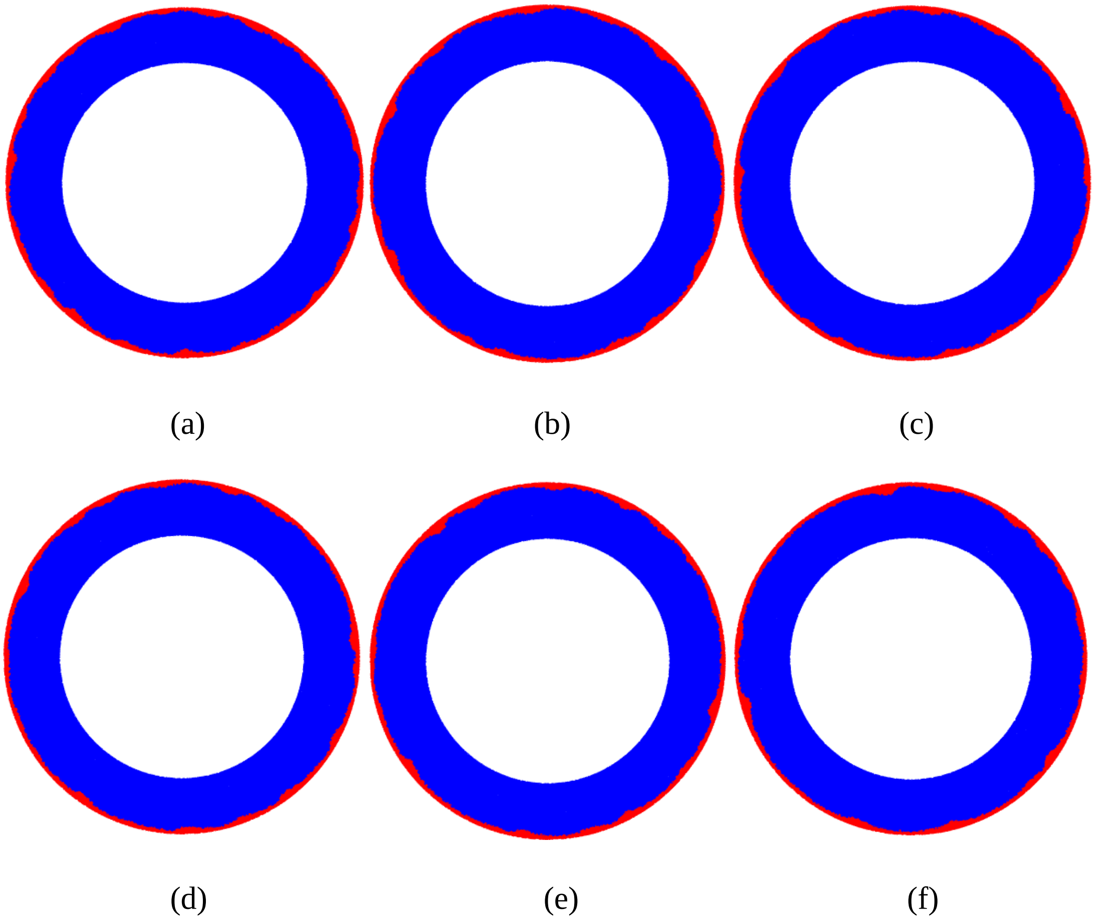

Fig. 98. Density distribution of SA (SPH). (a) 0.6 s, (b) 1.2 s, (c) 1.8 s, (d) 2.4 s, (e) 3.0 s, (f) 3.6 s.

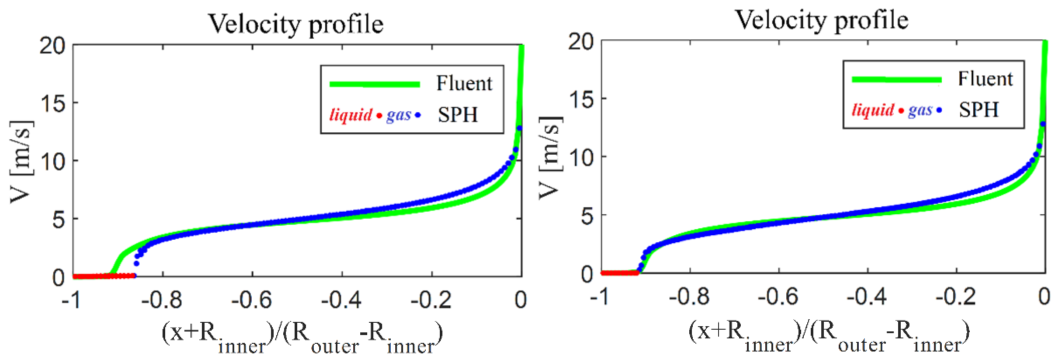

(a) (b)

Fig. 99. Velocity distribution of SA (SPH). (a) 1.8 s, (b) 3.6 s.

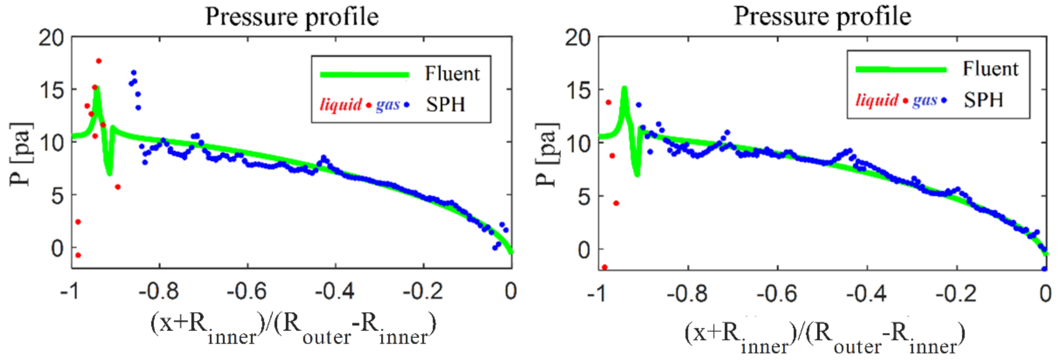

(a) (b)

Fig. 100. Pressure distribution of SA (SPH). (a) 1.8 s, (b) 3.6 s.

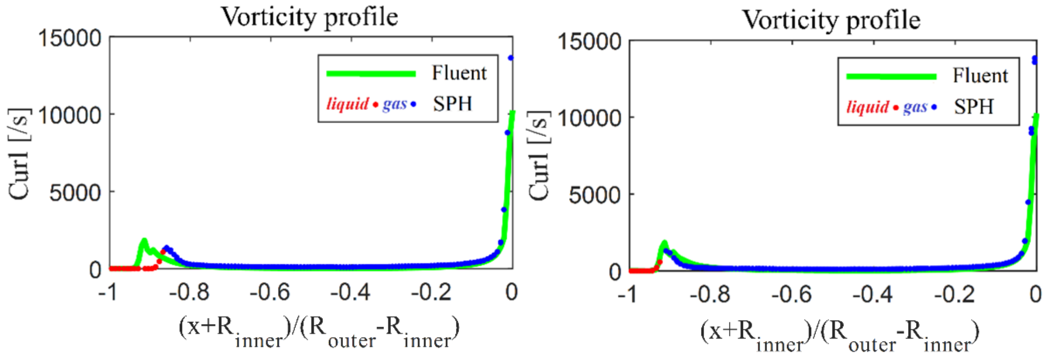

(a) (b)

Fig. 101 Vorticity distribution of SA (SPH). (a) 1.8 s, (b) 3.6 s.

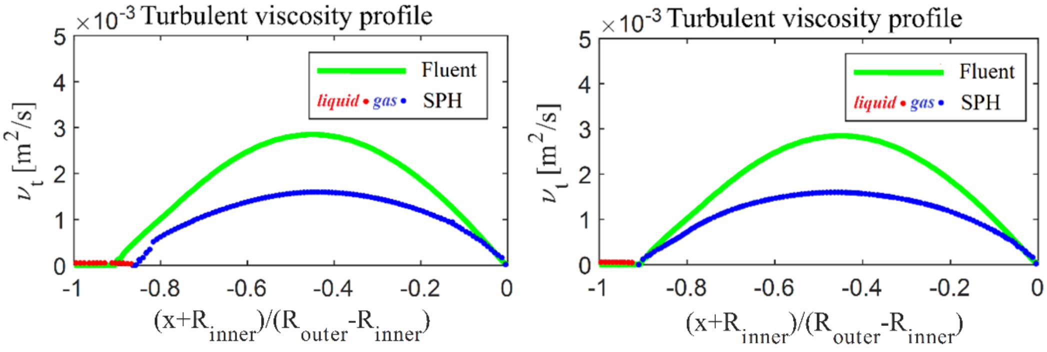

(a) (b)

Fig. 102. Turbulent viscosity distribution of SA (SPH). (a) 1.8 s, (b) 3.6 s.

Fig. 98 displays the density distribution of SA (SPH) at different instants, which closely resembles those of ML (SPH). In that the oil film moves along the outer wall driven by the airflow, the wavy oil film propagates along the wall with the wave speed. Simultaneously, the thickness of the oil film has also changed at the point (y = 0, x = $-R_{outer}$), and the height of the thickest and thinnest oil film of both ML and SA turbulence models is nearly the same. Fig. 99 to 101 show the velocity, pressure, vorticity and viscosity profiles along the line L_1 obtained with SA (SPH) at 1.8 s (thicker oil thickness) and 3.6s (thinner oil thickness). These simulation results are identical to those of ML (SPH) and $k-\omega$ (Fluent).

Fig. 102 shows the viscosity profiles at different instants. Similar to the viscosity of ML (SPH), the viscosity of SA (SPH) is still half the viscosity of $k-\omega$ (Fluent). Differing from the ML (SPH), the instability and discontinuity at the interface of the viscosity are absent in the profile obtained with SA (SPH). As shown in Fig. 102, the viscosity profile of SA (SPH) is stable, even at the interface. The modest improvement in viscosity makes the velocity profile slightly closer to that of $k-\omega$ (Fluent) than ML (SPH). The impact of the thickness of the oil film can be ignored with SA. The distance to the interface dominates the turbulent viscosity in the ML model. However, in SA, the distance to the interface is not that vital, so the error in the distance to the interface caused by the change of the oil film is acceptable.

7.3. Multiphase Taylor–Couette flow at a relatively higher rotational speed

To study the stability of the SPH and the adaptability of the turbulence models (SA and ML) at a higher rotational speed, the multiphase turbulent flow generated by the higher rotational speed of the inner shaft in the bearing chamber will be simulated. Due to the increased rotational speed, the simulation time has decreased to 1.44 s.

7.3.1. Simulation with mixing length turbulence model

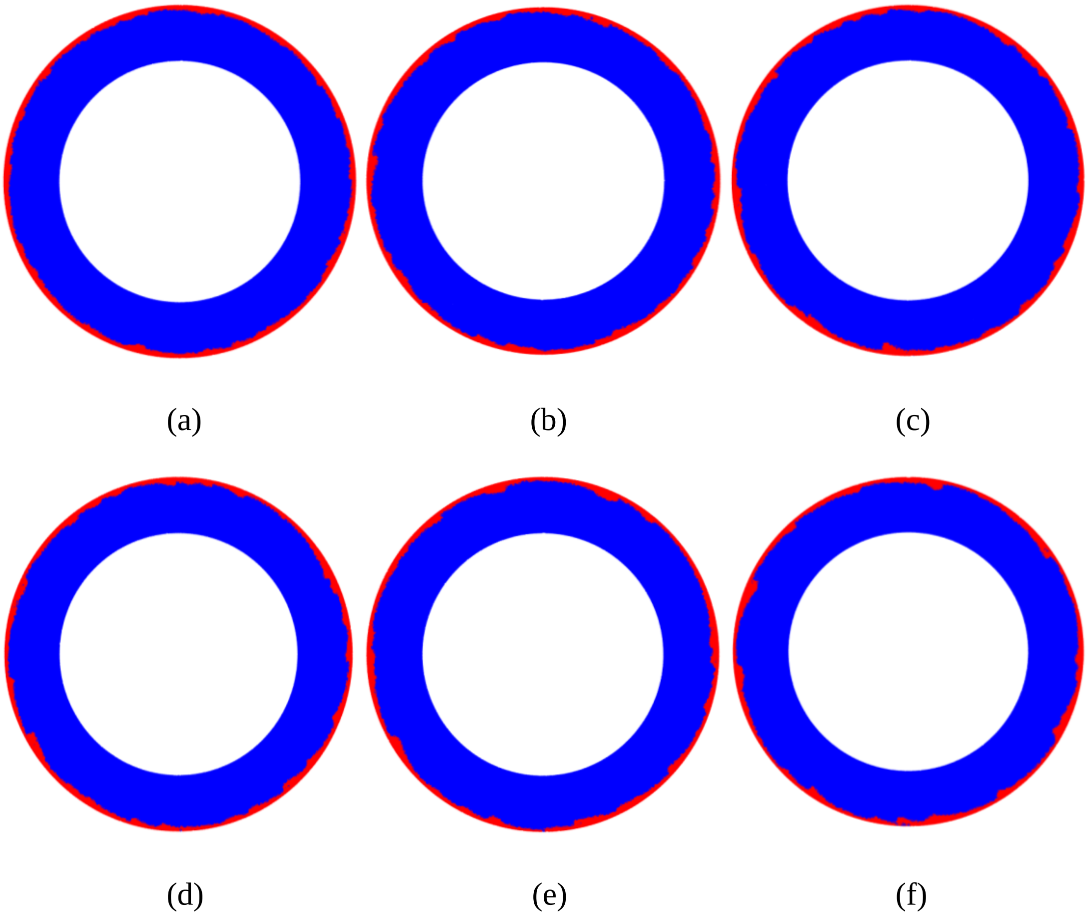

(a) (b) (c)

(d) (e) (f)

Fig. 103. Density distribution of ML (SPH). (a) 0.24 s, (b) 0.48 s, (c) 0.72 s, (d) 0.96 s, (e) 1.2 s, (f) 1.44 s.

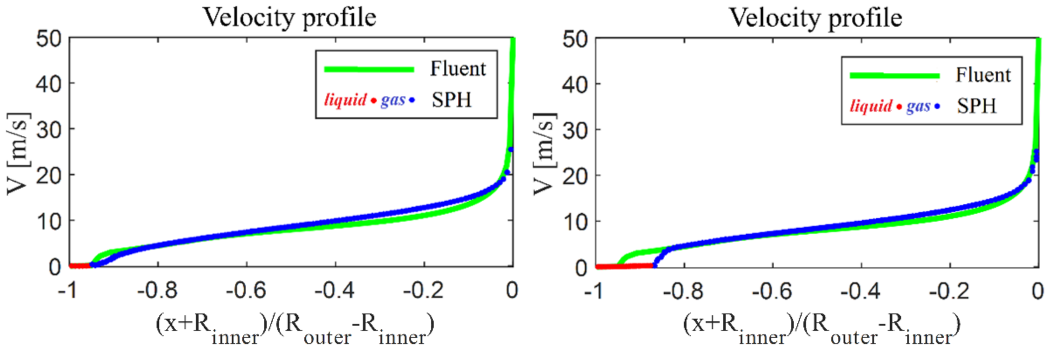

(a) (b)

Fig. 104. Velocity distribution of ML (SPH). (a) 0.72 s, (b) 1.44 s.

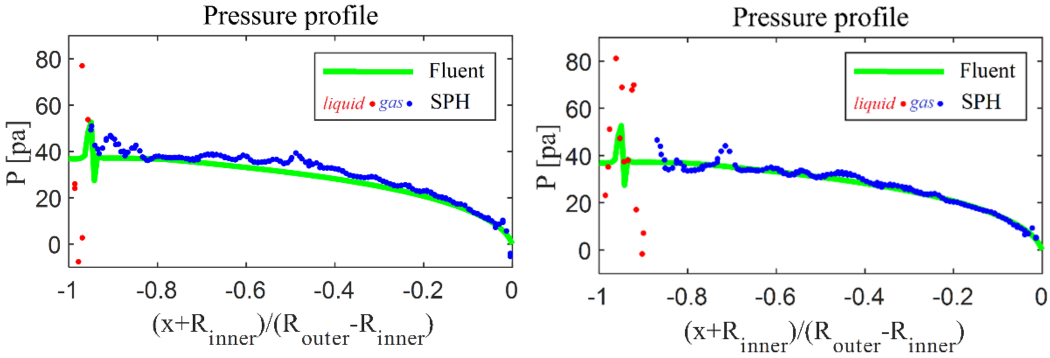

(a) (b)

Fig. 105. Pressure distribution of ML (SPH). (a) 0.72 s, (b) 1.44 s.

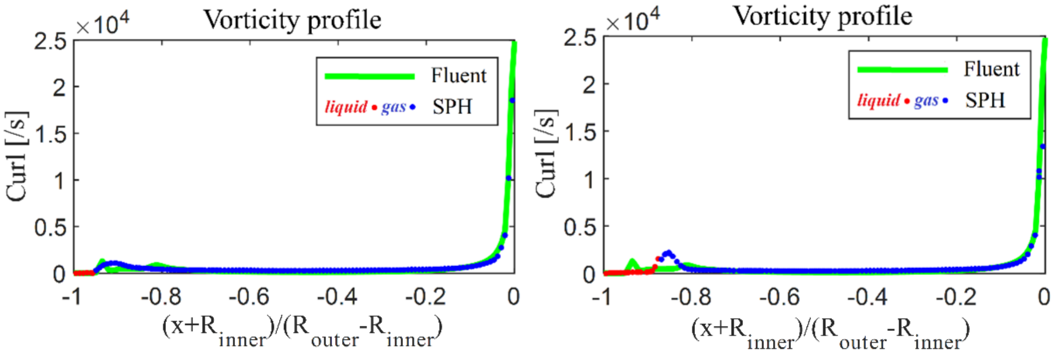

(a) (b)

Fig. 106. Vorticity distribution of ML (SPH). (a) 0.72 s, (b) 1.44 s.

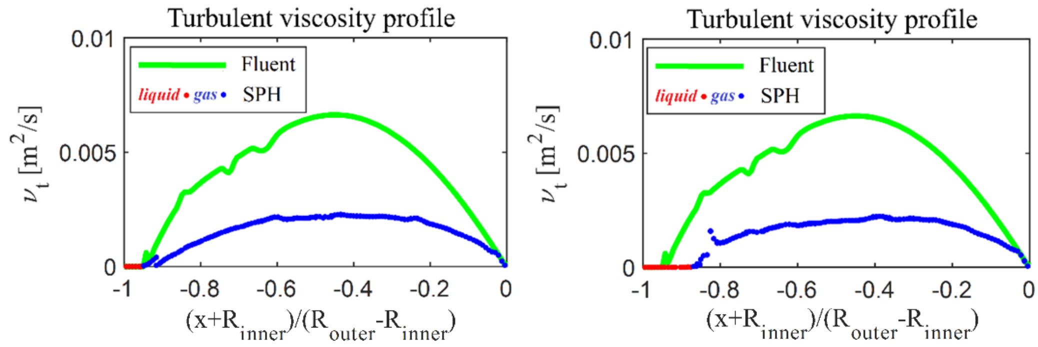

(a) (b)

Fig. 107. Turbulent viscosity distribution of ML (SPH). (a) 0.72 s, (b) 1.44 s.

Fig. 103 shows the density distributions obtained with ML (SPH) at different instants, from 0.12 s to 1.44s. The waveform of the oil film develops from a small to a large amplitude and the air will be rolled into the oil film. Fig. 104 to 106 illustrate the velocity, pressure and vorticity profile at a high rotation speed at two instants. Since the speed has been increased by 2.5 times, the velocity, pressure and vorticity have also been increased accordingly. Similar to the profiles obtained with ML (SPH) at a low rotation speed, the profiles of velocity, pressure and vorticity at a high rotation speed are also identical to $k - \omega$ (Fluent). Fig. 107 displays the viscosity profiles of ML (SPH) and $k - \omega$ (Fluent). The viscosity of ML (SPH) at a high rotation speed is similar to that at a low rotation speed. The small fluctuations and discontinuities at the interface also exist. However, the viscosity of $k - \omega$ (Fluent) also shows the instability.

7.3.2. Simulation with the Spalart-Allmaras turbulence model

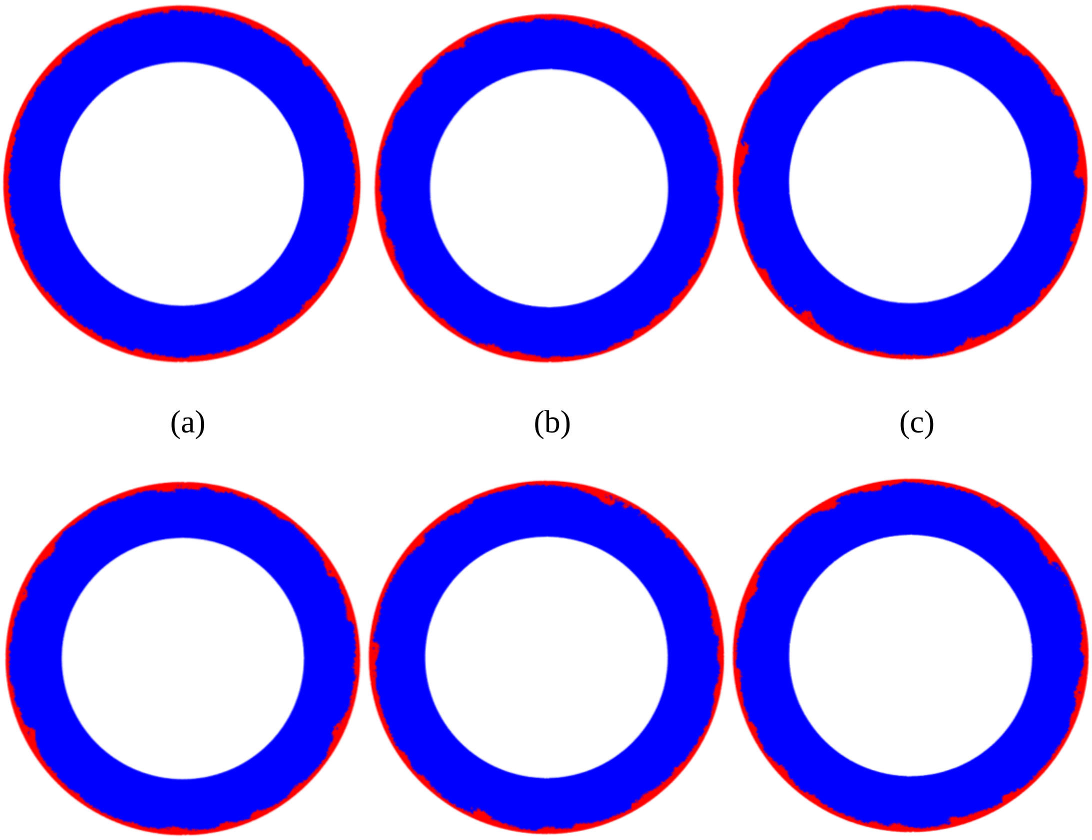
(a) (b) (c)

(d) (e) (f)

Fig. 108. Density distribution of SA (SPH). (a) 0.24 s, (b) 0.48 s, (c) 0.72 s, (d) 0.96 s, (e) 1.2 s, (f) 1.44 s.

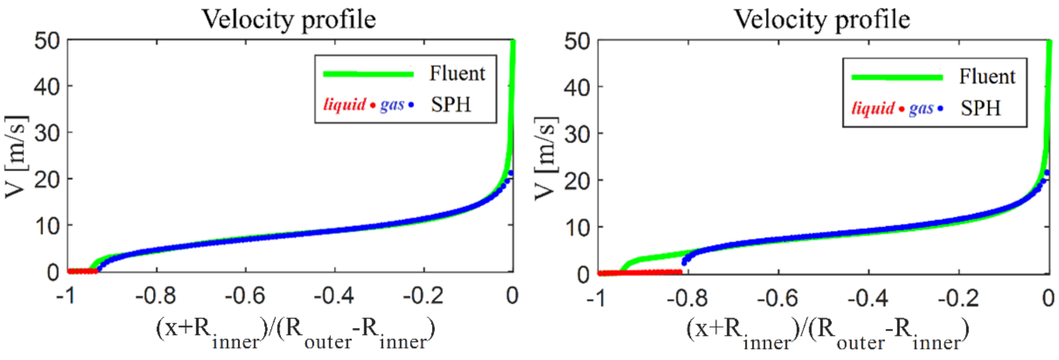

(a) (b)

Fig. 109. Velocity distribution of SA (SPH). (a) 0.72 s, (b) 1.44 s.

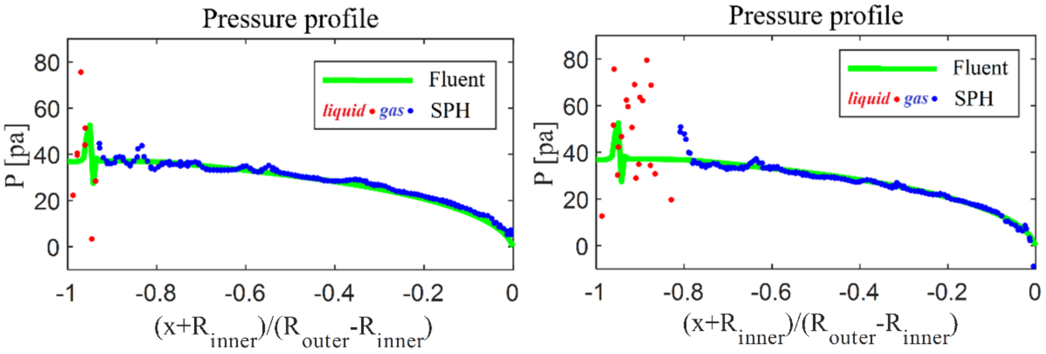

(a) (b)

Fig. 110. Pressure distribution of SA (SPH). (a) 0.72 s, (b) 1.44 s.

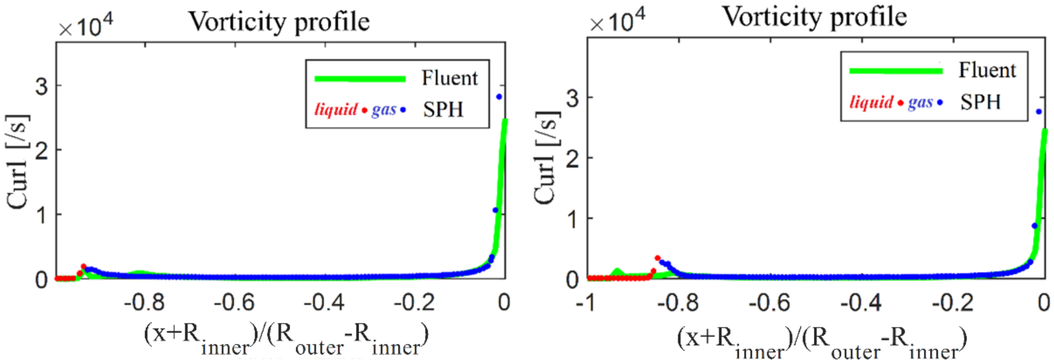

(a) (b)

Fig. 111. Vorticity distribution of SA (SPH). (a) 0.72 s, (b) 1.44 s.

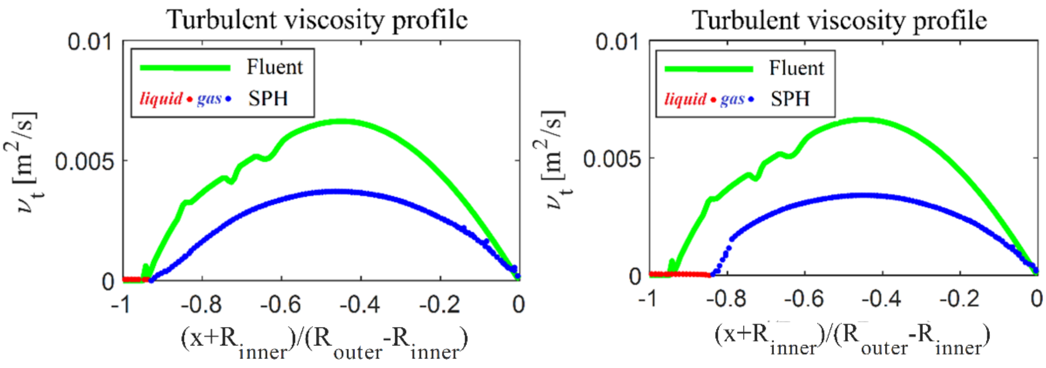

(a) (b)

Fig. 112. Turbulent viscosity distribution of SA (SPH). (a) 0.72 s, (b) 1.44 s.

Fig. 108 illustrates the density distribution obtained with SA (SPH) at different instants, from 0.12 s to 1.44 s. The development of the waveform is analogous to that of SA (SPH). The rolling of the oil film is also shown in Fig.108, which is not seen at a low rotation speed. Fig. 109 to Fig. 112 show the comparison between SA (SPH) and $k-\omega$ (Fluent) in terms of the velocity, pressure, vorticity and viscosity profile. Except for the viscosity profile, the other profiles of SA (SPH) are perfectly consistent with those of $k-\omega$ (Fluent). The viscosity of SA (SPH) is more stable than that of ML (SPH), which is already proven at the low rotation speed.

7.4. Analysis of results

In the two sections above, the results of SPH at line L_1 are compared with those of Fluent. To assess the results of the whole fluid domain, the density, pressure and velocity distribution obtained with SPH are compared with the results of Fluent in this section.

7.4.1. Relatively lower rotation speed

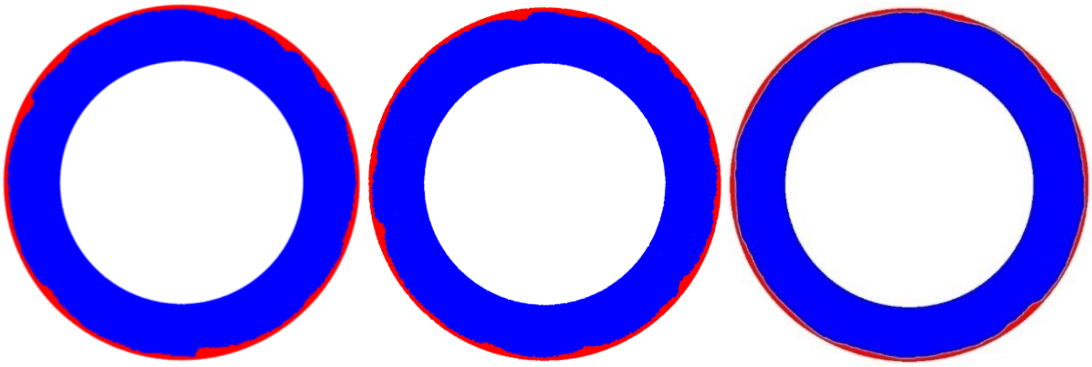

(a) (b) (c)

Fig. 113 . Density distribution. (a) ML (SPH), (b) SA (SPH), (c) $k-\omega$ (Fluent).

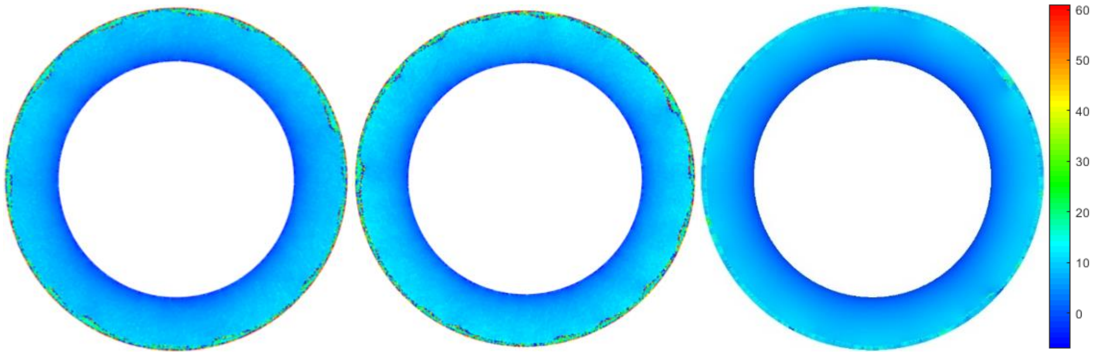

(a) (b) (c)

Fig. 114 . Pressure distribution. (a) ML (SPH), (b) SA (SPH), (c) $k-\omega$ (Fluent).

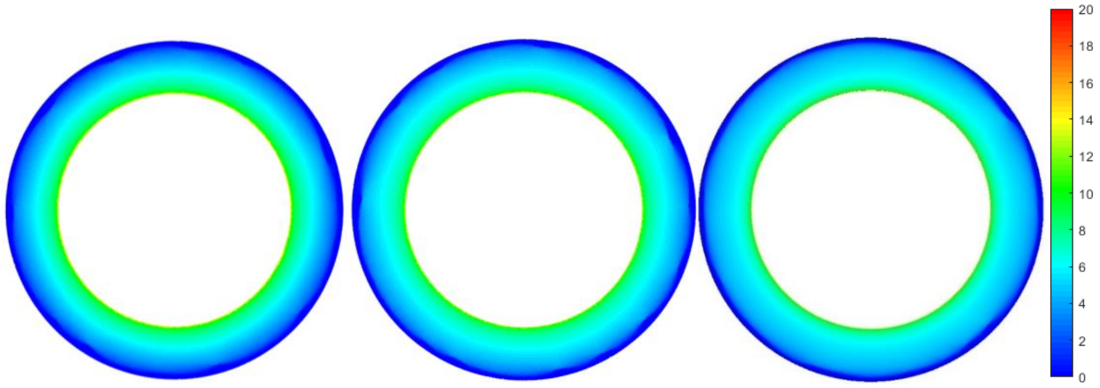

(a) (b) (c)

Fig. 115 . Velocity distribution. (a) ML (SPH), (b)SA (SPH), (c) $k-\omega$ (Fluent).

Fig. 113 depicts the density distribution obtained with ML (SPH), SA (SPH) and $k-\omega$ (Fluent). The waveform of SPH is comparable to that of Fluent. Figs. 114 and 115 illustrate the pressure and velocity distribution of ML (SPH), SA (SPH) and $k-\omega$ (Fluent). Both the pressure and velocity distribution of ML (SPH) and SA (SPH) are roughly the same as those of $k-\omega$ (Fluent). Although the pressure fluctuation of SPH is larger than that of Fluent, the interface is still quite stable, indicating that SPH is suitable for multiphase flow.

7.4.2. Relatively higher rotation speed

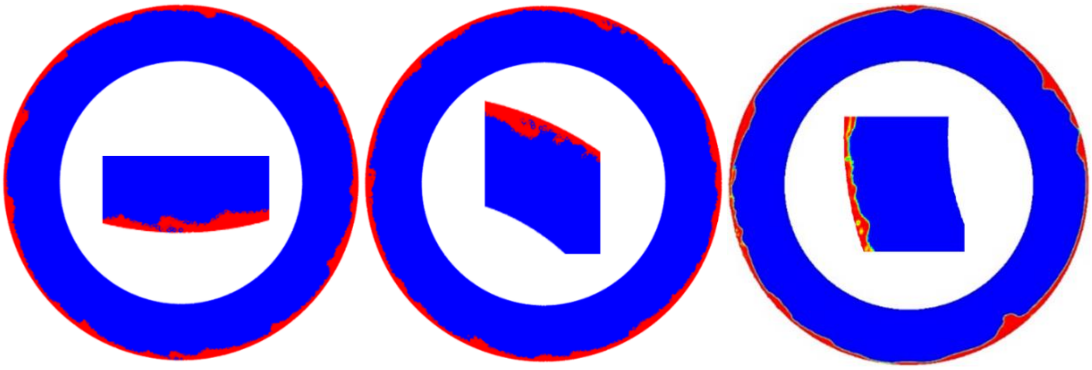

(a) (b) (c)

Fig. 116 . Density distribution. (a) ML (SPH), (b) SA (SPH), (c) $k-\omega$ (Fluent).

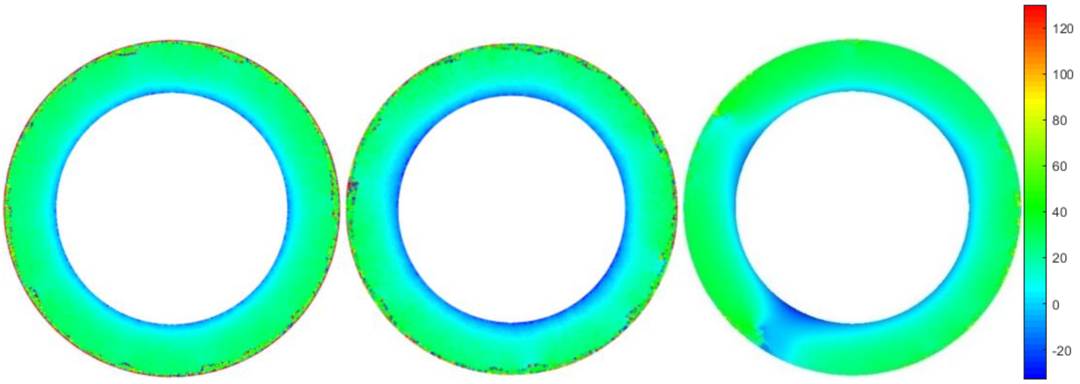

(a) (b) (c)

Fig. 117 . Pressure distribution. (a) ML (SPH), (b) SA (SPH), (c) $k-\omega$ (Fluent).

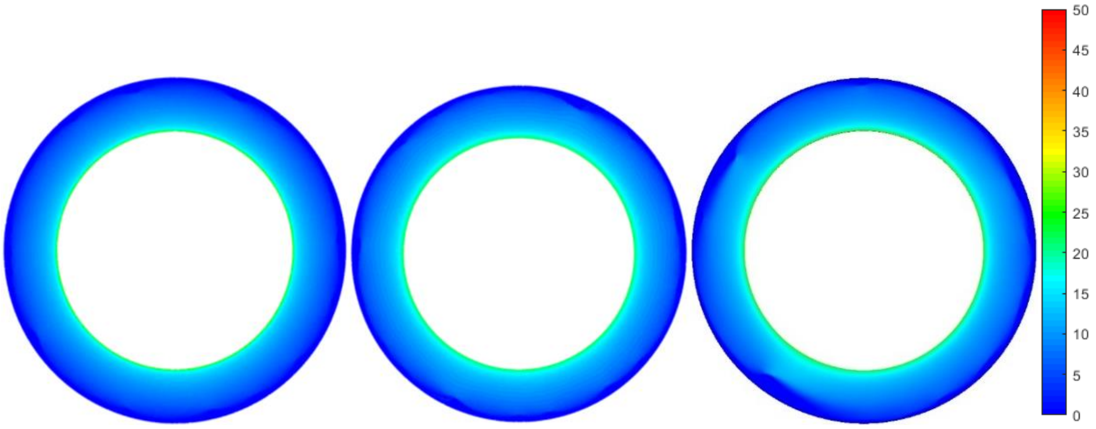

(a) (b) (c)

Fig. 118 . Velocity distribution. (a) ML (SPH), (b)SA (SPH), (c) $k-\omega$ (Fluent).

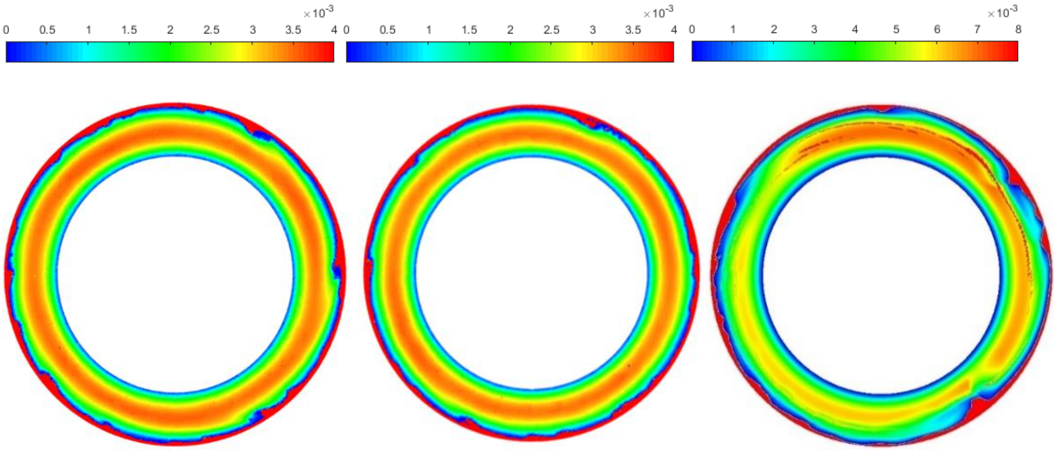

(a) (b) (c)

Fig. 119 . Turbulent viscosity distribution. (a) ML (SPH), (b)SA (SPH), (c) $k-\omega$ (Fluent).

Figs. 116 to 119 display the density, pressure, velocity and viscosity distribution at a high rotation speed obtained with ML (SPH), SA (SPH) and $k-\omega$ (Fluent). The results of these three methods are similar. With the speed of the inner shaft increased, the velocity and pressure also rose as well as the amplitude of the waveform. This process leads to some air being rolled into the oil film, as shown in Fig. 116. This phenomenon is not seen at low rotation speeds. In addition, the wave-rolling is captured by the VOF and LS models in Fluent, while only collision shift is used for the interface in the SPH method. The collision shift model is much simpler and computationally cheaper during the simulation. Fig.119 shows the viscosity distribution obtained with ML (SPH), SA (SPH) and $k - \omega$ (Fluent) at a high rotation speed. The viscosity distribution of ML (SPH), SA (SPH) is more stable than that of $k - \omega$ (Fluent), which is consistent with the viscosity profile in Fig. 112 in Section 7.3.2. Notably, there is a discontinuity in the pressure, as shown in Fig. 118(c), which can be resolved by reducing the time step in which the air rolls in a very thin oil film.

7.5. Summary

In this chapter, the two-dimensional multiphase Taylor–Couette flow is modelled using the hybrid SPH method, which is a combination of δ-SPH and the particle-collision shift model. Simulations are performed at two different rotational speeds of the inner shaft whilst the outer wall is fixed.

The SPH simulations were conducted under multiphase turbulent flow conditions with the mixing length (ML) turbulence model and the Spalart–Allmaras turbulence (SA) model as well as the surface tension model. Following [19], the results of the Fluent with *k*-*ω* turbulence model, volume of fluid (VOF), level-set (LS) model and the same surface-tension model are used to validate the results of the SPH simulation.

Differing from the single-phase 2D TC flow, the oil film will move along the outer wall with deformation. The simulation results are performed along a horizontal line (y = 0 on the horizontal axis (y = 0) between ($-R_{outer}$ < = x < = $-R_{inner}$)) as well as in the whole-fluid domain.

The SPH results for the configuration with a relatively low rotational speed show a reasonable match with Fluent. The oil moves along the outer wall, and the waveforms of SA and ML are quite similar. The pressure velocity and vorticity profiles obtained with ML and SA are roughly the same and are in good agreement with Fluent. Furthermore, the velocity profile of SA is closer to that of Fluent than ML. The turbulent viscosity profile of ML fluctuates and shows values about half of those of Fluent, while the result of SA is smoother, with almost the same values as ML. Here, the profiles of velocity, pressure and vorticity will have slight changes at different instants under the influence of the movement of the oil film. The influence of the movement of oil film is greater in the viscosity profile obtained with ML. When the thickness of oil film at the point ($-R_{outer}$, 0) is quite different from the initial value, the viscosity profile obtained with ML shows a visible discontinuity around the interface. However, this kind of discontinuity can be avoided using SA.

The SPH results for the configuration with a relatively high rotation speed show a similar match with Fluent. A higher amplitude waveform is obtained with SA and ML, and some air will be involved in the oil film. The pressure, velocity and vorticity profiles of SA and ML are now closer to those of Fluent. Similar to the viscosity profile at relative lower rotational speed, the value of viscosity of ML and SA is still half of

$k - \omega$ (Fluent). Moreover, there are still discontinuities in the viscosity profile of ML at the interface, which can still be prevented by SA. Varying from the viscosity profile at relative lower rotational speed, the viscosity of Fluent becomes unstable, and the fluctuation is even larger than ML, while the that of SA maintains its stability at the relatively high rotation speed. This finding might indicate that the stability of the high-rotation-speed multiphase flow is an advantage of the SPH method.

At both rotational speeds, the density, velocity and pressure distributions of the entire flow field obtained with ML(SPH), SA(SPH) and $k - \omega$ (Fluent) are almost the same. The rolling of the oil film can be well captured at a high rotation speed. Only the airflow between the two concentric circles is turbulent, while the oil film remains laminar at a very low velocity. The pressure fluctuations at the interface of SPH are also shown in the results of Fluent. Although the fluctuation of SPH is larger, the interface is still not clustering. Differing from Fluent, SPH can capture the interface without VOF and LS models, which is another advantage of the SPH method.

In conclusion, although the turbulence model in SPH differs from Fluent, the velocity and pressure are almost identical. This finding demonstrates that the turbulence model in SPH is effective for the multiphase turbulent TC flow. Due to the viscosity of SA is more stable, only SA (SPH) will be used for the multiphase turbulent flow in the bearing chamber, in the next chapter.

Chapter 8 Turbulent flow in a simplified bearing chamber

In the previous chapters, the Taylor–Couette (TC) case is examined under 2D multiphase turbulent flow conditions. In this chapter, the TC case is extended to a simplified bearing chamber, which is accomplished by adding a sump pipe. The suction effect of the pipe is taken into account by including gravitation. First a bearing chamber in 2D is examined, as a next step in the TC case (without gravitation) in 3D, and finally, the bearing chamber in 3D. The cases in this chapter are simulated with the particle-collision shift model (CS) in combination with δ-SPH, exactly as in the previous chapters. This combination of SPH models is further denoted as SPH and compared with the Fluent. In 3D TC case, this combination of SPH models is compared with standard WCSPH (Section 8.3.1).

8.1. Case description

8.1.1. Case setup

The 2D simplified bearing chamber consists of two concentric circles and one sump pipe, as shown in Fig. 120. The dimensions of the bearing chamber is the same as those in 2D TC flow.

SPH simulations performed at real rotational speeds on the order of 15,000 rpm appear to be quite challenging [23]. In that case, very small timesteps are needed, as well as a high artificial wave speed and very thin oil films. The very thin oil films require a high particle resolution. For these reasons, a lower rotational speed is chosen to allow for larger timesteps, whilst a higher film thickness is selected. The rotational speed of the shaft is scaled down from 15,000 rpm to ω_{inner}^{low} rpm. In a real case with high rotational speeds, the effect of gravity is relatively low compared to the centrifugal effects. For this reason, the gravitational acceleration is scaled down from 9.81 m/s^2 to 0.02 m/s^2. In addition, the thickness of the oil film is scaled up from $h_{oil} = 1.9 \times 10^{-4}$ m to h_{oil} . The scaling of the above three parameters is done in such a way that the ratio of shear and gravitational forces remains the same. For details of the scaling, it is referred to Kruisbrink [134].

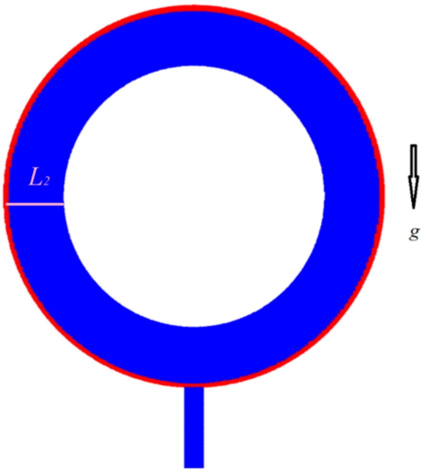

Fig. 120. Initial state of 2D turbulent multiphase flow in a bearing chamber.

8.1.2. Initial and boundary conditions

At the initial stage, a thin layer of oil film (red) is placed on the circumference of the outer wall, including the top of the sump pipe, which will be driven by the rotation airflow (blue) and moved into the sump pipe under gravity. In the chamber, oil is injected from the inner rotating shaft. Similar to the 2D multiphase TC flow, the initial condition is given by Eqs. (104) and (105).

8.1.3. SPH and CFD models and model coefficients

The SPH and CFD models used in this chapter are the same as those in Chapter 7. As a surface tension model, the continuum surface force model [39] is used here for both SPH and Fluent. The surface tension coefficient is 0.032 *N/m*. The SPH and CFD models' coefficients are described in Section 6.1.3.

8.2. Two-dimensional turbulent multiphase flow in bearing chamber

In this section, the 2D turbulence multiphase flow in the bearing chamber is simulated with SA (SPH). The rotation of the inner shaft is clockwise.

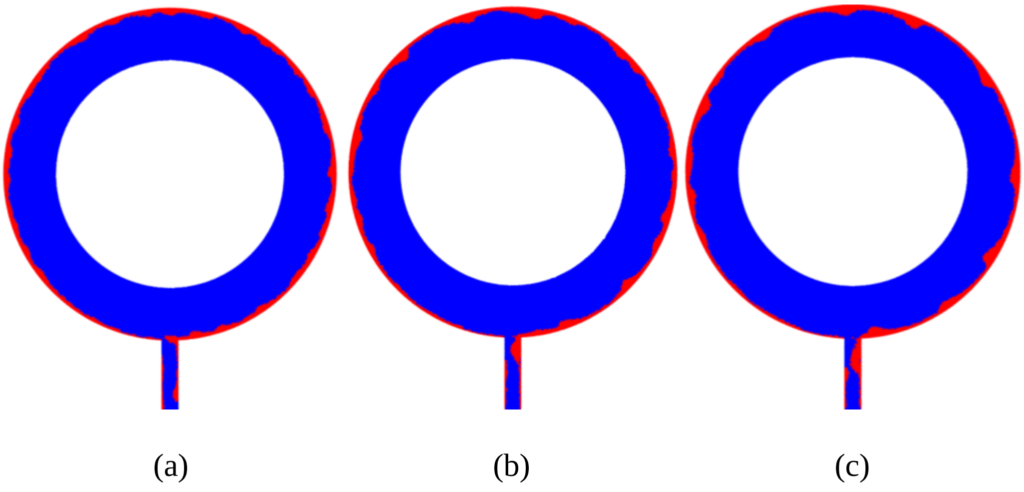
(a) (b) (c)

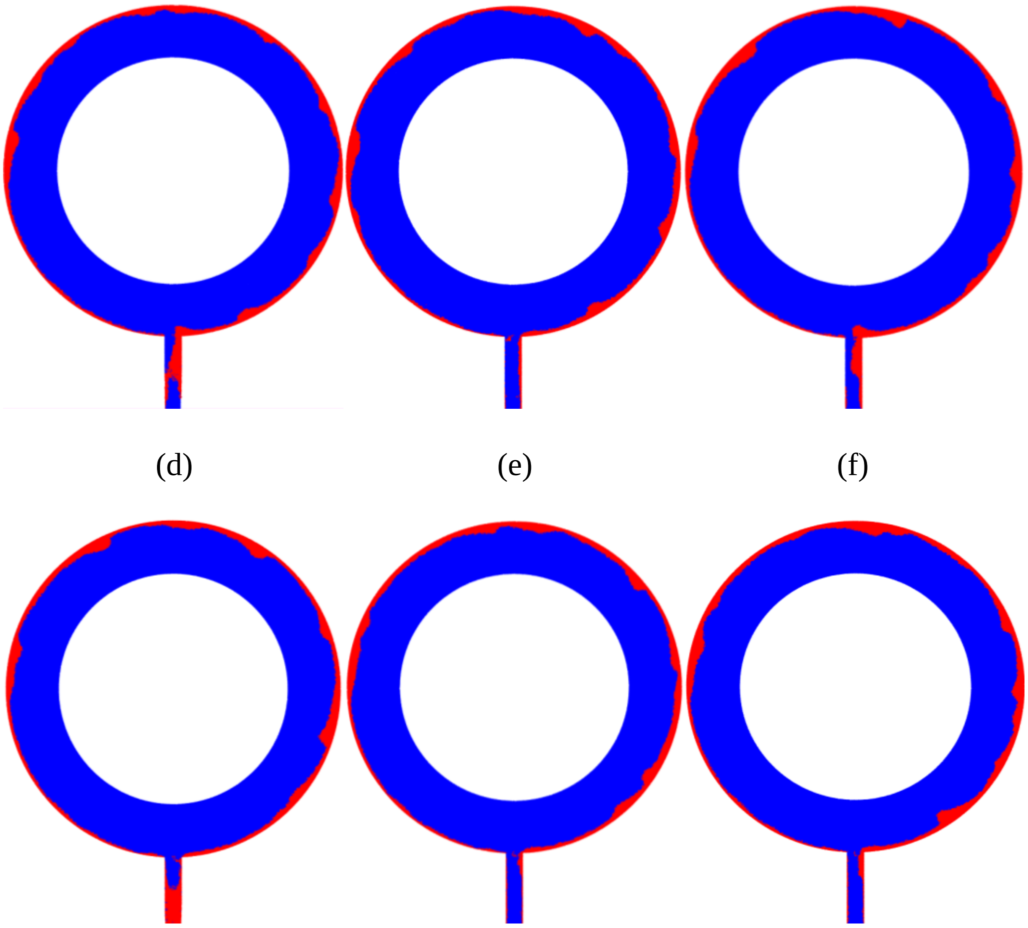

(d) (e) (f)

(g) (h) (i)

Fig. 121. Evolution of the multiphase turbulent flow in the simplified two-dimensional bearing chamber (thicker oil film) at instants (a) 0.3 s, (b) 0.6 s, (c) 0.9 s, (d) 1.2 s, (e) 1.5 s, (f) 1.8 s, (g) 2.1 s, (h) 2.4 s, (i) 2.7, together with the density distribution of SA (SPH).

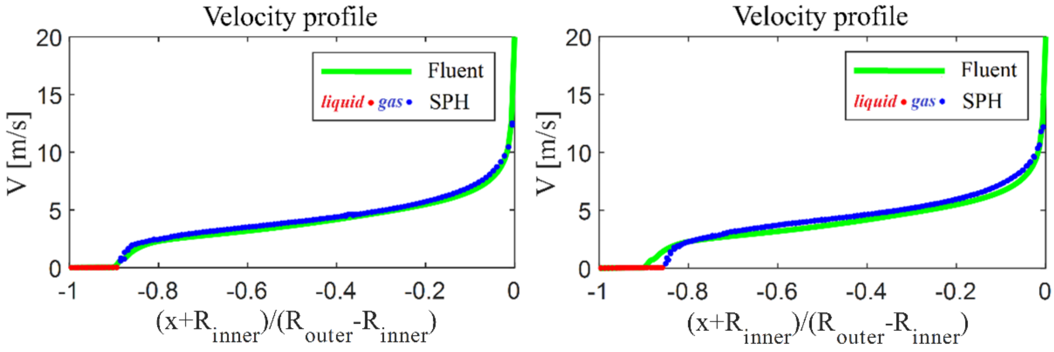

(a) (b)

Fig. 122 Velocity profiles of SA (SPH). (a) 1.8 s, (b) 3.0 s.

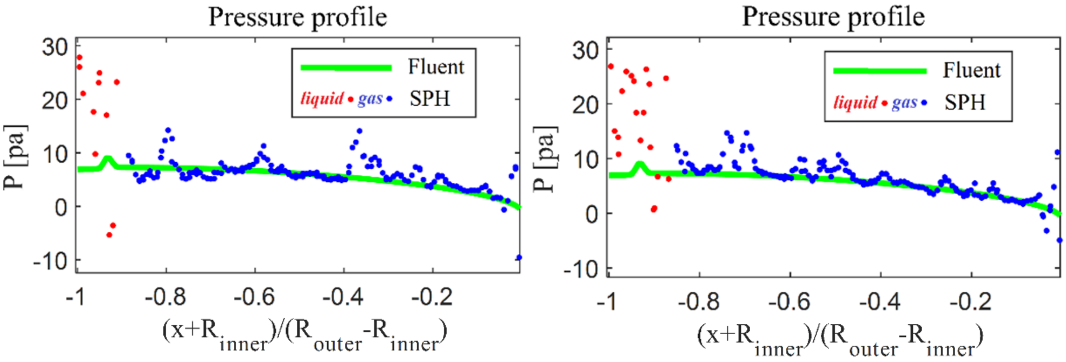

(a) (b)

Fig. 123 Pressure profiles of SA (SPH). (a) 1.8 s, (b) 3.0 s.

Fig. 121 displays the evolution of the turbulent flow in the bearing chamber from t = 0.3 s to t =2.7 s. Under the action of gravity and shear force from the air flow, the oil film not only rotates along the outer wall but also discharges from the bearing chamber along the sump pipe. When the simulation starts, the oil film above the pipe descends along the pipe. The remainder of the oil will then move clockwise, driven by the air. Regarding the oil on the chamber wall, some on the right side of the chamber wall will move through the gap to the left side of the chamber wall, and the rest of the oil will move into the sump pipe. Oil entering the pipeline will flow out of the outlet. The waveform amplitude remains similar to that of a 2D TC flow. Fig. 122 and Fig.

123 illustrate the velocity and pressure profiles along the line L_2 obtained with SA (SPH) and *k*-*ω* (Fluent) at two different moments. The velocity profile of SA (SPH) is almost identical to that of Fluent, and quite close to that in the 2D turbulent multiphase TC flow (Section 7.3.1.2). However, the pressure profile in the bearing chamber is not as smooth as that in 2D turbulent multiphase TC flow (Section 7.3.1.2). As shown in Fig. 123, though the trend of the pressure of SA (SPH) is the same as that of *k*-*ω* (Fluent), the pressure of SA (SPH) exhibits more fluctuation.

8.3. Three-dimensional multiphase turbulent flow

The turbulence model in the 2D multiphase flow in the bearing chamber is verified in the section above. In this section, to validate the turbulence model in the 3D case, SA (SPH) is used to simulate a 3D multiphase turbulent Taylor–Couette flow (without gravitation) and a 3D turbulent flow in the bearing chamber. For the particles will move across the side wall, their velocity component perpendicular to the side wall will be reversed to prevent the particle penetration.

8.3.1. Three-dimensional multiphase turbulent Taylor–Couette flow

A 3D TC multiphase flow is presented here. The initial particle distance is $\Delta x = 0.001$. In this case, all the parameters are the same as the 2D multiphase turbulent TC flow. w is the width (z direction) of the 3D TC flow.

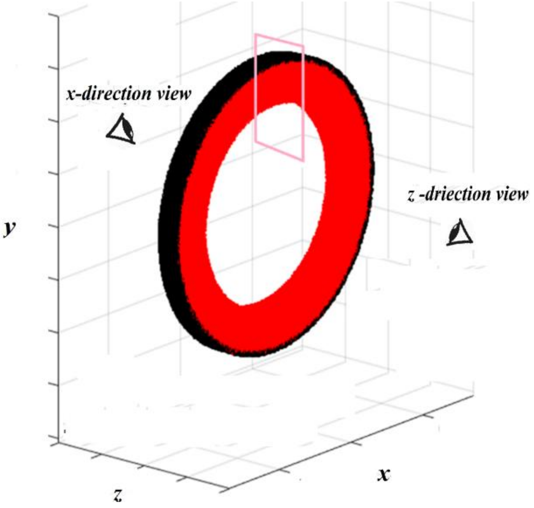

Fig. 124. Setup of the 3D TC flow.

Fig. 124 shows the setup of the 3D TC flow. In the three-dimensional case, the particle distribution is difficult to observe. For the convenience of checking the particle distribution, two sections are chosen for observation. The first section is taken up by the pink rectangle in Fig. 124, which is located at x = 0.

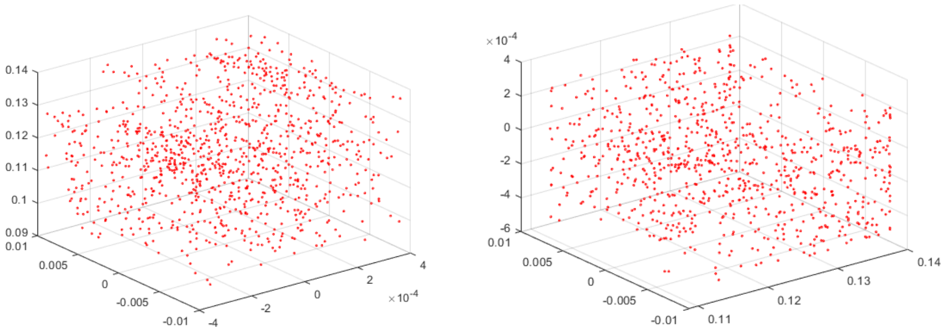

(a)

(b)

Fig. 125. Particle distribution around the first section at t = 0.007 s. (a) standard WCSPH, (b) SPH.

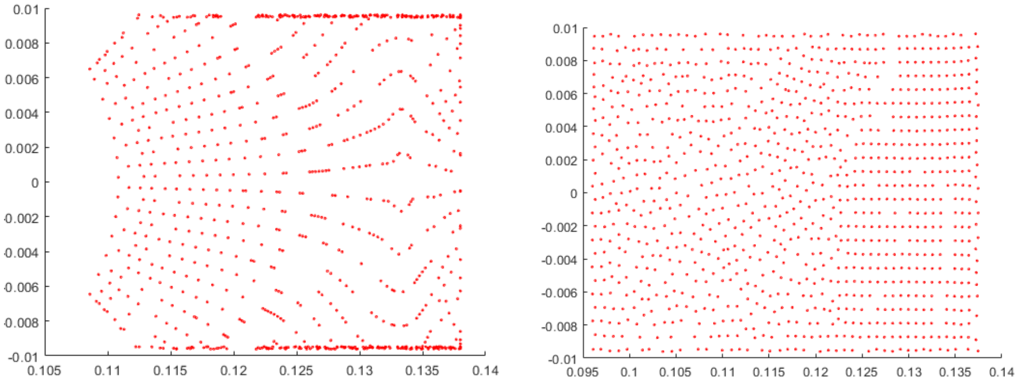

(a) (b)

Fig. 126. X-direction view of Fig. 125. (a) standard WCSPH, (b) SPH.

Fig. 125 illustrates the particle distribution around this section at t = 0.007 s. Fig. 126 depicts an x-direction view of the particle distribution in Fig. 125. With standard WCSPH, the particle suffers serious clustering, as shown in Fig. 126(a). With SPH, the particle distribution remains stable. The second section is taken up by the concentric circles section located at z = 0. Fig. 127 shows the particle distribution around this section.

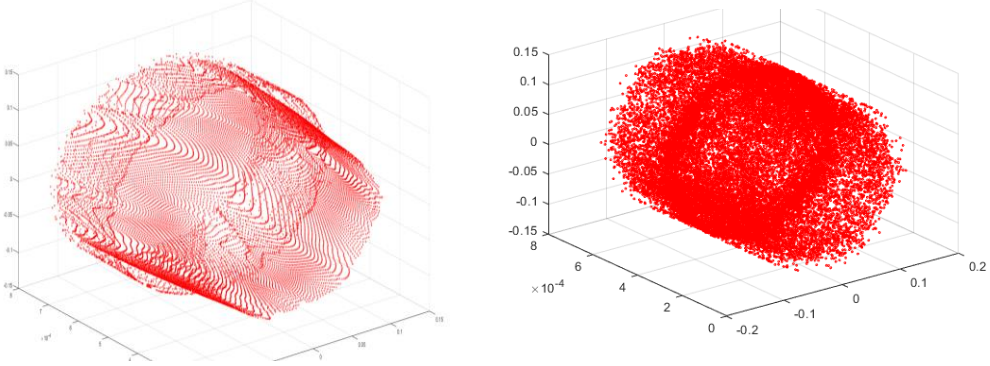

(a) (b)

Fig. 127. Particle distribution around the second section at t = 0.007 s. (a) standard WCSPH and (b) SPH.

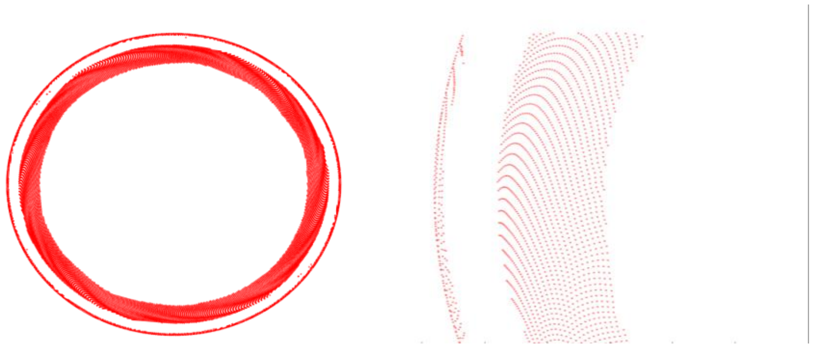

(a) (b)

Fig. 128. Z-direction view of Fig. 127(a) and detail.

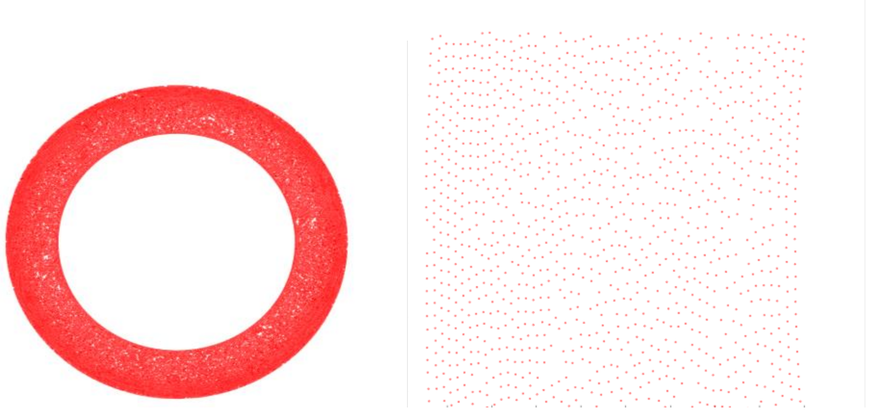

(a) (b)

Fig. 129. Z-direction view of Fig. 127(b) and detail.

The result obtained with standard WCSPH in Fig. 127(a) shows the particle layering and clustering. This result is not seen with SPH. To further consider the particle distribution, the z-direction view of Fig. 127(a) and 11(b) are presented in Fig. 128 and Fig. 129, respectively. From the z-direction view, it is seen that the standard WCSPH suffers from particle layering. In contrast, the result of SPH is much better than standard WCSPH.

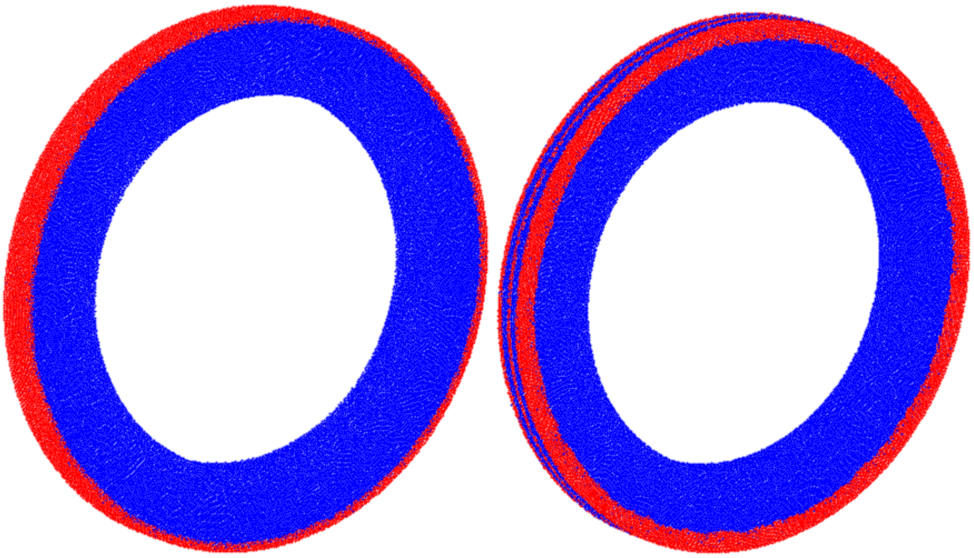

(a) **(b)**

Fig. 130. Evolution of the three-dimensional multiphase turbulent TC flow at instants (a) 0.04 s, (b) 0.4 s, together with the density distribution of SA (SPH).

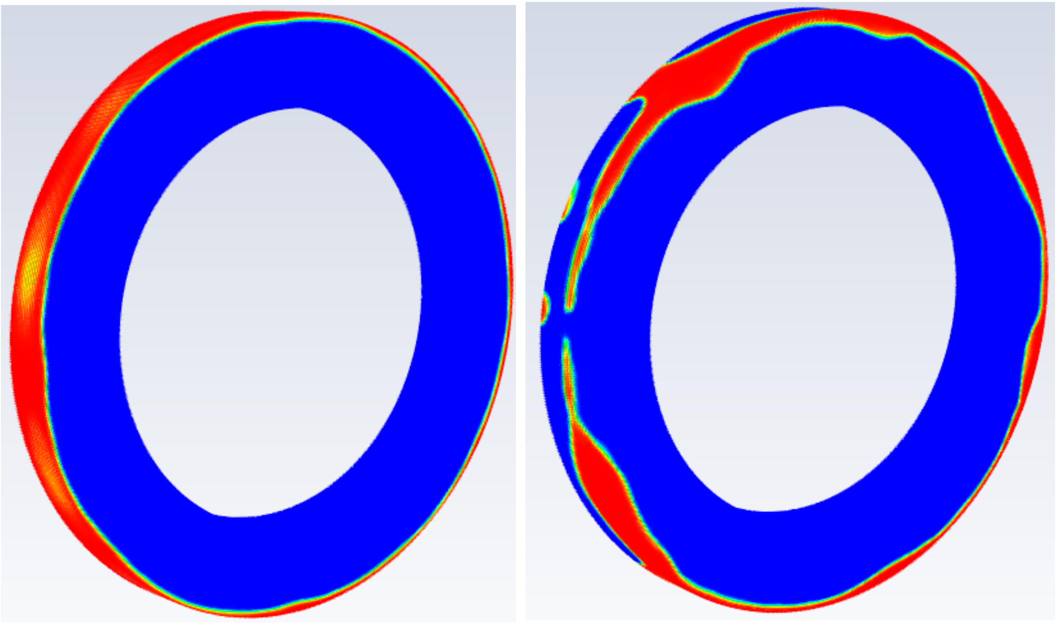

(a) **(b)**

Fig. 131. Evolution of the three-dimensional multiphase turbulent TC flow at instants (a) 6 s, (c) 10 s, together with the density distribution of *k*-ω (Fluent).

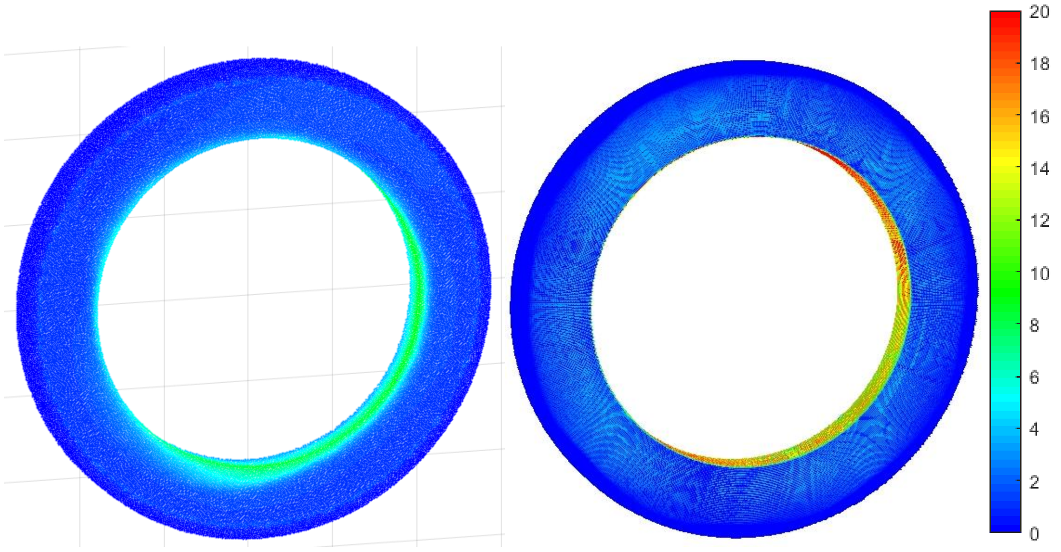

(a) **(b)**

Fig. 132. Velocity distribution of the multiphase turbulent TC. (a) SA (SPH) t = 0.4 s, (b) *k*-*ω* (Fluent) t = 6 s.

Fig. 130 and Fig. 131 show the evolution of the three-dimensional multiphase turbulent TC flow. As shown in Fig. 130, the oil film obtained with SA (SPH) will move from the middle to both side chamber walls in 0.4 s. Similar phenomena can be observed in Fig. 131. However, the oil film obtained with *k*-*ω* (Fluent) moves from the middle to the one side wall in 10 s. Although the instants are not the same, the oil film distribution of SPH is quite similar to that of Fluent

In the next part of this section, the results of t = 0.04 s and t = 0.4 s in SPH will be compared with those of Fluent.

The velocity distribution of the whole fluid domain is illustrated in Fig. 132. The results of both models are roughly the same. To obtain a detailed analysis, the profiles of velocity, pressure and viscosity are presented on the horizontal axis in Fig. 133: the first line (L_3) is the red line (y = 0, z =0, $-R_{outer} <= x <= -R_{inner}$) at the middle part and the second line (L_4) is the green line (y = 0, z =0.01, $-R_{outer}$ < = x < = $-R_{inner}$) close to the right side.

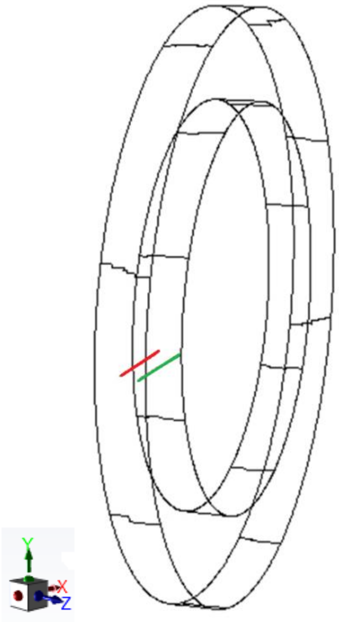

Fig. 133. Line to plot the velocity and pressure profiles inside the concentric cylinders.

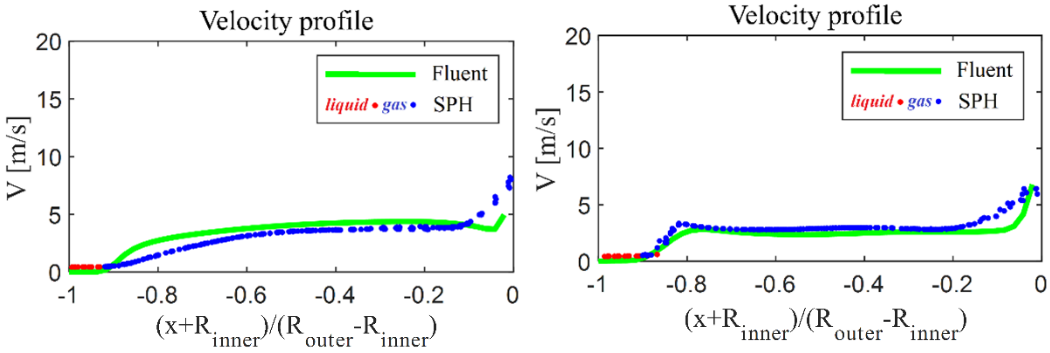

(a) (b)

Fig. 134. Velocity profile of SA (SPH) at t = 0.04 s. (a) L_3, (b) L_4.

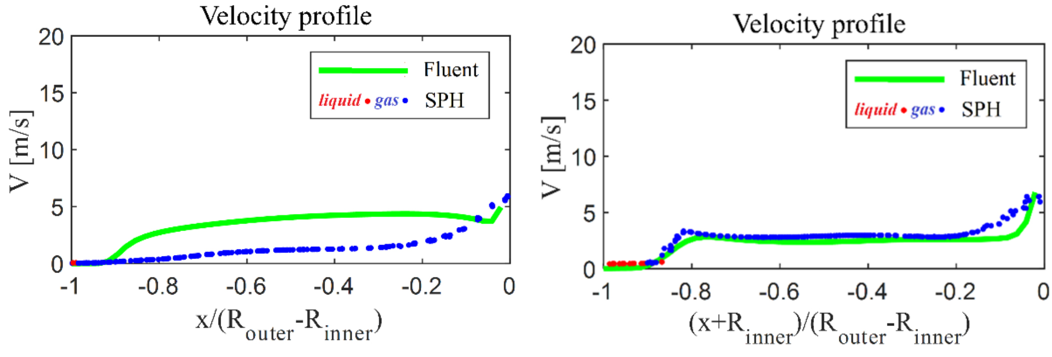

(a) (b)

Fig. 135. Velocity profile of SA (SPH) at t = 0.4s. (a) L_3, (b) L_4.

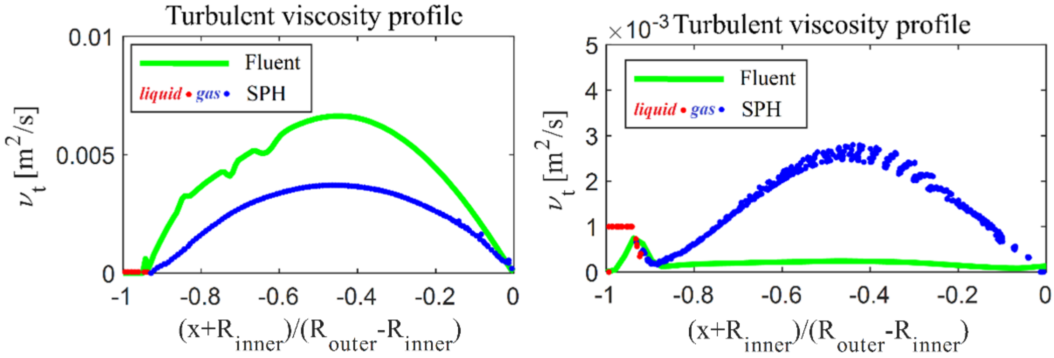

(a) (b)

Fig. 136. Turbulent viscosity profile of SA (SPH). (a) 2D, (b) 3D.

In the simulation results of Fluent, before the most of the oil moves to the side wall, the velocity profile is in a relatively stable state. Here, the simulation results of Fluent at t = 6 s are chosen to validate the results of SPH.

Fig. 134 and Fig. 135 illustrate the velocity profile obtained with SA (SPH) along the lines L_3 and L_4 at t = 0.04 s and 0.4 s, respectively. As shown in Fig. 134, the velocity profile of SA (SPH) is similar to that of *k-ω* (Fluent). However, afterward, as seen in Fig. 135, the velocity profile of SA (SPH) is lower than that of *k-ω* (Fluent) no matter whether the profile was plotted along L_3 or L_4.

Fig. 136 shows the turbulent viscosity profile of SPH in 2D and 3D. In 2D cases, the turbulent viscosity of *k-ω* (Fluent) is twice that of SA (SPH). However, the turbulent viscosity of SA (SPH) is nearly 20 times that of *k*-*ω* (Fluent) in 3D. This viscosity difference is one of the reasons for the variance in the velocity profile between SA (SPH) and *k*-*ω* (Fluent). The remaining reasons for the variances between the two models above need further investigation.

8.3.2. Three-dimensional multiphase turbulent flow in the bearing chamber

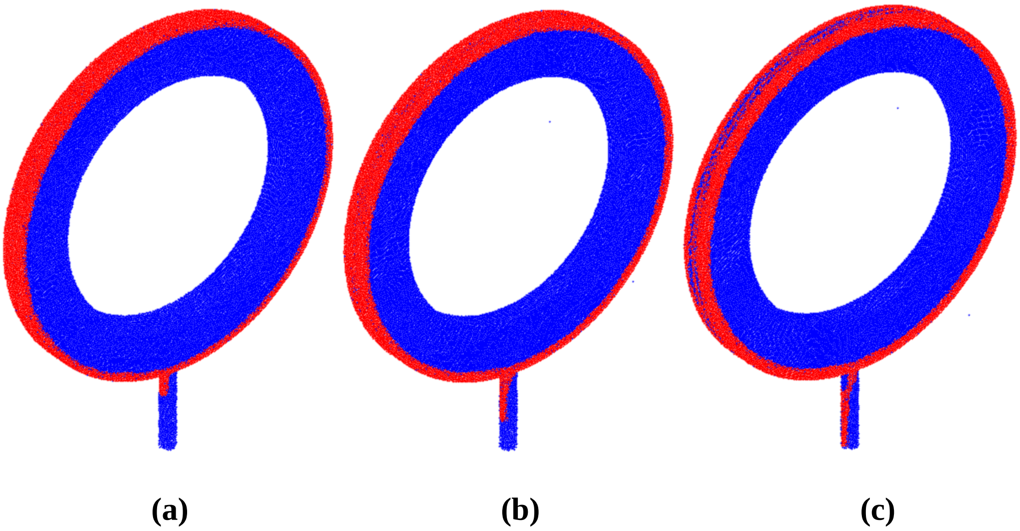
(a) **(b)** **(c)**

Fig. 137, Density distribution of SA (SPH). (a) 0.08 s, (b) 0.16 s, (c) 0.24 s.

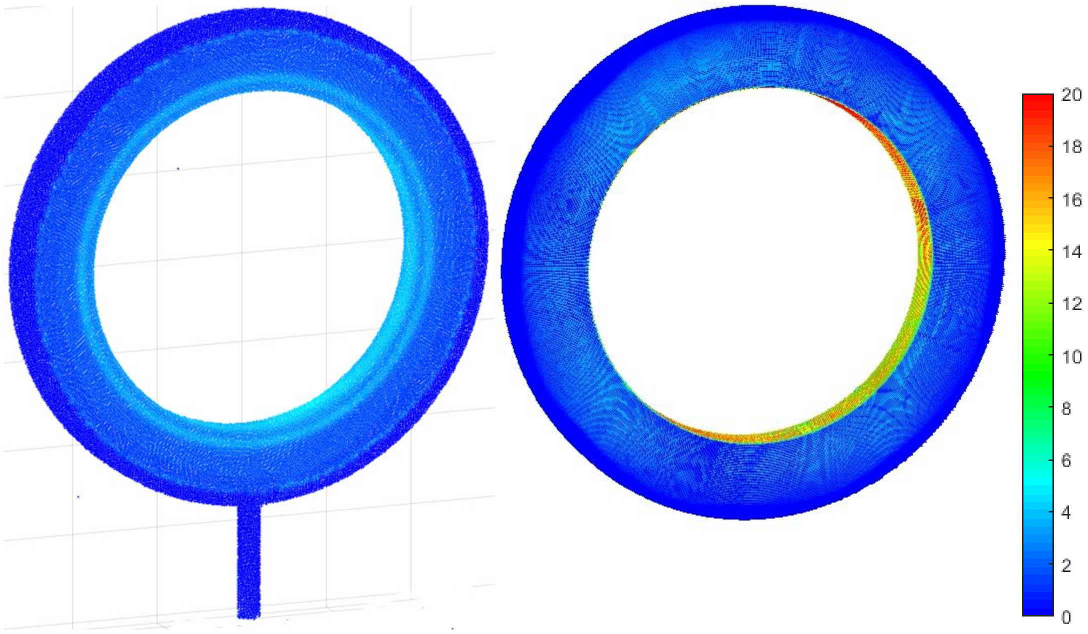

(a) (b)

Fig. 138. Velocity distribution. (a) Turbulent flow in the bearing chamber at t = 0.24 s obtained with SA(SPH), (b)Turbulent TC flow at t = 6 s obtained with *k*-*ω* (Fluent).

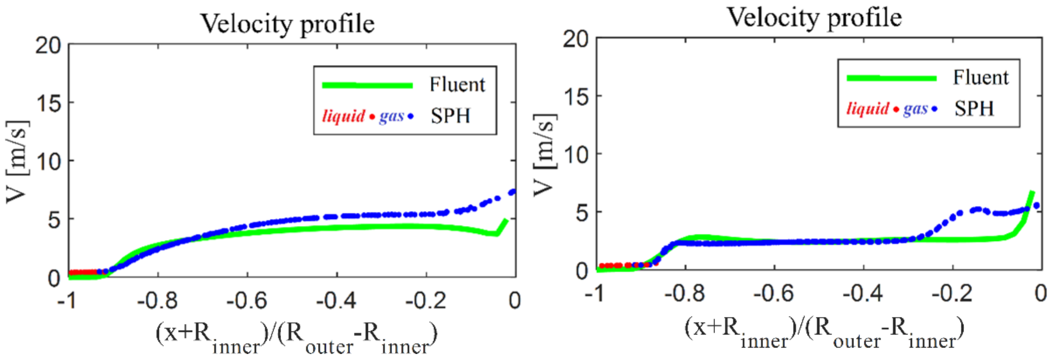

(a) (b)

Fig. 139. Velocity profile of SA (SPH) at t = 0.04 s. (a) L_3, (b) L_4.

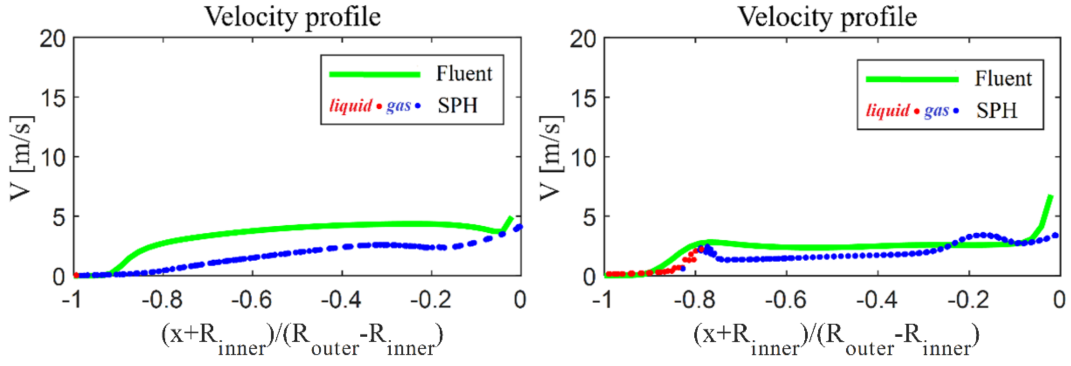

(a)

(b)

Fig. 140. Velocity profile of SA (SPH) at t = 0.24 s. (a) L_3, (b) L_4.

Under the high rotational speed, the effect of gravity can be ignored. Similar to the above section, the simulation results of 3D TC flow (without gravity) obtained with Fluent at t = 6 s are chosen to validate the results of SPH.

Fig. 137 displays the evolution of the 3D multiphase turbulent flow in the bearing chamber at 3 moments from 0 to 0.24 s. The oil film will move into the sump pipe and out of the bearing chamber. Fig. 138 illustrates the velocity distribution obtained with SA (SPH) of the entire bearing chamber, which is close to the results of *k*-*ω* (Fluent). Fig. 139 and Fig. 140 illustrate the velocity profile along the lines L_3 and L_4 at t = 0.04 s and 0.24 s, respectively. The velocity profiles of the turbulent flow in bearing chamber obtained with SA (SPH) are very similar to that in 3D TC flow. Compared with the results of Fluent, the velocity profile of SPH has a good agreement in the early stages of the simulation, and then it will decrease. The length of the red line in Fig. 139 and Fig. 140 represents the thickness of the oil film, it can be seen that the thickness of the oil film at the middle of the outer wall decreases, while the thickness of the oil film increases near the side wall. In the bearing chamber, the oil also moves from the middle to the side wall.

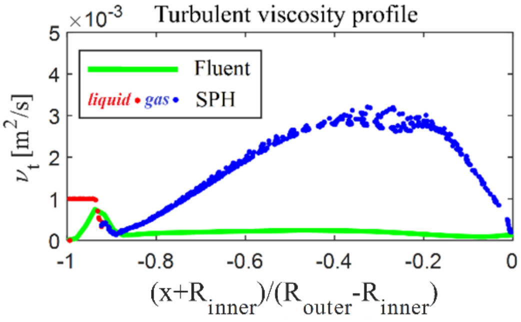

Fig. 141. Turbulent viscosity profile of SA (SPH).

Fig. 141 illustrates the turbulent viscosity profile in the bearing chamber. It is very similar to that in 3D TC flow, which again 20 times larger than that of Fluent. This may cause the dissipation of the velocity. At high rotational speed, gravity can be neglected, and the turbulent viscosity will dominate the evolution of the velocity.

8.4. Summary

In this chapter, the multiphase turbulent flow in the simplified two- and three-dimensional bearing chamber as well as the three-dimensional turbulent Taylor–Couette (TC) flow (without gravitation) are modelled using δ-SPH in combination with the particle-collision shift model. All simulations are performed with the Spalart–Allmaras (SA) turbulence model as well as the surface tension model. The results are validated against Fluent using the *k*-*ω* model with the same surface tension model.

In the two-dimensional bearing chamber case, the evolution of the oil film is reasonable – it will move out of the chamber under gravity and centrifugal force. The SPH results for the configuration of the turbulent flow in the two-dimensional bearing chamber show a reasonable match with Fluent. The velocity profiles obtained with SA

(SPH) are identical to Fluent. The pressure profile of SA (SPH) has the same trend as that of Fluent but with more fluctuation caused by the point-source particles.

In the 3D TC flow case, the evolution of the oil film is similar to that of Fluent. The oil will move from the middle of the outer wall to the side. However, the oil obtained with SPH will move to both sides of the outer wall symmetrically, while only to one side with Fluent. The velocity profile of SPH for the configuration is in good agreement with Fluent no matter whether at the centre of the outer wall (L_3) or near the side of the boundary (L_4) at the early stage. Later on, the velocity profile shows more deviation from those of Fluent.

In the 3D-bearing-chamber case, a sump pipe is added, and gravity is considered. Similar to the evolution of the above case, the oil film still tends to move from the middle of the chamber wall on both sides. In addition, the oil will move out from the sump pipe. Similar to the 3D turbulent TC flow, the velocity profile obtained with SPH of the bearing chamber is also comparable to that of Fluent at the early stage of the simulation. Subsequently, the velocity profile will decrease, and the final results will be lower than those of Fluent. The main reason is that the turbulent viscosity calculated by (SA) SPH is 20 times larger than that of k-ω (Fluent), which leads to more dissipation in the velocity.

The three-dimensional simulation was conducted using 132 cores on the University of Nottingham HPC at an average rate of about 0.32 s per week for 1,000,000 particles. The resolution is still not high enough to have an accurate interface which leads error distance to the boundary of SA model. That is one of the main reason of large difference of viscosity between SPH and Fluent.

Chapter 9 Conclusion and Recommendations

In this thesis, a novel particle shift SPH model is presented and applied it to the multiphase flow in jet engine bearing chambers.

9.1. Concluding remarks

The turbulence model in the SPH method was reviewed.

A new particle shift model based on the particle collision model from Kruisbrink [1] was proposed. This new model was designed to prevent particle clustering, including but not limited to unstable interface, particle wall penetration, and particle gathering and separating. The new model’s conservative and non-dissipative properties were demonstrated.

The accuracy, stability, computational efficiency and dissipative properties of the particle collision shift and Fickian shift were compared. These properties were explored through six case studies, including four academic and two benchmark engineering cases, using the incompressible SPH method. The collision shift is simpler (does not require special treatment at the free surface), more efficient (requires less CPU time) and more accurate.

A hybrid method, consisting of a combination of the particle collision shift model and δ-SPH, was proposed and named δ-SPH_CS. This hybrid method fits both single-phase and multiphase flows. The particle collision shift model's equation is the same for multiphase as for single-phase flow. This result was verified with four classical multiphase cases, including low- and high-density ratio cases.

For the two-dimensional, single-phase Taylor-Couette flow, the SPH simulation results for laminar flow were consistent with the laminar theoretical value. Moreover, the turbulent flow results were almost identical to the Ansys Fluent results at three different radius ratios.

The evolution of the two-dimensional, multiphase, turbulent Taylor-Couette flow was studied systematically at two different rotational speeds. The motion of the oil film was observed. The waveform, velocity, pressure and viscosity distributions matched those of Fluent for both rotational speeds.

The evolution of multiphase turbulent flow in bearing chambers was studied in both two and three dimensions. The two-dimensional bearing chamber's velocity profile was almost identical to those of Fluent. However, the pressure profile of the bearing chamber, unlike those produced by Fluent, had fluctuations caused by the point source particle. In the three-dimensional bearing chamber, the movement of oil film is similar to that of Fluent. Due to the higher turbulent viscosity created in the SPH method, the velocity profile only matched Fluent's results well in the early stages. After that, the velocity will be lower than that of Fluent.

9.2. Recommendations for future work

In this thesis, the particle collision shift model is used with a fixed restitution coefficient ($C_R = 0$; representing inelastic collisions), and a fixed collision distance equal to the initial particle distance ($d_{col} = d_{nat}$). It may be interesting to explore the effect of a variable collision distance and restitution coefficient. In weakly compressible SPH, the particle distribution represents the state of compression. The smaller the particle distance, the denser the particle distribution and the higher the pressure. This implies that under high pressure the collision distance should be chosen smaller. This leads to the concept of a collision distance that is pressure dependent ($d_{col} = f(p)$). The same potentially may be done for the restitution coefficient. A fluid becomes more stagnant at high pressures, which may be associated with inelastic collisions ($C_R = 0$). A fluid becomes more dynamic at low pressures, which may be associated with elastic collisions ($C_R > 0$). This leads to a concept of a restitution coefficient that is pressure dependent ($C_R = f(p)$).

In this thesis, the particle collision shift model is used without the original particle collision model. The combination of both models may be useful, particularly in turbulence modelling. In the original particle collision model, only the approach velocities of colliding particles are changed, not their positions. By combining these two models, colliding particles are not only separated (by shifting), but their velocities are also changed, such that they no longer approach each other. The latter avoids repetitive shifting. Moreover, the original particle collision model leads to better no-slip conditions [1]. This combination may be useful in the stabilization of turbulent flows, characterized by steep velocity gradients at walls. The original particle collision model is dissipative to some extent, which however, is acceptable in dissipative turbulent flows that are dominated by a turbulent viscosity that may be several orders higher than the laminar viscosity.

The Prandtl's mixing length model and the Spalart-Allmaras model are used in this work, and the distance from the wall must be known. In simple geometries, such as the Taylor-Couette flow between concentric cylinders, this can be calculated with a simple function. However, in complex geometries such as the real bearing with several sump pipes, this becomes less obvious. In SPH a fluid particle can only see particles within its kernel domain. This implies that ghost particles (that represent a wall) can only be seen at a short distance. Moreover, when running a parallel SPH code, walls may be present at other cores. Thus, the evaluation of wall distances in SPH is not straightforward. This needs further investigation.

At the current stage of the research, the mixing length turbulence model and the Spalart-Allmaras model are implemented in the SPH method. However, both models are based on the distance to the interface or boundaries. The k-ω and k-e models should be considered as options to potentially implement in the in-house code.

For multiphase fluid problems with rapid gradient changes in physical quantities (e.g. density, velocity), it may be useful to utilise adaptive particle splitting and merging schemes for refined resolution near the interface and the inlet particles on the shaft.

Given the success in modelling turbulent flow with an initially thin layer of oil film at the outer wall, the form of the oil film produced by the rotating shaft's action on the inlet oil particles should be studied further.

The turbulence model and δ-SPH_CS were successfully validated with Ansys Fluent's two-dimensional simulation. More numerical studies need to be conducted to validate the models in three dimensions.

Appendix

Appendix A

In this appendix the relationship between the approach velocity and the distance between particles *i* and *j* at subsequent time steps, according to Eq. (86), is proven. This is an important step in the derivation of the particle collision shift model.

The positions of particle *i* and a neighbour particle *j* at a new time step are

$$\begin{cases}\vec{r}_i(t+\Delta t)=\vec{r}_i(t)+\vec{v}_i(t)\Delta t\\ \vec{r}_j(t+\Delta t)=\vec{r}_j(t)+\vec{v}_j(t)\Delta t\end{cases} \tag{A1}$$

The relative particle position of particle *i* and *j* is

$$\overrightarrow{r_{ij}}(t+\Delta t)=\vec{r}_{ij}(t+\Delta t)=\vec{r}_{ij}(t)+\vec{v}_{ij}(t)\Delta t \tag{A2}$$

The particle distance at a new time step is

$${d_{ij}}^2(t+\Delta t)=\left(\vec{r}_{ij}(t)+\vec{v}_{ij}(t)*\Delta t\right)^2={d_{ij}}^2(t)+2\vec{r}_{ij}(t)\cdot\vec{v}_{ij}(t)\Delta t+\vec{v}_{ij}(t)\cdot\vec{v}_{ij}(t)(\Delta t)^2 \tag{A3}$$

Eq. (A3) can be rewritten as,

$$d_{ij}(t+\Delta t)=\pm d_{ij}(t)\sqrt{1+\frac{2\vec{r}_{ij}(t)\cdot\vec{v}_{ij}(t)\Delta t}{d_{ij}(t)^2}+[\frac{\vec{v}_{ij}(t)\cdot\vec{v}_{ij}(t)}{d_{ij}(t)^2}]\Delta t^2}. \tag{A4}$$

The negative sign is further ignored since the distance is always positive. For convenience, the terms under the square root are represented in short notation by

$$\begin{cases}\varepsilon_1=\frac{\vec{r}_{ij}(t)\cdot\vec{v}_{ij}(t)}{d_{ij}(t)^2}\\ \varepsilon_2=\frac{\vec{v}_{ij}(t)\cdot\vec{v}_{ij}(t)}{d_{ij}(t)^2}\end{cases} \tag{A5}$$

Substitution of Eq. (A5) into Eq. (A4) results in

$$d_{ij}(t+\Delta t) = d_{ij}(t)\sqrt{1+2\varepsilon_1\Delta t+\ \varepsilon_2\Delta t^2}. \tag{A6}$$

Note that for small time steps ($\Delta t \to 0$) the value of ε also tends to zero ($|2\varepsilon_1\Delta t+\ \varepsilon_2\Delta t^2| \to 0$). Therefore, the square root term in Eq. (A6) can be approximated by a Taylor series expansion, resulting in

$$d_{ij}(t+\Delta t) = d_{ij}(t)(1+\varepsilon_1\Delta t+\varepsilon_2\Delta t^2-{\varepsilon_1}^2\Delta t^2-\varepsilon_1\varepsilon_2\Delta t^3+O(\Delta t^2)). \tag{A7}$$

Neglecting higher-order terms (Δt^2, Δt^3, …), the first-order approximation of Eq. (44) becomes

$$d_{ij}(t+\Delta t) = d_{ij}(t)(1+\varepsilon_1\Delta t+O(\Delta t)). \tag{A8}$$

Ignoring the O(Δt) term and substituting Eq. (A5) into Eq. (A8) yields

$$d_{ij}(t+\Delta t) \approx d_{ij}(t) + [\frac{\vec{r}_{ij}(t)\cdot\vec{v}_{ij}(t)}{d_{ij}(t)}]\Delta t. \tag{A9}$$

Using -Δt to replace Δt in Eq. (A9)

$$d_{ij}(t-\Delta t) \approx d_{ij}(t) - [\frac{\vec{r}_{ij}(t)\cdot\vec{v}_{ij}(t)}{d_{ij}(t)}]\Delta t. \tag{A10}$$

Rewriting the above result, the relationship between the approach velocity and distance is approximated as

$$\frac{\vec{r}_{ij}(t)\cdot\vec{v}_{ij}(t)}{d_{ij}(t)} \approx \frac{d_{ij}(t)-d_{ij}(t-\Delta t)}{\Delta t}. \tag{A11}$$

This result is equal to Eq. (86), which was to be proven.

Appendix B

In this appendix, the conservative features of the collision shift model (CS) in itself are analysed. In CS, the velocity is not updated, so that the kinetic energy and linear momentum are conserved. The conservative features of potential energy and angular momentum are assessed in the sections B.1 and B.2. For this purpose, a set S of N particles is considered that take part in a single simultaneous collision.

B.1 Conservation of potential energy in a gravitation field

The change of potential energy of a particle $i \in S$, due to its shift is

$$\Delta E_i = - m_i \, [\vec{g} \cdot \Delta\vec{r}_i] \, . \tag{B1}$$

where $\vec{g}$ is the gravitational acceleration. The shift of particle i due to a simultaneous collision with (N-1) particles $j \in S$ is given in Eq. (95). Substitution of Eq. (95) in Eq. (B1) yields

$$\Delta E_i = \frac{\sum_{j=1}^{N} m_i m_j \, (1 + C_R) \, (d_{ij} - d_{col}) \, [\vec{g} \cdot \vec{e}_{ij}]}{\sum_{j=1}^{N} m_j}, \tag{B2}$$

where $\vec{e}_{ij} = \vec{r}_{ij} \, / \, d_{ij}$ is a unit vector. Note that the summation is extended to all (N) colliding particles, including particle i itself. This is allowed since particle i does not contribute to its own shift ($[\vec{g} \cdot \vec{e}_{ii}] = 0$). The change of potential energy of the set S now becomes

$$\Delta E = \frac{\sum_{i=1}^{N} \sum_{j=1}^{N} m_i m_j \, (1 + C_R) \, (d_{ij} - d_{col}) \, [\vec{g} \cdot \vec{e}_{ij}]}{\sum_{j=1}^{N} m_j}. \tag{B3}$$

The change of potential energy of particle i due to its collision with particle j is

$$\Delta E_{ij} = \frac{m_i m_j \, (1 + C_R) \, (d_{ij} - d_{col}) \, [\vec{g} \cdot \vec{e}_{ij}]}{\sum_{j=1}^{N} m_j}. \tag{B4}$$

The above result is symmetrical, swapping the indices i and j only changes its sign ($\vec{e}_{ij} = -\vec{e}_{ji}$). Thus, the pairwise contribution to the change of potential energy of the set is

$$\Delta E_{ij} + \Delta E_{ji} = \frac{m_i m_j \, (1 + C_R) \, (d_{ij} - d_{col}) \, [\vec{g} \cdot (\vec{e}_{ij} + \vec{e}_{ji})]}{\sum_{j=1}^{N} m_j}. \tag{B5}$$

Consequently, all pairwise contributions within the set are zero, so that the total potential energy of the set S is conserved. The above derivation holds for any value of the gravitational acceleration and thus for any constant conservative force field.

B.2 Conservation of angular momentum

The change of angular momentum of a particle *i* due to its shift is

$$\Delta L_i \; = \; - \, m_i \; [\Delta\vec{r}_i \times \vec{v}_i] \; . \tag{B6}$$

Substitution of Eq. (95) into Eq. (B6) gives for the shift due to collisions with the colliding particles

$$\Delta L_i \; = \; \frac{\sum_{j=1}^{N} \; m_i m_j \; (1 + C_R) \; (d_{ij} - d_{col}) \; [\; \vec{e}_{ij} \times \vec{v}_i]}{\sum_{j=1}^{N} \; m_j}. \tag{B7}$$

The change of angular momentum of the set now becomes

$$\Delta L \; = \; \frac{\sum_{i=1}^{N} \sum_{j=1}^{N} \; m_i m_j \; (1 + C_R) \; (d_{ij} - d_{col}) \; [\; \vec{e}_{ij} \times \vec{v}_i]}{\sum_{j=1}^{N} \; m_j} \tag{B8}$$

The change of angular momentum of particle *i* due to the collision with particle *j* is

$$\Delta L_{ij} = \frac{m_i m_j \; (1 + C_R) \; (d_{ij} - d_{col}) \; [\; \vec{e}_{ij} \times \vec{v}_i]}{\sum_{j=1}^{N} \; m_j}. \tag{B9}$$

The pairwise contribution to the change of angular momentum of the set now becomes

$$\Delta L_{ij} + \Delta L_{ji} = \frac{m_i m_j \; (1 + C_R) \; (d_{ij} - d_{col}) \; [\; \vec{e}_{ij} \times \vec{v}_{ij}]}{\sum_{j=1}^{N} \; m_j}. \tag{B10}$$

The cross product in Eq. (B10) is in general non-zero, so that the conservation of angular momentum is not satisfied. Angular momentum cannot be conserved in a shift process without a change of velocity. It thus may be concluded that kinetic energy and angular momentum cannot both be conserved in a shift process.

B.3 Case validation

Potential energy is assessed in the dam break and oscillating droplet cases. To quantify the effect of CS and FS (without velocity correction) on the potential energy, other dissipation effects (e.g. due to viscosity) must be eliminated. Therefore, the potential energy just before and immediately after a shift is considered at each instant. If energy is conserved for every shift step, for the longer term, the energy dissipation due to the collision shift can remain zero. And the shift process is after the movement calculated by the momentum equation and before the next time calculation start. Only the position of the particle is slightly changed. The properties such as velocity, density and temperature remain the same. The change of potential energy ($\Delta E = E_{after} - E_{before}$) is presented in Figs. A and B (below) for the dam break case and oscillation droplet case.

Dam break: Fig. A below shows that the change of potential energy with CS is zero, as expected. The change of potential energy with FS is small but not zero, which may be attributed to the free surface treatment and (small) numerical errors in the kernel estimates.

Fig. A is not included in the thesis, because it is analytically proven (in appendix B) that the change of potential energy due to the CS shifting in a gravitational field is zero, whilst it is shown that potential energy is not conserved without velocity correction.

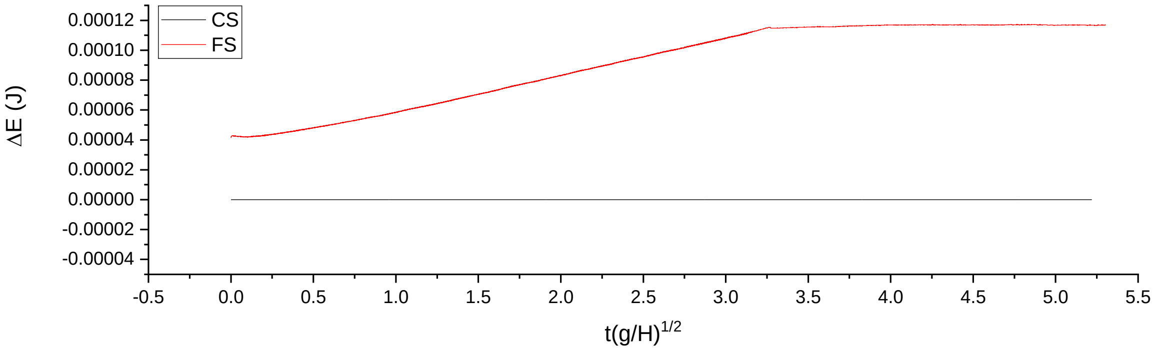

Fig. A. Dam break. Change of potential energy in time due to CS and FS shifting (without velocity correction).

Oscillating droplet (in section 4.4): In this case with radial (fictive) force field , potential energy is strictly not conserved in CS. However, in Fig. B below it is demonstrated that the change of potential energy is almost zero and still very low compared to FS. This figure is not included in the paper, because the potential energy was already assessed in section 4.4 Fig. 23. Fig. 23 in the paper shows that the potential energy varies periodically with the oscillation of the droplet, with almost no decay (at low resolution) and no visible decay (at high resolution).

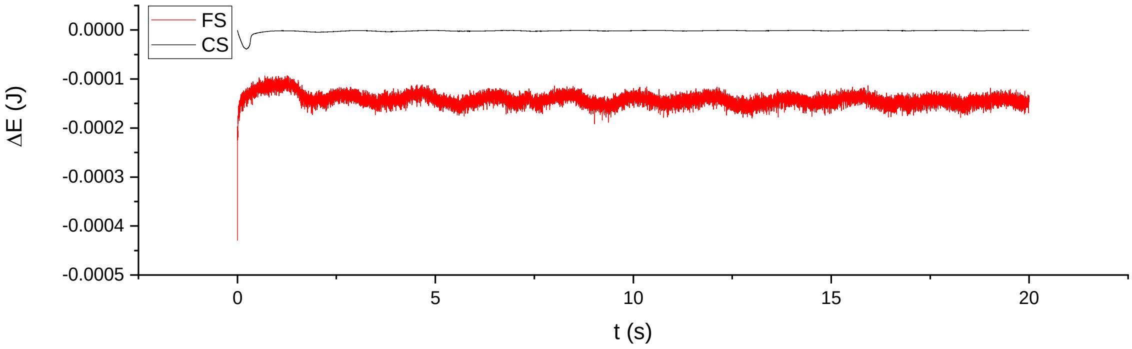

Fig. B. Oscillation droplet. Change of potential energy in time due to CS and FS shifting (no velocity correction).

The shift models, such as collision shift and Fickian shift models, are also applicable to non-Newtonian fluids, as they are unaffected by fluid particle viscosity.

References

[1] A. Kruisbrink, S. Korzilius, F. Pearce, H. Morvan, SPH Particle Collisions for the Reduction of Particle Clustering, Interface Stabilisation and Wall Modelling, Journal of Applied Mathematics and Physics. 06 (2018) 1860–1882. https://doi.org/10.4236/jamp.2018.69158.

[2] A.A. Adeniyi, A Coupled Lagrangian-Eulerian Framework to model droplet to film interaction with Heat Transfer, PhD Thesis. (2014).

[3] A. Skillen, S. Lind, P.K. Stansby, B.D. Rogers, Incompressible smoothed particle hydrodynamics (SPH) with reduced temporal noise and generalised Fickian smoothing applied to body-water slam and efficient wave-body interaction, Comput Methods Appl Mech Eng. 265 (2013) 163–173. https://doi.org/10.1016/j.cma.2013.05.017.

[4] R. Xu, P. Stansby, D. Laurence, Accuracy and stability in incompressible SPH (ISPH) based on the projection method and a new approach, J Comput Phys. 228 (2009) 6703–6725. https://doi.org/10.1016/j.jcp.2009.05.032.

[5] A. Khayyer, H. Gotoh, Y. Shimizu, Comparative study on accuracy and conservation properties of two particle regularization schemes and proposal of an optimized particle shifting scheme in ISPH context, J Comput Phys. 332 (2017) 236–256. https://doi.org/10.1016/j.jcp.2016.12.005.

[6] N. Zhang, X. Zheng, Q. Ma, W. Duan, A. Khayyer, X. Lv, S. Shao, A hybrid stabilization technique for simulating water wave – Structure interaction by incompressible Smoothed Particle Hydrodynamics (ISPH) method, Journal of

Hydro-Environment Research. 18 (2018) 77–94. https://doi.org/10.1016/j.jher.2017.11.003.

[7] M. Farrall, S. Hibberd, K. Simmons, Computational modelling of two-phase air/oil flow within an aero-engine bearing chamber, American Society of Mechanical Engineers, Fluids Engineering Division (Publication) FED. 253 (2000) 677–684.

[8] M. Farrall, K. Simmons, S. Hibberd, P. Gorse, A numerical model for oil film flow in an aeroengine bearing chamber and comparison to experimental data, J Eng Gas Turbine Power. 128 (2006) 111–117. https://doi.org/10.1115/1.1924719.

[9] A. Robinson, C. Eastwick, H. Morvan, Further computational investigations into aero-engine bearing chamber off-take flows, in: Proceedings of the ASME Turbo Expo, 2010: pp. 209–217. https://doi.org/10.1115/GT2010-22626.

[10] A. Glahn, S. Busam, S. Wittig, Local and mean heat transfer coefficients along the internal housing walls of aero engine bearing chambers, in: Proceedings of the ASME Turbo Expo, 1997. https://doi.org/10.1115/97-GT-261.

[11] S. Busam, A. Glahn, S. Wittig, Internal bearing chamber wall heat transfer as a function of operating conditions and chamber geometry, Proceedings of the ASME Turbo Expo. 3 (1999). https://doi.org/10.1115/99-GT-249.

[12] C. Young, J.W. Chew, Evaluation of the Volume of Fluid Modelling Approach for Simulation of Oil/Air System Flows, ASME Turbo Expo 2005: Power for Land, Sea, and Air. (2005) 1249–1257. https://doi.org/10.1115/GT2005-68861.

[13] A.A. Hashmi, K. Dullenkopf, R. Koch, H.J. Bauer, CFD methods for shear driven liquid wall films, in: Proceedings of the ASME Turbo Expo, 2010: pp. 1283–1291. https://doi.org/10.1115/GT2010-23532.

[14] D. Peduto, A.A. Hashmi, K. Dullenkopf, H.J. Bauer, H. Morvan, Modelling of an aero engine bearing chamber using enhanced CFD technique, Proceedings of the ASME Turbo Expo. 5 (2011) 809–819. https://doi.org/10.1115/GT2011-45635.

[15] A. Crouchez-Pillot, H.P. Morvan, CFD simulation of an aeroengine bearing chamber using an Enhanced Volume of Fluid (VOF) method: An evaluation using adaptive meshing, Proceedings of the ASME Turbo Expo. 5C (2014) 1–9. https://doi.org/10.1115/GT2014-26286.

[16] T. Ménard, S. Tanguy, A. Berlemont, Coupling level set/VOF/ghost fluid methods: Validation and application to 3D simulation of the primary break-up of a liquid jet, International Journal of Multiphase Flow. 33 (2007) 510–524. https://doi.org/10.1016/j.ijmultiphaseflow.2006.11.001.

[17] L. Yaguo, Z. Jingyu, L. Zhenxia, R. Guozhe, Numerical Study on the Effect of Oil Removal From Aero-Engine, 2016 STLE Annual Meeting & Exhibition. (2016) 2–5.

[18] A.A. Adeniyi, H.P. Morvan, K.A. Simmons, A transient CFD simulation of the flow in a test rig of an aeroengine bearing chamber, Proceedings of the ASME Turbo Expo. 5C (2014) 1–9. https://doi.org/10.1115/GT2014-26399.

[19] A.A. Adeniyi, H.P. Morvan, K.A. Simmons, A multiphase computational study of oil-air flow within the bearing sector of aeroengines, Proceedings of the ASME Turbo Expo. 5C (2015) 1–10. https://doi.org/10.1115/GT2015-43496.

[20] R.A. Gingold, J.J. Monaghan, Smoothed particle hydrodynamics - theory and application to non-spherical stars, Mon Not R Astron Soc. 181 (1977) 375–389.

[21] L.B. Lucy, A numerical approach to the testing of fusion HYPOTHESIS, Astron J. 82 (1977) 1013–1024. https://doi.org/10.1007/s00769-003-0757-y.

[22] A.C.H. Kruisbrink, H.P. Morvan, F.R. Pearce, Progress in Smoothed Particle Hydrodynamics to Simulate Bearing Chambers, in: Volume 5C: Heat Transfer, American Society of Mechanical Engineers, 2014: pp. 1–9. https://doi.org/10.1115/GT2014-26403.

[23] L. Wieth, C. Lieber, W. Kurz, S. Braun, R. Koch, H.-J. Bauer, Numerical Modeling of an Aero-Engine Bearing Chamber Using the Meshless Smoothed Particle Hydrodynamics Method, in: Volume 2B: Turbomachinery, American Society of Mechanical Engineers, 2015: pp. 1–13. https://doi.org/10.1115/GT2015-42316.

[24] J.J. Monaghan, Simulating free surface flows with SPH, J Comput Phys. 110 (1994) 399–406. https://doi.org/10.1006/jcph.1994.1034.

[25] M. Antuono, A. Colagrossi, S. Marrone, Numerical diffusive terms in weakly-compressible SPH schemes, Comput Phys Commun. 183 (2012) 2570–2580. https://doi.org/10.1016/j.cpc.2012.07.006.

[26] S. Marrone, M. Antuono, A. Colagrossi, G. Colicchio, D. le Touzé, G. Graziani, δ-SPH model for simulating violent impact flows, Comput Methods Appl Mech Eng. 200 (2011) 1526–1542. https://doi.org/10.1016/j.cma.2010.12.016.

[27] P.N. Sun, A. Colagrossi, S. Marrone, A.M. Zhang, The δplus-SPH model: Simple procedures for a further improvement of the SPH scheme, Comput

Methods Appl Mech Eng. 315 (2017) 25–49. https://doi.org/10.1016/j.cma.2016.10.028.

[28] and A.S. Mostafa Safdari Shadloo AmirZainali, Mehmet Yildiz,*, A robust weakly compressible SPH method and its comparison with an incompressible SPH, International. (2011) 939–956. https://doi.org/10.1002/nme.

[29] S. Shao, E.Y.M. Lo, Incompressible SPH method for simulating Newtonian and non-Newtonian flows with a free surface, Adv Water Resour. 26 (2003) 787–800. https://doi.org/10.1016/S0309-1708(03)00030-7.

[30] E.S. Lee, C. Moulinec, R. Xu, D. Violeau, D. Laurence, P. Stansby, Comparisons of weakly compressible and truly incompressible algorithms for the SPH mesh free particle method, J Comput Phys. 227 (2008) 8417–8436. https://doi.org/10.1016/j.jcp.2008.06.005.

[31] X.Y. Hu, N.A. Adams, An incompressible multi-phase SPH method, J Comput Phys. 227 (2007) 264–278. https://doi.org/10.1016/j.jcp.2007.07.013.

[32] J.J. Monaghan, A. Rafiee, A simple SPH algorithm for multi-fluid flow with high density ratios, (2013) 537–561. https://doi.org/10.1002/fld.

[33] J.J. Monaghan, A. Kocharyan, SPH simulation of multi-phase flow, Comput Phys Commun. 87 (1995) 225–235. https://doi.org/10.1016/0010-4655(94)00174-Z.

[34] A. Valizadeh, M. Shafieefar, J.J. Monaghan, S.A.A. Salehi Neyshaboori, Modeling two-phase flows using SPH method, Journal of Applied Sciences. 8 (2008) 3817–3826. https://doi.org/10.3923/jas.2008.3817.3826.

[35] A. Colagrossi, M. Landrini, Numerical simulation of interfacial flows by smoothed particle hydrodynamics, J Comput Phys. 191 (2003) 448–475. https://doi.org/10.1016/S0021-9991(03)00324-3.

[36] S. Adami, X.Y. Hu, N.A. Adams, A new surface-tension formulation for multi-phase SPH using a reproducing divergence approximation, J Comput Phys. 229 (2010) 5011–5021. https://doi.org/10.1016/j.jcp.2010.03.022.

[37] A.C.H. Kruisbrink, F.R. Pearce, T. Yue, H.P. Morvan, An SPH multi-fluid model based on quasi buoyancy for interface stabilization up to high density ratios and realistic wave speed ratios, Int J Numer Methods Fluids. 87 (2018) 487–507. https://doi.org/10.1002/fld.4498.

[38] B.X. Zheng, Z. Chen, A multiphase smoothed particle hydrodynamics model with lower numerical diffusion, J Comput Phys. 382 (2019) 177–201. https://doi.org/10.1016/j.jcp.2019.01.012.

[39] J.U. Brackbill, D.B. Kothe, C. Zemach, A continuum method for modeling surface tension, J Comput Phys. 100 (1992) 335–354. https://doi.org/10.1016/0021-9991(92)90240-Y.

[40] J.P. Morris, Simulating surface tension with smoothed particle hydrodynamics, Int J Numer Methods Fluids. 33 (2000) 333–353. https://doi.org/10.1002/1097-0363(20000615)33:3<333::AID-FLD11>3.0.CO;2-7.

[41] B.E. Launder, D.B. Spalding, The numerical computation of turbulent flows, Comput Methods Appl Mech Eng. 3 (1974) 269–289. https://doi.org/10.1016/0045-7825(74)90029-2.

[42] S. Shao, Simulation of breaking wave by SPH method coupled with k-ε model, Journal of Hydraulic Research. 44 (2006) 338–349. https://doi.org/10.1080/00221686.2006.9521686.

[43] S. Shao, Incompressible SPH simulation of wave breaking and overtopping with turbulence modelling, Int J Numer Methods Fluids. 50 (2006) 597–621. https://doi.org/10.1002/fld.1068.

[44] J.J. Monaghan, A turbulence model for smoothed particle hydrodynamics, European Journal of Mechanics, B/Fluids. 30 (2011) 360–370. https://doi.org/10.1016/j.euromechflu.2011.04.002.

[45] M. Ferrand, D.R. Laurence, B.D. Rogers, D. Violeau, C. Kassiotis, Unified semi-analytical wall boundary conditions for inviscid, laminar or turbulent flows in the meshless SPH method, Int J Numer Methods Fluids. 71 (2013) 446–472. https://doi.org/10.1002/fld.3666.

[46] A. Leroy, D. Violeau, M. Ferrand, L. Fratter, A. Joly, A new open boundary formulation for incompressible SPH, Computers and Mathematics with Applications. 72 (2016) 2417–2432. https://doi.org/10.1016/j.camwa.2016.09.008.

[47] S.E. Arena, J.F. Gonzalez, E. Crespe, Characterisation of SPH noise in simulations of protoplanetary discs, in: Proceedings of the International Astronomical Union, 2010: pp. 393–394. https://doi.org/10.1017/S1743921311020485.

[48] S. Shao, SPH-LES MODEL USING FOR WAVE DISSIPATION Here the Smoothed Particle Hydrodynamics, (2003) 397–402.

[49] S. Shao, C. Ji, SPH computation of plunging waves using a 2-D sub-particle scale (SPS) turbulence model, Int J Numer Methods Fluids. 51 (2006) 913–936. https://doi.org/10.1002/fld.1165.

[50] R.A. Dalrymple, B.D. Rogers, Numerical modeling of water waves with the SPH method, Coastal Engineering. 53 (2006) 141–147. https://doi.org/10.1016/j.coastaleng.2005.10.004.

[51] A. Mayrhofer, D. Laurence, B.D. Rogers, D. Violeau, DNS and LES of 3-D wall-bounded turbulence using Smoothed Particle Hydrodynamics, Comput Fluids. 115 (2015) 86–97. https://doi.org/10.1016/j.compfluid.2015.03.029.

[52] A. di Mascio, M. Antuono, A. Colagrossi, S. Marrone, Smoothed particle hydrodynamics method from a large eddy simulation perspective, Physics of Fluids. 29 (2017). https://doi.org/10.1063/1.4978274.

[53] D.D. Meringolo, Y. Liu, X.Y. Wang, A. Colagrossi, Energy balance during generation, propagation and absorption of gravity waves through the δ-LES-SPH model, Coastal Engineering. 140 (2018) 355–370. https://doi.org/10.1016/j.coastaleng.2018.07.007.

[54] D. Violeau, S. Piccon, J.-P. Chabard, TWO ATTEMPTS OF TURBULENCE MODELLING IN SMOOTHED PARTICLE HYDRODYNAMICS, in: Advances in Fluid Modeling and Turbulence Measurements, WORLD SCIENTIFIC, 2002: pp. 339–346. https://doi.org/10.1142/9789812777591_0041.

[55] D. de Padova, M. Mossa, S. Sibilla, E. Torti, 3D SPH modelling of hydraulic jump in a very large channel, Journal of Hydraulic Research. 51 (2013) 158–173. https://doi.org/10.1080/00221686.2012.736883.

[56] E. Kazemi, A. Nichols, S. Tait, S. Shao, SPH modelling of depth-limited turbulent open channel flows over rough boundaries, Int J Numer Methods Fluids. 83 (2017) 3–27. https://doi.org/10.1002/fld.4248.

[57] E. Kazemi, K. Koll, S. Tait, S. Shao, SPH modelling of turbulent open channel flow over and within natural gravel beds with rough interfacial boundaries, Adv Water Resour. 140 (2020). https://doi.org/10.1016/j.advwatres.2020.103557.

[58] A. Mayrhofer, B.D. Rogers, D. Violeau, M. Ferrand, Investigation of wall bounded flows using SPH and the unified semi-analytical wall boundary conditions, Comput Phys Commun. 184 (2013) 2515–2527. https://doi.org/10.1016/j.cpc.2013.07.004.

[59] D. López, R. Marivela, L. Garrote, Smoothed particle hydrodynamics model applied to hydraulic structures: A hydraulic jump test case, Journal of Hydraulic Research. 48 (2010) 142–158. https://doi.org/10.1080/00221686.2010.9641255.

[60] E. Bertevas, T. Tran-Duc, K. Le-Cao, B.C. Khoo, N. Phan-Thien, A smoothed particle hydrodynamics (SPH) formulation of a two-phase mixture model and its application to turbulent sediment transport, Physics of Fluids. 31 (2019). https://doi.org/10.1063/1.5122671.

[61] P.R. Spalart, S.R. Allmaras, One-equation turbulence model for aerodynamic flows, Recherche Aerospatiale. (1994) 5–21. https://doi.org/10.2514/6.1992-439.

[62] S.J. Lind, R. Xu, P.K. Stansby, B.D. Rogers, Incompressible smoothed particle hydrodynamics for free-surface flows: A generalised diffusion-based algorithm for stability and validations for impulsive flows and propagating waves, J

Comput Phys. 231 (2012) 1499–1523. https://doi.org/10.1016/j.jcp.2011.10.027.

[63] X. Zheng, Q.W. Ma, W.Y. Duan, Incompressible SPH method based on Rankine source solution for violent water wave simulation, J Comput Phys. 276 (2014) 291–314. https://doi.org/10.1016/j.jcp.2014.07.036.

[64] J. Bonet, S. Kulasegaram, Alternative total lagrangian formulations for corrected smooth particle hydrodynamics (CSPH) methods in large strain dynamic problems, Revue Europeenne Des Elements. 11 (2002) 893–912. https://doi.org/10.3166/reef.11.893-912.

[65] J. Bonet, S. Kulasegaram, Remarks on tension instability of Eulerian and Lagrangian corrected smooth particle hydrodynamics (CSPH) methods, Int J Numer Methods Eng. 52 (2001) 1203–1220. https://doi.org/10.1002/nme.242.

[66] J. Bonet, S. Kulasegaram, Correction and stabilization of smooth particle hydrodynamics methods with applications in metal forming simulations, 2000.

[67] C.H. Lee, A.J. Gil, O.I. Hassan, J. Bonet, S. Kulasegaram, A variationally consistent Streamline Upwind Petrov–Galerkin Smooth Particle Hydrodynamics algorithm for large strain solid dynamics, Comput Methods Appl Mech Eng. 318 (2017) 514–536. https://doi.org/10.1016/j.cma.2017.02.002.

[68] F.R. Ming, A.M. Zhang, X.Y. Cao, A robust shell element in meshfree SPH method, Acta Mechanica Sinica/Lixue Xuebao. 29 (2013) 241–255. https://doi.org/10.1007/s10409-013-0017-2.

[69] J.J. Monaghan, Smoothed Particle Hydrodynamics, Annu Rev Astron Astrophys. 30 (1992) 543–574. https://doi.org/10.1146/annurev.aa.30.090192.002551.

[70] M.schussler and D. Schmitt, Comments on Smoothed Particle Hydrodynamics, Astron Astrophys. 97 (1981) 373–379.

[71] H. Wendland, Piecewise polynomial, positive definite and compactly supported radial functions of minimal degree, Adv Comput Math. 4 (1995) 389–396. https://doi.org/10.1007/BF02123482.

[72] J.I. Read, T. Hayfield, O. Agertz, Resolving mixing in smoothed particle hydrodynamics, Mon Not R Astron Soc. 405 (2010) 1513–1530. https://doi.org/10.1111/j.1365-2966.2010.16577.x.

[73] S. Korzilius, A. Kruisbrink, T. Yue, W. Schilders, M. Anthonissen, Momentum conserving methods that reduce particle clustering in SPH, 2014.

[74] D.J. Price, Smoothed particle hydrodynamics and magnetohydrodynamics, J Comput Phys. 231 (2012) 759–794. https://doi.org/10.1016/j.jcp.2010.12.011.

[75] G.A. Dilts, Moving least-squares particle hydrodynamics II: conservation and boundaries, Int J Numer Methods Eng. 48 (2000) 1503–1524. https://doi.org/10.1002/1097-0207(20000810)48:10<1503::AID-NME832>3.0.CO;2-D.

[76] L.D.G. Sigalotti, H. López, Adaptive kernel estimation and SPH tensile instability, Computers and Mathematics with Applications. 55 (2008) 23–50. https://doi.org/10.1016/j.camwa.2007.03.007.

[77] V. Sriram, Q.W. Ma, Improved MLPG_R method for simulating 2D interaction between violent waves and elastic structures, J Comput Phys. 231 (2012) 7650–7670. https://doi.org/10.1016/j.jcp.2012.07.003.

[78] S. Adami, X.Y. Hu, N.A. Adams, A transport-velocity formulation for smoothed particle hydrodynamics, J Comput Phys. 241 (2013) 292–307. https://doi.org/10.1016/j.jcp.2013.01.043.

[79] C. Zhang, X.Y. Hu, N.A. Adams, A generalized transport-velocity formulation for smoothed particle hydrodynamics, J Comput Phys. 337 (2017) 216–232. https://doi.org/10.1016/j.jcp.2017.02.016.

[80] A.K. Chaniotis, D. Poulikakos, P. Koumoutsakos, Remeshed Smoothed Particle Hydrodynamics for the Simulation of Viscous and Heat Conducting Flows, 90 (2002) 67–90. https://doi.org/10.1006/jcph.2002.7152.

[81] M.B. Liu, G.R. Liu, Smoothed particle hydrodynamics (SPH): An overview and recent developments, 2010. https://doi.org/10.1007/s11831-010-9040-7.

[82] J.J. Monaghan, Particle methods for hydrodynamics, Computer Physics Reports. 3 (1985) 71–124. https://doi.org/10.1016/0167-7977(85)90010-3.

[83] J.J. Monaghan, Smoothed particle hydrodynamics, Reports on Progress in Physics. 68 (2005) 1703–1759. https://doi.org/10.1088/0034-4885/68/8/R01.

[84] J.J. Monaghan, Smoothed particle hydrodynamics, Annu Rev Astron Astrophys. 30 (1992) 543–574. https://doi.org/10.1146/annurev.aa.30.090192.002551.

[85] J.J. Monaghan, Why Particle Methods Work, SIAM Journal on Scientific and Statistical Computing. 3 (1982) 422–433. https://doi.org/10.1137/0903027.

[86] S.J. Watkins, A.S. Bhattal, N. Francis, J.A. Turner, A.P. Whitworth, A new prescription for viscosity in Smoothed Particle Hydro dynamics, Astron Astrophys Suppl Ser. 119 (1996) 177–187. https://doi.org/10.1051/aas:1996104.

[87] L. Brookshaw, A Method of Calculating Radiative Heat Diffusion in Particle Simulations, Publications of the Astronomical Society of Australia. 6 (1985) 207–210. https://doi.org/10.1017/S1323358000018117.

[88] J.P. Morris, P.J. Fox, Y. Zhu, Modeling Low Reynolds Number Incompressible Flows Using SPH, J Comput Phys. 136 (1997) 214–226. https://doi.org/10.1006/JCPH.1997.5776.

[89] P.W. Cleary, J.J. Monaghan, Conduction Modelling Using Smoothed Particle Hydrodynamics, J Comput Phys. 148 (1999) 227–264. https://doi.org/10.1006/jcph.1998.6118.

[90] A. Tartakovsky, P. Meakin, Modeling of surface tension and contact angles with smoothed particle hydrodynamics, Phys Rev E Stat Nonlin Soft Matter Phys. 72 (2005) 1–9. https://doi.org/10.1103/PhysRevE.72.026301.

[91] A.M. Tartakovsky, P. Meakin, A smoothed particle hydrodynamics model for miscible flow in three-dimensional fractures and the two-dimensional Rayleigh-Taylor instability, J Comput Phys. 207 (2005) 610–624. https://doi.org/10.1016/j.jcp.2005.02.001.

[92] P.W. Cleary, Modelling confined multi-material heat and mass flows using SPH, Appl Math Model. 22 (1998) 981–993. https://doi.org/10.1016/S0307-904X(98)10031-8.

[93] D. Violeau, R. Issa, Numerical modelling of complex turbulent free-surface flows with the SPH method: An overview, Int J Numer Methods Fluids. 53 (2007) 277–304. https://doi.org/10.1002/fld.1292.

[94] J. Bonet, T.S.L. Lok, Variational and momentum preservation aspects of Smooth Particle Hydrodynamic formulations, Comput Methods Appl Mech Eng. 180 (1999) 97–115. https://doi.org/10.1016/S0045-7825(99)00051-1.

[95] X. Zheng, X. Lv, Q. Ma, W. Duan, A. Khayyer, S. Shao, An improved solid boundary treatment for wave–float interactions using ISPH method, International Journal of Naval Architecture and Ocean Engineering. 10 (2018) 329–347. https://doi.org/10.1016/j.ijnaoe.2017.08.001.

[96] X. Zheng, Q. Ma, S. Shao, Study on SPH viscosity term formulations, Applied Sciences (Switzerland). 8 (2018) 1–17. https://doi.org/10.3390/app8020249.

[97] E.Y.M. Lo, S. Shao, Simulation of near-shore solitary wave mechanics by an incompressible SPH method, Applied Ocean Research. 24 (2002) 275–286. https://doi.org/10.1016/S0141-1187(03)00002-6.

[98] J.J. MONAGHAN, Simulating free surface flows with sph, J Comput Phys. 110 (1992) 399–406.

[99] J.J. Monaghan, A. Kos, Solitary Waves on a Cretan Beach, J Waterw Port Coast Ocean Eng. 125 (1999) 145–155. https://doi.org/10.1061/(ASCE)0733-950X(1999)125:3(145).

[100] M. Antuono, A. Colagrossi, S. Marrone, D. Molteni, Free-surface flows solved by means of SPH schemes with numerical diffusive terms, Comput Phys Commun. 181 (2010) 532–549. https://doi.org/10.1016/j.cpc.2009.11.002.

[101] P.N. Sun, A. Colagrossi, S. Marrone, M. Antuono, A.M. Zhang, Multi-resolution Delta-plus-SPH with tensile instability control: Towards high Reynolds number flows, Comput Phys Commun. 224 (2018) 63–80. https://doi.org/10.1016/j.cpc.2017.11.016.

[102] D. Molteni, A. Colagrossi, A simple procedure to improve the pressure evaluation in hydrodynamic context using the SPH, Comput Phys Commun. 180 (2009) 861–872. https://doi.org/10.1016/j.cpc.2008.12.004.

[103] I. Hammani, S. Marrone, A. Colagrossi, G. Oger, D. le Touzé, Detailed study on the extension of the δ-SPH model to multi-phase flow, Comput Methods Appl Mech Eng. 368 (2020). https://doi.org/10.1016/j.cma.2020.113189.

[104] M. Aguirre, A.J. Gil, J. Bonet, A. Arranz Carreño, A vertex centred Finite Volume Jameson-Schmidt-Turkel (JST) algorithm for a mixed conservation formulation in solid dynamics, J Comput Phys. 259 (2014) 672–699. https://doi.org/10.1016/j.jcp.2013.12.012.

[105] C.H. Lee, A.J. Gil, G. Greto, S. Kulasegaram, J. Bonet, A new Jameson–Schmidt–Turkel Smooth Particle Hydrodynamics algorithm for large strain explicit fast dynamics, Comput Methods Appl Mech Eng. 311 (2016) 71–111. https://doi.org/10.1016/j.cma.2016.07.033.

[106] B.K. Larkin, Numerical solution of the continuity equation, AIChE Journal. 12 (1966) 1027–1027. https://doi.org/10.1002/aic.690120538.

[107] S. Shao, E.Y.M. Lo, Incompressible SPH method for simulating Newtonian and non-Newtonian flows with a free surface, Adv Water Resour. 26 (2003) 787–800. https://doi.org/10.1016/S0309-1708(03)00030-7.

[108] E.S. Lee, C. Moulinec, R. Xu, D. Violeau, D. Laurence, P. Stansby, Comparisons of weakly compressible and truly incompressible algorithms for the SPH mesh free particle method, J Comput Phys. 227 (2008) 8417–8436. https://doi.org/10.1016/j.jcp.2008.06.005.

[109] B. Ren, M. He, P. Dong, H. Wen, Nonlinear simulations of wave-induced motions of a freely floating body using WCSPH method, Applied Ocean Research. 50 (2015) 1–12. https://doi.org/10.1016/j.apor.2014.12.003.

[110] B. Ren, M. He, Y. Li, P. Dong, Application of smoothed particle hydrodynamics for modeling the wave-moored floating breakwater interaction, Applied Ocean Research. 67 (2017) 277–290. https://doi.org/10.1016/j.apor.2017.07.011.

[111] D. Li, X. Li, Y. Lin, Numerical simulation of droplet impacting liquid surface by SPH, Sci China Technol Sci. 54 (2011) 1873–1880. https://doi.org/10.1007/s11431-011-4422-0.

[112] J.J. Monaghan, SPH without a Tensile Instability, J Comput Phys. 311 (2000) 290–311. https://doi.org/10.1006/jcph.2000.6439.

[113] J.J. Monaghan, J.B. Kajtar, SPH particle boundary forces for arbitrary boundaries, Comput Phys Commun. 180 (2009) 1811–1820. https://doi.org/10.1016/j.cpc.2009.05.008.

[114] M. Bayareh, A. Nourbakhsh, F. Rouzbahani, V. Jouzaei, Explicit incompressible SPH algorithm for modelling channel and lid-driven flows, SN Appl Sci. 1 (2019) 1040. https://doi.org/10.1007/s42452-019-1072-5.

[115] U. Ghia, K.N. Ghia, C.T. Shin, High-Re solutions for incompressible flow using the Navier-Stokes equations and a multigrid method, J Comput Phys. 48 (1982) 387–411. https://doi.org/10.1016/0021-9991(82)90058-4.

[116] M. Antuono, S. Marrone, A. Colagrossi, B. Bouscasse, Energy balance in the δ-SPH scheme, Comput Methods Appl Mech Eng. 289 (2015) 209–226. https://doi.org/10.1016/j.cma.2015.02.004.

[117] P.N. Sun, A. Colagrossi, S. Marrone, A.M. Zhang, ScienceDirect The δ plus -SPH model : Simple procedures for a further improvement of the SPH scheme, Comput. Methods Appl. Mech. Engrg. 315 (2017) 25–49. https://doi.org/10.1016/j.cma.2016.10.028.

[118] D. le Touzé, A. Colagrossi, G. Colicchio, M. Greco, A critical investigation of smoothed particle hydrodynamics applied to problems with free-surfaces, Int J Numer Methods Fluids. 65 (2013) n/a-n/a. https://doi.org/10.1002/fld.3819.

[119] Q.W. Ma, J.T. Zhou, MLPG-R method for numerical simulation of 2D breaking waves, CMES - Computer Modeling in Engineering and Sciences. 43 (2009) 277–303. https://doi.org/10.3970/cmes.2009.043.277.

[120] A. Colagrossi, M. Landrini, B.W. Ritchiew, P.A. Thomas, Numerical simulation of interfacial flows by smoothed particle hydrodynamics, J Comput Phys. 191 (2003) 448–475. https://doi.org/10.1016/S0021-9991(03)00324-3.

[121] J.O.D.K. and B.B. Z Q Zhou, A nonlinear 3D approach to simulate green water dynamics on deck, Seventh International Conference on Numerical Ship Hydrodynamics. (1999) 1–15. citeulike-article-id:10957463.

[122] J.C. Martin, W.J. Moyce, W.G. Penney, A.T. Price, C.K. Thornhill, Part IV. An experimental study of the collapse of liquid columns on a rigid horizontal plane, Philosophical Transactions of the Royal Society of London. Series A, Mathematical and Physical Sciences. 244 (1952) 312–324. https://doi.org/10.1098/rsta.1952.0006.

[123] G. Duan, B. Chen, S. Koshizuka, H. Xiang, Stable multiphase moving particle semi-implicit method for incompressible interfacial flow, Comput Methods Appl Mech Eng. 318 (2017) 636–666. https://doi.org/10.1016/j.cma.2017.01.002.

[124] N. Grenier, M. Antuono, A. Colagrossi, D. le Touzé, B. Alessandrini, An Hamiltonian interface SPH formulation for multi-fluid and free surface flows, J Comput Phys. 228 (2009) 8380–8393. https://doi.org/10.1016/j.jcp.2009.08.009.

[125] J.J. Monaghan, Smoothed particle hydrodynamics and its diverse applications, Annu Rev Fluid Mech. 44 (2011) 323–346. https://doi.org/10.1146/annurev-fluid-120710-101220.

[126] B.X. Zheng, L. Sun, P. Yu, A novel interface method for two-dimensional multiphase SPH: Interface detection and surface tension formulation, J Comput Phys. 431 (2021). https://doi.org/10.1016/j.jcp.2021.110119.

[127] O.M. Faltinsen, A Numerical Nonlinear Method of Sloshing in Tanks with Two-Dimensional Flow, Journal of Ship Research. 22 (1978) 193–202. https://doi.org/10.5957/jsr.1978.22.3.193.

[128] D. Liu, P. Lin, Three-dimensional liquid sloshing in a tank with baffles, Ocean Engineering. 36 (2009) 202–212. https://doi.org/10.1016/j.oceaneng.2008.10.004.

[129] A. Colagrossi, G. Colicchio, C. Lugni, M. Brocchini, A study of violent sloshing wave impacts using an improved SPH method, Journal of Hydraulic Research. 48 (2010) 94–104. https://doi.org/10.1080/00221686.2010.9641250.

[130] C. Lugni, M. Brocchini, O.M. Faltinsen, Wave impact loads: The role of the flip-through, Physics of Fluids. 18 (2006). https://doi.org/10.1063/1.2399077.

[131] P. Sun, A.M. Zhang, S. Marrone, F. Ming, An accurate and efficient SPH modeling of the water entry of circular cylinders, Applied Ocean Research. 72 (2018) 60–75. https://doi.org/10.1016/j.apor.2018.01.004.

[132] P.N. Sun, A. Colagrossi, S. Marrone, M. Antuono, A.M. Zhang, A consistent approach to particle shifting in the δ-Plus-SPH model, Comput Methods Appl Mech Eng. 348 (2019) 912–934. https://doi.org/10.1016/j.cma.2019.01.045.

[133] S. Grossmann, D. Lohse, C. Sun, High-Reynolds Number Taylor-Couette Turbulence, Annu Rev Fluid Mech. 48 (2016) 53–80. https://doi.org/10.1146/annurev-fluid-122414-034353.

[134] A.C.H. Kruisbrink, COAST 3.2 - SPH Modelling Report, (2018) 1–71.